NORTHWESTERN UNIVERSITY

Mechanistic Modeling of Hydrocarbon Autoxidation: Theory and Application to the Study of Lubricant Degradation

A DISSERTATION

SUBMITTED TO THE GRADUATE SCHOOL
IN PARTIAL FULFILLMENT OF THE REQUIREMENTS

for the degree

DOCTOR OF PHILOSOPHY

Field of Chemical Engineering

By

Jim Pfaendtner

EVANSTON, ILLINOIS

June 2007

ABSTRACT

Mechanistic Modeling of Hydrocarbon Autoxidation: Theory and Application to the Study of Lubricant Degradation

Jim Pfaendtner

Autoxidation is a primary route by which lubricants in working conditions undergo degradation. Degraded lubricants, if not replaced periodically, contribute to increased wear and product failure. Experimental studies of lubricant degradation have yielded useful results but have left important questions unanswered. While many computational studies of degradation have been carried out to address these questions, all degradation models which have been proposed thus far fail to agree quantitatively with experimental data and often do not even give qualitative agreement. The purpose of this research is to develop chemical kinetics models of lubricant degradation. Due to the complexity of autoxidation chemistry in the condensed phase, it is prohibitive to assemble a reaction mechanism manually. Therefore, the principles of automated mechanism generation were used to aid in the assembly of reaction networks which model lubricant degradation. Specifically, new reaction networks were established for condensed-phase autoxidation of n-octane and n-decane. The sensitivity of the kinetic parameters was explored and limited parameter estimation was used to improve the agreement between the models and experimental data.

Quick and reliable estimation of reaction kinetics is essential since complete experimental characterization of complex reacting systems is not currently possible. However, quantum mechanics and transition state theory can augment our knowledge of chemical reactivity where experiments have failed to provide sufficient information. A computational framework was developed that incorporates electronic structure methods with a rigorous treatment of one-dimensional anharmonic motions to provide accurate thermodynamic and kinetic properties for a wide range of reactions.

Using this approach we have developed structure-reactivity relationships for several reaction families important to lubricant degradation: hydrogen transfer, hydrogen abstraction and β-scission. These new relationships provided chemical and physical insight to the governing reaction families in lubricant degradation and added to a library of structure-reactivity relationships suitable for studying oxidation chemistry. For example, complex contrathermodynamic behavior in the reactions of alkylperoxy radicals and hydrocarbons was uncovered, and a new hypothesis to explain this behavior was given.

Acknowledgments

This work would not have been possible without the input and support from many people. I would like to take a moment to acknowledge the mentors, friends, and family who have helped me to complete my PhD.

For the last five years, I have been very fortunate to work under the supervision of Linda Broadbelt. Linda has an uncompromising commitment to her graduate students and I appreciate the intellectual and personal freedom she affords her research group. I have often commented to Linda that, "I am the happiest graduate student that I know." Such a statement is not possible without a great advisor. I would also like to thank my PhD committee for their time and suggestions. Vassily Hatzimanikatis, Peter Stair, John Torkelson and Jane Wang have been very helpful in all phases of completion of this work. In particular, I would like to acknowledge the mentorship of Vassily Hatzimanikatis who has helped me to prepare for an academic career.

I would like to thank the Broadbelt and Snurr research groups for their feedback and help throughout five years of group meetings. I have enjoyed the companionship of 17 different members of the Broadbelt group who have been my labmates. I would especially like to thank Simon Albo for helping me to learn that "sometimes you just have to figure it out."

My time at Northwestern was much more enjoyable because of the great friends that I made here. Simon Albo and Perla Rittigstein have been wonderful friends. I am also grateful for the friendship of Andrew Cho, Rodney Priestly, Daniel Stouffer, Xinrui Yu and the members of the

Shea research group – Tiffany Houchin Ray, Laura De Laporte, and Erin West – with whom I have run many hundreds of miles.

I would be remiss if I did not acknowledge the excellent friendship of John and Janet Moran, Alex and Jess Jones, and Nicole Robinson. I would like to thank my friends for their support as I completed my PhD. I would also like to thank my parents and siblings – Carrie, John and Amy – for their encouragement over the last five years. My parents John and Andrea have always encouraged me to excel academically and enthusiastically supported me during graduate school, and my sister Carrie and her husband Brad have been great friends during my time in Chicago.

Finally, I wish to dedicate this dissertation to my wife Jill. I could not have completed this undertaking without the sacrifice and support that Jill has given to me. Jill has continually cared for me and taken care of the menial details of life so that I could devote more time to my work. More importantly, Jill never failed to give me the encouragement and strength to keep working through the many struggles that my classes and research have offered over the years. Thank you Jill, this is for you.

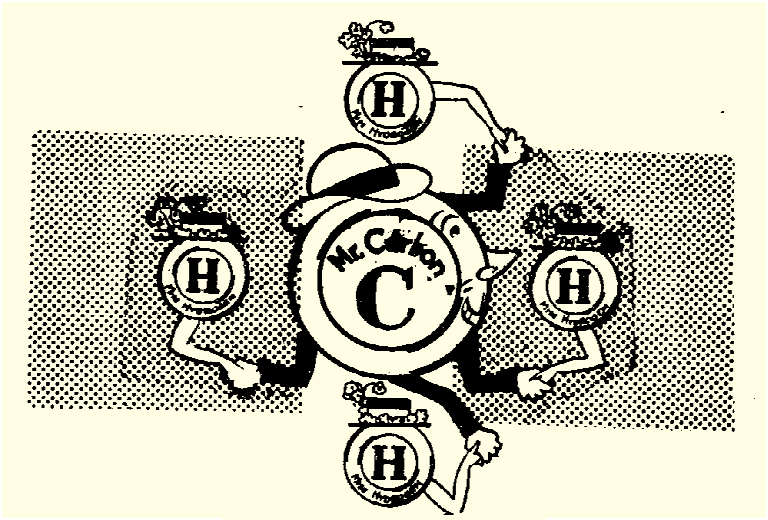

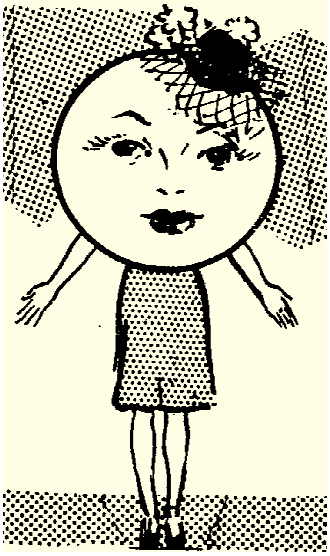

These graphic representations of “papa carbon”, “mama hydrogen”, and “miss oxygen” (Zamboni, 1945) have been the delight of nearly every ChBE graduate student at Northwestern in the past three years.

Contents

List of Tables

List of Figures

Chapter 1

Introduction

Modeling and simulation are essential parts of our toolkit for understanding complex reacting systems. Advances in experimental techniques have tremendously increased our ability to study smaller length and time scales with increased resolution. However, for complex reacting systems it is not generally possible to experimentally resolve the complete reaction network consisting of all of the reactive intermediates, elementary reaction pathways, and stable products. Furthermore, dynamic analysis of a complete reaction network requires specification of all reaction rate coefficients and the thermodynamic properties of all species – information that is also challenging and time consuming to capture from experiment. Kinetic modeling is an important and necessary tool for filling gaps in experimental studies, interpreting experimental results, and also providing data for which experimental studies are too difficult or even impossible to conduct.

One class of reacting systems in which advanced kinetic modeling techniques have not been widely applied is condensed-phase free-radical oxidation of hydrocarbons. Prominent examples include industrial air oxidation of petroleum products (Emanuel and Gál, 1986; Suresh et al., 2000) and the degradation of lubricating oils (Rudnick and Shubkin, 1999). These systems present unique challenges due to the immense diversity in the spectrum of products obtained, and also the large number of possible theoretical reaction channels. Due to its importance to the petrochemical and

automotive industries, this reaction class has received considerable attention in the research literature. However, there is still a fundamental need for mechanistic models of free-radical oxidation that can predict the behavior of these systems at the molecular level. This is particularly true for the case of lubricant degradation in which lubricant formulations and additive development could be further improved with more detailed models.

Free-radical oxidation is a primary route by which lubricants in working conditions undergo degradation. Degraded lubricants, if not replaced periodically, contribute to increased wear and product failure. Such wear and failure are major contributors to the estimated $100 billion that could be saved annually given improved attention to tribology (Krim, 2002). While many computational studies of degradation have been carried out to address these questions, all degradation models which have been proposed thus far fail to agree quantitatively with experimental data and often do not even give qualitative agreement. Due to the complexity of autoxidation chemistry in the condensed phase, it is prohibitive to assemble a reaction mechanism manually. Therefore, the principles of automated mechanism generation will be used to aid in the assembly of reaction networks which model lubricant degradation.

Using automated mechanism generation to build mechanistic models of free-radical oxidation presents a number of unique challenges. For example, compared to the gas-phase there are different reaction channels which dominate initiation and termination in condensed-phase free-radical oxidation. Furthermore, using an approach such as automated mechanism generation relies on the correct specification of all important reaction families. Therefore, it is imperative that the dominant reaction families be identified since they are specified as input parameters to the mechanism generation algorithm. Another major challenge in modeling low temperature free-radical chemistry is that the mechanism will be much more sensitive to small differences in activation energies between reactions than comparable high-temperature systems. Accordingly, there is a great need for accurate structure-reactivity relationships for all of the different reaction families in free-radical oxidation.

However, the research literature is only sparsely filled with kinetic data for alkylperoxy radicals and other radical types that are important in lubricant degradation. Fortunately, computational quantum chemistry and transition state theory can be used as a replacement for experimentally determined kinetic parameters such as the activation energy. Thus far, there has been very little attention given to the use of quantum chemistry in development of structure-reactivity relationships. Important questions remain regarding the specific quantum chemical method that is best suited to the development of kinetic correlations and also what elements of a computational approach are required for accurate calculation of kinetic and thermodynamic properties. There is a need for an overall framework from which we can specify how to quickly, accurately, and reliably determine structure-reactivity relationships from theoretical methods.

This thesis is devoted to the mechanistic modeling of hydrocarbon autoxidation with the specific application to the degradation of lubricating oils. This work is divided into three broad sections. A general approach for mechanistic modeling and associated background information is given in Chapter 2. Next, Chapters 3 – 6 develop a theoretical and computational framework from which structure-reactivity relationships can be resolved using computational quantum chemistry. Specifically, Chapter 3 is an overview of how accurate treatments of anharmonicity can be included in the calculation of kinetic and thermodynamic properties. Chapters 4 – 6 are three specific examples of how quantum chemistry and transition state theory can be used to resolve accurate structure-reactivity relationships for reaction families germane to lubricant degradation. Finally, Chapters 7 – 8 cover the development of mechanistic models of octane and decane autoxidation. Chapter 7 uses available experimental and theoretical studies to construct a library of structure-reactivity relationships for free-radical oxidation. This information is used to apply automated mechanism generation to octane and decane autoxidation in Chapter 8. Chapter 9 provides overall conclusions for this thesis research and offers recommendations for future work.

Chapter 2

Background: Lexicography of Kinetic Modeling of Complex Reaction Networks

2.1 Introduction

Complex reaction networks are ubiquitous. Reacting systems consisting of hundreds or thousands of species and reactions are common in many different types of seemingly disparate chemistries. Pyrolysis, oxidation, polymerization, amino acid biosynthesis, silicon nanoparticle growth and catalytic cracking all involve complex reaction networks that can originate in different ways. For example, hydrocarbon conversion processes in the petrochemical industry such as catalytic cracking, reforming and hydrocracking involve the transformation of complex mixtures of molecules via a large number of gas-phase and catalytic reactions, largely because petroleum feedstocks themselves are multicomponent mixtures (Froment, 2005; Narasimhan et al., 2004). Complex reaction networks can also manifest themselves for conversion of single components or simple mixtures of reactants, where the complexity is not derived from the feed but from the nature of the reactions. Oxidation and pyrolysis are classic examples of chemistries that create complex reaction networks of $O(10^2\text{-}10^4)$ of species from even simple molecules such as methane (Matheu et al., 2003) or

ethane (Tranter et al., 2002) because of the non-specificity of the free radical intermediates. Polymerization conditions are typically controlled such that only radical addition reactions are favored, but reaction networks for polymerization or depolymerization are indeed complex because of the thousands of possible chain lengths (Campbell et al., 2005; Hutchinson, 2001). Similarly, silicon nanoparticle production in the homogeneous phase starts with very simple reactants, silane and hydrogen, but thousands of different species are possible as particles grow to nanometer sizes that are of significance in semiconductor contamination (Wong et al., 2004a). Even with the specificity of enzymes, biochemical systems also involve numerous reactions of a large number of different species because of the wide range of functions that different enzymes perform (Hatzimanikatis et al., 2004, 2005; Holzhutter and Holzhutter, 2004; Li et al., 2004).

Although the chemistries enumerated here are seemingly diverse, they share many common features that can be uncovered by lexicography of kinetic modeling. A "dictionary" detailing the language of quantitative kinetic modeling can help unify the chemical principles underlying this wide array of systems, much in the same way that a dictionary unifies speakers of a common language. Chemical engineers are uniquely qualified to develop kinetic models of complex reaction systems that offer a quantitative framework to synthesize the efforts of chemists, biologists, mathematicians and other engineers. We understand the underlying physical sciences and also have the mathematical tools and modeling expertise to deconvolute the behavior of chemical and biochemical systems through kinetic models. It is thus important that we continuously refresh and refine our dictionary of kinetic modeling so that state-of-the-art methods can be brought to bear on the ever-widening array of reacting systems of interest to our discipline and that advances in quantitative analysis in one area – for example, metabolic engineering – that is seemingly disjoint from another – for example, silicon nanoparticle production – are seamlessly translated.

The lexicography of kinetic modeling of complex reaction networks begins with a definition of the key words. As illustrated in Figure 2.1, the building blocks of complex reaction networks are species (the nodes) and reactions (the edges). Foremost, it is necessary to know or postulate

which species are involved as reactants, products and reactive intermediates. It is then essential to define how they are connected, i.e., what the reactions are. The topology of the reaction network is essential, but it is not enough. In order to obtain quantitative insight from the reaction network, thermodynamics must be quantified to ensure microscopic reversibility and consistency with the thermodynamics of the overall reaction. The final, and most challenging, step is to specify a rate coefficient for each reaction. While analytical rate expressions still can provide tremendous insight into the controlling chemistry and are more compatible with process models because of their simplicity (Blackmond, 2003), we focus here on mechanistic kinetic, or microkinetic (Dumesic et al., 1993), modeling. Mechanistic models have the greatest potential for extrapolation and also allow the power of techniques such as computational quantum chemistry to be exploited.

Great success has already been achieved in kinetic modeling of homogeneous, gas-phase chemistries such as oxidation and pyrolysis. For example, reaction mechanisms have been proposed for a wide range of hydrocarbon substrates in combustion (Babushok and Tsang, 2004; Curran et al., 2002; Fournet et al., 2001; Ranzi et al., 2001; Westbrook et al., 2001), and understanding of the underlying chemistry is quite mature. Reaction networks that capture the essential reactions have been developed, and even adaptive kinetic modeling (Bhattacharjee et al., 2003; Schwer et al., 2003) can be performed so that coupling the reaction mechanisms with computational fluid dynamics models is facilitated. One reason that kinetic modeling has been so successful for these types of chemistries is that extensive experimental studies have been carried out to identify key reactive intermediates and even measure individual rate coefficients. Databases have been developed that summarize reactions and rate coefficients and "gold-standard" mechanisms are even available. These accomplishments underscore the importance of experimentalists and modelers working together and represent decades of concerted effort to develop quantitative pictures of complex chemistries.

Tremendous progress has also been made in heterogeneous catalytic systems in recent years, which are inherently more challenging than homogeneous, gas-phase systems because of the com-

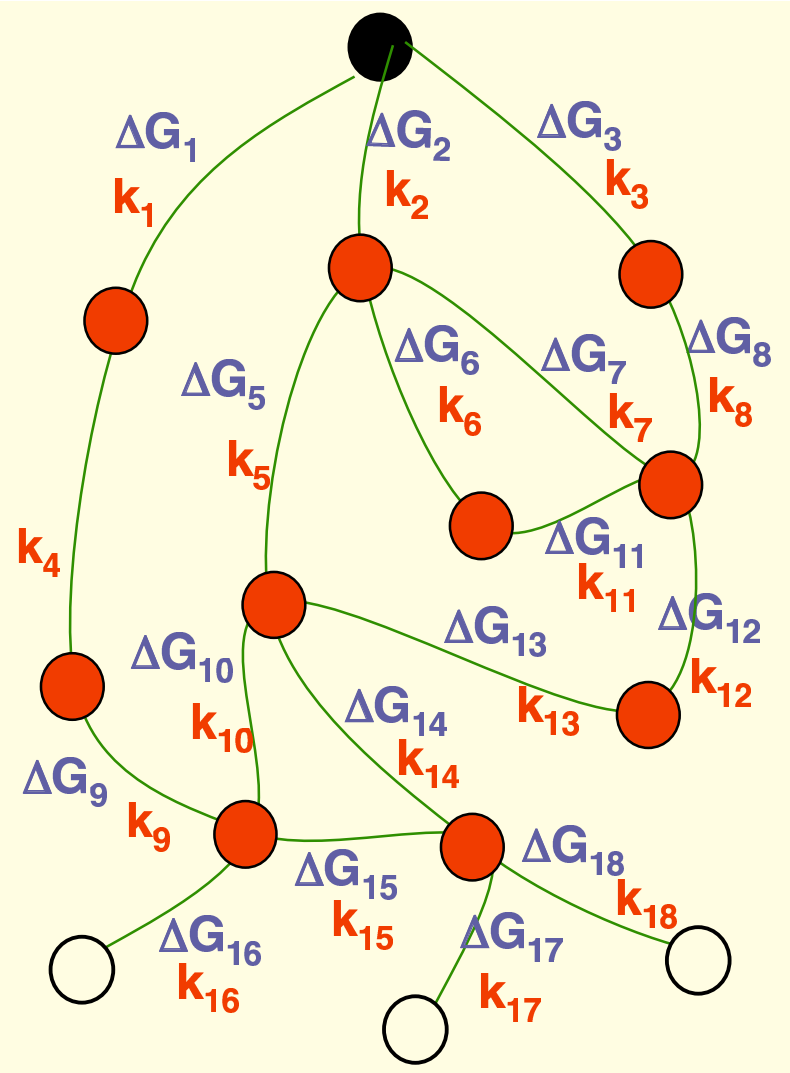

Figure 2.1: Complex reaction networks are composed of species as the nodes and reactions as the edges. The species can be global lumps, molecules, or reactive intermediates such as free radicals. For example, the network above might represent a reaction mechanism with the reactant represented as a solid circle, the products shown as open circles, and reactive intermediates denoted as shaded circles. The reactions are characterized by thermodynamics through free energies of reaction (ΔG_i) and kinetics through rate coefficients (k_i).

plexity of typical solid catalysts. Dumesic and coworkers helped spark this progress by demonstrating the power of microkinetic modeling for a number of different systems (Dumesic et al., 1993). For example, microkinetic modeling has been extremely valuable in developing a deep understanding of ammonia synthesis (Dooling et al., 1999b; Hinrichsen, 1999; Honkala et al., 2005; Mhadeshwar et al., 2004; Murzin, 2005; Zupanc et al., 2002). Another example is the work of Vlachos and coworkers (Mhadeshwar and Vlachos, 2004) who have recently demonstrated the ability to capture a wide array of different experimental studies for reactions of relatively small molecules (e.g., CO and H_2) on metal surfaces using a multiscale approach for specifying rate parameters. The ability to develop these microkinetic models has been greatly aided by computational quantum chemistry, which has allowed different configurations of surface intermediates to be interrogated in detail (Alcala et al., 2003, 2005; Ciobica et al., 2002; Klinke and Broadbelt, 1999b; Klinke et al., 1999, 1998; McMillan et al., 2003a,b).

On the cusp of the transformation of chemical engineering to chemical and biological (or biomolecular) engineering, an interesting question is what techniques and methods applied to "conventional" chemistries in the past can be exploited for applications to biochemical systems. If one adopts the viewpoint that quantification and understanding of the kinetics of complex biochemical reaction networks is in the same stage as combustion chemistry in the 1970s and factors in the tremendous advances in computational techniques and power in recent years, it is conceivable that complex biochemical reaction systems can be reliably modeled at the mechanistic level in the next two decades. One starting point for realizing this goal is to identify what commonalities exist that can be exploited and outline what new challenges must be overcome. To this end, this chapter describes the general elements of kinetic modeling of complex reaction networks, with an emphasis on computational techniques that have recently emerged. Techniques for uncovering the species and reactions are described first. Methods for specifying thermodynamic properties and rate coefficients are then discussed. Finally, future prospects for and challenges in kinetic model development are described.

2.2 Species (spē'shēz) and Reactions (rē-ăk'shenz)

The nodes of the reaction networks are species, and the edges connecting the nodes are the reactions. Depending on the level of detail included in the reaction network, the species can be molecules or intermediates such as free radicals or ions, and the reactions can be pathways or elementary steps. The first step in developing a kinetic model of a complex reaction network is to define its species space. One can imagine a species space that encompasses every possible permutation of every possible atom in the periodic table. However, it is clearly more practical to restrict the species space to the likely molecules and intermediates for the chemistry of interest and ultimately, the important species that are chiefly responsible for the observed chemical behavior.

The most obvious starting point for figuring out which species are involved in a particular reaction system is to observe and measure them experimentally, and the role of experimental methods in uncovering the details of complex reaction networks is certainly not discounted here. Rather, this chapter focuses on computational techniques that can serve as a complement or indeed, as a possible substitute, to experimental approaches. Quantum chemistry is becoming the kinetic modeler's computational method of choice to uncover details of species and reactions that are part of a complex reaction network. The approach is to use quantum chemistry to map the potential energy surfaces (PES) to determine the stability of intermediates and the likelihood that a reaction between a proposed set of species will take place. The potential energy landscape is revealed by solving the electronic Schrödinger equation, $\hat{H}\Psi = E\Psi$, where $\hat{H}$ is the Hamiltonian, E is the electronic energy, and Ψ is the wavefunction, for a number of nuclear configurations. This chapter is not meant to be a comprehensive review of computational quantum chemistry since there are several excellent texts and reviews available (Jensen, 1999; Leach, 2001; Santiso and Gubbins, 2004). Rather, we focus here on defining the important terms in the dictionary of kinetic modeling of complex reaction networks. To this end, a brief glossary of terms relevant to quantum mechanical methods is provided in Table 2.1. The essential message provided here is that the energy of a configuration

of atoms can be calculated, and minimum energy structures on the PES can be identified. These structures are likely stable intermediates along a reaction coordinate and provide some insight into the likely reactants and products of elementary steps.

Table 2.1: Glossary of terms relevant to computational **quantum chemistry.**

Word(s)	Abbreviation	Definition
Ab initio		From first principles. Used to denote molecular orbital methods that invoke a minimal number of approximations for solution of the Schrödinger equation.
Basis function		A function used in building up the description of molecular orbitals. Often, atomic orbitals are used but not always. Common forms of basis functions are Gaussians, planewaves, or numerical.
Basis set	3-21G, 6-311G*, LANL2DZ, cc-pVDZ, cc-pVTZ, cc-pVQZ	Complete set of basis functions that is used to represent the molecular orbitals. Gaussian functions are the most commonly used. The basis set simply consists of the relevant exponents and coefficients of the functions.
Configuration interaction	CIS, CISD	Introduces electron correlation by mixing in an optimum amount of different electronic configurations. The 'weightings' of these electronic configurations are called the CI coefficients.
Coupled cluster	CCSD, CCDT	Expresses the wavefunction using many determinants to include electron-electron correlation. Higher excitations are partially included, but the fact that their coefficients are determined by the lower order excitations helps reduce the computational demand.
Density functional theory	DFT	An approach for solving the Schrödinger equation that describes an interacting system of electrons via its density and not via its many-body wave function.
Functional	BP86, BLYP, B3LYP, PW91, XLYP	Relevant to density functional theory. In DFT, the exact exchange for a single determinant is replaced by a more general expression, the exchange-correlation functional, which can include terms accounting for both exchange energy and the electron correlation that are omitted from Hartree-Fock theory.

Word(s)	Abbreviation	Definition
Gaussian-3 theory	G3	A composite technique in which a sequence of well-defined *ab initio* molecular orbital calculations is performed to arrive at a total energy of a given molecular species.
Hartree-Fock	HF	A method that seeks to approximately solve the electronic Schrödinger equation. It assumes that the wavefunction can be approximated by a single Slater determinant made up of one spin orbital per electron. An electron is assumed to move in a mean field of the other electrons, i.e., electron-electron correlation is not included.
Møller-Plesset perturbation theory	MP2, MP4	Improves upon the Hartree-Fock solution by expanding the wavefunction in a Taylor series in a perturbation parameter. The X in MPX refers to the order of the expansion.
Semi-empirical method	PM3, AM1	Class of methods that solve the Schrödinger equation via parameterization against experimental data.

Solution of the Schrödinger equation has been brought into the hands of chemical engineers with the explosion of software packages (Gorelsky, 2004) that are readily available. The awarding of the Nobel Prize in Chemistry in 1998 to John Pople and Walter Kohn was in recognition of their accomplishments of putting computational chemistry in usable form. It is important, however, that the software not be treated as a "black box" since it is easy to obtain meaningless results. On the contrary, the user must be very prudent about selecting the method to solve the Schrödinger equation, as approximations must be made for all systems of practical interest. The different approaches for solving the Schrödinger equation are broadly classified as *ab initio* methods, density functional theory, and semi-empirical methods. The *ab initio* method to which other methods are often compared is Hartree-Fock (HF). The wavefunction is assumed to be a combination of molecular orbitals described as Slater determinants. Further, it is assumed that the molecular

orbitals are expanded linearly in terms of atomic orbitals with fixed coefficients. Solution is carried out self-consistently, with the coefficients of the molecular orbitals optimized until the electronic energy is minimized. Each electron is assumed to move in a mean field of the other electrons, such that the motion of the electrons is not correlated. It is this assumption upon which other *ab initio* methods seek to improve. These post-Hartree Fock methods include configuration interaction, coupled cluster and Møller-Plesset perturbation methods. As higher degrees of correlation are included, the computational demand increases. Hybrid methods, such as G3 (Curtiss et al., 1998), seek to mitigate this by using a lower level of theory to carry out geometry optimization and then use energies for a fixed nuclear configuration from a variety of different higher-level methods.

Density functional theory (DFT) is an alternative to HF and post-HF methods that formulates solution of the Schrödinger in terms of the electron density instead of the wavefunction. However, the problem of an approximate wavefunction is traded for the fact that the relationship between the electron density and the electronic energy is not known exactly. Specification of these relationships, or functionals, is one important controlling parameter of using DFT. There are also hybrid DFT functionals, where a small portion of the total energy is calculated via the HF methodology. Pure DFT is more computationally efficient than HF and has accuracy that is comparable to post-HF methods.

For all of these methods, the user must also select the way in which the molecular orbitals are represented in terms of atomic orbitals, which is referred to as the basis set. Broadly, there are four major types of basis sets: Gaussian-type, numerical, effective core potentials and plane waves. Gaussian, or Pople-type, basis sets are used most frequently because of their ease of integration, particularly for multi-centered overlap integrals. Effective core potentials treat valence electrons in detail and represent the core electrons in the form of a potential. These are appropriate for systems with heavy atoms with many electrons, such as transition metals, since they can make the calculation easier. Plane wave basis sets work well for extended periodic systems such as metals.

Successful demonstrations of the use of quantum chemistry to uncover details of reaction intermediates and reactions are growing. Quantum chemistry is an important entry in the dictionary of kinetic modeling of complex reaction systems because it can, in theory, be applied to any type of reaction system, from gas-phase pyrolysis and oxidation (Carstensen et al., 2005; Matheu et al., 2003) to heterogeneous catalysis (Alcala et al., 2003, 2005; Broadbelt and Snurr, 2000; Ciobica et al., 2002; Dooling et al., 1999a; Greeley and Mavrikakis, 2004; Heyden et al., 2005; Hinnemann et al., 2005; Vang et al., 2005; Wells et al., 2004a,b) to enzyme-catalyzed biotransformations (Gao and Truhlar, 2002; Rod and Ryde, 2005).

An alternative computational approach to studying reactions individually using quantum chemical calculations is to use prior, often minimal, knowledge about likely chemical transformations to construct rules and reaction types that can be applied systematically to reactants to create products. This is the central concept of automated network, or mechanism, generation. The underlying tenet is that complex reaction networks are simply the manifestation of a small number of reaction types being applied to a large number of species. Knowledge of the appropriate reaction types is gained through experimental studies or complementary theoretical investigations of the system of interest and then translated into a form that the computer can utilize to generate networks automatically.

A variety of research groups have developed algorithms for generating reaction networks via the computer in the last 15 years (Broadbelt et al., 1994a, 1995, 1996, 1994b; De Witt et al., 2000; Green et al., 2001; Hatzimanikatis et al., 2005; Iyer et al., 1998; Klinke and Broadbelt, 1997; Li et al., 2004; Matheu et al., 2003; Prickett and Mavrovouniotis, 1997a,b,c; Ratkiewicz and Truong, 2003; Susnow et al., 1997; Wong et al., 2003), and they all have common features. A representation of the constituent atoms and their chemical environment in a molecule is needed. A method for transforming reactants into products via an operator with a convenient computational representation is included. Finally, approaches for telling molecules apart and determining their uniqueness must be incorporated. The specific implementation that will be highlighted here is that of Broadbelt and coworkers which has been applied to a wide range of chemistries, including hydrocarbon

pyrolysis (Broadbelt et al., 1994a, 1995, 1996; De Witt et al., 2000; Susnow et al., 1997), silicon hydride clustering (Wong et al., 2004b), Fischer-Tropsch synthesis (Klinke and Broadbelt, 1999a), and amino acid biosynthesis (Hatzimanikatis et al., 2005; Li et al., 2004).

The species are represented in the computer as graphs, thereby unleashing all of the powerful algorithms that graph theory has to offer. A graph representation of a molecule is comprised of a finite set of vertices and edges and a set of rules describing the edge/vertex connectivity. A substantial amount of information about the species can be stored with or determined from the connectivity information, including formal charge, nonbonded electron count, stereochemistry, aromaticity, oxidation state and even three-dimensional structure given an appropriate conversion algorithm (Gasteiger et al., 1996; Sadowski et al., 1994). To tell species apart, their connectivity is transformed into an appropriate canonical representation which is typically a string code (Weininger et al., 1989; Wong et al., 2003) that allows for easy comparison in the computer.

Given a graph theoretic representation of species, chemical reaction is then implemented by applying rules for changing properties of the vertices and their connectivity. A simple way to illustrate this is using the concept of bond and electron (BE) matrices (Ugi et al., 1993) to represent species. The diagonal element, *ii*, of the BE matrix gives the number of non-bonded valence electrons of atom *i*, and off-diagonal entries, *ij*, provide the connectivity and bond order of atoms *i* and *j*. An example BE matrix for 1-propyl radical is shown in the middle right hand portion of Figure 2.2. The rows of the BE matrix correspond to the atoms in the order in which they are numbered in the picture at the top. Chemical reaction may then be carried out via simple manipulation of the BE matrices of reactant species which are temporarily created from species' graph representations. Because the number of atoms whose connectivity and electronic environment changes as a result of reaction is small, chemical reaction can be carried out by operating on a small, dense sub-matrix. To carry out a particular reaction type, the reaction matrix that quantifies the change in the electronic configurations and the connectivity among the atoms affected by reaction is determined. The reaction matrices can then be identified by simple matrix subtraction of the reactant

and product matrices. This is illustrated in Figure 2.2 for a radical addition reaction. First the reactants, methyl radical and ethylene, and products, 1-propyl radical, are represented by their BE matrices. The two matrices for the reactants are combined into one matrix, and the same is done for the products. The matrices are then permuted in a consistent manner so that the atoms that will experience the bond breaking, bond formation, or change in number of nonbonded electrons are moved to the upper left hand corner. The reaction matrix for radical addition is then calculated by the difference between the reactant and product matrices. The reaction matrix thus obtained is general and can now be applied to any combination of a radical and a substrate with an unsaturated bond.

Generation of a complex reaction network is thus distilled into specification of the set of reaction matrices, or operators, that the user deems likely based on chemical knowledge and rules for their implementation. For example, if the user desires to build a reaction network for amino acid biosynthesis, reaction matrices can be formulated for the generalized enzyme actions as defined using the third-level of the enzyme classification system. In fact, the Broadbelt and Hatzimanikatis groups have proposed that biochemical reactions, either known or novel, can be generated using the small number ($\sim$200) of known enzyme actions in the Kyoto Encyclopedia of Genes and Genomes (Hatzimanikatis et al., 2005; Li et al., 2004). Note that automated network generation is faithful to the reaction matrices that are provided by the user, i.e., new types of transformations are not suggested by the software. However, application of the reaction matrices to the reactants and their progeny does create species and reactions that are new to the user's current understanding of the reaction system because of the user's inability to conceive of all of the combinatorial possibilities.

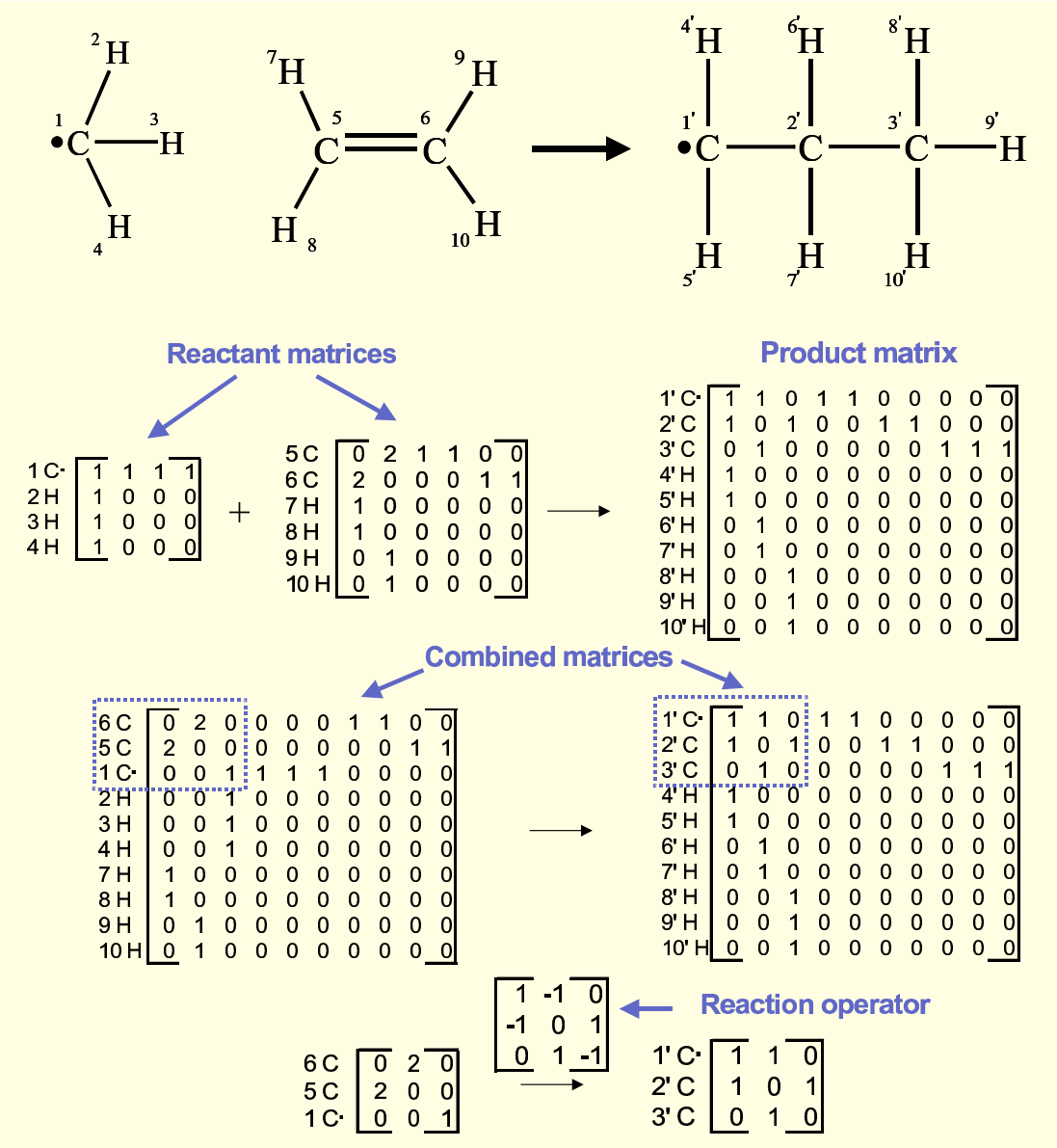

Figure 2.2: Development of a reaction matrix for radical addition. Atoms in reactants and products are numbered and converted into BE matrices. The matrices are combined and the atoms that are affected are moved to the top. The matrices for the affected atoms are separated and a reaction matrix is calculated.

2.3 Kinetic (ke -nĕt'ĭk) and Thermodynamic (thûr'mō-dī-nām'ĭk) Parameters

Once the reaction network is in hand, it is critical to specify thermodynamic and kinetic parameters for every reaction in the network. These parameters are required for model solution, and even if model reduction is the ultimate aim, rate parameters are needed to allow sensitivity analysis to be performed. Specification of rate parameters and thermodynamic properties for every reaction is a challenging task, particularly since automated network generation can easily generate $O(10^4)$ reactions or more. However, the advent of computational techniques that have recently emerged has made estimation of these quantities a practical reality.

Figure 2.3 summarizes a hierarchical approach for estimating kinetic and thermodynamic parameters that seeks to maximize accuracy while minimizing computational effort. To estimate rate coefficients, experimental values that are available in databases or in individual research articles and that are deemed reliable are at the top of the hierarchy. However, experimental values of rate coefficients for individual elementary steps or reactions are limited. It is an experimental challenge to detect and measure intermediates, and it is difficult to isolate an individual reaction of interest. Furthermore, many reactions are carried out in a complicated reaction environment, including solvents or catalysts. The second choice in the hierarchy is to use kinetic correlations. The idea is that rate coefficients, which are hard to measure or estimate, can be related to a reactivity index, such as thermodynamic quantities, that is easier to measure or predict. Kinetic correlations are the perfect complement to automated network generation since they can be derived from a small set of reactions that are well characterized, accessed quickly on-the-fly and applied to a broad set of related reactions. The final choice in the hierarchy for estimating rate coefficients is transition state theory. Transition state theory can be widely applied to a number of different reaction systems,

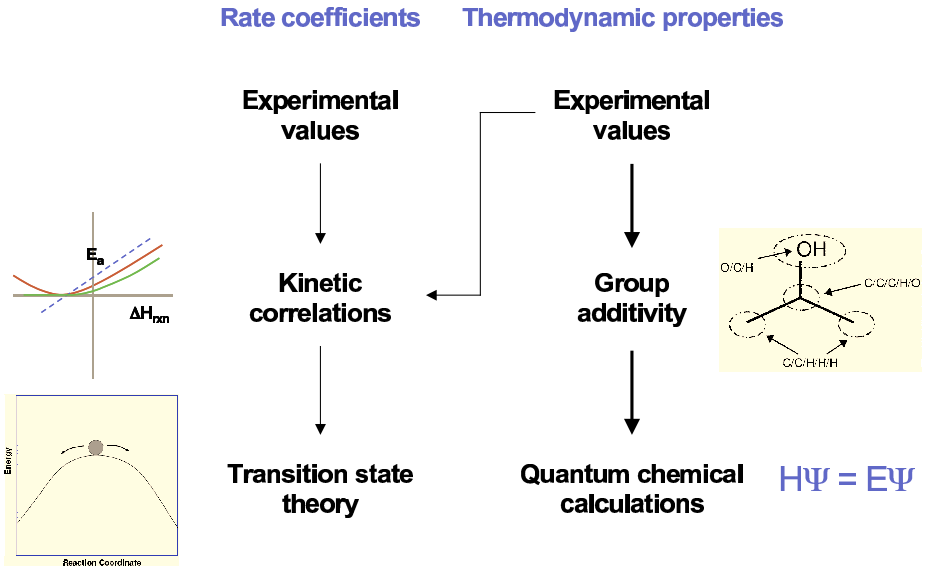

Figure 2.3: Hierarchical approach for estimating thermodynamic and kinetic parameters of complex reaction networks.

but it is currently too computationally intensive and requires substantial manual intervention to be realized on-the-fly.

A similar hierarchy is proposed for thermodynamic properties. Thermodynamic quantities are used to estimate equilibrium constants to ensure that reactions are thermodynamically consistent, and thermodynamic properties are one common choice as reactivity indices in kinetic correlations. The first choice for specifying thermodynamic quantities is experimental data. Although these data are more plentiful than experimental data for rate coefficients, tabulated data that have been well curated is restricted to certain systems. For example, gas-phase heats of formation for molecules are widely available, but values for radicals, ions, or surface intermediates are more rare. The next option in the hierarchy is to estimate properties using group additivity schemes. Group additivity estimates properties of species via summation of the contributions from its constituent groups. Finally, quantum chemical calculations can be used to calculate thermodynamic properties or other reactivity indices directly.

The following sections discuss computational approaches for calculating thermodynamic quantities and rate coefficients. Examples of the application of the various approaches from the literature will be provided so that their applicability to different types of chemistries will be highlighted. At this point, our dictionary of kinetic modeling expands rapidly, as there are many different techniques with which the kinetic modeler should be familiar.

2.3.1 Thermodynamics

Group additivity offers a rapid and reliable way to calculate thermodynamic and other properties. Pioneered by Benson (1976), a group is typically defined as a central atom and all of its ligands. Species are decomposed into groups, and then the property of the species is obtained as the summation of the constituent group values. Group additivity can be used to calculate heats of formation, entropies and heat capacities as a function of temperature for compounds that contain a wide range of atoms, including carbon, hydrogen, oxygen, nitrogen, phosphorous, halogens, and sulfur. Groups for intermediates such as free radicals are even available. Values are typically defined for the gas phase, but some liquid-phase and solid-phase values are available. More recently, the concept of group additivity was extended to biochemical compounds to calculate free energies at biologically relevant conditions (Mavrovouniotis, 1990). Group values can be easily organized in a computer database for facile lookup during automated network generation. Accuracies of less than 1 kcal mol^{-1} for heats for formation of gas-phase hydrocarbons, for example, are achieved.

It is important that all groups present in all molecules that might be encountered in a complex reaction network be available. Thus, there are continued efforts to derive new group values (Saeys et al., 2004; Sumathi et al., 2002; Sumathi and Green, 2002a; Swihart and Girshick, 1999; Wong et al., 2004b). Unknown groups can be regressed against experimental data, but it is becoming increasingly common to use quantum chemical methods to calculate properties of species from which new group values can be regressed. Hybrid methods such as G3 (Curtiss et al., 1998) and

CBS (Montgomery et al., 1999, 2000, 1994; Nyden and Petersson, 1981; Ochterski et al., 1996; Petersson and Al-Laham, 1991; Petersson et al., 1998) that can achieve accuracies comparable to that of experimental data have made this approach a viable one.

Calculation of thermodynamic properties from quantum chemistry has been used with increasing frequency. The approach is to optimize the geometry of a species, calculate vibrational frequencies by evaluating the Hessian matrix, and use statistical mechanics to calculate the enthalpy, entropy and heat capacity (McQuarrie and Simon, 1999) Heats of formation are often the desired thermodynamic quantity, but these are not obtained directly from an individual quantum chemical calculation. Rather, a series of calculations to obtain the atomization energy of individual species is used (Curtiss et al., 2000) or calculations are performed on reactants and products of isodesmic reactions, in which the bond types on either side of the reaction are conserved, is carried out. Typically, the harmonic oscillator approximation is used, but there are methods for identifying and treating hindered and free rotors (Ayala and Schlegel, 1998) to obtain more accurate values. Geometry optimization can be challenging for large molecules because of the presence of many low-energy conformations, but approaches that facilitate conformational searching are available (Haubein et al., 2003).

2.3.2 Rate coefficients

Prediction of rate coefficients is more challenging than estimating thermodynamic properties, yet there are computational methods that can predict values in good agreement with experiment (for a nice review see Sumathi and Green (2002b)). Furthermore, even with the advent of high throughput screening methods, one can envision that computational methods are the most viable choice for estimating individual rate coefficients for systems of $O(10^4)$ or more reactions. In accord with the hierarchy of Figure 2.3, we first focus on kinetic correlations, in which a property that can be estimated more easily than the rate coefficient itself is used to predict reactivity.

Historically, kinetic correlations with thermodynamic properties as the reactivity indices have been most widely used. One classic example is the Evans-Polanyí relationship, $E_A = E_o + \alpha * \Delta H_{rxn}$, where E_A is the activation energy, E_o is the intrinsic barrier, α is the transfer coefficient and ΔH_{rxn} is the heat of reaction. The underlying idea is that the Evans-Polanyí relationship will hold for reactions that have similar reaction coordinates such that the differences in the entropic changes during the reaction for all members of the reaction family are zero or proportional to the enthalpic changes. As a result, all members of the reaction family share the same Arrhenius pre-exponential factor, and E_A can be calculated by knowing only the heat of reaction. Variations of or improvements upon the Evans-Polanyí relationship include the Blowers and Masel correlation for atom transfer reactions (Blowers and Masel, 1999, 2000). Originally developed for intermolecular hydrogen transfer reactions, the Evans-Polanyí relationship has been extended to intramolecular cyclization reactions of hydroperoxyl radicals (Wijaya et al., 2003), radical addition/β-scission reactions (Saeys et al., 2003), catalytic cracking (Yaluris et al., 1995), and reactions relevant to silicon nanoparticle production (Wong et al., 2004a).

The Evans-Polanyí relationship is not a panacea, however, and thermodynamic properties are not always an appropriate reactivity index. For example, Hemelsoet et al. (2004) showed using density functional theory calculations that hydrogen abstraction reactions by methyl radical from polynuclear aromatics were not well described by an Evans-Polanyí correlation when a series of polyaromatics was studied. Instead, they showed that the principle of hard and soft acids and bases and the related concept of the Fukui function were good predictors of the activation barrier. In the same work, they also showed that the kinetics of cyclization reactions involving aromatic moieties were well correlated with magnetic susceptibility and proton chemical shift.

The majority of the kinetic correlations that have been developed in recent years are relying on performing a set of quantum chemical calculations on select reactions in a particular family and using transition state theory to predict energy barriers. The hope is that performing select calculations at a high level of theory that are computationally demanding but accurate will allow the

kinetics of related reactions to be easily predicted. Alternatively, one can envision, with sufficient computational resources, that transition state theory can be used directly to estimate a rate coefficient for every reaction in a complex network. It is thus important to understand the foundation of transition state theory and how quantum chemical calculations are used in conjunction with it as we add it to our dictionary of kinetic modeling.

The underlying concept of transition state theory is that a reaction proceeds via an activated complex that is located at a saddle point on the potential energy surface as illustrated in Figure 2.4. The reactants and the activated complex are assumed to be in equilibrium, and the activated complex, or transition state, decomposes with a rate constant equal to $k_b T/h$, where k_b is Boltzmann's constant, T is temperature, and h is Planck's constant. The transition state theory rate constant, k_{TST}, is thus:

$$k_{TST} = c_o^{1-n} \kappa\left(T\right) \frac{k_b T}{h} \frac{Q^{\ddagger}(T)}{Q^r(T)} \exp\left(-E_o/RT\right) \tag{2.1}$$

where $Q^{\ddagger}$ and Q^r are the total partition functions for the TS and reactants, respectively, and E_o is the reaction barrier, *i.e.*, the zero-point corrected difference between the ground-state electronic energies of the TS and the reactants. The value c_o^{1-n} is the standard-state concentration to which the translational partition function is referenced, P/RT, raised to the power of $1-n$ where n is the molecularity of the reaction. The quantity $\kappa\left(T\right)$ is the correction for quantum tunneling.

The role of quantum mechanics in calculating rate coefficients using transition state theory is to calculate the minimum energy or saddle point geometries, the corresponding vibrational frequencies, and the electronic energies of all species. These data are then used to calculate the total molecular partition functions within the rigid-rotor harmonic-oscillator approximation using the standard formulae (McQuarrie and Simon, 1999). In its conventional formulation, this involves locating and characterizing the reactants and the transition state on the electronic energy surface and using statistical mechanics to calculate free energies. The transition state is located at a saddle

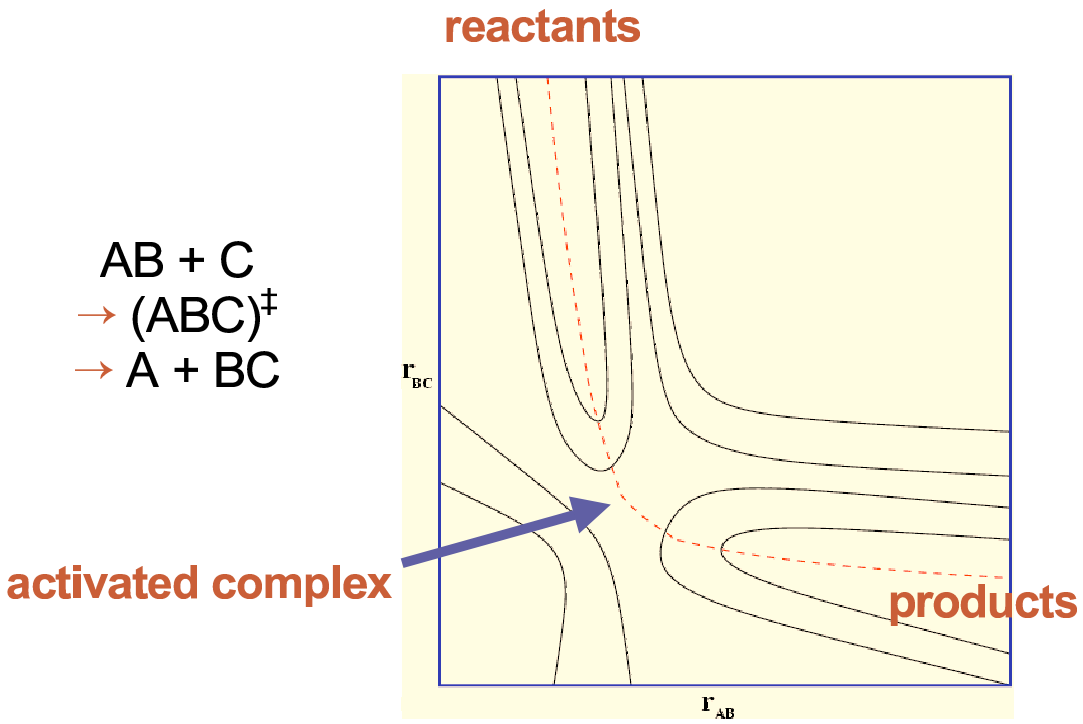

Figure 2.4: Transition state theory estimates rate coefficients by identifying and characterizing an activated complex that lies at a saddle point along the minimum energy path between reactants and products (shown as the dotted line).

point on the potential energy surface, so it is characterized by having one negative eigenvalue of the Hessian matrix. There are different approaches to locating transition states. Most simply, a reaction coordinate is postulated, and the potential energy surface is scanned at fixed values of the reaction coordinate to map the energy until a maximum is observed. The structure at the maximum can then be refined to ensure that it is a true saddle point. There are also methods in typical quantum chemical software that facilitate location of transition states, such as QST2 and QST3, but they are often not successful. The nudged elastic band method (Mills et al., 1995) is another popular approach for mapping reaction coordinates that has even been improved and extended to optimization of reaction paths for enzymatic systems (Xie et al., 2004) that have many flexible degrees of freedom. String methods and growing string methods (Peters et al., 2004) have also been developed.

Applications of transition state theory to estimate rate coefficients via quantum chemistry are growing, and many of these reports underscore the importance of choosing a sufficiently high level of theory and a large enough basis set to achieve results of desirable accuracy. For example, Wijaya et al. (2003) showed that CBS-QB3 agreed well with limited experimental data for cyclization of various hydroperoxyl radicals to form cyclic ethers, but a high level of theory that is commonly used, B3LYP, underestimated barrier heights by as much as 8 kcal mol^{-1}. There is also value in using transition state theory to estimate which intermediates on surfaces are not kinetically significant, even if reaction barriers with accuracy comparable to experiment are not obtained, since quantum chemistry does a very good job of ranking the relative stabilities of species. For example, Alcala et al. (2002, 2003, 2005) calculated transition state structures for reactions of ethanol-derived intermediates on platinum and platinum-tin catalysts, and showed that they could predict the relative likelihood of different carbon-carbon and carbon-oxygen cleavage reactions. Transition state theory is also being used successfully in conjunction with molecular orbital methods to study enzyme kinetics (Gao and Truhlar, 2002).

Methods to facilitate the use of transition state theory and improve its accuracy are also available. Recently, Saeys et al. (2004) and Sumathi et al. (2001a,b, 2002) have developed an approach for estimating the thermodynamic properties of activated complexes. They proposed that the energy of a reactive center in an activated complex may be calculated via group additivity through the introduction of "supergroups" which were obtained from quantum chemical calculations. Variational transition state theory (VTST) (Truhlar and Garrett, 1984) and other dynamical methods (Peters et al., 2004) seek to improve upon conventional transition state theory. VTST uses the concept of a generalized transition state that is a hypersurface in position and momentum space that divides reactants and products, which is varied to minimize the flux coefficients. A further basis of VTST is that a more accurate barrier to the reaction can be obtained by considering an energy surface of the Gibbs free energy, rather than the electronic energy.

2.4 Future Prospects

Although chemical engineers work on a large array of different reacting systems that can be characterized as complex, this chapter aims to reveal the links among them through the lexicography of kinetic modeling of complex reaction systems. Key entries have been defined that encompass computational techniques for the elucidation of species and reactions and characterization of the associated thermodynamic and kinetic parameters. While chemistries such as pyrolysis, combustion, polymerization, glycolysis, amino acid biosynthesis, silicon nanoparticle growth and Fischer-Tropsch synthesis may appear discordant, revelation of their common elements suggests harmony, and even synergy, among them.

Computational approaches are currently at hand for unraveling the species and reactions comprising complex reaction networks. Our lexicography starts with **quantum chemistry**, a general approach for uncovering details in reacting systems. Potential energy, or even free energy, surfaces can be mapped in detail, thereby revealing what reactive intermediates are stable and how one in-

termediate may be transformed into another. Quantum chemistry offers precise control over what reactions are explored, as it is possible to interrogate individual elementary steps.

Automated network generation is another important entry in the dictionary of complex kinetic modeling. It provides a framework for expressing chemical knowledge that can be universally applied to disparate reacting systems. It removes the tedium of developing complex reaction networks by hand, and it allows one to rapidly and reliably test hypotheses about possible reaction types and their rules. It even has the potential to reveal novel compounds and suggest new routes for their synthesis (Li et al., 2004). It can even be argued that a software package for performing automated network generation is as essential to kinetic model development as a stiff differential-algebraic equation solver is to model solution or a graphing program is to visualizing results.

The prospects for estimating thermodynamic properties for a wide variety of complex reaction systems are excellent. The key entries in the dictionary of kinetic modeling are **group additivity** and **quantum chemistry**. Group additivity databases are continually being developed and expanded and even encompass molecules in biochemical environments. In theory, quantum chemistry is a very general approach that can even be used to predict new group additivity values. It is much more computationally expensive, but its application to heterogeneous, liquid-phase, and biological systems has been demonstrated.

Estimation of rate coefficients is more difficult, but it is now possible to predict kinetic parameters within experimental accuracy by using transition state theory or its extensions. The use of **transition state theory** has increased with the advent of computational **quantum chemistry** for locating and characterizing activated complexes. Accurate results require high levels of theory and corrections to the conventional formulation. The development of **kinetic correlations** has also exploded with the growth of quantum chemistry because it is possible to predict kinetic parameters such as activation barriers while at the same time calculating other properties that may serve as appropriate reactivity indices. Emerging **group additivity** schemes for activated complexes demonstrate great promise to estimate rate coefficients quickly and reliably and offer an alterna-

tive to more conventional kinetic correlations. While it is still challenging to study the effects of the reaction environment such as solvents, catalysts, or enzymes when calculating rate coefficients, the theoretical foundation is in place, and the arsenal of computational approaches for including realistic reaction environments is growing at a rapid pace.

Chapter 3

The 1D Hindered Rotor Approximation

3.1 Introduction

Quantum chemistry is rapidly becoming the de facto choice for calculating estimates of thermochemical properties of radicals and molecular species as well as kinetic parameters of chemical reactions for a wide range of systems. The impressive success of density functional theory (DFT) and other *ab initio* methods in predicting desired properties with sufficient accuracy, the large amount of inexpensive computing power presently available, and the wide availability of user-friendly software such as GAMESS (Schmidt et al., 1993) and Gaussian (Frisch et al., 2003) continue to increase the number of practitioners of quantum chemistry. The ever-increasing number of examples of the success of quantum chemistry in addressing problems of practical interest has even motivated research groups who were traditionally experimental to add electronic structure calculations to their arsenal. Selected recent examples of the success of quantum chemistry include calculation of thermochemical properties and group additivity values (da Silva et al., 2006; Sabbe et al., 2005; Vansteenkiste et al., 2003; Wong et al., 2004b), studies of elementary gas-phase reaction kinetics (Hemelsoet et al., 2004; Peeters et al., 2004; Wijaya et al., 2003) and studies of addition reactions in polymerization (Izgorodina and Coote, 2006; Van Cauter et al., 2006). High-

level *ab initio* studies of real systems are now beginning to offer not only qualitative insights but also quantitative predictions of thermodynamic and kinetic properties.

Although quantitative predictions are available using commercial quantum chemistry software packages, continuous improvement in their accuracy is sought, and often this involves additional calculations and analyses that are beyond those available in a standard menu of choices within the codes. One example of this is the treatment of internal rotations. It has been understood for over 60 years that errors are introduced by applying the harmonic oscillator (HO) approximation to low frequency vibrational modes (Pitzer and Gwinn, 1942), yet no general procedure is in common use that offers improved treatment of anharmonic molecular vibrations (Katzer and Sax, 2002a). Treatment of anharmonicity is an area of active research as evidenced by the multitude of approaches presented in the literature to address this problem (Aubanel et al., 1991; Ayala and Schlegel, 1998; Barone, 2004; Chen and Bozzelli, 1999; Chuang and Truhlar, 2000; da Silva et al., 2006; East and Radom, 1997; Ellingson et al., 2006; Gang et al., 1996, 1997, 1998; Isaacson and Truhlar, 1981; Katzer and Sax, 2002a,b, 2003, 2005; Knyazev, 1998; Knyazev and Tsang, 1998; Lynch et al., 2004, 2006; Miller and Clary, 2002, 2003; Sebbarand et al., 2005; Truhlar, 1991; Van Cauter et al., 2006; Van Speybroeck et al., 2002, 2000, 2005; Vansteenkiste et al., 2006a, 2003; Wong et al., 2006). The method of Ayala and Schlegel (1998) has been incorporated into the Gaussian software packages but offers approximate corrections for hindered rotors that may not provide sufficient accuracy. Truhlar (1991) and later McClurg et al. (1997) offered a simple prescription for calculating the partition function between the high and low-temperature limits, *i.e.*, the hindered rotor regime. However, these methods are specific to tops whose rotational hindrance potential can be fit to a single cosine function, and many tops in species of practical interest do not fall into this category. At present, accurate treatment of internal rotation still requires substantial manual effort, which can be tedious and time-consuming when large species or studies which include a large number of reactions are of interest. A common approach for the treatment of hindered rotors is to assume uncoupled rotation. This is due to the fact that the exact Hamiltonian is very complicated, and it is

impossible to decouple any degrees of freedom exactly except for translational motion. However, accurate thermochemistry and (in many cases) kinetics can be calculated by making the rigid-rotor harmonic oscillator approximation. Accordingly, a common approximation in treating vibrational anharmonicity due to internal rotation is to treat internal rotors with an effective one-dimensional Hamiltonian. While it has been clearly shown that using this assumption may sacrifice accuracy in cases of complicated or highly coupled rotations (Van Cauter et al., 2006; Van Speybroeck et al., 2005), the computational demands introduced by multidimensional treatment to large systems still dictate that the assumption of uncoupled rotations will continue to be invoked in the foreseeable future. In addition, exact treatment of rotation-vibration in small, *i.e.* four atom, systems can be obtained at the expense of second derivative calculations as a function of the internal rotation coordinate (Bowman, 1986; Carter et al., 1998, 2005; Handy, 1987; Handy and Carter, 2004). However, we omit any detailed discussion and comparison of these methods for practical reasons due to difficulties in their application to medium to large species.

This chapter is motivated by our own journey in putting treatment of internal rotations into practice. We discovered that there are no freely distributed codes available that provide research-grade treatment of individual hindered rotations and subsequently incorporate these results into the calculation of properties of entire species or reactions. For example, calculating the properties of pentane requires treatment of the four internal rotations in the molecule. Presently, each internal rotation must be treated separately and its respective contribution to the partition function or thermodynamic properties must be manually counted. Performing all of these steps manually for more than a few internal rotations is very cumbersome and not practical. It is therefore desirable to have a single program that can extract data from existing electronic structure software, perform the internal rotation correction and apply this correction to all individual rotors, and output complete properties, *e.g.*, partition functions and thermodynamic quantities, for entire species or reactions. In addition, to the best of our knowledge, no source exists which describes all of the steps involved

in this multistep process in detail; rather the elements must be pulled from a wide array of literature sources.* This chapter seeks to remedy this by focusing on the following:

1. Review the elements of one-dimensional treatment of internal rotations applicable for low to moderate temperatures.

2. Describe how these steps have been formulated into software that is freely available and can be applied to an entire species or chemical reaction.

3. Place the one-dimensional hindered rotor treatment in context with other approaches for treating anharmonicity and review emerging methods for treatment of internal rotations that offer a higher degree of accuracy for more complex rotors.

4. Present several sample calculations that help to explore the impact of various decisions that must be made in the treatment of internal rotation. Namely, 1) the correct procedure for treating internal rotation in transition states, 2) what is the relationship between accuracy and method/basis set for determining the hindrance potential, 3) correctly establishing a functional form of the hindrance potential, 4) quantifying the ramifications of assuming that the reduced moment of inertia for rotating tops is invariant while undergoing rotation.

3.2 Treatment of Internal Rotation Using Quantum Mechanics

Pitzer and Gwinn's seminal work on the general treatment of internal rotation (Pitzer and Gwinn, 1942) as well as the subsequent works by Pitzer (1946) and Kilpatrick and Kilpatrick and Pitzer (1949) are the foundation for many present treatments of internal rotation. Additionally, this literature illustrates the challenges associated with accurate treatment of internal rotation. The essential

*The reader is referred specifically to references by Ellingson et al. (2006), Chuang and Truhlar (2000), and East and Radom (1997) and references therein for further reading.

change from Pitzer and Gwinn's original approach in the last 60 years is the extension to systems in which the quantum mechanical energy levels of one-dimensional rotations cannot be solved analytically. A common approach presently adopted by many researchers (Coote et al., 2002; da Silva et al., 2006; Gomez-Balderas et al., 2004; Sebbarand et al., 2005; Sumathi et al., 2001a; Sumathi and Green, 2002a; Van Speybroeck et al., 2005; Vansteenkiste et al., 2003) is to use electronic structure software to calculate minimum energy or transition-state structures, calculate the Hessian and resulting harmonic vibrational frequencies, and finally calculate the partition function and desired thermodynamic properties within the HO approximation. Typically, this entire process is completed within computational chemistry software or associated post-processing codes, *e.g.*, the "*freqchk*" utility of Gaussian 03 (Frisch et al., 2003). Each internal rotation is treated, and the HO partition functions and thermodynamic properties are then corrected to 1) remove the contribution of low-frequency vibrations that are hindered/free rotors and 2) include the associated contribution of each internal rotation. We review the procedure for treating hindered rotors within the one-dimensional approximation.

3.2.1 The one-dimensional hindered rotor (1DHR) model

One of the most successful methods for treating internal rotation is the one-dimensional hindered rotor model (Heuts et al., 1996; Van Speybroeck et al., 2000). In this model, each single bond between polyvalent atoms is treated as an axis of rotation between two counter-rotating tops. The potential energy surface for the rotation is determined by starting at a minimum energy or transition-state structure and then progressively rotating the top over 360 degrees. It is important to note that the assumption of separability implies that all internal coordinates except for the dihedral bond undergoing rotation remain fixed while obtaining the potential energy surface. Experience has shown (Pfaendtner et al., 2006c; Sumathi et al., 2001a) that this results in barriers to rotation that are much too high. Most researchers now obtain the one-dimensional potential energy surface by holding

the dihedral angle for the rotation fixed and then calculating the minimum energy structure using a constrained optimization routine. This process itself indicates that internal rotation is coupled to other motions, and this approximation should be remembered. Additionally, the barriers for rotation, *i.e.*, the difference in adjacent maxima and minima in the one-dimensional PES, can be further improved by performing a rigorous saddle point optimization at each peak obtained during the constrained geometry optimization. The increase in computational cost can be non-trivial due to the second derivative calculations that must be performed; as a result most researchers approximate the barrier for internal rotation as the value obtained by constrained geometry optimization alone. Finally, it is also possible to augment the potential energy surface by including zero-point corrections as a function of theta so that $V(\theta) = \epsilon_e(\theta) + ZPE(\theta)$. Rigorous calculation of the ZPE of hindered rotors was recently discussed by Ellingson et al. (2006). Regardless of the method in which it was obtained, the energy profile is fit to a trigonometric function and the reduced moment of inertia for the rotating top is calculated from the geometry of the stationary point. Once the potential is obtained, the energy levels for the rotation are obtained by solving a one-dimensional Schrödinger equation,

$$-\frac{h^2}{8\pi^2 I_{red}}\frac{d^2}{d\theta^2}\Psi + V(\theta)\Psi = E\Psi \tag{3.1}$$

where I_{red} is the reduced moment of inertia for the rotating top and $V(\theta)$ is the rotational hindrance potential. The energy levels from this calculation are used to calculate the partition function by direct counting for each internal rotation as a function of temperature,

$$q_{ir} = \frac{1}{\sigma_{r_i}} \sum_j g_j \exp\left(-\frac{\epsilon_j}{kT}\right) \tag{3.2}$$

where σ_{r_i} is the internal symmetry number of the rotating top and g_j is the degeneracy of the jth energy level, ϵ_j. Once the partition function for each internal rotation is known, thermodynamic properties, *i.e.*, *E, S, and* C_p, are easily obtained using standard formulae (McQuarrie and Simon,

1999). A classical treatment for 1D hindered rotors that is applicable at higher temperatures was given by Pitzer and Gwinn (1942). However, the classical treatment still requires that the hindrance potential, $V(\theta)$, be calculated. Given that the hindrance potential must be calculated for both the classical and quantum mechanical treatment and that the classical 1D treatment is not applicable at low temperatures, we restrict all subsequent discussion to quantum mechanical treatment of internal rotation.

The computational bottleneck in treating internal rotation comes from performing *n* constrained geometry optimizations to establish the hindrance potential, where *n* is the number of steps required to traverse the entire rotation. For a species with *m* hindered, or internal rotations, there are $n \times m$ constrained optimizations which must be performed to treat the entire species. Obtaining the energy levels for the rotation from equation 3.1 is performed at a fraction of the computational cost compared to actually determining the hindrance potential. An important consideration in defining the four atoms that constitute the dihedral angle is that the potential, $V(\theta)$, can be different depending on which atoms are chosen. Sterically hindered or bulky groups will have more or less interaction depending on whether they are constrained to be in a specific plane as the groups undergo rotation. To try to quantify the impact of this, we examined the backbone rotations in butane and 1,2-dichloroethane. For each species there are nine different ways to define the dihedral plane. Using increments of 30^o, we developed nine separate hindrance potentials for each species and compared their relative barrier heights. For these two species, very small differences between the barrier heights (less than 0.1 kcal/mol) were observed. However, it is important to be aware of this issue. The validity of a given rotational potential can easily be checked by defining the dihedral plane with the larger atoms/groups as well as smaller ones and comparing the two curves obtained. Additionally, this problem could be remedied by performing a saddle point optimization at each peak in the 1D potential in order to better approximate the true barrier height.

To assist in developing a general algorithmic approach to perform the 1DHR treatment as has been implemented in our software (Pfaendtner et al., 2006a,b), the entire process for a given species

is summarized in the flowchart shown in Figure 3.1. The flowsheet shows how information flows beginning with the minimum energy or saddle point (*e.g.*, transition state) structure and terminates with the output of the partition function and respective thermodynamic properties. Steps which are typically completed by researchers using standard electronic structure codes are denoted with an **E**; steps requiring manual input from the user are denoted with an **M**; the 1DHR treatment is labeled with an **A** reflecting the fact that this step is completed automatically once the user has completed the manual steps. Specifically, the two atoms constituting the axis of rotation for each top, the set of atoms which belong to each rotating top, and the symmetry number for each rotation must be identified as prescribed in the central box on the left hand side of Figure 3.1, and the hindrance potential must be inspected to ensure that no other conformations of lower energy exist. The return path denoted in Figure 3.1 allows for the case when initial attempts via conventional geometry optimization and even sampling configurational space by the traditional method of starting with different initial geometries did not identify the lowest energy conformation. Although performing constrained, one-dimensional rotations about all of the rotating tops in a species is certainly not a guaranteed method for obtaining the global minimum energy structure, this approach does sample a large part of conformational space and offers another route to the discovery of other minimum energy structures which may be lower in energy than the starting point. For example, we have recently observed (Pfaendtner et al., 2006c) that following the minimum energy path for some intramolecular hydrogen transfer reactions leads to a reactant which is not at the global minimum in electronic energy. The higher-energy structure is important in the reaction path since the intramolecular hydrogen shift reaction cannot take place unless the molecule is in this configuration. A consequence of performing the 1DHR correction is that low-energy conformers may be naturally detected.

The process represented by the flowsheet in Figure 3.1 could be, in principle, embedded directly within the electronic structure code or simply used as a post-processing component for obtaining the desired thermochemical or kinetic properties. For clarity, we have expanded the box

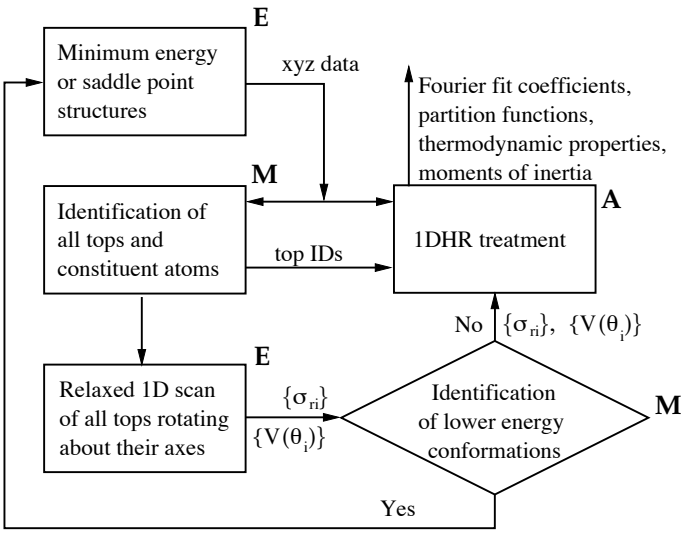

Figure 3.1: Flowsheet showing overall process of the 1DHR treatment. The process begins with a minimum energy or saddle point (*e.g.*, a transition state) structure, and the outputs are the partition functions and thermodynamic properties of each internal rotation for a given species. **E** denotes a step carried out with standard electronic structure software; **M** designates a step that requires manual intervention; **A** signifies that the 1DHR treatment is automated as implemented in our software.

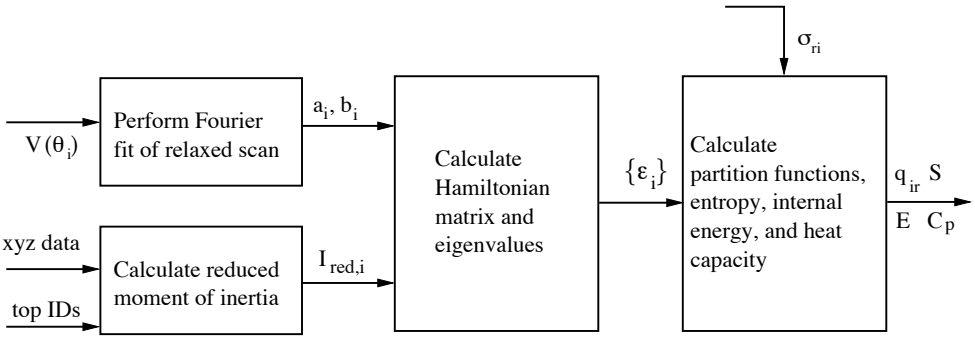

Figure 3.2: Flowsheet showing the calculations which are required specifically to calculate the energy levels and thermodynamic properties of each individual internal rotation. For each internal rotation in a given species, the process shown here is repeated.

denoted "1DHR" in Figure 3.1 into the sub-flowsheet given in Figure 3.2. The sub-flowsheet for the 1DHR treatment clearly shows how information flows through the 1DHR treatment and shows both the calculations which are required as well as the interdependence (or lack thereof) of these calculations. For each internal rotation in a given species, the sub-flowsheet "1DHR" is traversed one time. Each component of the "1DHR" block is briefly expanded upon below.

3.2.1.1 Reliable fits for hindrance potentials of any form

Pitzer and Gwinn (1942) treated symmetric tops whose rotational potentials could be fit to the simple form, $V(1 - cos\ n\theta)/2$, where V is the barrier height for rotation and n is the number of minima per rotation, *i.e.*, the rotational symmetry number for that top. In reality, only the most simple rotating tops can be described with a single trigonometric function. However, a Fourier series expansion with multiple terms easily fits top rotations of almost any form. The procedure for taking discrete data from a constrained geometry optimization and obtaining a set of coefficients for a Fourier series is very straightforward and briefly described here for reference.

The *n*-term Fourier expansion can be represented in the following form:

$$V(\theta_j) = \sum_{i=1}^{n} [a_i(1 - cos\ i\theta_j) + b_i sin\ i\theta_j] \tag{3.3}$$

The coefficients a_i and b_i can be obtained by using the discrete data points ($V(\theta_j)$) obtained from electronic structure calculations and performing a least-squares regression of the overdetermined system:

$$\begin{bmatrix} 1-cos\theta_1 & sin\theta_1 & ... & 1-cosn\theta_1 & sinn\theta_1 \\ 1-cos\theta_2 & sin\theta_2 & ... & 1-cosn\theta_2 & sinn\theta_2 \\ 1-cos\theta_3 & sin\theta_3 & ... & 1-cosn\theta_3 & sinn\theta_3 \\ & & .... & & \\ 1-cos\theta_{m-2} & sin\theta_{m-2} & ... & 1-cosn\theta_{m-2} & sinn\theta_{m-2} \\ 1-cos\theta_{m-1} & sin\theta_{m-1} & ... & 1-cosn\theta_{m-1} & sinn\theta_{m-1} \\ 1-cos\theta_m & sin\theta_m & ... & 1-cosn\theta_m & sinn\theta_m \end{bmatrix} \begin{bmatrix} a_1 \\ b_1 \\ ... \\ a_n \\ b_n \end{bmatrix} = \begin{bmatrix} \varepsilon_1 \\ \varepsilon_2 \\ \varepsilon_3 \\ ... \\ \varepsilon_{m-2} \\ \varepsilon_{m-1} \\ \varepsilon_m \end{bmatrix} \tag{3.4}$$

The dimensions of the three matices, denoted as A, x and E from left to right, are $m \times 2n$, $2n \times 1$ and $m \times 1$, where n is the number of coefficient pairs and m is the number of energy points in the potential energy scan. The number of coefficient pairs must be lower than the number of energy points if the least squares method is used to solve for the coefficients. In systems in which a large number of points are used, *i.e.* the step size in scanning the rotation is small, we found that 10 terms in the Fourier series (five sine and five cosine terms) fit the calculated data extremely well for all cases that we tested. For test cases in which 10 or fewer data points were used to establish the hindrance potential, we typically chose $2n = m - 2$. The coefficient matrix x can be solved as:

$$x = (A^T A)^{-1} A^T E \tag{3.5}$$

It is important to note that as n approaches m over-fitting can occur and the functional form obtained from this procedure will give nonsensical values. This can be easily checked by using equation 3.3 and plotting the potential over the entire range, 0-2π. If too many coefficients have been used, the curve will agree with the discrete points $V(\theta_j)$ but not follow the general shape of

the potential at intermediate points. Another way to test the quality of the fit is to make sure that the following two conditions are met at $\theta = 0$:

$$\frac{dV}{d\theta}|_{\theta=0} = 0, \textit{i.e.} \sum_{i=0} i * b_i = 0 \tag{3.6}$$

$$\frac{d^2V}{d\theta^2}|_{\theta=0} > 0, \textit{i.e.} \sum_{i=0} i * a_i > 0 \tag{3.7}$$

This is based on $V(0)$ being located at a global minimum.

One question which has not been addressed in the literature is the sensitivity of the hindered rotor partition function (and associated thermodynamic quantities) to the step size used in obtaining the hindrance potential, $V(\theta_j)$, for each rotation. Many researchers have adopted a standard step size of 30^o while traversing the rotation of 360^o (Pfaendtner et al., 2006c; Sumathi and Green, 2002a; Wijaya et al., 2003), whereas others use increments as small as 10^o (Izgorodina and Coote, 2006; Sumathi et al., 2001a) or even 5^o (da Silva et al., 2006) for obtaining the hindrance potential. The relationship between the step size of the hindrance potential and the resulting partition function/thermodynamic properties is further discussed in the Results section. Additionally, we build on the results of East and Radom (1997) by calculating the hindrance potential using several DFT and MO methods in conjunction with three different basis sets. The impact of the choice of method on the calculated properties is discussed in the Results section.

3.2.1.2 Calculation of the reduced moment of inertia

The next block in Figure 3.2 shows the calculation of the reduced moment of inertia. In the limit of a molecule with only one rotation axis, there is an exact reduced moment of inertia that correctly couples both counter-rotation of the two rotating portions, or tops, as well as the internal/external molecular rotation (East and Radom, 1997; Pitzer, 1946; Pitzer and Gwinn, 1942). In general, the two sides of the molecule are not equally balanced and calculation of an appropriate effective moment of inertia requires consideration of the coupling of internal rotation with total molecular

rotation as well as the coupling of the counter-rotation of the two parts of a molecule separated by a rotation axis. There are many different approximations used in determining the reduced moment of inertia that is used in equation 3.1. Ellingson and Truhlar have recently provided a thorough discussion of many alternate approaches to calculating effective moments of inertia (Ellingson et al., 2006). Additionally, East and Radom (1997) provided a convenient formalism for distinguishing between these moments of inertia. A popular approximation for the coupling of internal rotation and total molecular rotation was given by Herschbach et al. (1956) and discussed further by East and Radom (1997). In the notation of East and Radom, this approximation is I(2,n) where n refers to the degree of coupling between the two counter-rotating tops. The user-specified input is comprised of the structure of the species, the axis of rotation, and the identity of all the atoms on each side of the molecule (separated by the two atoms defining the twisting bond under consideration).

$$\frac{1}{I^{2,n}} = \frac{1}{I_L^{2,n}} + \frac{1}{I_R^{2,n}} \tag{3.8}$$

where the designations L and R in equation 3.8 refer to the fact that the molecule has been separated into two halves (designated "left" and "right", arbitrarily) by the rotation axis for each internal rotation. Each quantity I is the moment of inertia for each side of the species about the axis of internal rotation, which is expressed as:

$$I_{L\ or\ R}^{2,n} = \sum_i m_i d_i^2 \tag{3.9}$$

where d_i is the distance from the i-th atom in the top to the rotation axis. Equation 3.9 is a summation only over the atoms in one of the counter-rotating groups, *i.e.*, the "top" and is calculated for the "left" and "right" sides of the molecule. This process is repeated for each internal rotation in a given species in order to calculate all of the effective reduced moments of inertia.

An important consideration is the designation of the axis of internal rotation (the n classification in the notation of East and Radom). If $n = 1$ the axis of rotation is the single bond undergoing

rotation. Coupling the counter-rotation of the two sides of the molecule is accomplished through the approximations $n = 2$ (the axis of rotation is parallel to the bond but passes through the center of mass of the smaller of the two rotating tops) and $n = 3$ (the axis of rotation is defined as the line connecting the centers of mass for the two rotating groups). Since each of the successive approximations brings the axis of rotation closer to the heavier atoms in the molecule, we should expect that the reduced moment of inertia will decrease in magnitude, *i.e.*, $I^{2,1} > I^{2,2} > I^{2,3}$. This mode of approximation to the reduced moment of inertia is attractive for species with more than one internal rotation because exact treatment in species with many rotors is extremely complicated. We recommend using the $I^{2,3}$ approximation when species with big, bulky groups are examined, and we investigated the ramifications of using the different $I^{2,n}$ in the Results and Discussion.

In addition, there is also a small Coriolis contribution to all effective moments of inertia. This is typically neglected (as has been done in this work), but may become important in cases where the rotating groups are not rigid or the separability approximation breaks down (Carbonniere and Barone, 2004; Vansteenkiste et al., 2006a; Wong and Green, 2005). Equation 3.1 implies that I_{red} is not a function of θ and therefore is constant throughout rotation. However, this is not the case for tops that are not rigid while rotating (Pitzer and Gwinn, 1942; Sumathi et al., 2001a). The reduced moment of inertia for a given top can, in principle, be calculated as a function of the rotation angle. It is therefore interesting to probe what effect the assumption that I_{red} is constant has on the calculated properties, which would be expected to be more dramatic as larger molecules are treated. We explore the impact of this assumption quantitatively in the Results and Discussion.

3.2.1.3 Obtaining the energy levels of the hindered rotor

Following the scheme in Figure 3.2, the hindrance potential (as a Fourier series) and reduced moment of inertia are then used in solving equation 3.1 to obtain the resulting energy levels. One common approach to solve equation 3.1 is to use a grid-based method wherein the Hamiltonian is discretized over the rotation. The eigenvalues and eigenvectors of the resulting diagonal matrix

directly give the energy levels and wavefunctions for the rotation. A number of different grid methods have been employed for studying 1DHR problems (Balint-Kurti et al., 1992, 1991; Marston and Balint-Kurti, 1989; Nordholm and Bacskay, 1976; Van Speybroeck et al., 2000). We have implemented the Fourier Grid Hamiltonian (FGH) method of Marston and Balint-Kurti (Balint-Kurti et al., 1992, 1991; Marston and Balint-Kurti, 1989) that is general for potentials of any form, is easily implemented numerically and has relatively fast convergence. It is therefore an ideal method for solving the 1D Schrödinger equation when implementing the 1DHR treatment in a generalized way such as that described here. The convergence of numerical methods for solving equation 3.1 is dependent on the magnitude of the reduced moment of inertia, the shape and size of the rotational potential, and the temperature (for considering convergence of properties like q_{ir} and S_{ir}). We tested a wide range of these parameters and found that in all cases 1000 grid points were sufficient to converge the energy levels and properties such that increasing the number of grid points changed their values by much less than 1%.

3.2.1.4 Calculating the properties of each internal rotation

The final block in Figure 3.2 is calculation of the partition function and thermodynamic properties of each internal rotation. Once the energy levels for the hindered rotor are known, this step becomes trivial and is completed using standard formulae (McQuarrie and Simon, 1999). One caveat in this step is that for high temperatures or very small barriers, *i.e.* $kT >> V$, a free rotor description is more appropriate for that particular internal rotation (Ayala and Schlegel, 1998; Chuang and Truhlar, 2000). For example, when reporting thermodynamic properties of hydrocarbons the heat capacity is typically reported up to 1500 K. At this temperature RT is 3 kcal/mol and so for much lower barrier heights or much greater temperatures, a free-rotor description is more appropriate. The free-rotor/hindered-rotor transition has been discussed in detail elsewhere (Ayala and Schlegel, 1998; McClurg et al., 1997; Truhlar, 1991). While the partition function for hindered rotors is

calculated using equation 3.2, the free rotor partition function can be estimated using the symmetry number, σ_{r_i}, and reduced moment of inertia for the rotation, I_{red} (Ayala and Schlegel, 1998):

$$q_{fr} = \sqrt{\frac{8\pi^3 kTI_{red}}{\sigma_{r_i}^2 h^2}} \tag{3.10}$$

Equation 3.10 is also based on the approximation that the reduced moment of inertia is constant throughout the angle of rotation. The associated thermodynamic properties for hindered rotors calculated in the final block of Figure 3.2 are:

$$S_{hr} = k\ ln\ q + \frac{1}{T}\frac{\sum_j g_j\ \epsilon_j \exp\left(-\frac{\epsilon_j}{kT}\right)}{\sum_j g_j\ \exp\left(-\frac{\epsilon_j}{kT}\right)} \tag{3.11}$$

$$E_{hr} = \frac{\sum_j g_j\ \epsilon_j \exp\left(-\frac{\epsilon_j}{kT}\right)}{\sum_j g_j\ \exp\left(-\frac{\epsilon_j}{kT}\right)} \tag{3.12}$$

$$Cv_{hr} = \frac{\left(\sum_j g_j\ e^{\left(-\frac{\epsilon_j}{kT}\right)} * \sum_j g_j\ \frac{\epsilon_j^2}{kT^2} e^{\left(-\frac{\epsilon_j}{kT}\right)}\right) - \left(\sum_j g_j\ \frac{\epsilon_j}{kT^2} e^{\left(-\frac{\epsilon_j}{kT}\right)} * \sum_j g_j\ \epsilon_j e^{\left(-\frac{\epsilon_j}{kT}\right)}\right)}{\left(\sum_j g_j\ e^{\left(-\frac{\epsilon_j}{kT}\right)}\right)^2} \tag{3.13}$$

whereas the thermodynamic properties of free rotors are:

$$S_{fr} = k\left(ln\ q_{fr} + \frac{1}{2}\right) \tag{3.14}$$

$$E_{fr} = \frac{kT}{2} \tag{3.15}$$

$$Cv_{fr} = \frac{R}{2} \tag{3.16}$$

Within the framework described here we can easily select a point for the FR/HR transition and use the appropriate formulae accordingly.

3.2.1.5 Correcting the harmonic oscillator partition function

As stated previously, the common approach in correcting for internal rotation involves first calculating the corresponding partition function and thermodynamic properties within the HO approximation, *i.e.*, using all of the vibrational frequencies, and subsequently removing the contributions (partition functions and thermodynamic properties) of low-frequency vibrations that correspond to internal rotations. One way to carry this out is simply to select the n lowest vibrational frequencies where n is the number of internal rotations treated. This often is an acceptable approach for species which are minimum energy structures. However, in some cases, *e.g.*, transition states, some of the lowest energy vibrations do not correspond to internal rotations. In this case, an internal modes analysis[†] can be used to identify the contribution of various moments (bending, stretching, torsion) to each harmonic frequency. The internal modes analysis is performed at negligible incremental computational cost once the Hessian is calculated. Therefore, this more rigorous approach is recommended to identify the harmonic frequencies most closely corresponding to each internal rotation. The internal modes analysis also reveals that there can be substantial mixing between various modes when the HO frequencies are calculated. Van Cauter et al. (2006) have addressed this in the context of calculated kinetic data for radical addition in polyethylene propagation reactions. They have offered a method for calculating the frequency which corresponds to pure internal rotation, thus improving the 1DHR correction. Even when there is mixing of the vibrational modes, it is generally possible to choose a single harmonic frequency that corresponds to each individual internal rotation. If, based on the internal modes analysis, there are two possible harmonic frequencies that correspond to a single internal rotation, we choose the lower vibrational frequency since these are generally associated with hindered rotors. Implicitly included in the process of calculating the HR corrected partition function is a consideration of the ZPE for each internal rotation. Since the

[†]For example, the keyword "*freq=intmodes*" can be used in Gaussian 03 (Frisch et al., 2003) to perform the internal modes analysis.

energy levels for the 1D hindered rotor partition function are not referenced to 0, the HR-ZPE is directly included in the partition function. Barone (2004) gave a nice discussion of how anharmonic motions affect the ZPE and Ellingson et al. (2006) discuss various approximations to ZPE for separable and nonseparable cases.

3.3 Alternatives and Extensions of 1D Uncoupled Rotation

3.3.1 Alternate model schemes

Treating anharmonicity and, in particular, internal rotation continues to be an area of active research, and there are a number of possible approaches put forth in the literature. Although the subject of the present work is a detailed review of one popular approach, the one-dimensional hindered rotor model, we sought to put this model in context by giving a brief overview of several other methods. One important class of methods seeks improved accuracy by explicitly coupling internal and external rotation within a single rotational partition function (Aubanel et al., 1991; Gang et al., 1996, 1997). These methods provide extremely accurate prediction of the entropy and heat capacity and also give analytical expressions for the overall rotational partition function. This makes calculation of the density of states straightforward, and use of these methods dovetails well with RRKM theory (in which the density of states is explicitly required). In spite of the accuracy of these methods, their broad application is hindered by the complex algebra and extensive numerical integration required to calculate the partition functions (Knyazev, 1998). Knyazev (1998) quantified the impact of decoupling internal and external rotation, and Knyazev and Tsang (1998) presented a straightforward algorithm for calculating partition functions and densities of states for one-dimensional nonharmonic degrees of freedom. Extensions of these methods are several approaches that employ Monte Carlo techniques for evaluating complex integrals found in more complex varieties of the partition functions (Chempath et al., 2006; Gang et al., 1998; Lynch

et al., 2004; Miller and Clary, 2002, 2003; Tafipolsky and Schmid, 2005). These methods are all presented in the context of anharmonic motion within a well-behaved, *e.g.* sinusoidal, potential. The one-dimensional hindered rotor model and related methods, while limited in other areas, are formulated to be general for potentials of any shape. Additionally, the vibrational self-consistent field (VSCF) method can provide exact calculations of rotational-vibrational coupling within the limit of small molecules (Bowman, 1986; Bowman et al., 2003; Carter and Bowman, 1998; Carter et al., 1998, 1997, 2005; Handy, 1987; Handy and Carter, 2004).

3.3.2 Extension of the 1DHR scheme to multiple rotors and other anharmonic degrees of freedom

The limitations of the 1DHR model are well understood and have been discussed in detail elsewhere (Sumathi et al., 2001a; Sumathi and Green, 2002b; Van Speybroeck et al., 2005; Wong and Green, 2005). A major assumption which can lead to compromised accuracy of the 1DHR model is that the potentials of the rotating tops within a single species are uncoupled with respect to the other internal rotations/vibrations. Van Speybroeck and coworkers (Van Speybroeck et al., 2005) recently studied the thermochemistry of pentane and hexane and showed that cancellation of errors resulted in excellent agreement between the 1DHR model and a fully coupled treatment for internal rotation. The effect of coupled internal rotations on calculated kinetic data has also been studied (East and Radom, 1997; Van Speybroeck et al., 2002; Wong and Green, 2005). In essence, the approach to studying coupled internal rotations is similar to the 1D approach. A two-dimensional PES is generated for two rotations that are assumed *a priori* to be coupled, and a simple two-dimensional Hamiltonian similar in form to equation 3.1 is solved. The computational expense in this case increases dramatically since the PES which must be traversed in calculating the hindrance potentials becomes multi-dimensional. For example, studying two uncoupled 1D internal rotations for 12 discrete angles requires only 24 constrained geometry optimizations, whereas calculating a

2D PES for the same two rotations with the same degree of angular resolution for each rotation angle requires 144 constrained geometry optimizations. In addition, calculation of the energy levels for the subsequent coupled internal rotation is more complex. Thus, the application of coupled models to problems of engineering interest is currently limited.

In principle, other anharmonic motions such as puckering and inversion can be treated in an analogous manner to that outlined in Figures 3.1 and 3.2. A corresponding one-dimensional anharmonic potential is determined for the motion under consideration along with an appropriate reduced moment of inertia, and equation 3.1 is solved analytically or numerically depending on the nature of the potential obtained. Katzer and Sax gave an overall review of how many other anharmonic motions can be treated within the "1D uncoupled motion" paradigm (Katzer and Sax, 2002a, 2005), and Vansteenkiste and coworkers show application of this model to ring puckering in small cyclic compounds (Vansteenkiste et al., 2006b).

Finally, several methods have been offered to treat internal rotation that depart from the scheme described here, *i.e.*, application of quantum mechanics to establish a hindrance potential and subsequent calculation of the energy levels for each rotation. Katzer and Sax (2005) developed a method in which internal rotations are automatically identified from the geometry and Hessian, and the internal rotation partition functions are calculated using model potentials whose parameters are also informed by the calculation of the Hessian. This approach offers an economical and accurate route to approximating the contributions of internal rotation to the calculated partition functions and thermodynamic properties. Vansteenkiste and coworkers have presented a new method, the extended hindered rotor model, that relies on separation of large amplitude motions from harmonic vibrations and also offers direct calculation of associated partition functions (Vansteenkiste et al., 2006a).

3.3.3 Probing 1D uncoupled rotation

The remainder of this chapter focuses on investigating aspects of the 1DHR treatment which have not yet been examined quantitatively in the literature using representative calculations. Specifically, we have addressed what effect the type of optimization has when treating internal rotations of transition states. We have also explored the effect of computational method/basis set and the step size used when rotating each 1D top and establishing the hindrance potential. Finally, we have quantified the impact of the assumption that the reduced moment of inertia is invariant while rotating.

To probe these questions, we investigated two different systems. The first was the radical addition reaction

$CH_3C{\cdot}HCl + C_2H_3Cl \rightarrow CH_3CHClCH_2C{\cdot}HCl$

that is one of the first steps in poly(vinychloride) (PVC) polymerization. The complex hindrance potentials of the product, $CH_3CHClCH_2C{\cdot}HCl$, provide a nice opportunity to study the sensitivity of the calculated partition functions and thermodynamic properties to the step size used to calculate the potentials. The second reaction was the intramolecular hydrogen transfer reaction

$(CH_3)_2CHO_2{\cdot} \rightarrow HO{\cdot} + CH_3COCH_3$

that is a prototype reaction of an important reaction family in atmospheric chemistry. Note that the intramolecular product $CH_3C{\cdot}OOHCH_3$ is not observed, but rather the subsequent β-scission products are formed directly (Denisova and Denisov, 2001). The insights derived from studying the transition states of these reactions are applicable to a wide range of related systems.

3.4 Computational and Theoretical Details

All molecular orbital (MO) and DFT calculations were completed using the Gaussian 03 (Frisch et al., 2003) software package. The torsional hindrance potentials were calculated within Gaus-

sian 03, and the partition functions and thermodynamic properties were calculated according to the method described in section 3.2.1 which has been coded in the "Calctherm" and "Calc*k*" software packages (Pfaendtner et al., 2006a,b). Calctherm and Calc*k* provide partition functions, thermodynamic properties and TST rate constants that are fully corrected for internal rotation by first reading in structural and vibrational data from electronic structure software and then correcting internal rotations that have been identified by the user. The hindered rotor correction is performed by using the FGH method (Marston and Balint-Kurti, 1989) to solve equation 3.1, and the energy levels for each internal rotation are used to calculate the partition function (equation 3.2) and associated thermodynamic properties (equations 3.11 through 3.13). For all internal rotations and temperatures considered, kT was less than or approximately equal to the barrier height, V; thus the hindered rotor scheme was used for all corrections. Each internal rotation is processed to additively correct an entire species by 1) including the contribution to q, S, C_v, and E of each IR and 2) removing the corresponding contribution (within the HO approximation) for each low-frequency vibration matched to a hindered rotor. Calctherm is used to treat individual species, and calc*k* can be used to calculate rate coefficients, activation energies and pre-exponential factors using transition state theory. Molecular geometries were optimized using the B3LYP hybrid density functional (Becke, 1993) and the CBSB7 basis set that is represented as an extension of the Pople formalism as 6-311G(2d,d,p) and adds an additional 2d polarization function to third row atoms (Montgomery et al., 1999). This is the basis set used in the hybrid model chemistry CBS-QB3 (Montgomery et al., 1999) which has been applied to study many problems of practical interest. Frequencies used in computing thermodynamic properties were scaled as recommended by Scott and Radom (1996). Additionally, for the study comparing methods and basis set we used MP2 and HF levels of theory with two additional basis sets, 3-21G and 6-31G(d).

3.5 Results and Discussion

The optimized structures of the transition state and product from the PVC addition reaction and the transition state from the intramolecular hydrogen transfer reaction are shown in ball-and-stick format in Figure 3.3. These are the structures that will be referred to in the Results and Discussion below.

3.5.1 Calculation of the hindrance potential in transition states

In Chapter 4, we studied the intramolecular hydrogen transfer of a large number of peroxy radicals. These reactions proceed through a cyclic transition state before isomerizing to form a peroxy radical or peroxide moiety. To maintain the basic structure of the transition state while calculating the hindrance potentials, we simply chose to freeze all of the atoms which constituted the ring structure of the transition state. For example, a 1,5-hydrogen shift forms a six-membered ring with two oxygen atoms, one hydrogen atom and three carbon atoms. Using this approximation, the coordinates of all six of these atoms were frozen while performing the geometry optimization to establish the hindrance potential. Rigorously, it is correct to calculate the partition function for the transition state, $Q^{\ddagger}(T)$, by identifying the saddle point at each point along the scan to obtain the hindrance potential. However, the additional computational demands imposed by this approach are significant, and we introduced this approximation to save computational cost. It would be reassuring to know that the simpler approach provides acceptable approximations to the more rigorous hindrance potentials.

To investigate the impact of the "frozen TS" assumption, we first located the transition state for both the radical addition and hydrogen transfer reactions. We then calculated the hindrance potential for the internal rotation(s) in each transition state using both methods: 1) re-optimizing the saddle point at each step, or 2) freezing the positions of the atoms defining the transition state to those occupied at θ=0. In the case of the radical addition reaction, the 4-3 bond length was frozen

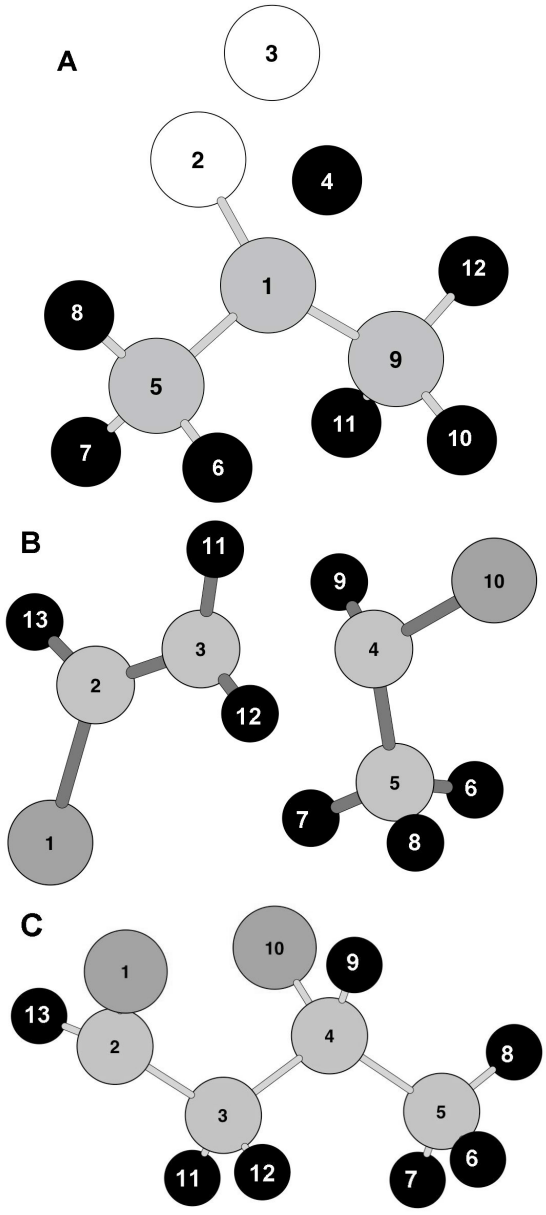

Figure 3.3: Ball-and-stick diagrams of three compounds under consideration. Structure A is the transition state of a 1,3-hydrogen shift of 2-propyl peroxy radical. Structure B is the transition state for the first radical addition reaction in PVC polymerization. Structure C is the optimized product from the addition reaction of PVC. Carbon atoms are shown in grey; hydrogen atoms are shown in black; oxygen atoms are shown in white; and Cl atoms are shown in dark grey.

(structure "B", Figure 3.3); for the intramolecular hydrogen transfer reaction, the bond lengths, bond angles and dihedral angles involving atoms 1, 2, 3, and 4 were frozen (structure "A", Figure 3.3). For the sake of the comparisons done here, we treated the TS bond in the radical addition reaction as an internal rotation as done by Izgorodina and Coote (2006) and calculated a hindrance potential using the TS bond as the axis of rotation. For structure "A" in Figure 3.3, we examined the 1-5 bond as the axis of rotation.

The results given in Figure 3.4 show the hindrance potentials for the rotation about the 4-3 bond of the TS of the radical addition reaction (Figure 3.4a; structure "B" in Figure 3.3) and the rotation about the 1-5 bond of structure "A" in Figure 3.3 (Figure 3.4b) for the two different approaches. Remarkably, the hindrance potentials for the two methods are nearly indistinguishable, even for the much more complicated backbone rotation of the TS of the addition reaction. When equation 3.1 is solved with two identical potentials, the energy levels, partition functions and associated thermodynamic properties will also be identical. Although a limited sample was examined here, the results are encouraging that continued refinement of the atoms defining the transition state as θ is varied is not necessary. This offers a significant savings in computational time; the computational cost for establishing the hindrance potentials (using 30^o increments) when the atoms defining the TS are frozen was roughly one-eighth that compared to re-optimization of the saddle point at each step for the two cases examined here. For kinetic studies of large systems with many internal rotations or studies which involve many reactions, the advantage of the more simplified approach is clear. We note that if this approach is applied to transition states in which the transition state itself becomes an axis of rotation and there are also three atoms in the transition state moiety, *e.g.*, intermolecular hydrogen transfer, it is not possible to simultaneously constrain (freeze) more than two out of four atoms that define a dihedral angle and subsequently scan that dihedral angle to obtain the hindrance potential.

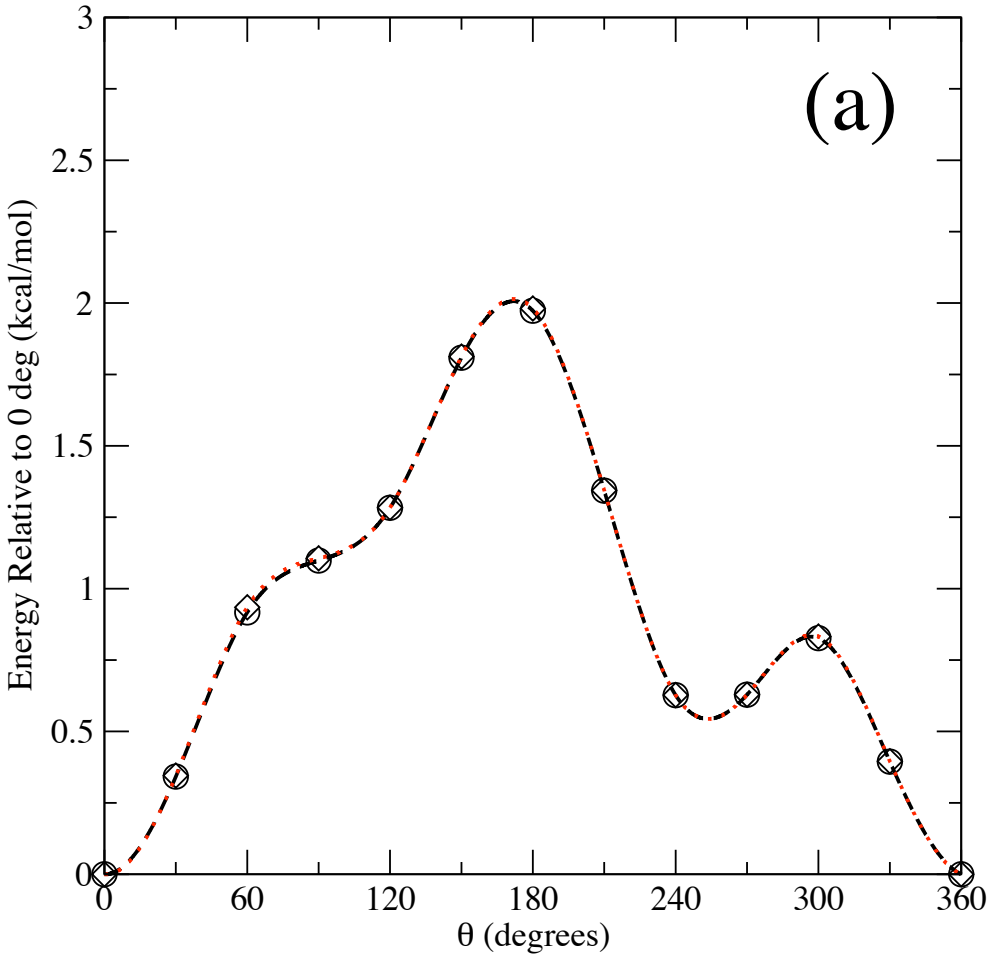

Figure 3.4: Comparison of hindrance potential calculated for internal rotation in transition states calculated using two different approaches. Data calculated freezing the coordinates of the atoms defining the TS center are given with open circles and a black dashed line. Data calculated by re-optimizing the TS at each point throughout the rotation are shown as open diamonds and a dotted line. Each hindrance potential is calculated using 30^o increments. The top figure (a) shows the results for rotating around the 4-3 bond in structure "B" of Figure 3.3. The bottom figure (b) presents results for rotation around the 1-5 bond in structure "A" in Figure 3.3. Continued on next page.

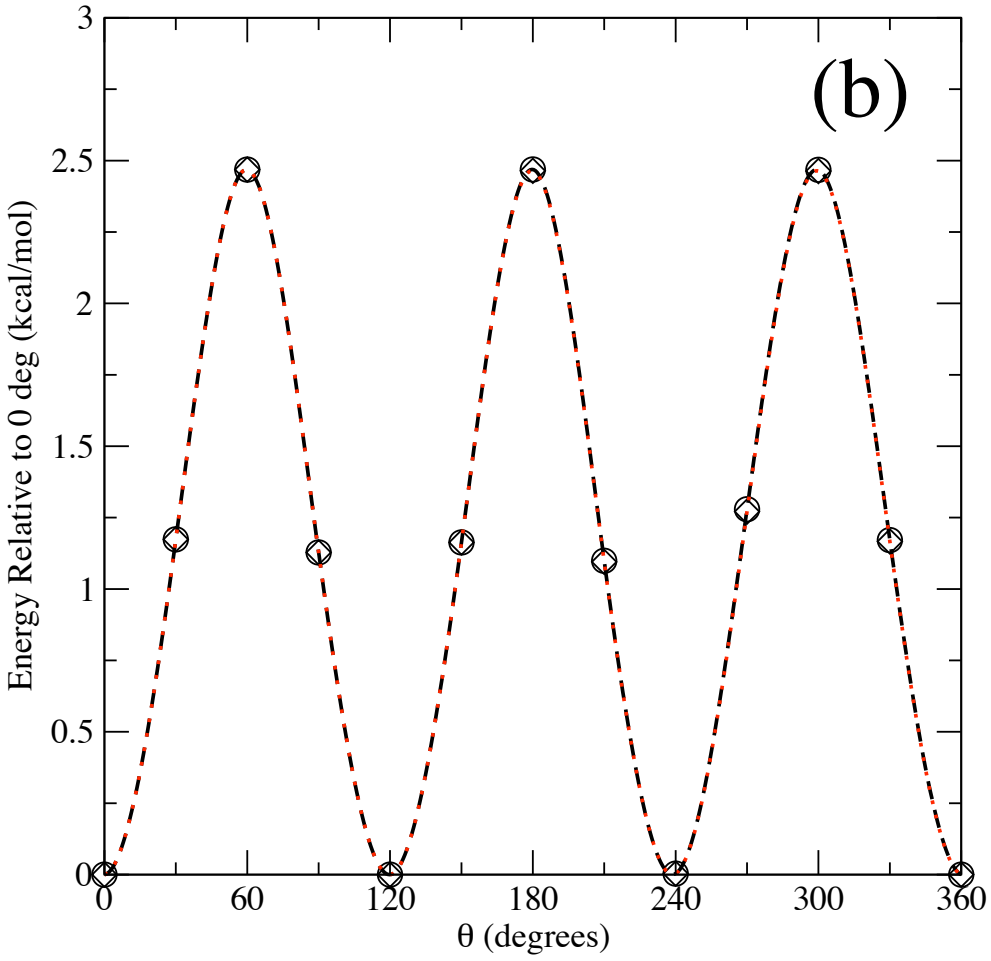

Figure 3.4: (continued)

3.5.2 Choice of method and basis set when establishing the hindrance potential

An important question regarding use of the 1DHR scheme is the choice of quantum method and basis set (East and Radom, 1997; Vansteenkiste et al., 2006b). To probe the effect of this choice we examined the "4-3" backbone and "4-5" methyl group rotations of structure "C" in Figure 3.3. To compare a variety of methods, we used HF, MP2, and B3LYP with three different basis sets 3-21G, 6-31G(d), and 6-311G(2d,d,p) (CBSB7). The hindrance potential was obtained by first optimizing each structure at the respective method/basis set combination and then scanning the rotation using 30^o increments. It is interesting to compare the different hindrance potentials obtained to see their respective shapes and barrier heights as well as the impact these potentials have on the calculated properties. The calculated potentials are given in Figure 3.5. The methyl group rotation is well behaved, and there is not much variability among methods and basis sets. However, some variability is seen for the "4-5" backbone rotation. For the medium and large basis sets, the barrier heights for all methods are in reasonable agreement. On the other hand, the HF/3-21G potential for the backbone rotation (filled squares in panel A of figure 3.5) fails to show periodic behavior. That is, the energy of the structure after rotating the full 360^o is no longer equal to the starting energy. These data help shed light on both the absolute barrier heights obtained as a function of method and basis set as well as the variability between the shapes of potentials obtained using different methods.

The potentials shown in Figure 3.5 for the nine different methods and basis set combinations were then used to calculate the hindered rotor partition function and hindered rotor entropy at 200 K and 1000 K. These data are given in Table 3.1. While the quantities obtained for each method (HF, MP2, or B3LYP) differ slightly in absolute magnitude, it is clear that the hindered rotor entropy is less sensitive to the size of the basis set than the partition function. These data

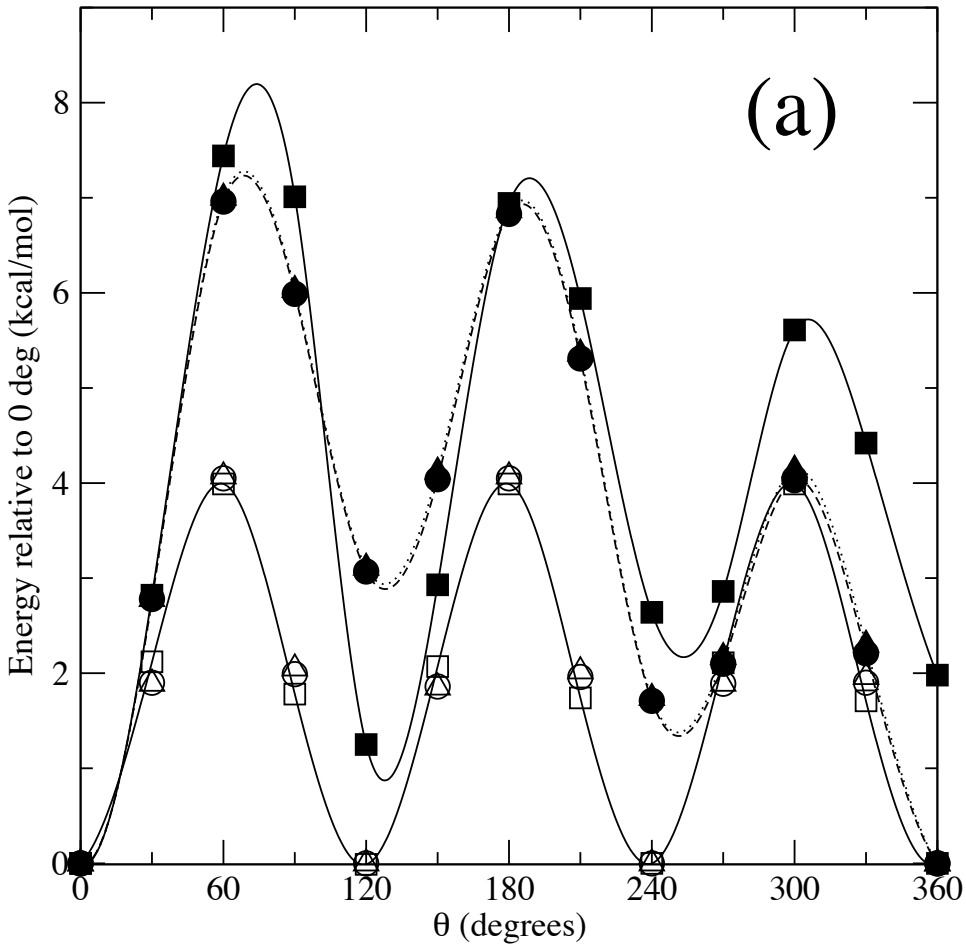

Figure 3.5: Comparison of the hindrance potential calculated for the "4-3" (closed symbols) and "4-5" (open symbols) rotations in structure "C" of Figure 3.3 using different methods and basis sets. The methods used were HF (panel A), MP2 (panel B), and B3LYP (panel C). The basis sets used were 3-21G (squares, solid lines), 6-31G(d) (triangles, dotted lines), and 6-311G(2d,d,p) (circles, dashed lines). To guide the eye, the fits for each data set in the "4-3" rotation are shown and only the data for the fit of the small basis set are shown for the "4-5". Continued on next page two pages.

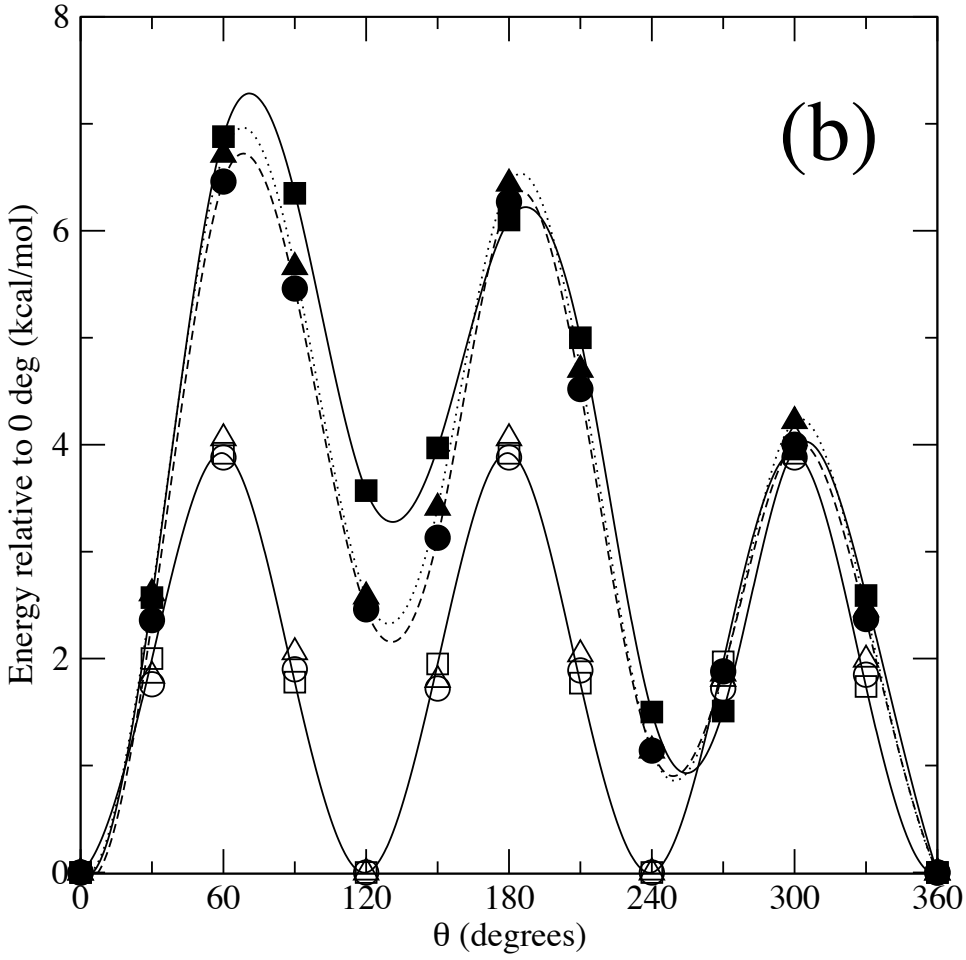

Figure 3.5: (continued)

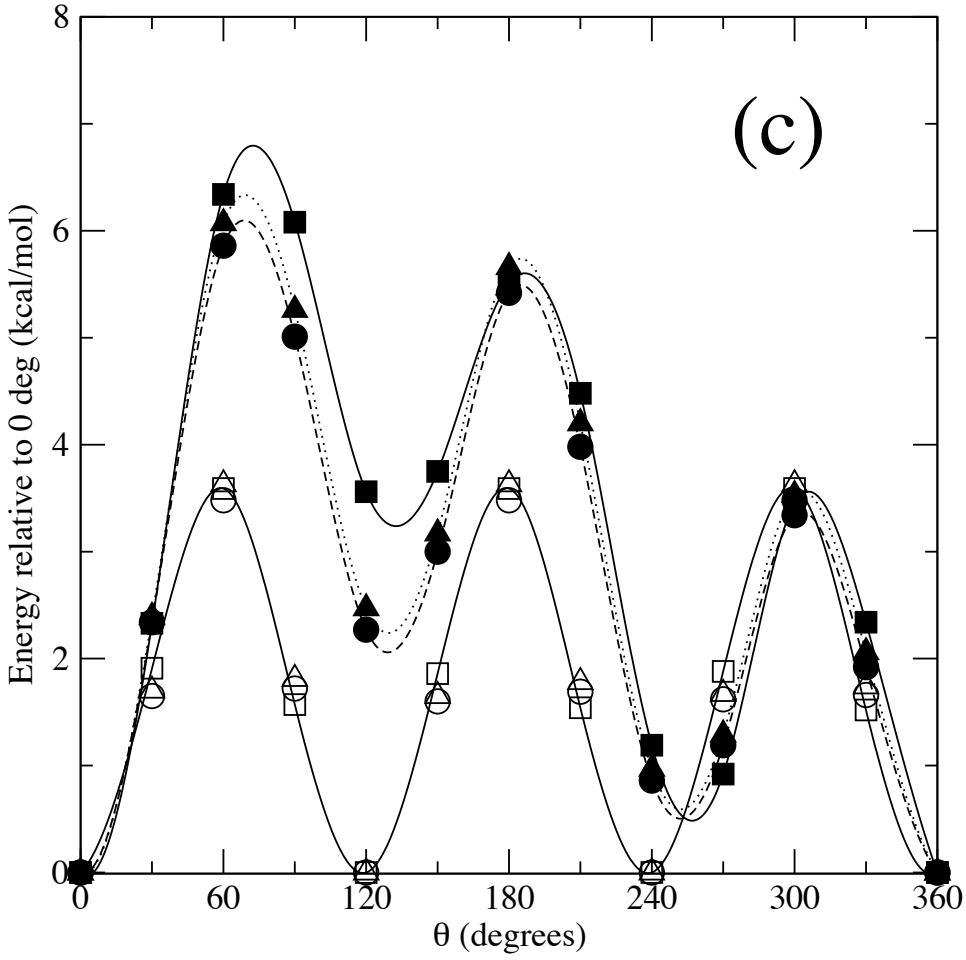

Figure 3.5: (continued)

Table 3.1: Calculated thermochemistry data for the potentials shown in Figure 3.5. The data given in the table are the hindered rotor partition function and entropy (cal/mol-K).

		3-21G		6-31G(d)		6-311G(2d,d,p)	
	T (K)	q_{hr}	S	q_{hr}	S	q_{hr}	S
HF	200	2.28	3.66	1.99	3.68	2.02	3.73
	1000	19.05	8.70	19.32	8.81	19.68	8.83
MP2	200	2.26	4.08	2.18	4.11	2.27	4.11
	1000	21.25	8.89	21.64	8.89	22.50	8.95
B3LYP	200	2.83	4.64	2.62	4.59	2.82	4.74
	1000	24.01	8.95	24.71	9.02	25.96	9.06

give limited yet useful insight into the relative sensitivity of the calculated partition functions and entropy to method and basis set.

3.5.3 Selection of appropriate step size while traversing hindrance potentials

Researchers who use the 1DHR correction typically choose a step size between 10^o and 30^o in order to traverse the hindrance potential and establish V(θ). Obviously, this can vary the computational cost of a given study greatly given that these increments correspond to 37 and 13, respectively, constrained geometry optimizations in order to traverse one 360^o rotation and ensure that the energies at the starting and ending points, *i.e.*, 0^o and 360^o, are identical. To the best of our knowledge, there are no reported studies which probe the sensitivity of the calculated properties to this choice.

To study the effect of the fineness of the hindrance potential scan, we investigated the rotations of both the backbone (atoms 4-3 as the rotation axis) and the CHCl group (atoms 2-3 as the rotation axis) in the product of the radical addition reaction shown as structure "C" in Figure 3.3. The "4-5" rotation is very well behaved so no comparison using different step sizes is provided. Step sizes of 1^o, 15^o, 30^o, and 40^o were used for each rotation, and the data were fit to a full Fourier series using 10, 10, 10, or 8 coefficients, respectively. The Fourier coefficients are given in Table 3.4 of the

Supplementary Information for reference, and the calculated data and best fits are plotted in Figure 3.6. The plot in Figure 3.6a shows that for the more complicated backbone rotation (bond "4-3"), all of the data are essentially in perfect agreement. It is a bit surprisng that the 40^o scan which uses only eight terms in the Fourier series is able to perfectly capture the data from the much more computationally expensive 1^o scan. It is also interesting that even though the scan in increments of 40^o has points which are substantially further (as compared to the 1^o, 15^o and 30^o scans) from the three peaks in energy, the fitted terms can still capture the data as well as the finer scans. This good agreement is very encouraging given the complexity involved with this and other backbone rotations.

The "2-3" rotation of the CHCl group is much less regular than the backbone rotation as shown in Figure 3.6b. In this case, while the Fourier fit of the 40^o scan captures the 40^o data well, it clearly differs from the other three fits. This is especially apparent near 300 degrees. Furthermore, the fit of the 30^o data is observed to deviate slightly from the more fine 1^o scan. While the shape of the curve is correct in the neighborhood of 300 degrees, quantitative deviations between the two fits are apparent. One interesting feature of the "2-3" rotation is that the 1^o scan contains a sharp peak when the C and Cl (atoms 4 and 1) are perfectly eclipsed near 120^o and an additional, although less pronounced, peak around 330^o when one of the hydrogen atoms and Cl are nearly eclipsed (atoms 12 and 1). An additional small peak is visible around 210^o when the other hydrogen atom and Cl are nearly eclipsed (atoms 11 and 1). The 1^o scan was generated by constraining the dihedral angle of atoms 11-3-2-13 (H-C-C-H) so as to give the bulkier groups/atoms more mobility. As a check, we re-generated this plot using atoms 4-3-2-13 (C-C-C-H) and obtained the exact same curve. To investigate the peak at 120^o, we performed a saddle point optimization on this structure, and the barrier obtained was only slightly above the peak energy at 120^o for the 15^o/30^o/40^o scans, indicating that the sharp peak in the 1^o scan is artificially high because of the forced eclipsing of the C/Cl atoms. We also performed the 1^o scan in reverse. The two sharp peaks were slightly offset from those shown in Figure 3.6b, but the rest of the curve overlapped.

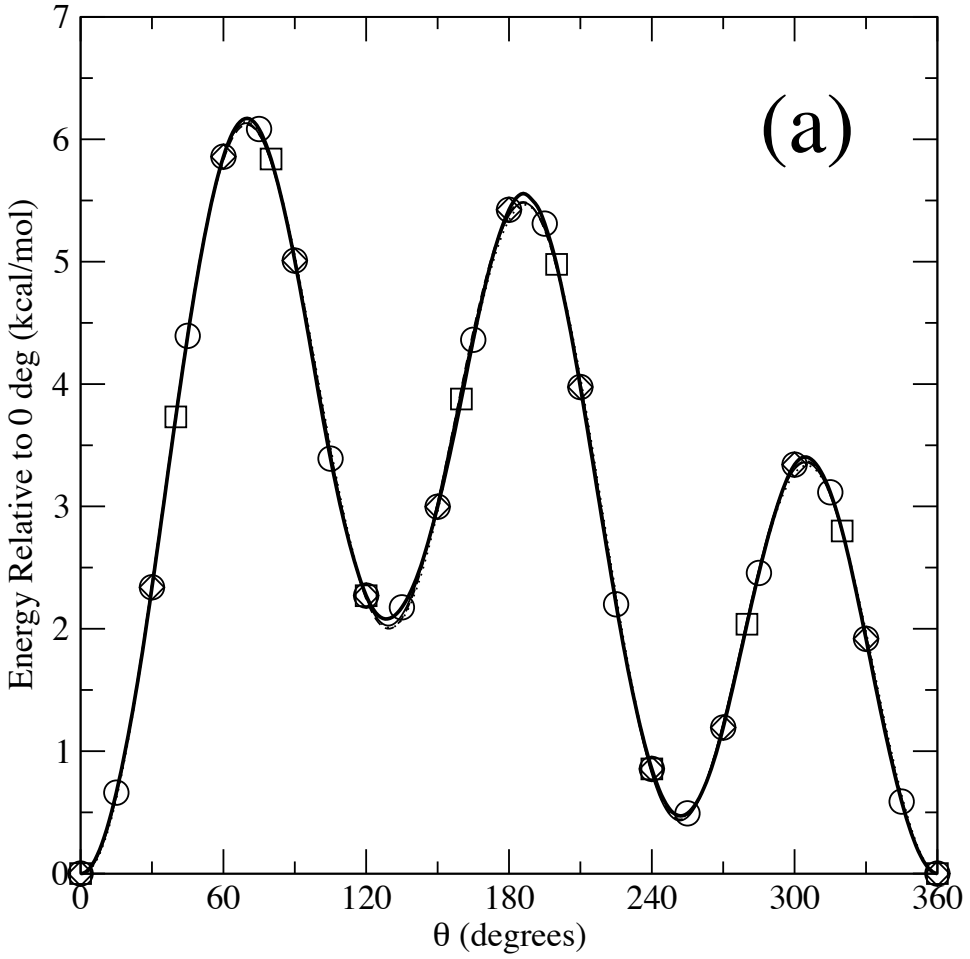

Figure 3.6: Comparison of hindrance potential (kcal mol^{-1}) and corresponding Fourier series fits calculated for the "4-3" (a) and "2-3" (b) rotations in structure "C" of Figure 3.3. The potentials were calculated by traversing a step size of 1^o (heavy solid line), 15^o (circles/solid line), 30^o (diamonds/dashed line), and 40^o (squares/dotted line). For the 1^o step size, the actual data from electronic structure calculations are shown as a single line. The coefficients for the Fourier series are given in the Supplementary Information. Continued on next page.

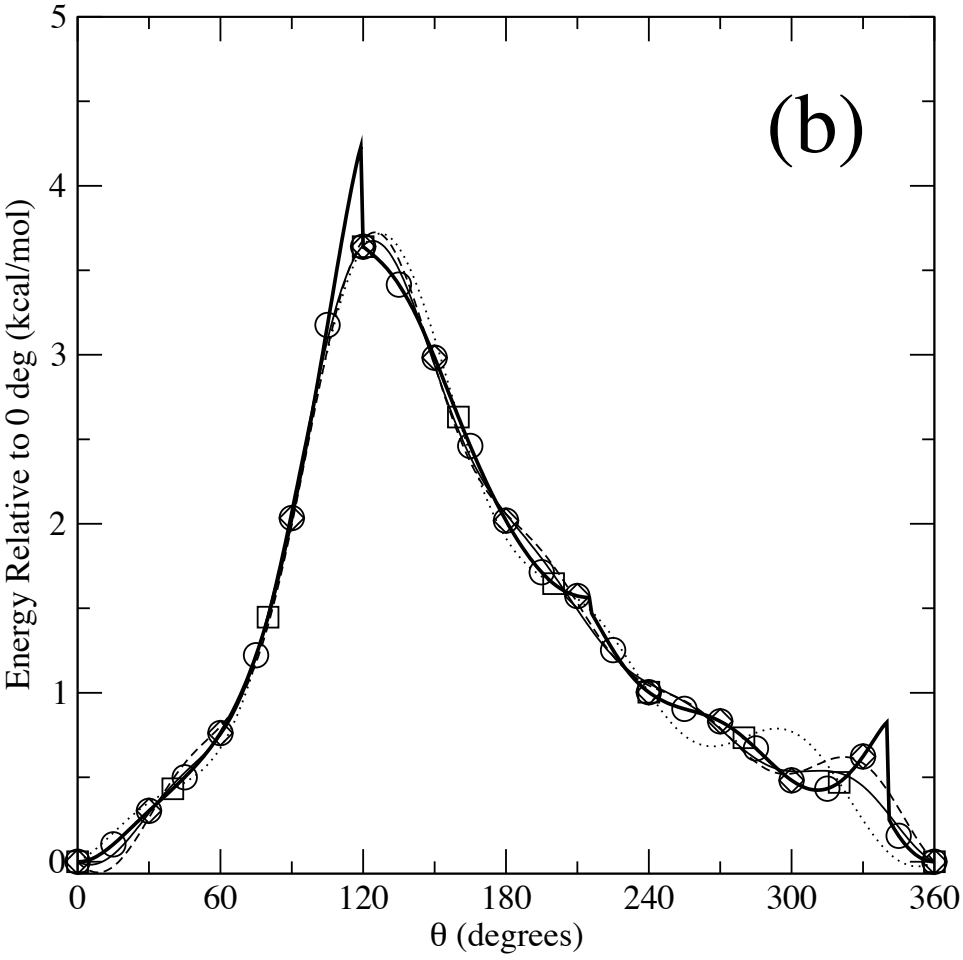

Figure 3.6: (continued)

It was therefore interesting to calculate what impact these discrepancies had on thermodynamic properties. We calculated the entropy, heat capacity and the thermal contribution to the internal energy for these two rotations ("2-3" and "4-3") using the energy levels obtained from solution of equation 3.1. The calculated entropy, heat capacity, and internal thermal energy for the temperature range 200 K to 1000 K are given in Table 3.2. As expected all of the data agree well for the rotation about the "4-3" bond given the similarities in the hindrance potentials that were fit. The data for the 40^o scan of the "2-3" rotation agree surprisingly well with the 1^o data, suggesting that the deviations between the fit hindrance potentials as shown in Figure 3.6 do not affect the calculated thermodynamic properties substantially. This is especially surprising given the two sharp peaks in the 1^o data for the "2-3" rotation. Although we show the actual 1^o data points in Figure 3.6, the Fourier fits of this data were used to calculate the properties in Table 3.2. Plotting the 1^o Fourier fit data using the coefficients in the Supplementary Information gives a curve that is almost identical to the 15^o and 30^o curves, indicating that our fitting procedure does not exactly follow the sharp, pronounced peaks in the 1^o data in Figure 3.6b. In generalizing these results to complex molecules with many internal rotations, it should be remembered that small deviations for each internal rotation may result in significant deviations for the property of a species as a whole since the contributions are additive. Finally, the data in Table 3.2 also include the corresponding harmonic oscillator data if one were to simply use the HO approximation for all calculations. The comparison between all four step sizes and the HO data clearly shows strong deviation between the HO approximation and the 1DHR correction.

Calculations such as the type illustrated in Figure 3.6 and Table 3.2 are helpful because they offer a rational template for deciding how much computational resource to expend while exploring the hindrance potential and performing the 1DHR correction. Especially given the complex, asymmetric rotation potentials produced by the bulky chlorine atoms, these results should give insight for a wide range of systems. To our knowledge, these results are the first systematic, quantitative comparison of using different step sizes for the constrained geometry optimization.

Table 3.2: Calculated thermochemistry data for the potentials shown in Figure 3.6. The data given in the table are the entropy (cal/mol-K), heat capacity (cal/mol-K) and internal energy (kcal/mol)[a]. Both rotations were calculated to be hindered rotors over the temperature range considered. The values based on the harmonic oscillator approximation[b] (including ZPE) are given for reference.[c] The frequency assigned to each internal rotation is given in the table.

T (K)	1^o scan			15^o scan			30^o scan			40^o scan			harmonic oscillator		
	S	C_v	E	S	C_v	E	S	C_v	E	S	C_v	E	S	C_v	E
Rotation about the "4-3" backbone C-C bond. ν = 84.4 cm^{-1}.															
200	4.74	0.53	2.78	4.74	0.53	2.78	4.74	0.54	2.80	4.72	0.54	2.84	2.92	6.83	0.41
400	6.74	1.11	2.92	6.74	1.11	2.92	6.74	1.12	2.92	6.74	1.12	2.94	4.27	3.71	0.80
600	7.87	1.67	2.63	7.87	1.67	2.63	7.88	1.67	2.63	7.88	1.68	2.63	5.07	3.02	1.19
800	8.58	2.16	2.28	8.58	2.16	2.28	8.58	2.16	2.27	8.59	2.17	2.27	5.64	2.72	1.59
1000	9.06	2.59	1.99	9.06	2.59	1.99	9.06	2.59	1.98	9.06	2.59	1.98	6.09	2.56	1.99
Rotation about the "2-3" C-C bond. ν = 48.6 cm^{-1}.															
200	5.64	0.52	2.48	5.67	0.52	2.40	5.58	0.51	2.62	5.65	0.50	2.43	4.16	3.85	0.40
400	7.13	0.94	1.88	7.14	0.94	1.87	7.13	0.95	1.91	7.13	0.92	1.88	5.53	2.77	0.80
600	7.84	1.29	1.62	7.84	1.29	1.62	7.85	1.30	1.63	7.84	1.27	1.62	6.33	2.48	1.19
800	8.28	1.59	1.45	8.28	1.59	1.45	8.29	1.61	1.45	8.28	1.57	1.45	6.91	2.35	1.59
1000	8.59	1.87	1.34	8.59	1.87	1.33	8.60	1.89	1.33	8.59	1.85	1.34	7.35	2.27	1.99

[a]The thermal contribution to the internal energy is calculated as $E = RT^2 \left(\frac{\partial ln\ q}{\partial T}\right)_V$. The total internal energy is not reported since it includes the electronic energy which is very large compared to the values reported here. The energy levels for the hindered rotor include the ZPE, *i.e.*, the ground-state energy is not 0; therefore the HO values include the ZPE, $\frac{1}{2}h\nu$, for fair comparison.

[b]Following the recommendation of Scott and Radom (1996), the frequencies were scaled by 1.0015 (calculation of entropy), 0.9989 (calculation of E_{vib}^{HO}), 0.9806 (ZPE), and 0.9989 (C_v).

[c]There are three low-frequency vibrations which could potentially be assigned to the two rotations ("4-3" and "2-3"). Normal mode analysis reveals the contributions of these backbone rotations to each of the frequencies as: 48.6 cm^{-1} ["2-3" : 54.7% , "4-3" : 35.3%] , 88.2 cm^{-1} ["2-3" : 35.3% , "4-3" : 52.7%], 190.4 cm^{-1} ["2-3" : 63.1% , "4-3" : 11%]. For illustration purposes, we chose the two lowest frequencies to assign as hindered rotors, although the mixing of vibrational modes is known to present difficulties (Van Cauter et al., 2006).

3.5.4 Investigation of the reduced moment of inertia as a function of the rotation angle

In spite of the importance of the reduced moment of inertia in calculating the 1DHR correction, there are no reported studies quantifying I_{red} as a function of θ for bulky, asymmetric groups, although East and Radom (1997) probed the sensitivity of calculated entropy values to changes in I_{red} within the Pitzer-Gwinn formalism. One potential solution is to calculate the reduced moment of inertia for a top using the formulae in Section 3.2.1.2 as a function of θ, fit the data to a functional form, and then use that function in solving the energy levels for the rotating top (Sumathi and Green, 2002b). Further work must be done, however, to assess *1)* the degree to which I_{red} changes as an asymmetric top rotates and *2)* the degree to which these changes impact the partition function and calculated thermodynamic properties.

One final consideration in examining the accuracy of the 1DHR calculation is the degree to which the reduced moment of inertia changes as a function of the dihedral angle that specifies a given internal rotation. The relaxation of the structure subject to 1) the constraint of the fixed dihedral angle and possibly 2) the constraint to freeze the atoms defining the transition state could result in changes in I_{red} as a function of rotation. To investigate this, each dihedral angle (bonds "2-3", "4-3" and "4-5") in the product of the PVC addition reaction, structure "C" in Figure 3.3, was scanned in 30^o increments. Each scan has 13 steps, thereby giving 13 distinct optimized geometries, and the reduced moment of inertia for each particular rotation bond was calculated for each of the 13 structures, affording I_{red} as a function of the angle of rotation. We calculated all three of the different $I^{2,n}$ presented in Section 3.2.1.2, and these data are summarized graphically in Figure 3.7.

The rotation involving the methyl group, as expected, has a nearly constant reduced moment of inertia as a function of rotation angle. In addition, the three $I^{2,n}$ all give roughly the same value for the rotation of the methyl group. The values of $I^{2,n}$ for the backbone ("4-3"' bond) and CHCl

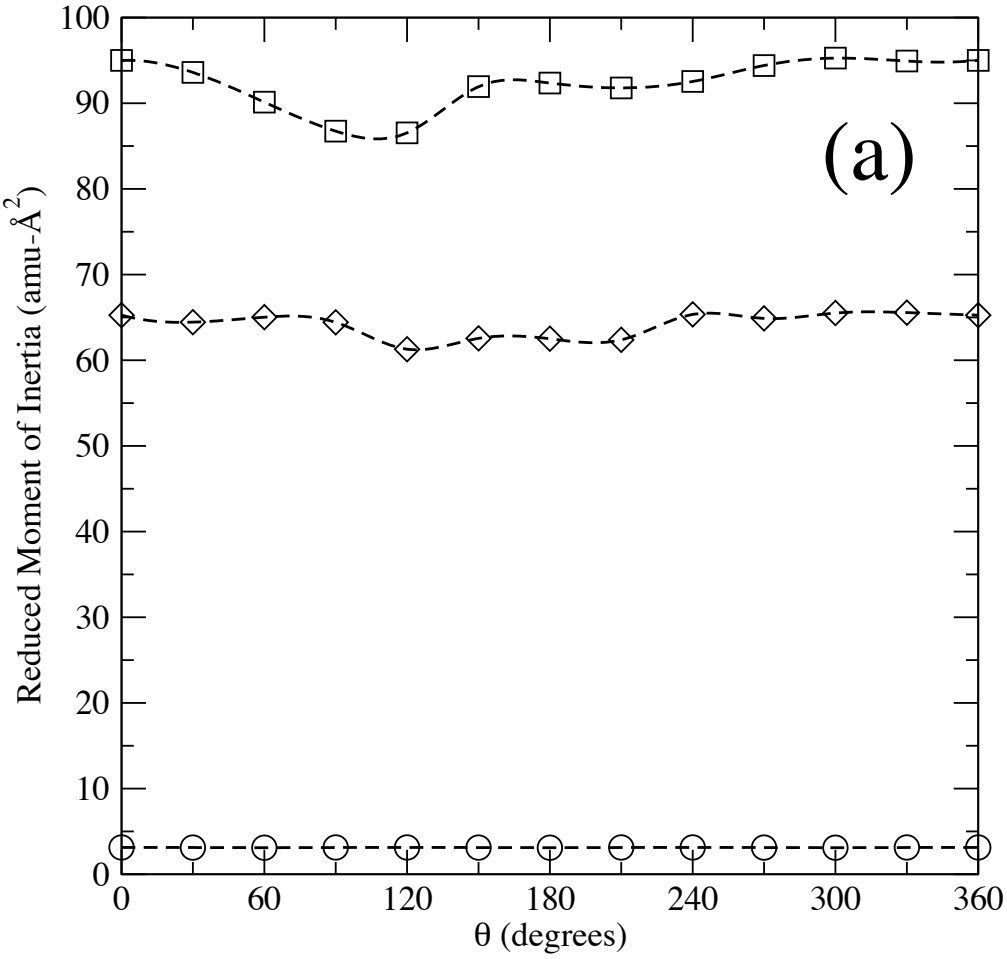

Figure 3.7: Comparison of the reduced moment of inertia as a function of rotation angle for each of three different rotating tops in structure "C" in Figure 3.3 calculated according to the prescription in Section 3.2.1.2. The data are calculated using three different approximations of rotor-rotor coupling: $I^{2,1}$ (panel A), $I^{2,2}$ (panel B), and $I^{2,3}$ (panel C). The data in the figure show the reduced moment of inertia calculated in 30^o increments. The "4-5" (methyl group) rotation is denoted by open circles, the "4-3" (backbone) rotation is shown with squares, and the "2-3" (CHCl) group is denoted by open diamonds. A cubic spline (dashed line) is drawn for each data set for reference. Continued on next two pages.

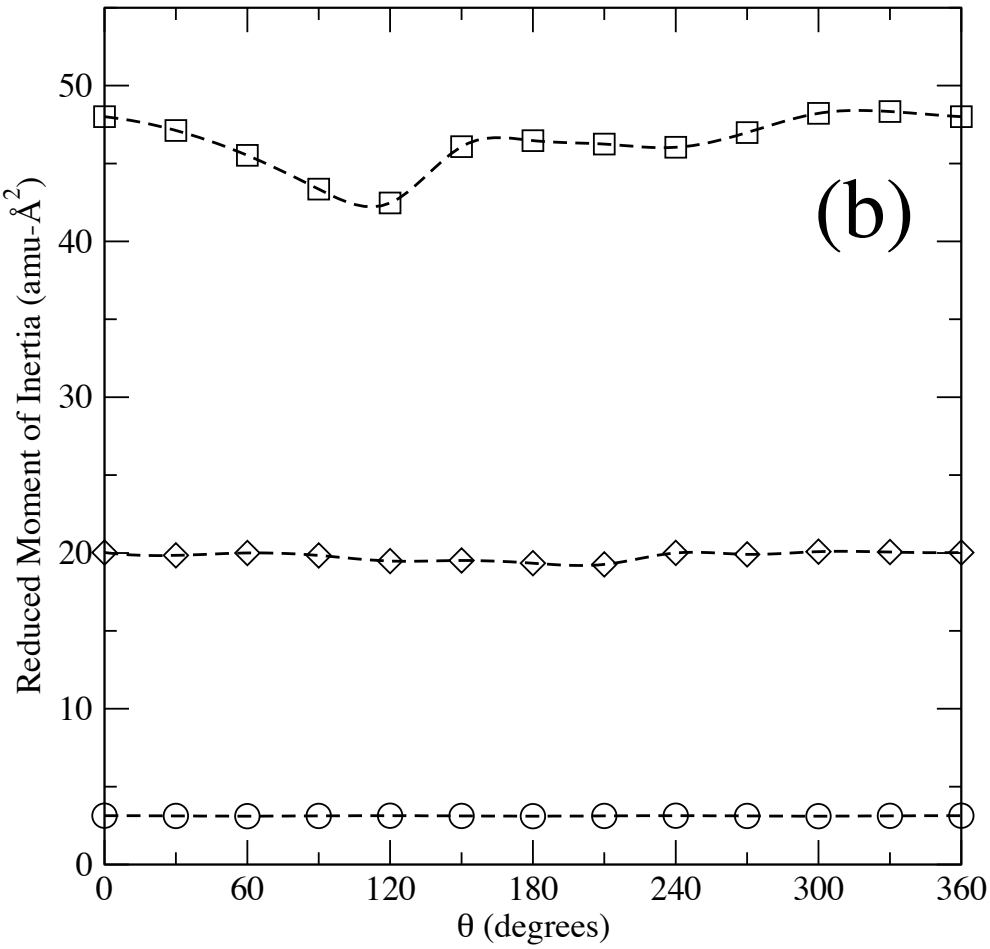

Figure 3.7: (continued)

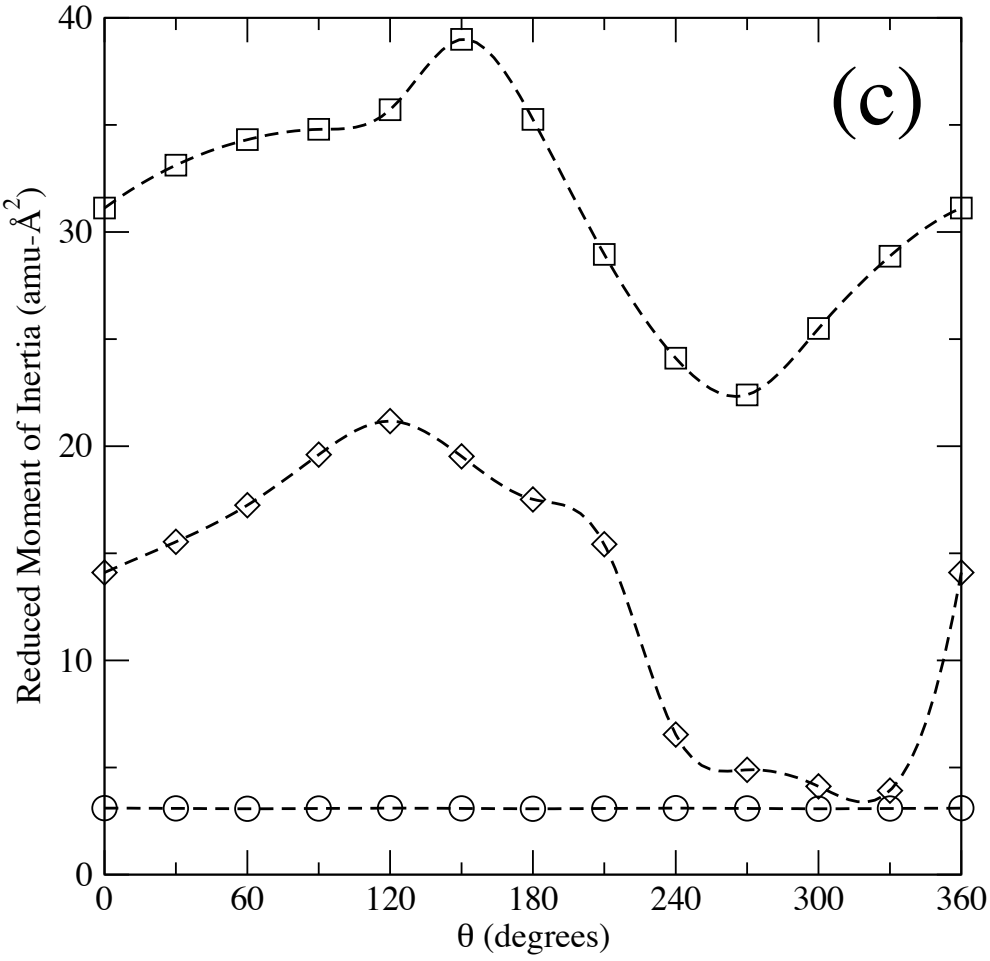

Figure 3.7: (continued)

("2-3" bond) rotations are very different and follow the expected trend, *i.e.*, $I^{2,1} > I^{2,2} > I^{2,3}$. To help understand the large differences between the various $I^{2,n}$ shown in Figure 3.7, it is helpful to remember that the reduced moment of inertia combines the moments for each of the "tops" and that each top contains a single heavy chlorine atom. It is therefore not surprising that such large and disparate I_{red} values are obtained given their strong dependence on the square of the Cl-*axis of rotation* distance. It is interesting to observe that for the approximations $n = 1$ and $n = 2$ (panel A and panel B, respectively) in Figure 3.7, the reduced moments of inertia are essentially constant as the dihedral angle is scanned. We hypothesize that this is because the axis of rotation is either fixed ($n = 1$) or can move but stays parallel to the single bond connecting the rotating groups ($n = 2$). For the third approximation of rotor-rotor coupling ($n = 3$), the axis of rotation is only defined by the two centers of mass and can vary greatly as the dihedral angle is scanned. Therefore, the distance between the Cl atoms and the axis of rotation can change much more and make a stronger impact on the effective moment of inertia. Examining panel C in Figure 3.7 shows that dramatic changes are seen in the reduced moment of inertia as a function of angle for the backbone rotation ("4-3" bond) and the rotation of the CHCl group ("2-3" bond). The stationary points have reduced moments of inertia of 31.1 amu-Å^2 ("4-3") and 14.1 amu-Å^2 ("2-3"), but the range of values for the two rotations is 22-39 amu-Å^2 ("4-3") and 4-21 amu-Å^2 ("2-3") as the angle is changed from 0 to 360 degrees.

The rotation about the "2-3" bond was used to probe the sensitivity of changes in I_{red} to calculated properties because it is one of the rotations that has the largest changes in the reduced moment of inertia as a function of θ. As a first approximation, we solved equation 3.1 by using the same rotational potential and systematically changed its value between 4 and 21 amu-Å^2 in order to explore the sensitivity of the partition function and thermodynamic properties to the value of I_{red}. The calculated partition function and entropy at 298.15 K are given in Table 3.3. Within the 1DHR approximation, the large relative changes in the reduced moment of inertia can have a meaningful impact on the calculated thermodynamic properties. The partition function is seen to change from

Table 3.3: Calculated partition function and entropy (cal/mol-K) for the rotation "2-3" of structure "C" in Figure 3.3. The reduced moment of inertia (amu-Å^2) is given for reference and adjusted to cover the full range seen in this rotation, as shown in Figure 3.7c. The data are calculated at 298.15 K.

Ired	q_{hr}	S
4	3.39	4.94
10	5.38	5.85
14.1[a]	6.39	6.19
20	7.61	6.53
21	7.80	6.58

[a]The reduced moment of inertia calculated at the minimum energy structure.

approximately -47% to +22% of its value at the equilibrium structure and the entropy changes are less drastic varying from -20% to +6% of their equilibrium values. Additionally, we found that the calculated changes in q_{hr} and S vary only a small amount as a function of temperature.

It is interesting to compare these calculated results to the results of East and Radom (1997) who also studied the sensitivity of the calculated entropy to changes in the reduced moment of inertia. Within the Pitzer and Gwinn formalism, they varied the height of the rotational potential for a top with symmetry number (σ_r) of three between 0.96 and 2.63 kcal mol^{-1}, and the reduced moment of inertia was changed between 0.65 and 3.0 amu-Å^2. Their results show the calculated entropy to be strongly dependent on both terms. This is consistent with the results given in Table 3.3 since the hindered rotor entropy was observed to be dependent on the reduced moment of inertia for the PVC radical product. For example, the data from East and Radom show that an increase by a factor of 4.6 in I_{red} corresponds to an increase of 1.5 cal/mol-K in the hindered rotor entropy, and an increase of a factor of 5 (changing from 4 to 20) in I_{red} from the data in Table 3.3 corresponds to an increase of 1.6 cal/mol-K in the hindered rotor entropy. To explore this further, we compared the results of East and Radom in terms of S versus I_{red} as a function of V/RT, where V is the barrier to rotation, with results from our method for V/RT of 1.6, 4.4, and 10. The values V/RT = 1.6 and 4.4 correspond to those chosen by East and Radom in their study, and the value of V/RT

= 10 was chosen because it represents a barrier height of 6 kcal mol^{-1} at 298.15 K which is the barrier height of the "4-3" rotation in the product of the PVC addition reaction (see Figure 3.6a). The calculated data are summarized graphically in Figure 3.8 using a logarithmic axis for I_{red} since the entropy is dependent on the logarithm of the reduced moment of inertia.

The data presented here show that the main consideration in studying the effect of changes in I_{red} as a function of the rotation angle is the relative difference and not the absolute difference. For example, the data in Table 3.3 shows that changing I_{red} from 14.1 to 20 amu-Å^2 changes the entropy by only 0.39 cal/mol-K whereas a comparable absolute change in the regime explored by East and Radom (changing I_{red} from 0.65 amu-Å^2 to 5.65 amu-Å^2) causes a change in the entropy of 2.07 cal/mol-K. Although these results are given for symmetric tops, the conclusions are general for tops of any symmetry number. Manipulation of equation 3.11 shows that for tops with a symmetry number greater than one the hindered rotor entropy is uniformly decreased by the quantity $k\ ln\ \sigma_{r_i}$. Thus, the trend of the curves shown in Figure 3.8 is invariant with the internal symmetry number of the top. These results are important in the development of heuristics for using the 1DHR model. If the relative changes in I_{red} as a function of the rotation angle are not large, then accurate properties are still obtained using the 1DHR model.

3.6 Summary and Future Outlook

We have provided a brief summary of the current practice in quantum-mechanical treatment of internal rotation. The uncoupled, one-dimensional hindered rotor model has been widely applied to study numerous problems of chemical and engineering interest. We expect the 1DHR model to continue to be a general part of the modeling toolkit for *ab initio* studies since there are few alternatives to the 1DHR model that are both computationally tractable and general for tops of any symmetry. In response to the lack of general electronic structure codes that make the 1DHR model part of the standard menu of choices, we have offered two codes, "Calctherm" and "Calc*k*", that

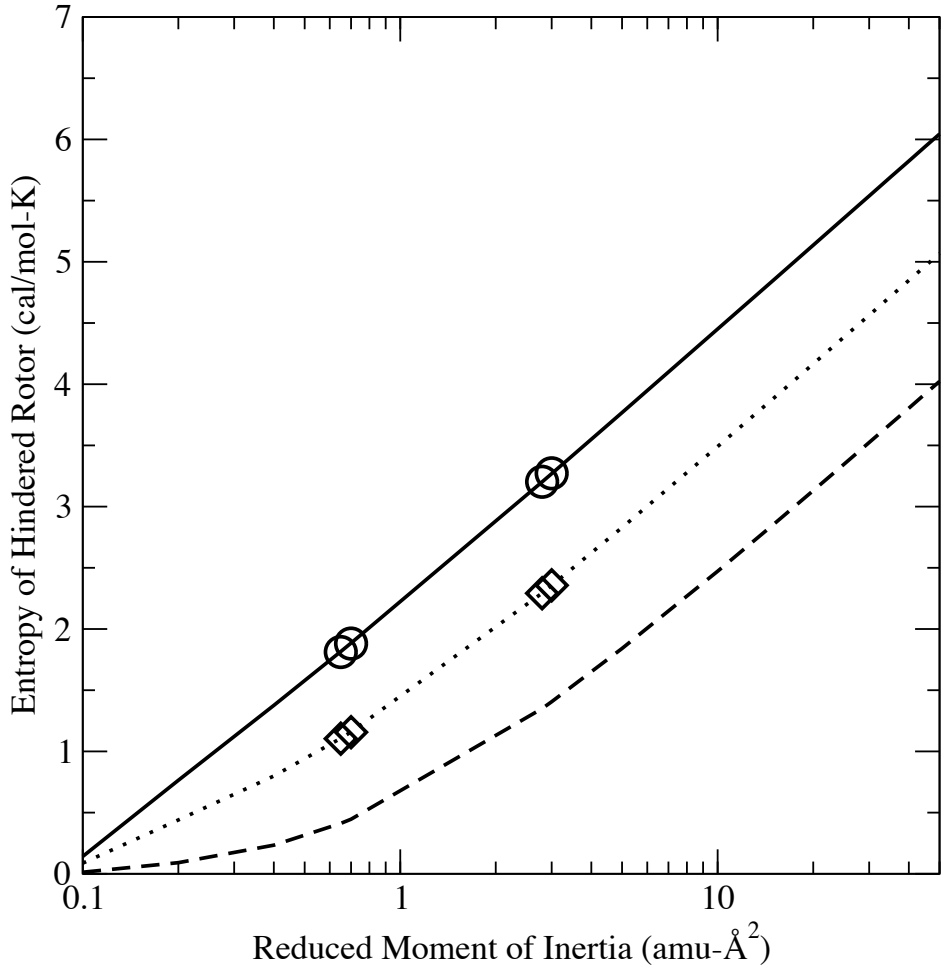

Figure 3.8: Comparison of the hindered rotor entropy with changes in the reduced moment of inertia for several different potentials of varying V/RT. The data are calculated at 298.15 K and all potentials represent a top with a rotational symmetry number (σ_r) of three. The symbols are taken from East and Radom (1997) and the data in lines are calculated using the approach given in this chapter and the Calctherm software. The potentials considered V/RT = 1.6 (open circles, solid line), 4.4 (open diamonds, dotted line), and 10 (dashed line).

extract data from electronic structure software output, perform the 1DHR correction, and finally output thermodynamic and kinetic properties which have been fully corrected for internal rotation.

Several calculations were performed to test the applicability of the 1DHR model to a wide range of systems and revealed how the 1DHR model may be more efficiently applied in general. We have shown that rotational hindrance potentials in the transition state can be determined by simply freezing the atoms defining the transition state instead of re-optimizing to a transition state at each point throughout the rotation. Additionally, we have explored the sensitivity of calculated properties to the choice of step size (in scanning each rotational top) and the method and basis set. These results can help modelers make rational choices and realize significant savings in computational cost when applying the 1DHR model. Finally, we used highly asymmetric rotating tops to quantify how much the reduced moment of inertia changes as it undergoes rotation. The sensitivity of calculated properties to the changes in the reduced moment of inertia was calculated, and we showed that in general changes in the reduced moment of inertia do not compromise the accuracy of the 1DHR model.

3.7 Supplementary Information

Table 3.4: Fourier series coefficients for various step sizes of the "4-3" and "2-3" rotations of structure "C" in Figure 3.3. The hindrance potential can be calculated as $V(\theta) = V_o + \sum_{i=1}^{n}[a_i(1 - cos\ i\theta) + b_i sin\ i\theta]$, where V_o is the energy of the structure at the stationary point, -1077.09027 hartrees. The calculated coefficients have units of hartrees and are ordered left to right from 1-5 (or 1-4).

			Rotation about 4-3 bond			
1 deg	a_i	1.252E-03	3.456E-04	3.045E-03	4.415E-05	-1.015E-05
	b_i	1.847E-03	5.774E-04	-1.160E-03	6.956E-05	8.850E-06
15 deg	a_i	1.252E-03	3.456E-04	3.046E-03	4.526E-05	-1.245E-05
	b_i	1.847E-03	5.768E-04	-1.158E-03	6.798E-05	1.187E-05
30 deg	a_i	1.251E-03	3.445E-04	3.046E-03	3.317E-05	1.474E-06
	b_i	1.844E-03	5.750E-04	-1.161E-03	6.870E-05	3.508E-05
40 deg	a_i	1.244E-03	3.706E-04	3.012E-03	4.574E-05	
	b_i	1.839E-03	6.020E-04	-1.217E-03	6.536E-05	
			Rotation about 2-3 bond			
1 deg	a_i	1.876E-03	3.073E-04	-3.930E-04	1.954E-04	1.701E-04
	b_i	1.151E-03	-9.607E-04	-5.529E-06	1.767E-04	-1.780E-04
15 deg	a_i	1.850E-03	3.271E-04	-3.615E-04	1.693E-04	1.511E-04
	b_i	1.163E-03	-9.158E-04	-5.468E-06	1.779E-04	-1.264E-04
30 deg	a_i	1.833E-03	2.896E-04	-3.565E-04	2.229E-04	1.631E-04
	b_i	1.135E-03	-9.404E-04	-3.033E-05	1.436E-04	-2.069E-04
40 deg	a_i	1.867E-03	3.323E-04	-3.412E-04	2.670E-04	
	b_i	1.168E-03	-9.600E-04	7.217E-05	2.976E-04	

Chapter 4

Quantum Chemical Investigation of Low-Temperature Intramolecular Hydrogen Transfer Reactions of Hydrocarbons

4.1 Introduction

The low-temperature oxidation of hydrocarbons is of interest to researchers in a number of different fields. Examples include the oxidative degradation of lubricating oils (Blaine and Savage, 1992; Jensen et al., 1981) and combustion of fuels in novel engines (Wijaya et al., 2003). Despite decades of detailed experimental and theoretical investigations, a number of fundamental questions remain unanswered about elementary step reaction networks which can describe the low-temperature condensed-phase oxidation of large hydrocarbons. One main obstacle in answering these questions is the accurate resolution of the kinetic parameters of the important elementary reactions.

The fundamental reaction pathways in condensed-phase oxidation are basically well established and have been reviewed extensively including recent comprehensive reviews by Emanuel and Gál (1986) and Denisov and Denisova (2000). However, successful generation of a large-scale complex reaction network requires kinetic data for hundreds or thousands of reactions, and in the case of condensed-phase oxidation, published data can be contradictory or lacking altogether. Therefore, the use of kinetic correlations, or structure-reactivity relationships, has become widespread in the modeling community as a means of estimating rate coefficients of reactions in large-scale mechanisms. In the case of bimolecular atom-transfer reactions, the Blowers-Masel correlation has been shown to be particularly effective in estimating the activation energy (Blowers and Masel, 2000). The Blowers-Masel correlation is an improvement upon the classic Evans-Polanyí correlation (Evans and Polanyí, 1938), which has been shown to work well for a number of different elementary reaction types in free radical chemistry (Boock and Klein, 1994; De Witt et al., 2000; Kruse et al., 2003).

One reaction class that is of particular interest in the early phase of oxidation is intramolecular hydrogen transfer (Chan et al., 1998). These reactions are driven by the growth of peroxy radicals ($RO_2\cdot$) which are formed from the very fast addition of molecular oxygen to primary radical species. Subsequent isomerization of $RO_2\cdot$ species leads to hydroperoxyalkyl radicals ($\cdot$QOOH) that are able to directly yield molecular products or introduce bifunctional moieties along the hydrocarbon backbone. Wijaya et al. (2003) have recently performed a thorough investigation of the fate of $\cdot$QOOH in the low-temperature regime. Herein we investigate the isomerization reactions which lead to the formation of $\cdot$QOOH.

Intramolecular hydrogen transfer reactions of $RO_2\cdot$ species are difficult to study experimentally, and kinetic parameters must often be inferred from data rather than directly measured. Denisova and Denisov (2001) tabulated a number of the experimentally available rate constants for unimolecular hydrogen shifts of peroxy radicals. In their review of condensed-phase oxidation, Mill and Hendry (1980) give accepted experimental values for the pre-exponential factor of intramolecular

abstraction by peroxy radicals of log A (1/s) equal to 12.5, 11.5, and 11.0 for ring sizes (transition state) of five, six, and seven, respectively. Van Sickle and coworkers studied the 1,5-hydrogen shift (six-membered ring formed) of 2-peroxy pentane (Sickle et al., 1973). They reported a unimolecular rate constant of 0.87 s^{-1} at 373 K. The 1,5-hydrogen shift of 2-peroxy-2,4-dimethylpentane was reported by Mill and Montosori (1973) to have a rate constant of 18 s^{-1} at 373 K. Mill and Hendry (1980) derived a rate constant of 8 s^{-1} at 373 K from the data of Rust (1957) for the 1,6-hydrogen shift of 2-peroxy-2,5-dimethylhexane. Given the experimentally accepted rate constants and pre-exponential factors, it is possible to derive activation energies of 19.7, 17.5 and 17.2 kcal mol^{-1} for these three reactions, respectively.

There have been few attempts to theoretically characterize the intramolecular hydrogen shift reactions of peroxy radicals. Denisova and Denisov (2001) estimated activation energies by applying an analog of the Marcus equation. Their method requires *a priori* knowledge of both the dissociation energies as well as the frequencies of bonds being broken and formed in the reaction. To accurately apply this method to a wide range of systems, a rigorous quantum mechanical treatment would be necessary in order to obtain these unknown quantities. An alternative approach is to use transition state theory (TST) to obtain rate constants applicable in the condensed phase as well as in the high-pressure limit.

Quantum mechanical studies of this reaction class are limited to the works by Chan et al. (1998) and Merle et al. (2005). Chan et al. studied the self-abstraction by peroxy radicals for a small series of aliphatic hydrocarbons using the BHandHLYP functional with a 6-311G(d,p) basis set. It was recently demonstrated by Wijaya et al. (2003) that BHandHLYP has the potential to be a predictive tool for studying kinetics of some peroxy radical reactions, but not without including corrections for internal rotation and errors associated with the peroxy ligand. Merle et al. studied the unimolecular isomerization of the *n*-propylperoxy radical using B3LYP/6-31+G(d,p) and CBS-QB3.

The purpose of this chapter is to study the intramolecular hydrogen transfer of several peroxy radicals using quantum mechanical calculations. The effect of substituents and transition state (TS) ring size will be used to elucidate kinetic correlations suitable for calculating rate constants in the high-pressure limit. In the past several years, the B3LYP functional has been used extensively in similar kinetic studies. Gomez-Balderas et al. (2004) and coworkers have recently provided an extensive evaluation of many quantum mechanical methods for several addition reactions. However, a broader consensus as to which basis set is appropriate for various systems is still lacking. In order to help guide selection of an appropriate method, we studied the three reactions for which experimental data is available as noted above using the B3LYP functional with seven different basis sets as well as BHandHLYP/6-311G(d,p), MP2/6-311+G(d,p), G3(MP2), G3//B3LYP, and CBS-QB3 methods. The BHandHLYP/6-311G(d,p) functional and basis set were selected for comparison with previously obtained results using this level of theory (Chan et al., 1998; Wijaya et al., 2003). These reactions are pictured as reactions 1-3 in Figure 4.1. A larger set of reactions (reactions 4-11 in Figure 4.1) was studied at the B3LYP/6-311+G(d,p) level of theory in order to develop kinetic correlations for estimating rate constants or developing reaction mechanisms.

4.2 Computational and Theoretical Details

All molecular orbital (MO) and density functional theory (DFT) calculations were completed using the Gaussian 03 (Frisch et al., 2003) software package. At each level of theory and basis set, the geometries of all reactants and products were optimized to minimum energy structures using the Berny algorithm (Peng et al., 1996). Transition states were identified as first-order saddle points on the potential energy surface. After locating a TS of a particular ring size, other similar transition states were located efficiently and successfully using the quadratic synchronous transit (QST3) (Peng and Schlegel, 1993) method. All transition states were first validated by verification that only one large amplitude imaginary frequency was present in the proposed TS. The true reactant and

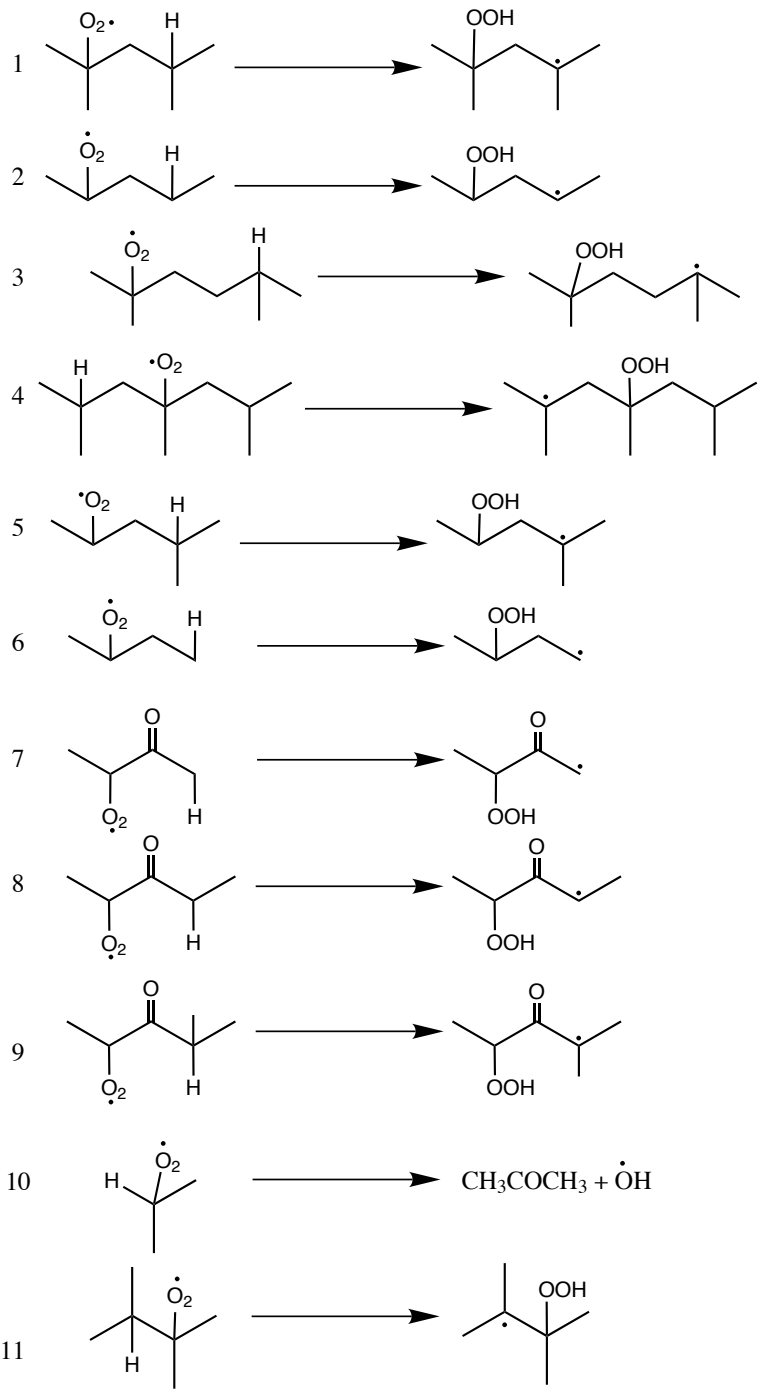

Figure 4.1: Intramolecular hydrogen abstraction reactions involving peroxy radicals studied using quantum chemistry. For brevity, each reaction is given a numerical identification.

product(s) corresponding to each TS were obtained by using intrinsic reaction coordinate following (Gonzalez and Schlegel, 1989).

Transition states were determined using a number of different MO and DFT prescriptions. In response to its immense popularity in the literature, we screened Becke's (Becke, 1993) three parameter hybrid functional, B3LYP, most extensively. Seven different basis sets were employed including Pople Gaussian-type basis sets as well correlation consistent basis sets of Dunning. Within the Pople formalism split-valence double and triple zeta basis sets optionally including d, f, and p-type polarization functions on first or second row atoms as well as an optional single set of diffuse functions on first-row atoms were used. The different basis sets examined were: 6-31G(d), 6-31G(d,p), 6-311G(d,p), 6-311+G(d,p), 6-311+G(df), and 6-311+G(3df,2p). For further comparison, restricted open-shell wavefunctions were used in two of the B3LYP cases; unless noted all calculations are done with unrestricted, open-shell wavefunctions. A single calculation using a correlation consistent basis set was carried out employing polarized valence triple zeta functions augmented with diffuse functions (B3LYP/cc-pVTZ+d). Additionally, for comparison with results obtained previously (Chan et al., 1998; Wijaya et al., 2003), the Becke (1993) half and half functional, BHandHLYP, was used with a single basis set, 6-311G(d,p). Structures optimized using MP2/6-311+G(d,p) allowed further comparisons to be made. The results were additionally benchmarked using high-level extrapolation methods. Two composite methods which have been shown to provide accurate results in radical chemistry (Coote et al., 2002), CBS-QB3 (Montgomery et al., 1999) and G3//B3LYP (Baboul et al., 1999), were used. Calculations were also performed using G3(MP2) (Curtiss et al., 1999) in order to probe the effect of a high-level correction using MP2 optimized geometries. Accepted B3LYP scaling factors of 0.9806 for zero-point energies and 0.9614 for other calculations, *e.g.*, partition functions, were used (Scott and Radom, 1996). Scott and Radom optimized these scaling factors specifically for the 6-31G(d) basis set, but given the absence of scale factors for other basis sets, it has become commonplace to scale results using these values for B3LYP, regardless of the basis set (Merle et al., 2005; Van Speybroeck et al., 2000). Finally,

solvation effects were studied using a polarizable continuum model (PCM) (Cancés et al., 1997). The solvent cavity was established using radii obtained from the universal force field (Rappé et al., 1992) with hydrogen atoms explicitly defined. Full geometry optimization and energy calculations were performed with *n*-heptane as the solvent using B3LYP/6-31G(d).

Using the optimized geometry and frequencies obtained from a Hessian calculation, the total microcanonical partition function can be calculated for each molecule within the rigid-rotor harmonic oscillator (HO) assumption. The formulae for electronic, translational, rotational and vibrational partition functions are well established (McQuarrie and Simon, 1999). However, the HO approximation incorrectly treats low-frequency rotations as harmonic oscillators. If left uncorrected, this can induce substantial error in calculated kinetic and thermodynamic data. Internal rotations whose barrier to rotation is much less than kT are characterized as free rotors and corrected easily (Frenkel et al., 1994). In the temperature range of interest to the current study (300-1000 K), the barrier to rotation for all dihedrals is on the order of kT, therefore requiring that internal rotations be treated as hindered rotors. Our approach in treating internal rotation was similar in principle to previously reported methods (Sumathi et al., 2001a; Van Speybroeck et al., 2000) and is detailed in Chapter 3. First, the hindrance potential energy surface (PES) for each rotation about polyvalent single bonds was obtained by scanning the dihedral angle in 30^o increments. The dihedral angle was fixed and the rest of the structure was allowed to relax with the geometry optimized using the B3LYP/6-31G(d) level of theory. While rigid scans are more computationally efficient, significant errors were encountered due to the branching of the molecules under consideration. In particular, the peroxy radical and hydroperoxide moieties gave nonphysical PES results when the superstructure was kept rigid. Examples of this are provided in Section 4.5. In order to preserve the structure of the reactive center during relaxed PES scans of transition states, all coordinates which constituted the ring of each transition state were frozen, while all other coordinates except the dihedral angle being scanned were optimized. Once the PES for each rotation was obtained, the one-dimensional Schrödinger equation was solved in order to obtain the energy levels for each

rotation. This step was performed using the Fourier grid Hamiltonian (FGH) method developed by Marston and coworkers (Balint-Kurti et al., 1992; Marston and Balint-Kurti, 1989). To obtain the correct energy levels, the numerical algorithm for the FGH method was implemented using published source code (Balint-Kurti et al., 1991). The energy levels from this calculation were used to calculate the partition function for each internal rotation as a function of temperature:

$$Q_{ir} = \frac{1}{\sigma_r} \sum_i g_i \exp\left(-\frac{\epsilon_i}{kT}\right) \tag{4.1}$$

where σ_r is the internal symmetry number of the rotating top and g_i is the degeneracy of the ith energy level, ϵ_i (Van Speybroeck et al., 2000).

In making the correction to the HO partition function, the vibrational modes corresponding to internal rotation must be identified and their contribution to the HO partition function removed (Sebbarand et al., 2005; Sumathi et al., 2001a). For each vibration, the contributions from various bonds, angles, and dihedrals were analyzed using the internal mode analysis provided by Gaussian 03. In large molecules, there is often substantial mixing of vibrational modes resulting in a number of low frequencies corresponding to multiple different internal rotations. Potential problems arising from this mixing of vibrational modes have recently been outlined (Van Cauter et al., 2006). Our present approach is to use the internal mode analysis to identify a single low-frequency vibration for each internal rotation in a given molecule. Thus, the HO partition function for a molecule with *n* dihedral angles was corrected by (i) removing the contribution of *n* low frequency vibrational modes and (ii) including the contribution of *n* internal rotations.

Once the partition functions for each reactant and transition state were corrected for internal rotation, the rate constant as a function of temperature was calculated using the standard expression,

$$k_{TST} = \mathit{rpd} * \kappa\left(T\right) \frac{k_b T}{h} \frac{Q^{\ddagger}(T)}{Q^{r}(T)} \exp\left(-E_o/RT\right) \tag{4.2}$$

where *rpd* is the reaction path degeneracy, determined by the number of identical hydrogen atoms a particular radical can self-abstract, $Q^{\ddagger}$ and Q^{r} are the total partition functions for the TS and reactant, respectively, and E_o is the reaction barrier, *i.e.*, the zero-point corrected difference between the ground-state electronic energies of the TS and the reactant. The quantity $\kappa\left(T\right)$ is the correction for quantum tunneling. To quantify the effect of quantum tunneling on the reactions of interest here, we calculated various approximations to the transmission coefficient including the Wigner (Hirschfelder and Wigner, 1939) correction, the Eckart approximation (Gonzalez-Lafont et al., 1991), the zero-curvature tunneling approximation (ZCT) (Gonzalez-Lafont et al., 1991), and the small curvature tunneling (SCT) (Gonzalez-Lafont et al., 1991) approximation. Calculation of the Eckart, SCT and ZCT corrections was performed using the software package "Virtual Kinetic Laboratory" of Zhang and Truong (2001). Once the temperature dependent partition functions were known, rate constants as a function of temperature were calculated, and the Arrhenius parameters A and E_A were obtained from a straight-line fit of $\ln k$ vs $1/T$. Unless otherwise stated, we used a temperature range of 300-1000 K for regression of A and E_A. To calculate the enthalpy of reaction, all thermodynamic parameters were obtained from ensemble energy averages <E> using standard formulae (McQuarrie and Simon, 1999).

4.2.1 Thermochemistry of peroxide species

While the B3LYP functional has been repeatedly shown to give accurate results for the heat of reaction and heat of formation, especially when compared to other methods of similar computational cost, it has been documented that B3LYP systematically gives errors in the bond dissociation energy of the O-O and O-H bonds in hydroperoxide moieties (Brinck et al., 1999; Wijaya et al., 2003). The standard approach is to use isodesmic reactions to obtain a corrected heat of formation (Redfern et al., 2000). While this correction for reactants and products is straightforward, an analogous treatment for the TS is not obvious. Therefore, the heats of reaction reported are the

difference in the quantum chemical enthalpies between the reactant and product species, which offered a method that was consistent with the manner in which the activation energy was calculated for the structure/reactivity relationships that were developed.

4.2.2 Treatment of rotational isomers

It was observed that in some cases the IRC-derived reactants were not the minimum energy structures. Subsequent rotation of the C-O bond in the peroxy radical or rotation about the backbone of the molecule could yield a reactant lower in energy typically by no more than 1 kcal mol^{-1}. While these were relatively subtle differences, it was still important to account for them in the evaluation of methods and development of the structure/reactivity relationships. For reactants in which a lower energy structure was found, the following modified rate constant was used:

$$k_{apparent} = K_{eq}^{rot}(T) * k_{TST}(T) \tag{4.3}$$

where K_{eq}^{rot} is the equilibrium constant between two rotational isomers:

$$K_{eq}^{rot} = e^{-\Delta G^{rot}(T)/RT} \tag{4.4}$$

Thus, the activation energy and pre-exponential factor were regressed from a fit of $ln(k_{apparent})$ versus $1/T$. A full derivation of this relationship is provided in the Supplementary Information.

4.3 Results and Discussion

4.3.1 Effect of basis set on results obtained from the B3LYP functional

Results for the comparison of 16 different methods and the three different reactions studied in detail (reactions 1-3 in Figure 4.1) are listed in Table 4.1. The first eleven entries in each section of the table list B3LYP calculations performed with increasingly larger basis sets. The one non-Pople

basis set used was listed as the last of these eleven for clarity. The bottom five lines in each section of Table 4.1 contain results for these reactions with different MO, DFT and hybrid methods. The results show that the choice of the basis set has a strong impact on both the reaction barrier and the heat of reaction. As expected, increasing the size of the basis set generally improves the agreement between the B3LYP results and experimental data or results from the high-level compound methods. With one exception in which the calculated activation energy was equal to the experimental value, all of the B3LYP methods overestimate the experimental activation energies. This corresponds to an underprediction of the reaction rate coefficient. One possible explanation for this could be the type of calculation used to estimate the contribution of quantum tunneling, but our results show that the type of tunneling correction used did not change the calculated activation energies significantly. We calculated the Eckart, ZCT, and SCT transmission coefficients for reactions 1 and 2 using the B3LYP/6-31G(d) and B3LYP/6-311+G(d,p) basis sets. The Wigner correction was a good approximation of the SCT transmission coefficient (within a factor of two or less at the temperature of interest (373 K)). Accordingly, we calculated all kinetic data in Table 4.1 using the Wigner correction. Furthermore, the transmission coefficient had a maximum value of 3.7 at 300 K for the reactions we studied, which is much lower than that observed for intermolecular hydrogen transfer reactions of small molecules studied by Truong and coworkers (Truong et al., 1999) and Gonzalez-Lafont and coworkers (Gonzalez-Lafont et al., 1991). The small contribution of tunneling is consistent with the adiabatic ground state potential clearly showing a *very* late transition state. The potential is nearly flat as the reaction goes from the transition state to the product hydroperoxide radical (forward direction as depicted in Figure 1). Since tunneling is not observed to have a strong impact in these reactions, it is not surprising that for each reaction in Table 4.1, a plot of ln k versus 1/T gave a perfect straight-line fit, thereby validating our method of obtaining the Arrhenius parameters A and E_A.

Because we are seeking kinetic correlations for use in condensed-phase hydrocarbon oxidation chemistry, we tested the sensitivity of the calculated data to the presence of a non-polar solvent, *i.e.*,

a typical oxidation substrate of interest. We used the PCM model to simulate a solvent cavity of *n*-heptane and re-optimized the reactants, TS, and products for reactions 1-3 using B3LYP/6-31G(d). As shown in Table 4.1 the PCM model does not result in any appreciable change in the calculated kinetic properties or enthalpy of reaction. This agreement between gas-phase TST calculations and condensed-phase kinetic data has also been observed for other reaction classes (Henry and Radom, 2001). However, it is important to note the rate of hydrogen abstraction in the condensed phase has also been shown to be a strong function of the polarity of the solvent (Avila et al., 1995).

These results add to the growing database of activation energies predicted by B3LYP which collectively suggests that B3LYP does not exclusively under- or overestimate reaction barriers. Furthermore, it is not generally possible *a priori* to state in which direction B3LYP will err. For example, Wijaya and coworkers (Wijaya et al., 2003) report an underestimation by B3LYP of the barrier height for different cyclization reactions while Henry and Radom (Henry and Radom, 2001) report that B3LYP always overpredicts the barrier for the cyclization of but-3-enyl-radical. The heats of reaction are not available from experiment, but two observations can be drawn based on the results provided. First, results from very small basis sets deviate strongly from the CBS and G3 methods, with errors as large as 4 kcal mol^{-1}. Moving to very large basis sets improves the agreement with the CBS and G3 results, with some B3LYP heats of reaction higher than the CBS-QB3 values by only 1 kcal mol^{-1}. Finally, it is worthwhile to note that the barriers calculated using B3LYP/6-311+G(3df,2p) differ from those calculated using single point calculations from the same method but with geometries optimized using B3LYP/6-31G(d). Using the smallest basis set (6-31G(d)) for geometry optimization and the largest basis set (6-311+G(3df,2p)) for single point calculations gives activation energies that may deviate significantly from the experimental, CBS, and G3 results.

It is next interesting to compare the five higher level methods in the bottom of each section of Table 4.1 with each other. Barriers calculated at the MP2 and G3(MP2) levels of theory are in very poor agreement with the experimental data for all three reactions. To test if the cause of this

discrepancy was from the optimized geometries or from the single point/hybrid energies, we calculated the G3//B3LYP energy of the reactant and TS of the MP2/6-311+G(d,p) optimized structures for reaction 2. The calculated activation energy was nearly identical to the full G3//B3LYP activation energy, thus indicating that the energies calculated using MP2 are poor. The BHandHLYP/6-311G(d,p) method also substantially overpredicts the activation barrier compared to the CBS-QB3 method. In spite of their poor predictions of the barrier height, BHandHLYP/6-311G(d,p), MP2/6-311+G(d,p) and G3(MP2) still give pre-exponential values that are in good agreement with the value obtained from CBS-QB3, and the heats of reaction are in reasonable agreement with the B3LYP values using large basis sets. In comparing the two hybrid methods, the results reveal that in the case of the first and second reactions, CBS-QB3 gives results which are much closer to the experimentally reported values, whereas the experimental values for the third reaction more closely match the G3B3 results. However, each activation energy was obtained from a single source without any repeatability reported. Therefore, the comparison set is too limited to draw any definitive conclusion about the superiority of either of these methods. Additionally, in all cases, the calculated rate coefficients ($k_{TST}(373\ K)$) from the CBS-QB3 method give the best agreement with the available experimental data. For calculating rate coefficients, the G3//B3LYP method performs noticeably better than pure B3LYP methods for reaction 3, but at a comparable (or lower) level of accuracy for reactions 1 and 2. For example, in the data set for reaction 1, B3LYP/cc-pVTZ+d gives a rate coefficient of 7.24*10^{-1} (1/s), whereas the prediction of G3//B3LYP is 3.54*10^{-1} (1/s). Both calculations are far from the single experimental value of 18 (1/s), but the cc-pVTZ+d value is a factor of two closer.

Given the variability of the results from all of the different methods and basis sets, it is instructive to compare their computational cost. Figure 4.2 gives the relative computational cost for B3LYP using the 6-31G(d), 6-311+G(d,p), 6-311+G(3df,2p), and cc-pVTZ+d basis sets, as well as CBS-QB3 and G3//B3LYP for the reactants of reactions 2 and 3 in Figure 4.1. The largest basis sets which most closely approximate the hybrid methods cost slightly more than the CBS-QB3

calculation, whereas G3//B3LYP is noticeably more expensive than the other methods. The high computational cost of G3//B3LYP is due almost entirely to the single point calculation using the MP4/6-31G(2df,p) level of theory. Based on the relatively good performance of the B3LYP/6-311+G(d,p) calculations on all three reactions and its modest computational cost, we selected this basis set to study other substituent and structural effects in this reaction family. Our performance criterion was based on the ability of a given method to accurately calculate the activation energy. This is based on an approach for estimating reaction rate coefficients that is often applied to large reaction mechanisms that consist of thousands of reactions in which a representative frequency factor is assumed for all reactions in a given reaction family and the activation energy for individual reactions is calculated using structure-reactivity relationships based on thermodynamic properties (Boock and Klein, 1994; Broadbelt and Pfaendtner, 2005; Van Geem et al., 2006). While CBS-QB3 would be the best choice based on agreement of the calculated rate coefficients with experimental data, a full exploration of substrate size and substituent effects is not feasible using such an expensive hybrid method due to the large number of reactions proposed for study in Figure 4.1 as well as the poor scaling of hybrid methods. Therefore, we selected B3LYP/6-311+G(d,p) as a good compromise between cost and accuracy for calculating activation energies. Combining the calculated activation energies with a representative frequency factor based on experimental data would yield values of rate coefficients in very good agreement with experiment.

Table 4.1: Comparison of basis set and method for three intramolecular hydrogen abstraction (reactions 1-3 in Figure 4.1). Unless alternate MO or hybrid method is given, the B3LYP functional is used and only the basis set is provided. Calculated data provided are the reaction barrier (in kcal/mol), heat of reaction (in kcal/mol) at 298 K, Arrhenius activation energy (in kcal/mol), pre-exponential factor (in 1/s), and rate coefficient (in 1/s) at 373 K.

method	Eo	ΔH_{rxn}	E_A	log A	$k_{TST}(373\ K)$
reaction 1[a]	$C(CH_3)_2(O_2\cdot)CH_2CH(CH_3)_2 \rightarrow C(CH_3)_2(O_2H)CH_2C\cdot(CH_3)_2$				

Table 4.1: (continued)

method	Eo	ΔH_{rxn}	E_A	log A	$k_{TST}(373\ K)$
6-31G(d)	19.8	17.8	21.1	10.8	2.73 x 10^{-2}
6-31G(d)[b]	19.4	17.2	20.6	10.7	4.26 x 10^{-2}
RO 6-31G(d)[c]	20.0	17.7	21.2	10.8	2.38 x 10^{-2}
6-31G(d,p)	18.0	15.5	19.2	10.8	3.54 x 10^{-1}
6-311G(d,p)	17.7	14.3	19.0	10.7	3.69 x 10^{-1}
6-311+G(d,p)	17.7	13.7	18.7	10.6	4.39 x 10^{-1}
RO 6-311+G(d,p)[c]	17.8	13.6	18.8	10.6	3.83 x 10^{-1}
6-311+G(df)	20.2	16.7	21.3	10.7	1.65 x 10^{-2}
6-311+G(3df,2p)	17.4	13.4	18.5	10.7	7.24 x 10^{-1}
6-311+G(3df,2p)[d]	16.6	13.4	19.1	10.8	4.05 x 10^{-1}
cc-pVTZ+d	17.4	13.6	18.5	10.7	7.24 x 10^{-1}
MP2/6-311+G(d,p)[e]	34.1	17.7	35.7	10.6	4.79 x 10^{-11}
BHandHLYP/6-311G(d,p)	23.4	14.7	24.7	10.7	1.68 x 10^{-4}
G3(MP2)	43.7	13.7	44.8	10.9	4.45 x 10^{-16}
G3\\B3LYP	17.9	12.9	19.2	10.8	3.54 x 10^{-1}
CBS-QB3	16.3	12.3	17.5	10.6	2.22
Experimental			17.5	11.5	18
reaction 2			$CH_3C(O_2\cdot)H(CH_2)_2CH_3 \rightarrow$ $CH_3C(O_2H)HCH_2C\cdot HCH_3$		
6-31G(d)	24.0	19.6	23.1	10.9	2.31 x 10^{-3}
6-31G(d)[b]	23.5	19.1	22.5	10.8	4.13 x 10^{-3}
RO 6-31G(d)[c]	24.9	20.2	23.9	10.8	6.24 x 10^{-4}
6-31G(d,p)	22.7	17.9	21.7	10.8	1.21 x 10^{-2}
6-311G(d,p)	22.5	16.8	21.5	10.8	1.59 x 10^{-2}
6-311+G(d,p)	22.3	16.3	21.3	10.8	2.08 x 10^{-2}
RO 6-311+G(d,p)[c]	22.5	16.0	21.5	10.8	1.59 x 10^{-2}
6-311+G(df)	25.1	19.2	24.1	10.8	4.76 x 10^{-4}
6-311+G(3df,2p)	22.1	15.8	21.1	10.8	2.73 x 10^{-2}
6-311+G(3df,2p)[d]	20.6		19.7	10.9	2.27 x 10^{-1}
cc-pVTZ+d	21.3	15.3	20.4	10.8	7.02 x 10^{-2}
MP2/6-311+G(d,p)[e]	40.6	19.3	39.4	10.7	4.10 x 10^{-13}
BHandHLYP/6-311G(d,p)	27.6	16.0	26.3	10.8	2.45 x 10^{-5}
G3(MP2)	40.9	15.3	38.9	9.9	1.28 x 10^{-13}
G3\\B3LYP	21.7	14.7	20.8	10.9	5.15 x 10^{-2}
CBS-QB3	20.2	14.4	19.3	10.9	3.90 x 10^{-1}

Table 4.1: (continued)

method	Eo	ΔH_{rxn}	E_A	log A	$k_{TST}(373\ K)$
Experimental			19.7	11.5	8.7 x 10^{-1}
reaction 3[a]	$C(CH_3)_2(O_2\cdot)(CH_2)_2CH(CH_3)_2 \rightarrow C(CH_3)_2(O_2H)(CH_2)_2C\cdot(CH_3)_2$				
6-31G(d)	20.0	16.6	19.9	9.4	5.48 x 10^{-3}
6-31G(d)[b]	19.7	16.2	19.6	9.4	8.22 x 10^{-3}
RO 6-31G(d)[c]	20.3	16.4	20.1	9.4	4.19 x 10^{-3}
6-31G(d,p)	18.3	14.3	18.0	9.4	7.12 x 10^{-2}
6-311G(d,p)	17.9	13.1	17.7	9.3	8.48 x 10^{-2}
6-311+G(d,p)	17.8	13.1	18.0	9.3	5.66 x 10^{-2}
RO 6-311+G(d,p)[c]	17.9	12.8	18.1	9.3	4.94 x 10^{-2}
6-311+G(df)	20.2	16.0	20.4	9.3	2.22 x 10^{-3}
6-311+G(3df,2p)	17.7	12.8	18.0	9.3	5.66 x 10^{-2}
6-311+G(3df,2p)[d]	16.7		19.3	9.4	1.23 x 10^{-2}
cc-pVTZ+d	17.8	12.9	18.0	9.3	5.66 x 10^{-2}
MP2/6-311+G(d,p)[e]	34.2	18.4	34.9	9.3	7.07 x 10^{-12}
BHandHLYP	23.4	13.7	23.0	9.2	5.28 x 10^{-5}
G3(MP2)	47.0	12.0	44.7	7.5	2.03 x 10^{-19}
G3\\B3LYP	17.9	10.6	16.7	9.4	4.11 x 10^{-1}
CBS-QB3	16.5	10.6	15.9	9.3	9.62 x 10^{-1}
Experimental			17.2	11	8

[a]Lower energy rotational isomer of IRC-derived reactant or product was found and equation 4.3 was used to calculate the pre-exponential factor and activation energy for the forward reaction.

[b]Geometry optimization and energy calculation performed using UB3LYP/6-31G(d) and a PCM model using the properties of *n*-heptane to describe the solvent cavity.

[c]Calculation performed with restricted-open shell wavefunctions.

[d]Geometry optimization performed at UB3LYP/6-31G(d) with single point and frequency calculation at given basis set.

[e]MP2 scaling factors of 0.9670 (ZPE) and 0.9434 (fundamental frequencies) were used according to the recommendation of Scott and Radom.(Scott and Radom, 1996)

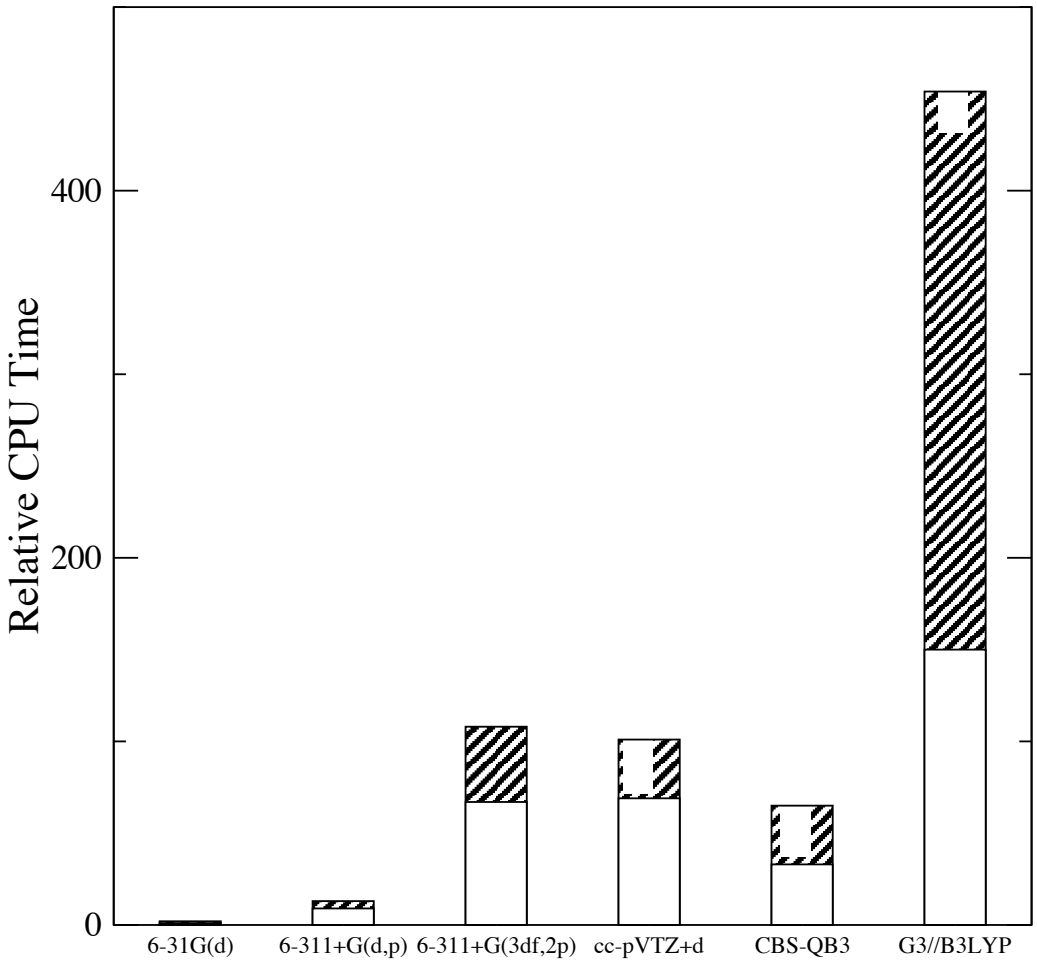

Figure 4.2: Comparison of computational cost for the B3LYP functional with several basis sets and two hybrid methods. Two reactants are compared: $CH_3C(O_2\cdot)HC_3H_7$ (white bars) and $C(CH_3)_2(O_2\cdot)(CH_2)_2CH(CH_3)_2$ (striped bars). All times are relative to the B3LYP/6-31G(d) calculation of $CH_3C(O_2\cdot)HC_3H_7$.

4.3.2 Effect of ring size

To probe the effect on the rate coefficient for this class of reactions of the relative position from which the hydrogen was abstracted, we varied the ring size of the transition state from four to seven. The four-membered ring corresponds to a 1,3-hydrogen shift and the seven-membered ring results from a 1,6-hydrogen shift. The degree of substitution of the carbon atoms attached to the reacting hydrogen and to the OO· moiety was the same for all four reactions so that rate constants could be compared fairly. The four reactions examined are reactions 1, 3, 10, and 11 in Figure 4.1. The activation energies and pre-exponential factors are summarized in Table 4.2. The relationship between ring size and activation energy is a decreasing, non-linear function as seen in Figure 4.3. The decrease in the activation energy is particularly marked beyond a ring size of six as the ring strain becomes minimized. As the ring size of the TS is increased, an additional internal rotation is lost or frozen within the TS ring structure. Thus, the partition function for the reactant increases more than the partition function for the TS as the ring size is increased, causing the pre-exponential factor to decrease with increasing ring size. The proportional decrease in the pre-exponential factor with increasing ring size is clearly seen in the plot of the pre-exponential factor as a function of ring size in Figure 4.3. While the correlation is empirical, it can be explained based on changes in internal rotations and the straight line behavior of the pre-exponential factor as a function of ring size may offer a simple template for the development of structure-reactivity relationships for systems in which intramolecular hydrogen transfer plays an important role.

4.3.3 A simple structure-reactivity relationship to describe 1,5- intramolecular hydrogen transfer

For reactions in the 1,5-hydrogen shift family, structural changes were introduced via substitution of various groups and atoms along the backbone to create diversity in thermodynamic and kinetic parameters of the reaction as delineated by reactions 1-2 and 4-9 in Figure 4.1. Starting with a very

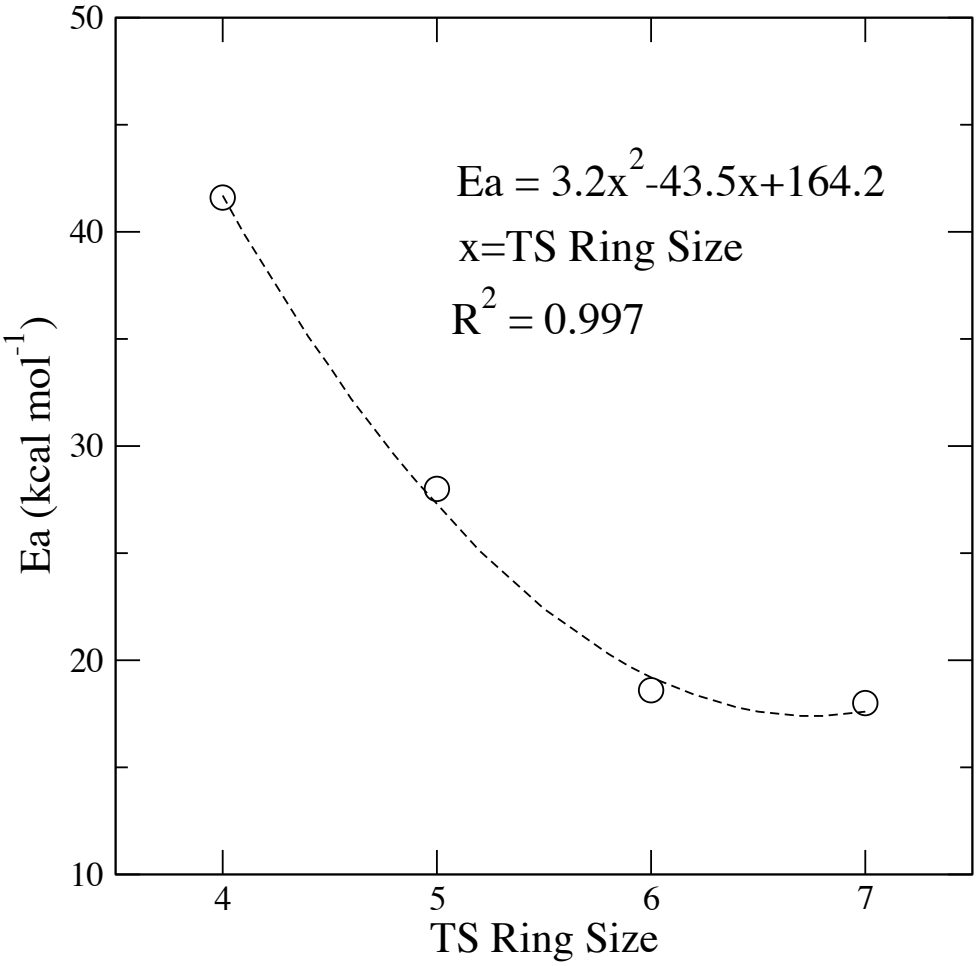

Figure 4.3: Variation of Arrhenius activation energy and pre-exponential factor with transition state ring size. A regression line is given to show the variation of each parameter as the ring size is increased. Continued on next page.

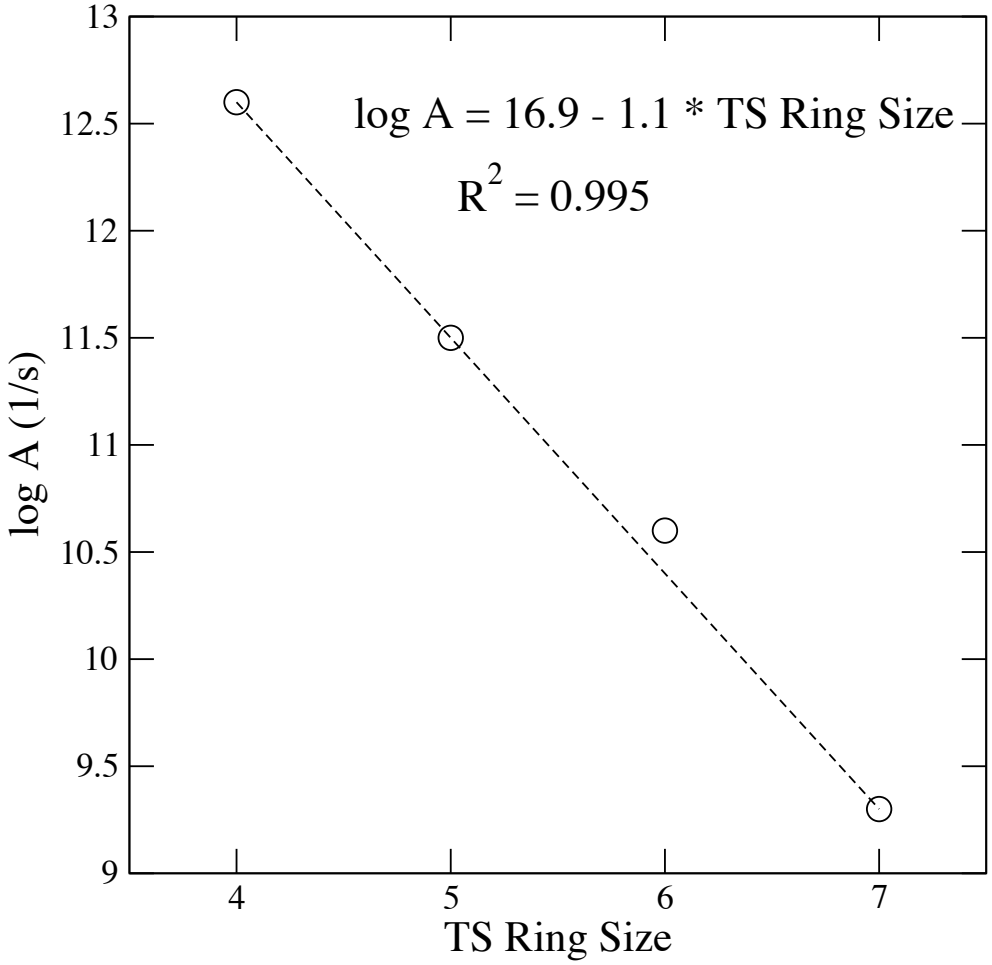

Figure 4.3: (continued)

Table 4.2: Comparison of activation energy and pre-exponential factor as the ring size of the transition state is varied from four to seven. Geometry optimization and energy calculations were performed using B3LYP/6-311+G(d,p)

reaction	TS ring size	E_A[a]	log A (1/s)
$CH_3CH(O_2\cdot)CH_3 \rightarrow CH_3COCH_3 + HO\cdot$ [b]	4	41.6	12.6
$(CH_3)_2C(O_2\cdot)CH(CH_3)_2 \rightarrow (CH_3)_2C(O_2H)C\cdot(CH_3)_2$	5	28.0	11.5
$C(CH_3)_2(O_2\cdot)CH_2CH(CH_3)_2 \rightarrow C(CH_3)_2(O_2H)CH_2C\cdot(CH_3)_2$	6	18.7	10.6
$C(CH_3)_2(O_2\cdot)(CH_2)_2CH(CH_3)_2 \rightarrow C(CH_3)_2(O_2H)(CH_2)_2C\cdot(CH_3)_2$	7	18.0	9.3

[a] Quantity in kcal mol^{-1}.

[b] The 1,3-hydrogen shift creates the unstable $\cdot COOH$ containing radical which directly yields the β -scission products shown in the table.

small substrate (reaction 6), we systematically introduced additional substitutions both near the hydrogen undergoing abstraction as well as the peroxy radical moiety. This approach ensured that a broad range of heats of reaction was explored, thus creating a more general structure-reactivity relationship. It is interesting to note that even though almost all degrees of substitution were explored, there were no forward reactions with a heat of reaction less than 8.5 kcal mol^{-1}. In addition, we investigated the effect of introducing structural changes to the TS ring by adding a carbonyl linkage to reactions 6, 2, and 5 to create carbonyl-containing reactants in reactions 7-9, respectively. Thermodynamic and kinetic data for sixteen reactions (forward and reverse pairs) considered are summarized in Table 4.3, and the heats of reaction and activation energy data in Table 4.3 are plotted in Figure 4.4. Also included in Table 4.3 are data for reaction 8 calculated using CBS-QB3.

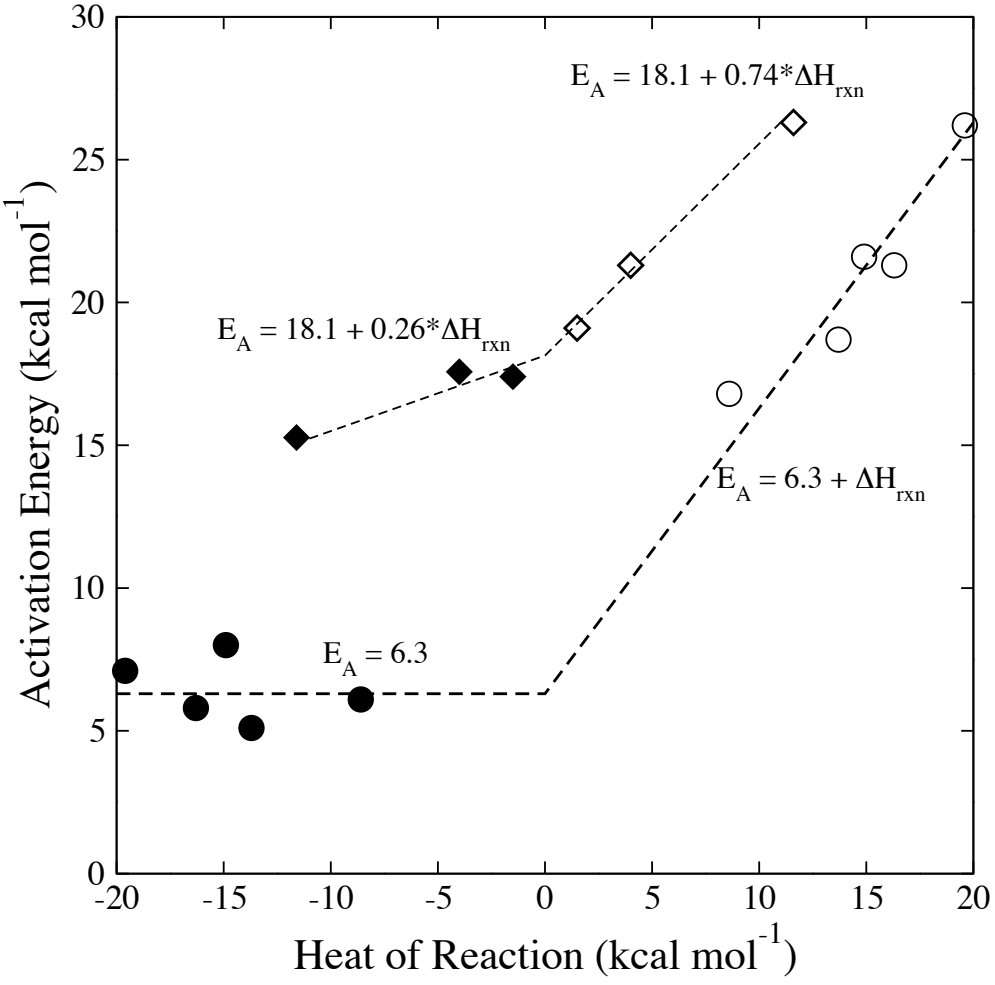

Figure 4.4: Plot of activation energy versus heat of reaction for all reactions studied in the 1,5-hydrogen shift family. All of the B3LYP/6-311+G(d,p) data from Table 4.3 are included in the figure, but two different regressions were performed to reflect the different relationships observed. The open and closed circles indicate all data which are forward/reverse reaction pairs of the alkylperoxy radicals (reactions 1-2 and 4-6 in Figure 4.1). The open and closed diamonds indicate the data which contain carbonyl moieties within the TS ring structure (reactions 7-9 in Figure 4.1). The recommended structure-reactivity relationships are given within the figure with units of kcal mol $^{-1}$.

Table 4.3: Data used in development of structure-reactivity relationship for 1,5-hydrogen shift family. When applicable, lower energy rotational isomers were used, according to equation 4.3. Unless noted, all calculations were performed using B3LYP/6-311+G(d,p).

		forward reaction			reverse reaction	
number	reaction	ΔH_{rxn}[a]	E_A[a]	log A (1/s)	E_A[a]	log A (1/s)
1	$C(CH_3)_2(O_2\cdot)CH_2CH(CH_3)_2 \rightarrow C(CH_3)_2(O_2H)CH_2C\cdot(CH_3)_2$[b]	13.7	18.7	10.6	5.1	9.7
2	$CH_3C(O_2\cdot)H(CH_2)_2CH_3 \rightarrow CH_3C(O_2H)HCH_2C\cdot HCH_3$	16.3	21.3	10.8	5.8	10.7
4	$(CH_3)_2CHCH_2C(O_2\cdot)(CH_3)CH_2CH(CH_3)_2 \rightarrow$ $(CH_3)_2C\cdot CH_2C(O_2H)(CH_3)CH_2CH(CH_3)_2$	8.6	16.8	11.3	6.1	11.1
5	$(CH_3)CH(O_2\cdot)CH_2CH(CH_3)_2 \rightarrow (CH_3)CH(O_2H)CH_2C\cdot(CH_3)_2$ [b]	14.9	21.6	10.6	8.0	10.9
6	$(CH_3)CH(O_2\cdot)CH_2CH_3 \rightarrow (CH_3)CH(O_2H)CH_2C\cdot H_2$[b]	19.6	26.2	11.2	7.1	11.6
7	$(CH_3)CH(O_2\cdot)COCH_3 \rightarrow (CH_3)CH(O_2H)COC\cdot H_2$	11.6	26.3	11.1	15.3	12.5
8	$(CH_3CH(O_2\cdot)HCOCH_2CH_3 \rightarrow (CH_3CH(O_2H)HCOCH\cdot CH_3$	4.0	21.3	11.6	17.6	12.0
8	$(CH_3CH(O_2\cdot)HCOCH_2CH_3 \rightarrow (CH_3CH(O_2H)HCOCH\cdot CH_3$ [c,d]	2.7	20.8	11.7	17.8	11.0
9	$(CH_3)CH(O_2\cdot)COCH(CH_3)_2 \rightarrow (CH_3)CH(O_2H)COC\cdot(CH_3)_2$	1.5	19.1	10.4	17.4	10.1

[a] Quantity in kcal mol^{-1}.

[b] Lower energy rotational isomer of IRC-derived reactant was found and equation 4.3 was used to calculate the pre-exponential factor and activation energy for the forward reaction.

[c] Value not used in regression of structure/reactivity relationship.

[d] Reaction thermodynamics and kinetics calculated using CBS-QB3.

For the forward reactions, the first five reactions listed in Table 4.3 fall on an Evans and Polanyí (1938) correlation, *i.e.*, $E_A = E_o + \alpha \Delta H_{rxn}$. The parameters regressed from these data are E_o = 6.3 kcal mol^{-1} and α = 1. The regressed transfer coefficient indicates that this reaction family is more sensitive to the influence of substituents than intermolecular hydrogen transfer which is often approximated with a transfer coefficient of 0.8 (Blowers and Masel, 2000). In this case, the approximated activation energy is the heat of reaction added to the intrinsic reaction barrier. The best fit for the activation energy of the reverse reactions as a function of heat of reaction is a straight line with a slope equal to zero and an intercept equal to the intrinsic reaction barrier for the forward reactions of 6.3 kcal mol^{-1}. This enthalpic consistency is clarified by examining the relationship $E_A = \Delta H^{\ddagger} + nRT$ from transition state theory, where n is the molecularity of the reaction. When manipulated algebraically, this equation reveals that for forward and reverse reaction pairs of reactions in the intramolecular hydrogen transfer reaction family, the sum of the transfer coefficients is equal to 1, and the intrinsic barriers are equal, as observed here. In the practice of creating detailed kinetic models, overall thermodynamic consistency would be enforced by using only one of the two Evans-Polanyí relationships to calculate the rate coefficient in one direction while the other would be calculated based on a known equilibrium constant. However, the two distinct Evans-Polanyí relationships are clearly enthalpically consistent within the approximation of $E_A = \Delta H^{\ddagger} + nRT$, and thus, each relationship may be used independently to estimate the activation energy depending on the specific type of reaction of interest. A transfer coefficient of one is also known to correspond to a very late transition state which is consistent with the IRCs calculated.

Blowers and Masel (2000) have proposed a modified form of the Marcus equation to estimate the activation energy of hydrogen transfer reactions for endo- and exothermic reactions using a single formulation as shown in equation 4.5.

$$E_A = \begin{cases} 0 & \text{for } \Delta H_{rxn}/4E_o < -1 \\ E_o\left(1 + \Delta H_{rxn}/4E_o\right)^2 & \text{for } -1 \leq \Delta H_{rxn}/4E_o \leq 1 \\ \Delta H_{rxn} & \text{for } \Delta H_{rxn}/4E_o > 1 \end{cases} \tag{4.5}$$

Their proposed relationship is second order in the heat of reaction and nicely captures the curved transition region between exothermic and endothermic reactions in bimolecular hydrogen transfer reactions. We varied E_o to fit our data to the Blowers-Masel relationship, but the fit was very poor due to the inability of the Blowers-Masel relationship to asymptotically approach a non-zero value for strongly exothermic reactions. A modified Blowers-Masel relationship in which a constant was added to the equation for each regime in equation 4.5 fit the data well with a value of E_o = 3.7 kcal mol^{-1} and a constant factor of 6.2 kcal mol^{-1}. This suggests that the intrinsic barrier for strongly exothermic reactions approaches a value of 6.2 kcal mol^{-1} instead of zero for this class of reactions. However, because of the lack of data in the endo- to exothermic transition region, it is not possible to estimate whether the Blowers-Masel relationship is superior to the simple Evans-Polanyí relationship.

Reactions 7-9 are also plotted in Figure 4.4 and clearly fall on a different correlation than the corresponding reactants without carbonyl groups. The calculation for reaction 8 was repeated using CBS-QB3 to verify that higher-level methods also capture this difference. The data in Table 4.3 show that B3LYP/6-311+G(d,p) and CBS-QB3 are in very good agreement. Linear regression shows that the data for reactants containing a carbonyl linkage in the TS ring have a different Evans-Polanyí relationship. The intrinsic barrier, E_o, was 18.1 kcal mol^{-1}, and the endothermic/exothermic transfer coefficients, α, were 0.74 and 0.26, respectively. While these transfer coefficients are much more similar to typical hydrogen transfer values, the intrinsic barrier is much larger than typical hydrogen transfer values of 7-10 kcal mol^{-1}. One possible explanation for this is increased ring strain due to the carbonyl linkage. Also, in the product structure, the carbonyl group offers significant stabilization to the radical center on the adjacent carbon atom, resulting

in a heat of reaction that is much lower than the alkyl counterpart. We also explored the effect of tunneling on this reaction class given the distinct structure-reactivity relationship and the markedly different heats of reaction compared to the analogous reactions without the intervening carbonyl group. For all three reactions, we calculated the SCT, ZCT and Eckart transmission coefficients as a function of temperature. The Eckart model was observed to significantly overestimate the SCT values in the low temperature region. Conversely, the ZCT and Wigner transmission values were noticeably lower than the SCT values. Using equation 4.2 with the transmission coefficient based on the SCT method, we recalculated the activation energies using rate constants over a small temperature range (300-600 K). The SCT/TST activation energies were lower than the corresponding Wigner/TST activation energies with the deviation between the two methods ($E_A^{Wigner} - E_A^{SCT}$) ranging between 1.6-2.8 kcal mol $^{-1}$; however, the same form of structure-reactivity relationship was observed, with E_o and α values of 15.6 kcal mol $^{-1}$ and 0.83/0.17.

4.4 Conclusions

The B3LYP functional was evaluated as a method to calculate reaction barriers and structure-reactivity relationships for intramolecular hydrogen transfer reactions involving peroxy radicals. Nine different basis sets as well as five other MO/DFT and hybrid methods were used in comparing three reactions to available experimental data. It was shown that B3LYP/6-311+G(d,p) offers a good compromise between speed and accuracy for studies in which thermodynamic and kinetic data of many reactions are required. The BHandHLYP functional and methods based on MP2 geometries gave very poor predictions of experimental activation energies, and their reaction barriers disagreed substantially from those obtained with CBS-QB3 and G3//B3LYP, whose applicability has been extensively tested.

We probed the effect of varying the transition state ring size as well as the effect of substituent groups for the 1,5-hydrogen shift family. Clear trends were observed when the ring size was varied

and all other substituents were held constant. As expected, increasing the ring size led to decreased activation barriers as well as decreasing pre-exponential factors. Evans-Polanyí relationships were shown to capture the activation energy as a function of heat of reaction for reactions in the 1,5-hydrogen shift family. A pre-exponential factor of log A (s^{-1}) = 10.9 and $E_A = 6.3 + \Delta H_{rxn}$, where E_A and ΔH_{rxn} are in kcal mol $^{-1}$ are recommended if there are no carbonyl groups in the transition state ring structure. Rate coefficients for reverse reactions in this family can be approximated using a pre-exponential factor of 10.8 (log A (s^{-1})) and an activation energy of 6.3 kcal mol^{-1}. If a carbonyl group within the ring structure was present, an Evans-Polanyí relationship $E_A = 18.1 + 0.74\Delta H_{rxn}$ (α = 0.26 for exothermic reactions) was shown to capture the data well. The vast difference in the parameters of the two distinct correlations demonstrates that different structure-reactivity relationships are warranted. Based on the results obtained, B3LYP/6-311+G(d,p) is an attractive choice for obtaining insights into structure-reactivity relationships.

4.5 Supplementary Information

This section contains a comparison of rigid and relaxed PES scans for the C-O bond of a peroxy radical and a derivation of the apparent rate constant for combined rotational isomers and hydrogen transfer.

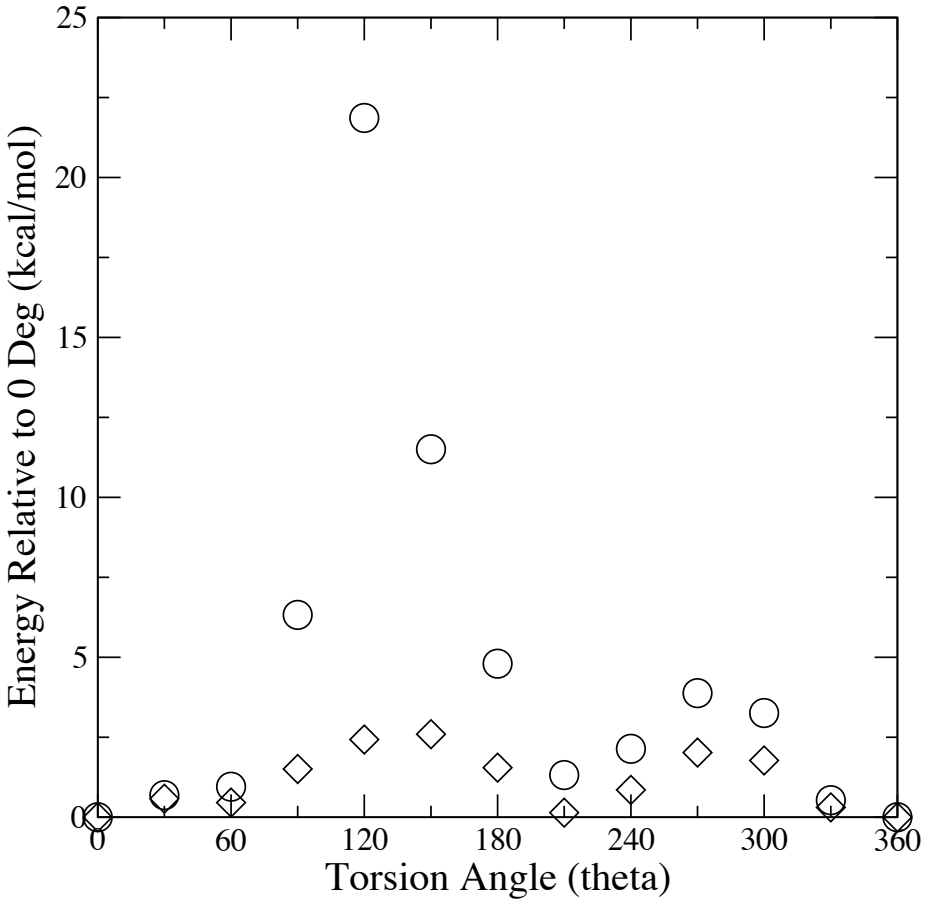

Figure 4.5: Comparison of rigid versus relaxed rotational PES scan. Both scans were performed using the B3LYP/6-31G(d) level of theory. The dihedral angle being scanned is the C-O bond of $CH_3C(O_2\cdot)HC_3H_7$. Data points were calculated in 30^o increments. The rigid scan is represented with open circles and the relaxed scan is represented with open diamonds.

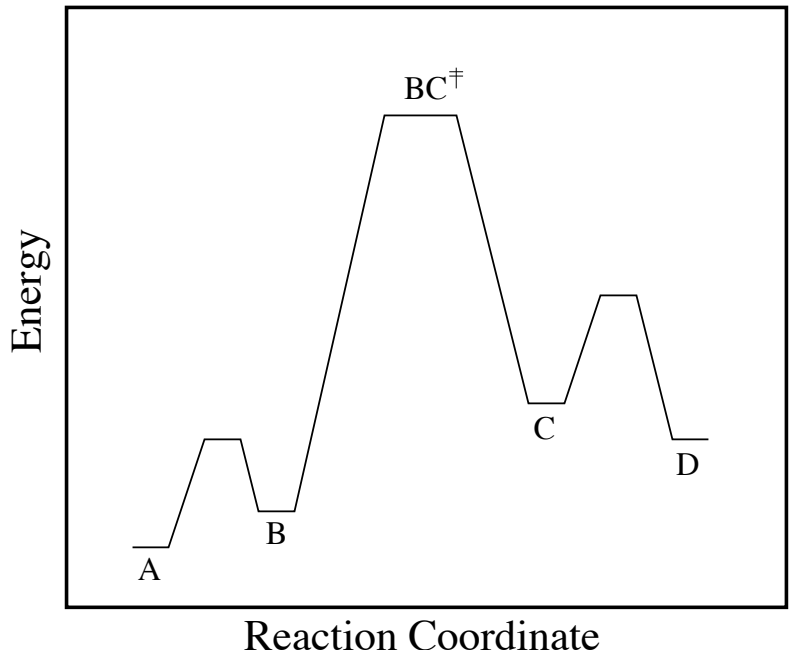

Figure 4.6: Typical reaction coordinate for intramolecular hydrogen abstraction with rotational isomers present of lower energy (*i.e.*, A and D) in the reactants and products. The barrier for reactions in this reaction family is normally at least 10x the barrier for rotation between rotational isomers.

Derivation of equation 4.3. Assume rotational isomers A and B are in equilibrium with an equilibrium constant equal to K_{eq}^{rot}. According to transition state theory, B and BC‡ are in equilibrium with an equilibrium constant equal to $K_C^{\ddagger}$. The transition state, BC‡, decomposes to C with a rate constant equal to $k_b T/h$.

The rate of appearance of C, r_C, is equal to:

$$r_C = \frac{k_b T}{h} C_{BC^{\ddagger}}$$

Substituting for $C_{BC^{\ddagger}}$

$$r_C = \frac{k_b T}{h} K_C^{\ddagger} C_B$$

where $\frac{k_b T}{h} \mathrm{K}_C^{\ddagger}$ is the conventional TST rate constant, k_{TST}. Further substituting for C_B:

$$r_C = \frac{k_b T}{h} K_C^{\ddagger} K_{eq}^{rot} C_A$$

reveals that the effective rate coefficient is $k_{TST} * \mathrm{K}_{eq}^{rot}$, where both k_{TST} and K_{eq}^{rot} are functions of temperature.

Chapter 5

Elucidation of Structure-Reactivity Relationships in Hindered Phenols Via Quantum Chemistry and Transition State Theory

5.1 Introduction

Phenolic antioxidants are important in a wide range of systems including human health (Wang et al., 2006), food science (Balasundram et al., 2006), polymer science (Lundback et al., 2006), and lubricants (Migdal, 2003). Typical antioxidants in the first two categories include phenols that are mono- or di-substituted with various organic or inorganic atoms or small moieties. In the latter two cases, hindered phenols are the radical scavengers more commonly employed. Hindered phenols are often characterized by large and/or multiple organic substituents on the aromatic ring.

In commercial lubricant formulations, hindered phenols are used as additives to the base stock to guard against chemical degradation involving oxygen (Pirro and Wessol, 2001). Oxidation in-

hibitors such as hindered phenols have been studied in a variety of environments, and several volumes have been written that are devoted solely to inhibitors (Denisov and Denisova, 2000; Migdal, 2003). These materials are helpful for disrupting autoxidation chemistry under moderate oxidation conditions, *i.e.*, near 100 ^{o}C. In spite of widespread use of these compounds, a quantitative mechanistic description of their interaction with lubricating oils during degradation is absent from the literature.

There are currently numerous challenges which prevent inclusion of antioxidant chemistry directly into lubricant degradation models. First, the mechanism, *i.e.*, the elementary reaction steps governing how antioxidants interact with lubricant-derived radicals, requires validation. When the additive functions properly, it is proposed that each hindered phenol can sacrificially scavenge two peroxy radicals as shown by the scheme in Figure 5.1. Second, the thermochemistry of antioxidants and radical intermediates comprising the mechanism needs to be calculated. Accurate thermodynamic properties are crucial for estimating kinetic rate constants using structure-reactivity relationships. Finally, estimates of kinetic data, *i.e.*, rate constants and structure-reactivity relationships, are required. This information is requisite for establishing accurate reaction networks (Broadbelt and Pfaendtner, 2005).

Experimentally, reactions of antioxidants have received considerable attention due to their wide ranging use and importance in the human body. Selected examples include the work of Denisov and Denisova who have reported numerous reaction rate coefficients for phenolic antioxidants (Denisov, 1974; Denisova and Denisov, 2001) and also gave a general review of the kinetics and mechanism of free-radical inhibitors (Denisov and Khudyakov, 1987). The Landolt-Bornstein compendium also contains numerous experimental reaction rate coefficients, predominantly for t-butyl peroxy radical which is the most commonly studied (Howard and Scaiano, 1997). As a final example the works of Mahoney and Korcek (Hamilton et al., 1980; Mahoney et al., 1978) and Nakanishi (Nakanishi and Onodera, 1996) nicely illustrate the method in which researchers integrate studies of antioxidants and lubricant degradation.

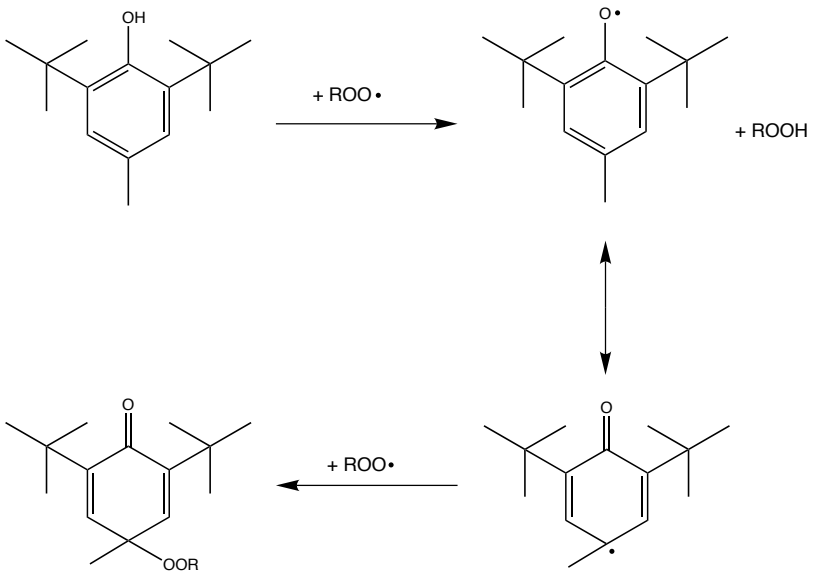

Figure 5.1: Radical trap mechanism of hindered phenol stabilizers adapted from Migdal (2003). The common antioxidant butylatedhydroxytoluene is used for reference. Each molecule of stabilizer consumes two radicals.

There are several recent computational and theoretical studies of the substituted phenols relevant to antioxidant chemistry of phenols. Singh et al. (2005) developed structure-reactivity relationships for a set of mono-substituted phenols interacting with HOO· using density functional theory. Their work also gave insight into the nature of hydrogen transfer between HOO· and phenolic antioxidants. Theoretical investigations by Zavitsas have also increased understanding in hydrogen transfer reactions in general (Zavitsas, 1996; Zavitsas and Chatgilialoglu, 1995). Additionally, Singh and coworkers have recently presented a new method for calculating the O-H bond dissociation energy in phenolic antioxidants (Singh et al., 2006). Loader et al. (2006) used the geometrical properties of substituted phenols to develop correlations for assessing toxicity. However, there are no computational studies of large hindered phenols interacting with alkylperoxy lubricant mimics (ROO·). While the set of experimental values for t-butyl peroxy radical interacting with phenolic compounds is reasonably extensive (Howard and Scaiano, 1997), there is insufficient experimental data to be able to construct structure-reactivity relationships that capture changes in

either ROOH or R'H of the hydrogen transfer step in Figure 5.1. It has been shown that activation energies of intra- and intermolecular hydrogen transfer reactions of small molecules can be estimated with reasonable success using the Evans-Polanyí (Evans and Polanyí, 1938; Méreau et al., 2000; Pfaendtner et al., 2006c; Singh et al., 2005) relationship, $E_A = E_o + \alpha * DeltaH_{rxn}$, or the Blowers-Masel (Blowers and Masel, 2000) correlation:

$$E_A = \begin{cases} 0 & \text{for } \Delta H_{rxn}/4E_o < -1 \\ E_o\left(1 + \Delta H_{rxn}/4E_o\right)^2 & \text{for } -1 \leq \Delta H_{rxn}/4E_o \leq 1 \\ \Delta H_{rxn} & \text{for } \Delta H_{rxn}/4E_o > 1 \end{cases} \tag{5.1}$$

However, extension of these methods to lubricant-like molecules interacting with large hindered phenols is yet to be evaluated.

To address these challenges, we have completed quantum chemical studies of 10 prototypical reactions shown in Figure 5.2: three alkylperoxy radicals (methyl, ethyl and n-propyl peroxy radical) interacting with three different antioxidants. The antioxidants in Figure 5.2 are phenol (reactions 1-3), p-hydroxyanisole (reactions 4-6), and butylatedhydroxytoluene (BHT) (reactions 7-9). One additional reaction (phenol + HOO·) was also investigated to determine the effect of tunneling and estimate the contribution of internal rotation to the thermodynamic and kinetic properties. Transition state theory was used to calculate kinetic data and structure-reactivity relationships were developed from the results obtained.

5.2 Computational and Theoretical Details

All molecular orbital (MO) and density functional theory (DFT) calculations were completed using the Gaussian 03 (Frisch et al., 2003) software package. Transition states were identified as first-order saddle points on the potential energy surface. The quadratic synchronous transit method

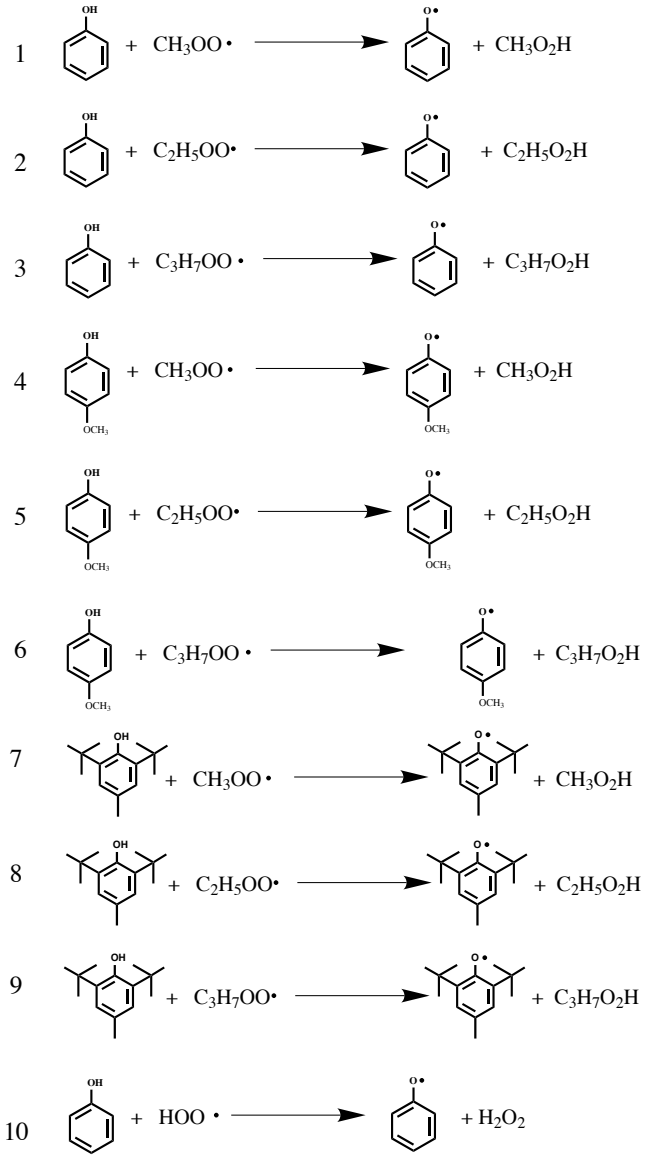

Figure 5.2: Reactions investigated using quantum chemistry and transition state theory.

(Peng and Schlegel, 1993) was used to help locate many of the transition states. All transition states were verified by obtaining the true reactants/products using intrinsic reaction coordinate following (Gonzalez and Schlegel, 1989). Calculations were performed using the B3LYP (Becke, 1993) hybrid functional with a split-valence double or triple zeta basis set optionally including an additional set of diffuse functions on first row atms and d or p-type polarization functions on second row atoms, 6-31G(d) or 6-311+G(d,p). Additionally we used the hybrid model chemistry CBS-QB3 (Montgomery et al., 1999) to study a single reaction. Solvent effects were studied using a polarizable continuum model (PCM) (Cancés et al., 1997). The solvent cavity was established using radii obtained from the universal force field (Rappé et al., 1992) with hydrogen atoms explicitly defined.

Using the optimized geometry and frequencies obtained from a Hessian calculation, the total microcanonical partition function can be calculated for each molecule within the rigid-rotor harmonic oscillator (HO) assumption. It is known that the HO approximation incorrectly treats low-frequency torsional modes as harmonic oscillators (Pitzer and Gwinn, 1942). However, it has recently been shown that the internal rotation correction has a very minor effect on the activation energy, even for molecules with many dihedrals (Van Cauter et al., 2006). To estimate the effect of internal rotation corrections on the reactions of the type of interest here, reaction 10 in Figure 5.2 was examined. Assuming the O-H-O linkage in the reactive moiety is frozen at the TS, one internal rotation can be seen at the O-O bond in the H-O-O-H linkage. We calculated the hindrance potential for this rotation using B3LYP/6-31G(d). Our approach in treating internal rotation (IR) was similar in principle to previously reported methods (Pfaendtner et al., 2006c; Sumathi et al.,

2001a; Van Speybroeck et al., 2000) and we have described it in detail in Chapter 3. The internal rotation correction altered the activation energy by less than 0.6 kcal mol^{-1}, in agreement with previously obtained results. Therefore, we only used the HO partition functions in calculating activation energies and heats of reaction in this study. The impact of the internal rotation correction on the Arrhenius pre-exponential factor is addressed in the Results and Discussion.

The rate constant as a function of temperature was calculated using the standard expression,

$$k_{TST} = rpd * c_o^{1-n} * \kappa\left(T\right) \frac{k_b T}{h} \frac{Q^{\ddagger}(T)}{Q^r(T)} \exp\left(-E_o/RT\right) \tag{5.2}$$

where rpd is the reaction path degeneracy, determined by the number of hydrogen atoms a particular radical can abstract (and equal to one for all reactions in Figure 5.2, c_o is the concentration in the standard state to which the thermodynamic parameters are referred, *i.e.*, P/RT, n is the molecularity of the reaction, $Q^{\ddagger}$ and Q^r are the total partition functions for the TS and reactants, respectively, and E_o is the reaction barrier, *i.e.*, the zero-point corrected difference between the ground-state electronic energies of the TS and the reactants. The quantity $\kappa\left(T\right)$ is the correction for quantum tunneling. To quantify the effect of quantum tunneling, various approximations to the transmission coefficient including the Wigner (Hirschfelder and Wigner, 1939) correction, the Eckart approximation (Gonzalez-Lafont et al., 1991), the zero-curvature tunneling approximation (ZCT) (Gonzalez-Lafont et al., 1991), and the small curvature tunneling (SCT) (Gonzalez-Lafont et al., 1991) approximation were calculated for reaction 10 in Figure 5.2. Calculation of the Eckart, SCT and ZCT corrections was performed using the software package "Virtual Kinetic Laboratory" of Zhang and Truong (2001). As detailed in the Results and Discussion section, the Wigner correc-

tion was a good approximation to the more rigorous SCT approximation, so the Wigner correction was used for all reactions. For further detail about the use of quantum chemistry and transition state theory, the reader is referred to several excellent reviews (Santiso and Gubbins, 2004; Sumathi and Green, 2002b; Truhlar et al., 1996).

Once the temperature dependent partition functions were known, rate constants as a function of temperature were calculated, and the Arrhenius parameters A and E_A were obtained from a straight-line fit of $\ln k$ vs $1/T$. Unless otherwise stated, we used a temperature range of 300-1500 K for regression of A and E_A. To calculate the enthalpy of reaction, all thermodynamic parameters were obtained from ensemble energy averages <E> using standard formulae (McQuarrie and Simon, 1999). Although the results obtained in the study are strictly representative of gas-phase reactions, there is precedent in the literature for comparing gas-phase results to kinetic data experimentally determined from condensed-phase systems (Henry and Radom, 2001). However, it is important to note the rate of hydrogen abstraction in the condensed phase has also been shown to be a strong function of the polarity of the solvent (Avila et al., 1995). The impact of this approximation is further discussed in the Results and Discussion. Additionally, it has been documented that B3LYP systematically gives errors in the bond dissociation energy of the O-O and O-H bonds in hydroperoxide moieties (Brinck et al., 1999; Wijaya et al., 2003). The standard approach is to use isodesmic reactions to obtain a corrected heat of formation (Redfern et al., 2000). While this correction for reactants and products is straightforward, an analogous treatment for the TS is not obvious. Cancellation of error between reactants/TS and reactants/products should help mitigate these effects. Even so, thermodynamic constraints dictate that the absolute error of the forward and

reverse activation energies will be at least as big as the absolute error in the enthalpy of reaction. To try to assess whether theory more accurately predicts the forward or the reverse activation energy, we used the CBS-QB3 method, which is known to be very accurate for reproducing experimental activation energies in radical chemistry (Coote et al., 2002), to study HOO· + phenol → Ar· + HOOH. The barrier obtained from B3LYP/6-31G(d) for the reverse reactions, *i.e.*, HOOH + ArO· → HOO· + ArH, agreed better with the result from CBS-QB3 than the barrier for the forward reaction. However, without extensive high-level calculations, which are computationally intractable, and a more extensive experimental database, this observation cannot be generalized.

5.3 Results and Discussion

5.3.1 Reaction intermediates

For all reactions studied, an IRC calculation was performed in order to verify the TS found corresponds to the correct reactants and products. The structures obtained from each IRC calculation were then subject to geometry optimization and yielded, in every case, a structure which was lower in energy than the sum of the corresponding reactants or products. This is depicted in Figure 5.3 for reaction 9 in Figure 5.2. This behavior is similar to that observed in other studies of mono-substituted phenols (Singh et al., 2005) and also in atmospheric chemistry (Smith and Ravishankara, 2002) One reason for the dramatic lowering of energy compared to the individual reactants or products is basis set superposition error (BSSE) which artificially lowers the energy of the complex due to the interaction of orbitals on neighboring molecules. To estimate the effect

of BSSE, we calculated the counterpoise (CP) correction (Simon et al., 1996) for reaction 10 in Figure 5.2. In this case, the reactant and product complexes are each artificially reduced in energy by about 2.5 kcal mol^{-1}. This difference does not account for the total difference in energy between the reactants or products and their respective complexes. Therefore, our results suggest the presence of a stable hydrogen-bonded complex.

Although these states exist as minima on the electronic and enthalpic energy surfaces, they appear as higher energy plateaus on the free energy surface. This is due to the large decrease in entropy upon formation of the hydrogen-bonded state. Since these intermediates are substantially higher in free energy than the reactants in either direction, they will not affect the approach to equilibrium to any measurable extent and their equilibrium concentrations are negligible. Accordingly, an overall reaction rate coefficient was formulated based on equation 5.2 that involves the transition from reactants to products directly without considering the hydrogen-bonded states. Analysis of this rate coefficient yields Arrhenius parameters that can be used in a kinetic model describing the overall reaction of antioxidants and lubricant-derived peroxy radicals. The hydrogen-bonded states do become important in many cases (Smith and Ravishankara, 2002) and must be considered if 1) their presence affects the approach to equilibrium or 2) the species has an appreciable equilibrium concentration. We note that the structure-reactivity relationship presented by Singh and coworkers (Singh et al., 2005) was derived using the hydrogen-bonded states to calculate the activation energy and would therefore need to be re-evaluated to be used with experimental heats of reaction as would be typical when kinetic modeling of the action of antioxidants is carried out.

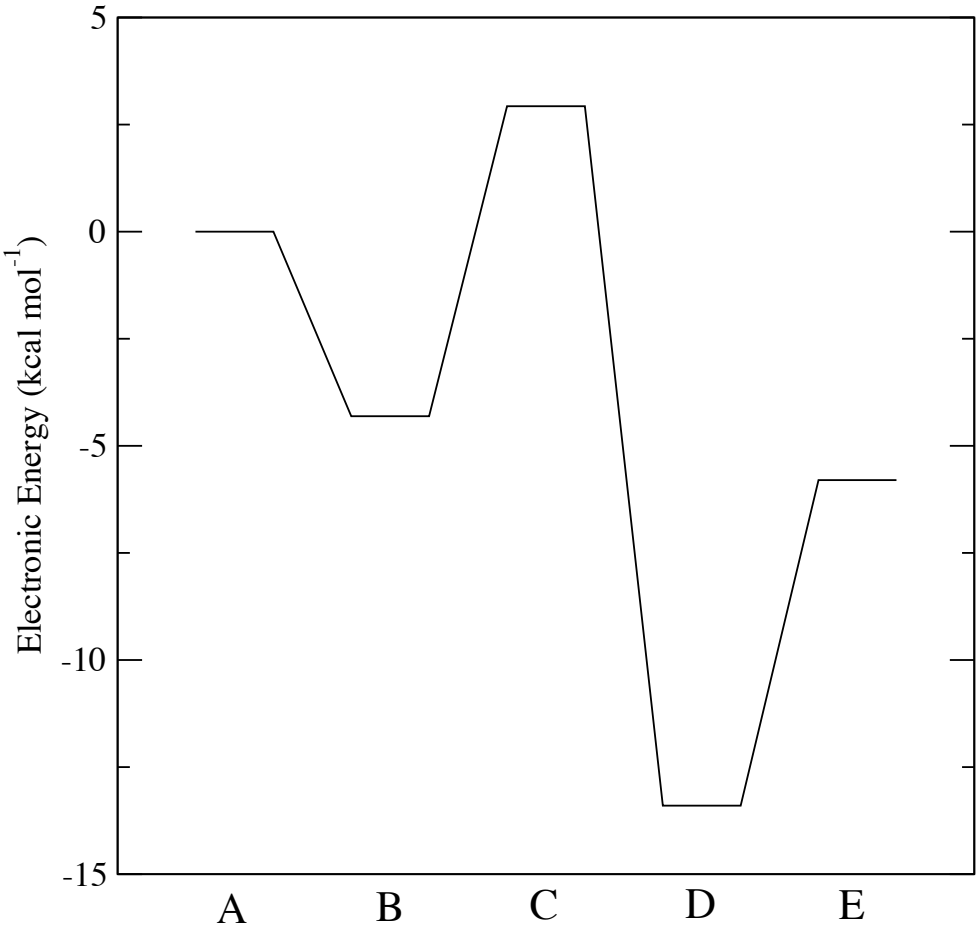

Figure 5.3: Reaction coordinate diagram for reaction 9 in Figure 5.2. The electronic energy for each state is given relative to the reactants ($\epsilon_{BHT} + \epsilon_{ROO\cdot}$) where BHT stands for butylatedhydroxy-toluene. The states shown in the figure are: A) reactants separated in space, B) proposed hydrogen bonded state (reactants), C) transition state, D) proposed hydrogen bonded state (products), E) products separated in space.

5.3.2 Tunneling effects

Our usage of a straight-line fit of *ln* k vs 1/T implies that quantum tunneling is not substantial at low temperatures and that the temperature dependence of the activation energy is very slight. For some hydrogen transfer reactions, quantum tunneling is known to be important at low to moderate temperatures (Gonzalez-Lafont et al., 1991). To explore this, several classical and semi-classical approximations to the transmission coefficient were calculated for reaction 10 in Figure 5.2, and the results are given in Table 5.1. The SCT coefficient is the most rigorous and computationally demanding calculation, requiring evaluation of the Hessian along the minimum energy path (MEP) (Gonzalez-Lafont et al., 1991). The data in Table 5.1 show that the Wigner correction agrees very well with the SCT model at the temperatures of interest (300-1500 K) and that the SCT, ZCT, and Wigner coefficients are relatively small. Typically, the Wigner correction does not agree well with the more rigorous SCT and ZCT methods for bimolecular hydrogen transfer, and the Eckart approximation is usually in better agreement with more rigorous methods (Gonzalez-Lafont et al., 1991; Truong et al., 1999). To understand why this was not the case in the reaction studied here, the adiabatic ground state potential ($V_a^G(s)$ is simply the sum of electronic and zero point energies along the reaction path) was examined as shown in Figure 5.4. Reaction 10 has a late transition state, and in the region where tunneling is considered (approximately -0.9 to +0.25), the PES is very wide, reducing the transmission probability. Given the good agreement between the Wigner and SCT approximations, we used the Wigner correction in calculating the activation energies from equation 5.2. The imaginary frequencies for all transition states were similar in magnitude, indicating the small contribution from tunneling is uniform for the entire set of reactions studied.

Table 5.1: Various transmission coefficients calculated for reaction 10 in Figure 5.2. The coefficients given are the Wigner correction, κ_W, the Eckart approximation, κ_E, and the semi-classical ZCT and SCT coefficients (κ_{ZCT} and κ_{SCT}).

Temperature (K)	κ_W	κ_E	κ_{ZCT}	κ_{SCT}
300	4.08	26.10	3.19	6.66
400	2.73	6.36	1.89	2.98
500	2.11	3.44	1.47	2.00
600	1.77	2.49	1.27	1.59
700	1.57	2.05	1.17	1.38
800	1.43	1.81	1.11	1.26
900	1.34	1.65	1.07	1.19
1000	1.28	1.54	1.04	1.14
1500	1.12	1.30	0.99	1.03

The poor agreement between the Eckart and SCT models is due to the fact the late-TS PES shown in Figure 5.4 is very different from the shape of an Eckart function.

5.3.3 An Evans-Polanyí relationship to describe ROO· + phenolic antioxidants

The calculated data for reactions 1-9 are summarized in Table 5.2. The goal of this work is establishing structure-reactivity relationships for use in modeling lubricant degradation chemistry, and therefore, we did not include reaction 10 in the development of the kinetic correlation below. The properties of reaction 10 were calculated both using the HO approximation and also using the IR-corrected partition functions. The IR correction has a modest effect on the activation energy and enthalpy of reaction 10, and therefore, we would expect that E_A and $\Delta \mathrm{H}_{rxn}$ of the other reactions would be affected only slightly as well if internal rotation corrections had been included. For reaction 10 the pre-exponential factor is lowered by a factor of 4 when internal rotation is taken into

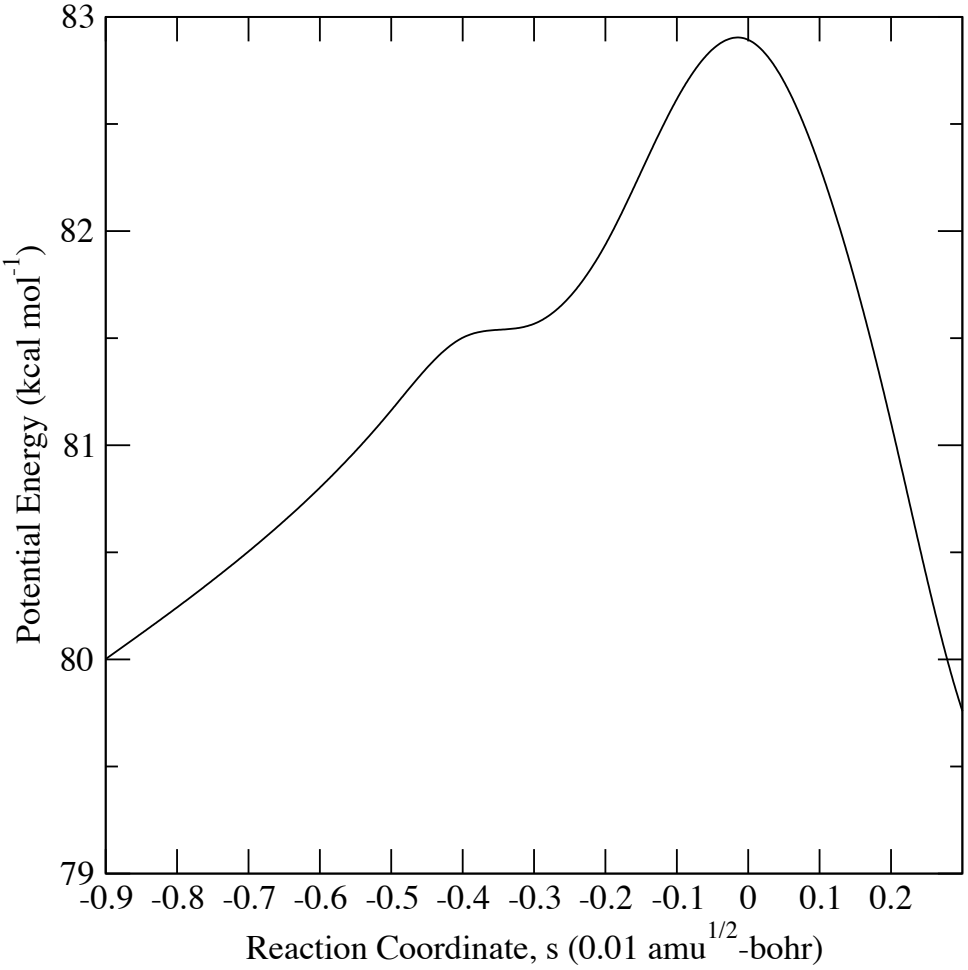

Figure 5.4: Adiabatic ground state potential for reaction 10 in Figure 5.2. The reaction coordinate (s) is given in Cartesian mass-weighted coordinates. The transition state is located at s=0 and the reactants are defined at $s = -\infty$.

Table 5.2: Kinetic and thermodynamic properties[a] for reactions 1-9 in Figure 5.2 (forward and reverse reactions). Calculated data provided are the heat of reaction (kcal/mol), ΔH_{rxn}, at 298 K, the Arrhenius activation energy (kcal/mol), E_A, and Arrhenius pre-exponential factor (m^3/mol-s), A.

		forward		reverse	
Reaction number	ΔH_{rxn}	E_A	$log\ A$	E_A	$log\ A$
1	2.5	4.2	5.7	2.3	5.5
2	3.2	4.8	5.9	1.5	5.5
3	3.1	4.6	5.8	1.5	5.6
4	−2.6	0.6	5.4	1.4	5.6
5	−1.9	1.3	5.8	3.1	5.3
6	−2.0	1.1	5.5	3.1	5.6
7	−7.2	1.8	5.3	3.1	5.5
8	−6.5	2.2	5.2	8.9	4.9
9	−6.7	1.8	5.2	8.7	4.8
10(HO)[b]	1.6	4.0	6.0	8.4	4.9
10(IR)[b]	1.6	4.2	5.4		

[a]Unless noted, the data are calculated entirely within the harmonic oscillator approximation.

[b]HO refers to results obtained using only the harmonic oscillator approximation. The IR value corrects for the hindered rotor present in the H-O-O-H linkage in the transition state.

account. While the other A values in Table 5.2 should be used with caution since they are only calculated within the HO approximation, these results do show that the A values do not substantially change as a function of the peroxy radical or, more importantly, the antioxidant. This result points to the conclusion that the relative performance between various antioxidants can be understood in terms of the effect on the barrier to reaction as opposed to differences in the pre-exponential factor. Taking into account the average value of A from Table 5.2 and the ratio of A(IR)/A(HO) for reaction 10, we recommend an approximate A value of 10^5 m^3/mol-s for the abstraction of a phenolic hydrogen by ROO· (*i.e.*, the forward reactions in Table 5.2).

The activation energy is plotted versus the heat of reaction in Figure 5.5 for both the forward and reverse directions. The data are clearly organized into clusters signifying which antioxidant

is involved in each reaction. The clusters from left to right (forward reactions/open symbols) correspond to the reactions with BHT, p-hydroxyanisole, and phenol. The two hindered phenols only have reactions which are exothermic, whereas phenol reacts endothermically with all of the peroxy radicals. The additional substitution along the aromatic ring clearly provides substantial stabilization of the corresponding phenolic radical, lowering the heat of reaction and activation barrier. The data in Figure 5.5 show surprising contrathermodynamic behavior. That is, for the exothermic reactions, the reactions which are more exothermic are observed to have higher activation energies. We have shown that this behavior is correlated to the strength of the binding in the hydrogen-bonded complex (Pfaendtner and Broadbelt, 2007b). Contathermodynamic behavior was also observed in a series of radical addition reactions (Gomez-Balderas et al., 2003), and it has been proposed (Donahue et al., 1998) that the C-H bond strength, *i.e.*, the enthalpy of reaction, should not be used as a predictor for chemical reactivity. Nevertheless, the activation energy is clearly correlated to the heat of reaction, which is useful for kinetic modeling applications.

Using this data, parameters for the Evans-Polanyí relationship were regressed. Note that the Blowers-Masel correlation given in equation 5.1 is not suitable for the data shown in Figure 5.5 since the correlation is truncated before it can curve upwards in the strongly exothermic regime. Least-squares regression was used to fit the data in Table 5.2 to the Evans-Polanyí equation while constraining the E_o value to be equal for endo- and exothermic reactions and the sum of the transfer coefficients for endo- and exothermic reactions to be equal to 1. These constraints are requisite in order to obtain thermodynamic consistency for the forward/reverse reaction pairs. Values of E_o = 0.85 kcal mol^{-1} and α = 1.16/-0.16 (endo/exothermic) were obtained. The correlation is shown in

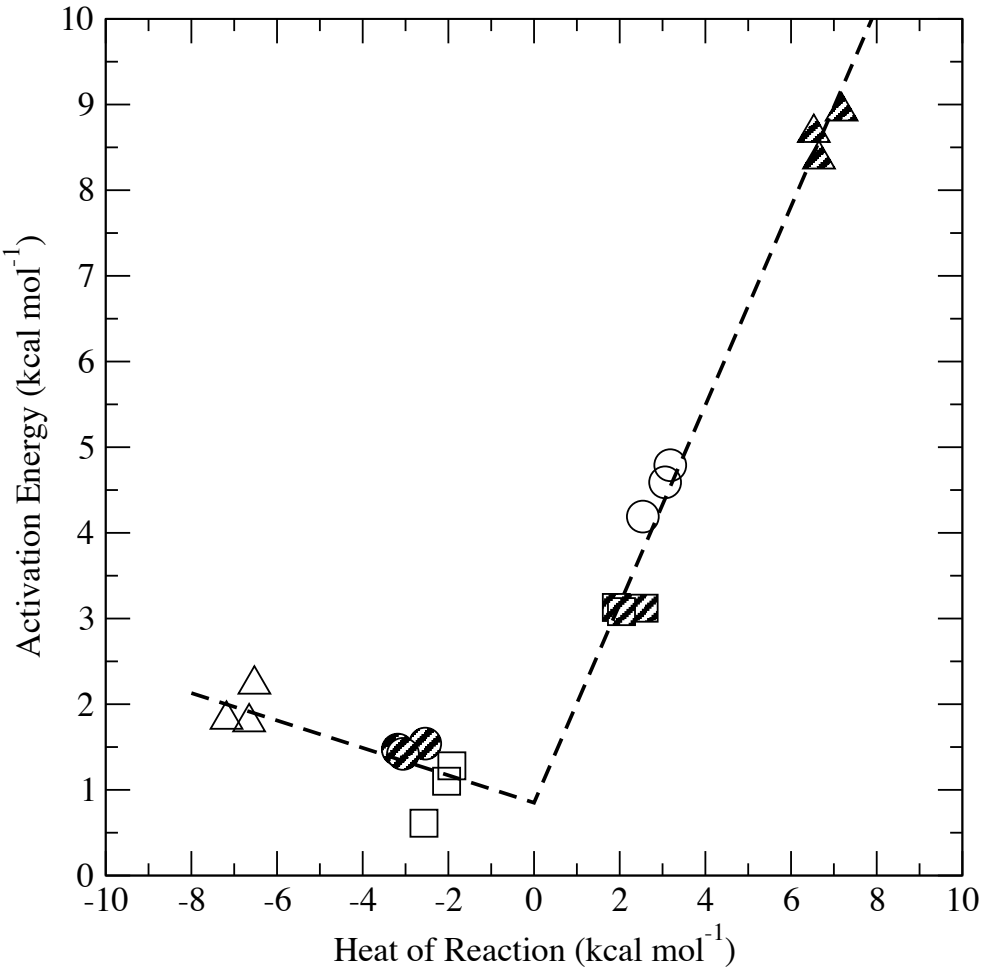

Figure 5.5: Heat of reaction versus activation energy for reactions 1-9 in Figure 5.2. The data are given for forward (open symbols) and reverse (filled symbols) reactions. Reactions 1-3 (phenol) are shown with a circle, reactions 4-6 (p-hydroxyanisole) are shown with a square and reactions 7-9 (BHT) are given with triangles. The fitted Evans-Polanyí correlation is shown with a dashed line. The correlation is given by E_A (kcal/mol) $= 0.85 + \alpha * \Delta H_{rxn}$ with α = 1.16 for endothermic and -0.16 for exothermic reactions. The activation energy is calculated for the A-E transition in Figure 5.3, and the heat of reaction is the difference in enthalpy between E and A.

Figure 5.5 and is observed to predict the quantum chemistry results very well. For alkyl radicals abstracting hydrogen, the Evans-Polanyí relationship is typified by intrinsic reaction barriers in the range of 7.3-8.1 kcal mol^{-1} and transfer coefficients near 0.75/0.25 for endo- and exothermic reactions, respectively (Blowers and Masel, 2000). The reduction in activation energy compared to other hydrogen transfer reactions is consistent with experimental observations that the hindered phenols are efficient radical scavengers.

An important consideration regarding the correlation presented in Figure 5.5 and its general use in kinetic modeling is that these calculations were performed in the gas phase, while many of the example systems listed in the introduction are in solvent or the condensed phase. Additionally, the choice of basis set can have a measurable impact on kinetic data when B3LYP is used (Henry and Radom, 2001; Pfaendtner et al., 2006c). Solvation effects were calculated using the PCM model, and the effect of the level of theory was examined by performing single point calculations with a larger basis set, 6-311+G(d,p), based on the B3LYP/6-31G(d) optimized structures. We previously found (Pfaendtner et al., 2006c) that B3LYP/6-311+G(d,p) is a reasonable compromise between speed and accuracy for hydrogen transfer involving alkylperoxy radicals. The species studied here are among some of the largest examined using B3LYP/6-31G(d), and performing minimum energy or saddle point optimization on these structures with larger basis sets or levels of theory, *i.e.* CBS or G3, is computationally intractable. Specifically, we performed the following calculations on reactions 1-9: 1) single point energy calculations using B3LYP/6-311+G(d,p) and 2) single point energy calculations using B3LYP/6-311+G(d,p) with the PCM solvent model and the solvent approximated using the properties of heptane. The contrathermodynamic behavior observed in

Figure 5 was still observed in both cases, and the Evans-Polanyí parameters in both cases agreed well with those obtained from the 6-31G(d) results.

Finally, it is possible to use the correlation shown in Figure 5.5 in a predictive mode to estimate properties of other reactions and compare the results to experimental data. The Landoldt-Bornstein compendium (Howard and Scaiano, 1997) contains kinetic data for tert-butylperoxy radical interacting with BHT and a derivative of p-hydroxyanisole (3,5-di-tert-butyl-p-hydroxyanisole). From available experimental data at 175 K and 236 K, the activation energies for these reactions were calculated to be 0.30 kcal/mol and 0.19 kcal/mol, respectively. Using B3LYP/6-31G(d), we calculated the enthalpy of reaction for tert-butylperoxy radical abstracting hydrogen from BHT (-4.95 kcal/mol) and p-hydroxyanisole (-0.33 kcal/mol). Next, using the B3LYP/6-31G(d) enthalpies of reaction and the correlation we developed, activation energies of 1.64 and 0.90 kcal/mol, respectively, were obtained. Although this comparison with experimental data is limited, the results are in very good agreement with experiment. An important feature of these results is that the correlation developed using quantum chemistry is able to capture the surprising contrathermodynamic behavior manifested in the experimental data, *i.e.*, the more strongly exothermic reaction (BHT) has the higher activation energy.

5.4 Conclusions

The chemistry of phenolic radical scavengers interacting with peroxy radical lubricant mimics has been studied to develop a structure-reactivity relationship suitable for use in kinetic modeling. Ten different reactions were studied using density functional theory and transition state theory. It was

shown that hydrogen-bonded intermediate states were present in all reactions, but for this reaction class, their presence does not affect the approach to equilibrium for the overall reaction. Thus, E_A and ΔH_{rxn} values based on the reactants and products can be used for kinetic modeling. The effects of quantum tunneling were shown to be well approximated using the simple Wigner correction. Many bimolecular hydrogen transfer reactions require computationally expensive treatment for quantum tunneling which severely restricts the application of quantum chemistry to systems of practical interest. For the reaction family of alkylperoxy radicals abstracting phenolic hydrogens from phenol and hindered phenols, using the Evans-Polanyí relationship with a new parameter set captured the results from quantum chemistry very well, even though contrathermodynamic behavior for the kinetics of the overall reaction was observed.

Chapter 6

Uncovering the Cause of Contrathermodynamic Behavior in Intermolecular Hydrogen Transfer of Alkylperoxy Radicals

6.1 Introduction

Obtaining theoretical estimates of the kinetic parameters for hydrogen transfer reactions has been the subject of active research for decades (Blowers and Masel, 1999; Evans and Polanyí, 1938; Marcus, 1968; Roberts and Steel, 1994; Saeys et al., 2004; Sumathi et al., 2001a; Zavitsas, 1996). Recently, the advent of computational chemistry and powerful experimental techniques has led

to great advances in our understanding of radical reactivity and hydrogen transfer. One notable example is in the field of atmospheric chemistry and the properties of reactions of the OH radical (Donahue et al., 1998; Neeb, 2000; Smith and Ravishankara, 2002). In contrast, the reactions of alkylperoxy radicals have received comparatively little attention despite their great importance in oxidation processes of hydrocarbons. The use of quantum chemistry and transition state theory in the study of the free-radical oxidation of alkanes holds great promise both for informing our fundamental understanding of this chemistry and also for elucidation of structure-reactivity relationships.

The low-temperature oxidation of hydrocarbons is of interest to researchers in a number of different fields. Examples include the oxidative degradation of lubricating oils (Blaine and Savage, 1992; Jensen et al., 1981) and combustion of fuels in novel engines (Wijaya et al., 2003). The fundamental reaction pathways in condensed-phase oxidation are basically well established and have been reviewed extensively including recent comprehensive reviews by Emanuel and Gál (1986) and Denisov and Denisova (2000). Despite decades of detailed experimental and theoretical investigations, there are few examples of reaction networks based on elementary steps that describe all of the important reaction pathways for the oxidation of large hydrocarbons. Successful generation of a reaction network describing free-radical oxidation of hydrocarbons at the mechanistic level requires kinetic data for hundreds or thousands of reactions, and in the case of condensed-phase oxidation, published data can be contradictory or lacking altogether. Therefore, the use of kinetic correlations, or structure-reactivity relationships, has become widespread in the modeling community as a means of estimating rate coefficients of reactions in large-scale mech-

anisms (Broadbelt and Pfaendtner, 2005). In the case of bimolecular atom-transfer reactions, the Blowers-Masel correlation has been shown to be particularly effective in estimating the activation energy (Blowers and Masel, 2000). The Blowers-Masel correlation is an improvement upon the classic Evans-Polanyí correlation (Evans and Polanyí, 1938), which has been shown to work well for a number of different elementary reaction types in free radical chemistry (Boock and Klein, 1994; De Witt et al., 2000; Kruse et al., 2003). However, the application of these correlations to the reactions of alkylperoxy radicals undergoing hydrogen transfer with alkanes has not, to our knowledge, been reported on in the literature. Further investigation of these reactions is merited given that this reaction family ($ROO\cdot + R'H \rightarrow ROOH + R'\cdot$) constitutes a vast majority of reactions in the free-radical oxidation mechanism of hydrocarbons.

Experimentally, it is very difficult to resolve individual rate coefficients for bimolecular hydrogen transfer reactions involving alkylperoxy radicals. This stems largely from the fact that free-radical oxidation proceeds via a degenerative chain branching mechanism which generates large numbers of reactions and radical intermediates. However, a number of high-pressure limit rate coefficients are available for methylperoxy radical abstracting hydrogen from various alkane substrates as part of the NIST kinetics database (NIST, 2006). We report here rate coefficients at 300 K since these will be used for comparison with theoretical estimates. Tsang and Hampson (1986) recommend rate coefficients of 6.22 x 10^{-9} (m^3/mol-s) for the reaction of methylperoxy radical and methane and 3.83 x 10^{-6} (m^3/mol-s) for the reaction of methylperoxy radical and ethane. These data are derived by inference from analogous reactions and are given with an uncertainty estimate of a factor of 10. Tsang (1988) recommends a rate coefficient of 7.52 x 10^{-7} (m^3/mol-s)

for the reaction of methylperoxy radical and propane (abstraction of the central hydrogen). This data is recommended based on two experimentally reported studies of analogous systems and is given with an uncertainty of a factor of 5. Finally, Tsang (1990) recommends a rate coefficient of 1.59 x 10^{-4} (m^3/mol-s) for the reaction of methylperoxy radical and *i*-butane (abstraction of the tertiary hydrogen). This data is also estimated from an analogous system and is given with an uncertainty estimate of a factor of 10. The Landolt-Bornstein Compendium (Howard and Scaiano, 1997) contains rate coefficients for two additional reactions relevant to this study. The reaction of *tert*-butylperoxy radical and *i*-butane has a rate coefficient of 6.1 x 10^{-4} (m^3/mol-s) at 373 K (abstraction of the tertiary hydrogen), and the reaction of the same radical with *n*-hexane at 303 K has a rate coefficient of 3.5 x 10^{-7} (m^3/mol-s) (abstraction of a hydrogen atom from the third carbon). It is clear from inspection of the available rate coefficients in the literature that there is not sufficient data to develop mechanistic models wholly based on experimental parameters. However, these rate coefficients can be used to verify the quality of estimates calculated using quantum chemistry or other theoretical approaches.

Theoretically, this reaction class has not received extensive treatment in the literature. Several works have investigated the reactions of HO and HOO radicals and various alkanes or oxygenated alkane derivatives (Anglada and Domingo, 2005; Anglada et al., 2006; Chen and Bozzelli, 1999). Quantum chemical investigations of these systems universally show the presence of loosely-bound complexes as precursors to transition state crossing. The hydroxyl radical and hydroperoxy radical are very polar, and it is not surprising to find the formation of weak, long-range bonds as reactants come into contact. Since the alkylperoxy radicals under consideration have comparable or

larger dipole moments, it is reasonable to expect these complexes may also play an imporant role in their hydrogen transfer reactions as well. Smith and Ravishankara (2002) summarized recent experimental and theoretical data on the role of these intermediate states in hydrogen transfer for many different substrates. They concluded that for the reactions of hydroxyl radical with alkanes, experimental and theoretical evidence shows that hydrogen transfer is not influenced by weakly bound intermediate states. Making accurate theoretical estimation of the reactivity of hydrogen transfer reactions is additionally complicated by the observation that tunneling and internal rotation are known to be very important in analogous systems (Gonzalez-Lafont et al., 1991; Truong et al., 1999). To our knowledge, no research groups have applied rigorous treatments of tunneling and internal rotation in conjunction with high-level hybrid methods such as the Complete Basis Set (CBS) methods to calculate highly accurate reaction rate coefficients for bimolecular hydrogen transfer in alkane oxidation.

The purpose of this chapter is quantum chemical investigation of the reactions of alkylperoxy radicals and alkane substrates in order to address the following questions:

1. What is the role of loosely-bound intermediate complexes, or adducts, in crossing the energy barrier from reactants to products?

2. Are quantum tunneling effects important in the temperature range of interest for these reactions ($>$ 300 K)?

3. How do structure-reactivity relationships determined based on quantum chemical calculations compare to the Evans-Polanyí, Marcus, and Blowers-Masel correlations for estimating the activation energy for hydrogen transfer?

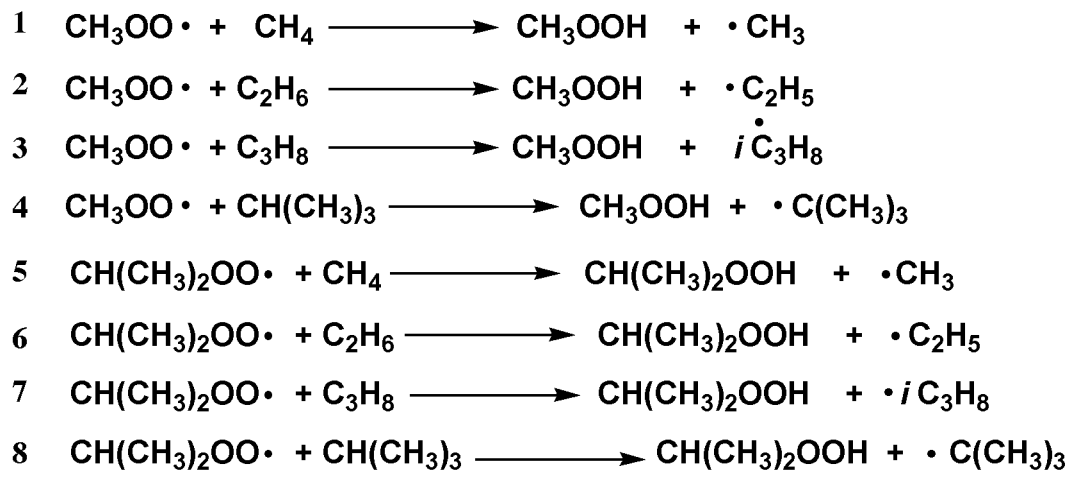

Figure 6.1: Bimolecular hydrogen transfer reactions studied using quantum chemistry and transition state theory.

Herein we investigate a series of hydrogen transfer reactions of alkylperoxy radicals. Substituent effects in the radical and substrate were explored by systematically varying the environment in which hydrogen transfer occurs. The reactions under consideration are listed as 1-8 in Figure 6.1. Two different alkylperoxy radicals, methylperoxy radical and *i*-propylperoxy radical, are combined with methane, ethane, propane and isobutane to give sixteen different reactions (forward and reverse pairs). The set of reactions was chosen to give diversity in the calculated thermodynamic properties, *e.g.*, enthalpy of reaction, and offer a large data set from which structure-reactivity relationships can be derived. Drawing by analogy from our previous studies of intramolecular hydrogen transfer of alkylperoxy radicals (Pfaendtner et al., 2006c), we have chosen the CBS-QB3 method to perform the quantum chemical calculations. Additionally, we have used B3LYP/6-31G(d), G3//B3LYP, MP2/6-31G(d), B3LYP/6-311+G(d,p), and B3LYP/CBSB7 for comparison of calculated kinetic data for selected reactions.

6.2 Computational and Theoretical Details

All molecular orbital (MO) and density functional theory (DFT) calculations were completed using the Gaussian 03 (Frisch et al., 2003) software package. At each level of theory and basis set, the geometries of all reactants and products were optimized to minimum energy structures using the Berny algorithm (Peng et al., 1996). Transition states (TS) were identified as first-order saddle points on the potential energy surface. The quadratic synchronous transit (QST3) (Peng and Schlegel, 1993) method was used to rapidly locate many transition states once a single, representative TS was found. All transition states were first validated by verification that only one large amplitude imaginary frequency was present. The true reactant and product(s) corresponding to each TS were obtained by using intrinsic reaction coordinate following (Gonzalez and Schlegel, 1989).

The chief method employed in this chapter was the hybrid model chemistry CBS-QB3 (Montgomery et al., 1999). CBS-QB3 relies on geometry optimization and frequency calculation using density functional theory (DFT) and Becke's (Becke, 1993) three-parameter hybrid functional, B3LYP, in conjunction with the 6-311G(2d,d,p) basis set. This basis set is represented as an extension of the Pople formalism by adding an additional 2d polarization function to third row atoms (Montgomery et al., 1999). CBS-QB3 seeks to extrapolate the QCSID(T) energy using an infinite basis set and is well known to provide highly accurate estimates of thermochemical properties. For additional comparison, we used B3LYP with a split-valence, double zeta basis set with additional d-type polarization functions, 6-31G(d). According to the recommendation of Montgomery and coworkers, all vibrational frequencies within the CBS-QB3 calculation were scaled by 0.99. Fre-

quencies obtained using B3LYP/6-31G(d) were scaled according to the recommendation of Scott and Radom, *i.e.*, 0.9806 for ZPE, 1.0015 for S_{vib}, 0.9989 for H_{vib}, and 0.9614 for other quantities calculated using fundamental frequencies (Scott and Radom, 1996). Solvent effects were studied using a polarizable continuum model (PCM) with heptane as the model solvent (Cancés et al., 1997). The solvent cavity was established using radii obtained from the universal force field (Rappé et al., 1992) with hydrogen atoms explicitly defined.

Using the optimized geometry and frequencies obtained from a Hessian calculation, the total microcanonical partition function can be calculated for each molecule within the rigid-rotor harmonic oscillator (HO) assumption. The formulae for electronic, translational, rotational and vibrational partition functions are well established (McQuarrie and Simon, 1999). However, the HO approximation incorrectly treats low-frequency rotations as harmonic oscillators. If left uncorrected, this can induce substantial error in calculated kinetic and thermodynamic data. In the present chapter we have used the same approach outlined in Chapter 3. Free rotors are treated using the standard approach (Frenkel et al., 1994), and hindered rotors are treated within the uncoupled 1D-hindered rotor approximation (Heuts et al., 1996; Pfaendtner et al., 2007). Once the partition functions for each reactant and transition state were corrected for internal rotation, the rate constant as a function of temperature was calculated using the standard expression,

$$k_{TST} = \textit{rpd} * c_o^{1-n} \kappa\left(T\right) \frac{k_b T}{h} \frac{Q^{\ddagger}(T)}{Q^r(T)} \exp\left(-E_o/RT\right) \tag{6.1}$$

where *rpd* is the reaction path degeneracy, determined by the number of identical hydrogen atoms that may undergo abstraction, $Q^{\ddagger}$ and Q^r are the total partition functions for the TS and reac-

tants, respectively, and E_o is the reaction barrier, *i.e.*, the zero-point corrected difference between the ground-state electronic energies of the TS and the reactants. The value c_o^{1-n} is the standard-state concentration to which the translational partition function is referenced, P/RT, raised to the power of $1-n$ where n is the molecularity of the reaction. The quantity $\kappa(T)$ is the correction for quantum tunneling. To quantify the effect of quantum tunneling on the reactions of interest here, we calculated various approximations to the transmission coefficient including the Wigner (Hirschfelder and Wigner, 1939) correction, the Eckart approximation (Gonzalez-Lafont et al., 1991), the zero-curvature tunneling approximation (ZCT) (Gonzalez-Lafont et al., 1991), and the small curvature tunneling (SCT) (Gonzalez-Lafont et al., 1991) approximation. Calculation of the Eckart, SCT and ZCT corrections was performed using the software package "Virtual Kinetic Laboratory" of Zhang and Truong (2001). Once the temperature dependent partition functions were known, rate constants as a function of temperature were calculated, and the Arrhenius parameters A and E_A were obtained from a straight-line fit of $\ln k$ vs $1/T$. Unless otherwise stated, we used a temperature range of 298.15-1500 K for regression of A and E_A. To calculate the enthalpy of reaction, all thermodynamic parameters were obtained from ensemble energy averages <E> using standard formulae (McQuarrie and Simon, 1999).

6.3 Results and Discussion

After performing all of the requisite electronic structure calculations and making corrections for internal rotation, we analyzed the kinetic and thermodynamic properties obtained for reactions one through eight. This section is organized as follows: first, we discuss our findings related to the

formation of loosely-bound intermediate states that exist prior to crossing the TS; next, we discuss the impact of tunneling on the calculation of the reaction rate coefficient and associated kinetic quantities; finally, we discuss development of kinetic correlations from the calculated data.

6.3.1 Hydrogen bonded intermediates do not affect approach to equilibrium

An important step in performing accurate calculations of rate coefficients is validation of the TS using intrinsic reaction coordinate following. The minimum energy path (MEP) that connects the reactant(s) to product(s) via the transition state is obtained by beginning at the TS and following the steepest descent in energy in each direction away from the saddle point. For all of the reactions in Figure 6.1, the IRC was followed to verify the proposed TS corresponded to the correct reactants and products. In every case we observed that the IRC-derived structure for the products, *i.e.*, ROOH + R'·, was a loosely-bound state whose CBS-QB3 energy[a] was substantially lower in energy than the sum of the energies of each individual product. The energy of the IRC-derived structure for the reactants was slightly lower than the sum of the energies of each individual reactant. Schematics for the reaction coordinate for reactions 1 and 4 in Figure 6.1 are shown in Figure 6.2. The CBS-QB3 energy, enthalpy, entropy and free energy of the reactants, IRC-derived reactant complex, TS, IRC-derived product complex, and products are shown to give a clear picture of the energetic, enthalpic and entropic changes as the reaction proceeds.

One possible reason for the dramatic lowering of the energy of the IRC-derived product complex compared to the individual products could be basis set superposition error (BSSE) which

[a]The CBS-QB3 energy is the electronic + zero point energy.

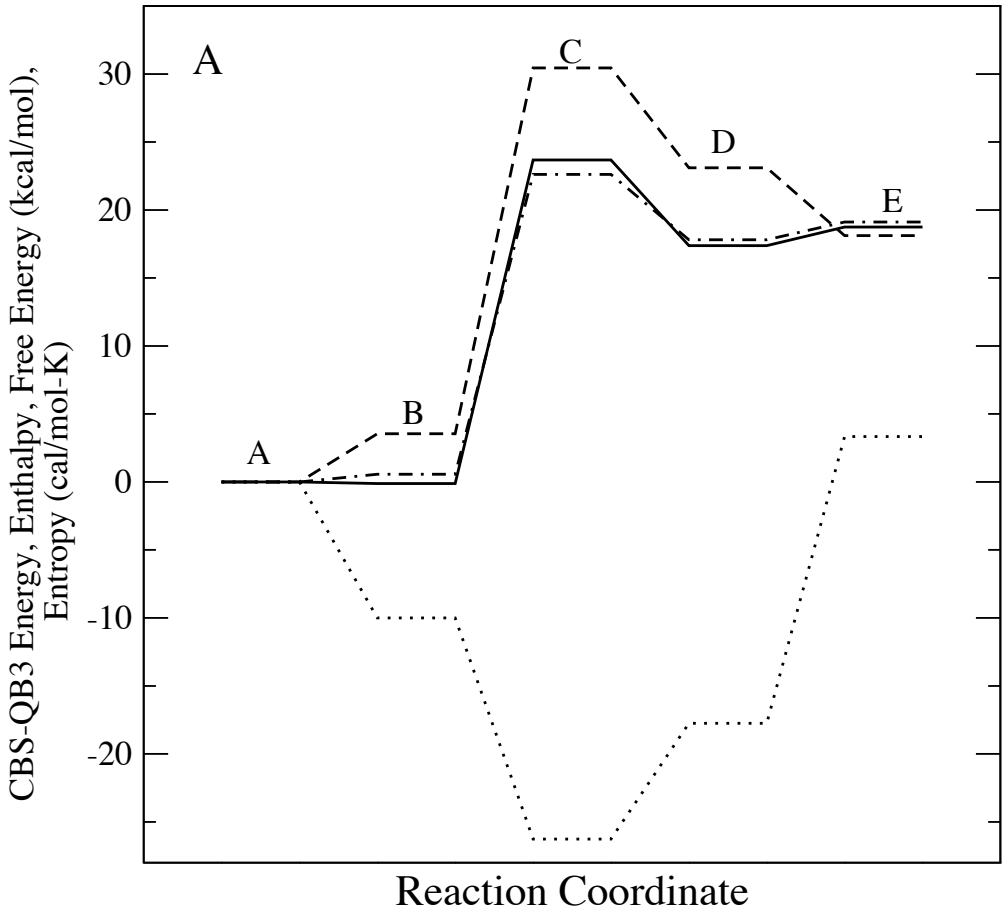

Figure 6.2: Changes in CBS-QB3 energy (solid line, kcal/mol), free energy (dashed line, kcal/mol), enthalpy (dash-dot line, kcal/mol), and entropy (dotted line, cal/mol-K) as a hydrogen transfer reaction proceeds (data at 300 K). Panels A and B correspond to reactions 1 and 4, respectively, in Figure 6.1. The states shown in the Figure are **A/E** (sum of individual reactants/products), **B/D** (IRC-derived loosely-bound states), and **C** transition state. Each quantity is with respect to the sum of each reactant calculated separately (state **A**). Continued on next page.

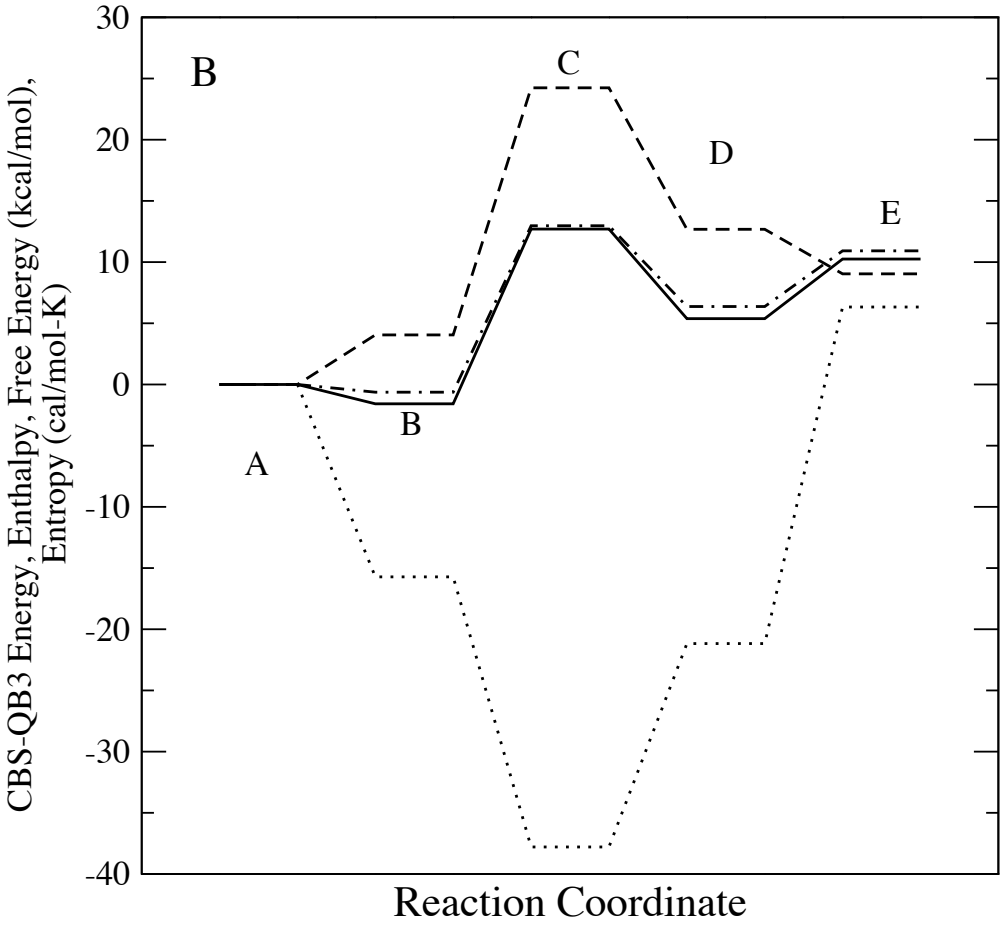

Figure 6.2: (continued)

artificially lowers the energy of the complex due to the interaction of orbitals on neighboring molecules. To estimate the effect of BSSE, we calculated the counterpoise (CP) correction (Simon et al., 1996) for the reactant/product complexes of reactions 1 and 4 in Figure 6.1 at the B3LYP/6-311G(2d,d,p) level of theory. After including the CP correction, there is essentially no difference in the B3LYP electronic energy between the separated reactants and the reactant complex for both reactions, whereas there is still a marked difference between the isolated products and the product complex. Compared to the isolated reactants, the CP-corrected reactant complexes were found to be -0.06 kcal/mol lower and 0.13 kcal/mol higher in electronic energy for reactions 1 and 4, respectively. In contrast, relative to the isolated products, the CP-corrected product complexes were observed to be -1.6 and -2.4 kcal/mol lower in electronic energy. Based on this, a stable loosely-bound state for the product complex is clearly indicated. This is further supported by inspecting the geometry of the IRC-derived structures shown in Figure 6.3. The structures suggest that the stability of the bound states in the products is related to the radical-hydrogen separation distance involving O-H-C in the equilibrium structure. In both cases, the O-H separation distance for the reactant complexes is 2.8 Å whereas the C-H separation distance in the product complexes is less than 2.2 Å. Our calculated geometries and energies are in agreement with the work of Espinosa and coworkers (Espinosa et al., 1998) who reported that the long-range bonds created by the O-H-C moiety can be considered to be purely electrostatic interactions and were not observed to have distances greater than 2.59 Å. Their work supports our own conclusion that the reactant complexes we observed are equivalent to the isolated reactants.

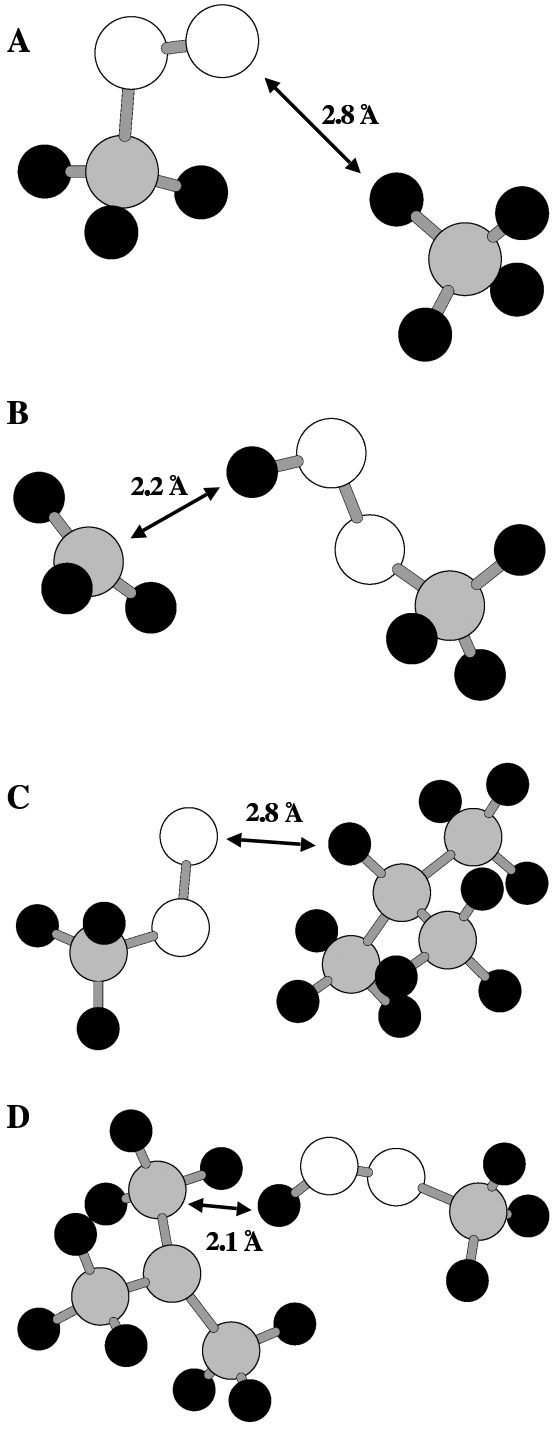

Figure 6.3: IRC-derived reactant (panels A and C) and product (panels B and D) complexes for reactions 1 and 4 in Figure 6.1. The radical-hydrogen separation (Å) is given for reference. Hydrogen atoms are shown in black, carbon atoms in grey and oxygen atoms in white.

Further inspection of the diagrams in Figure 6.2 shows that the entropy change upon formation of the loosely-bound complex (transition between states A $\rightarrow$ B and states E $\rightarrow$ D) is strongly negative. The transition from isolated reactants/products (state A or E) to loosely-bound complex (state B or D) results in an approximate two-fold decrease in the translational contribution to the entropy and a moderate decrease in the rotational contribution to the entropy, and due to the additional six low-frequency vibrations present in the complex state[b], there is a large increase in the entropy of the vibrational contribution of the complex compared with the isolated species. Summing all of these changes, the large decreases in translational and rotational entropies outweigh the increase in vibrational entropy and result in the total decrease in entropy between the isolated species and the loosely-bound complex. The large decrease in entropy going from isolated reactants/products to their respective complexes results in a positive change in free energy.

Because states B and D are endogonic with respect to states A and E, respectively, the rate coefficients for the A to E and E to A overall reactions can be quantified using the free energy changes from A to C and E to C, respectively. Microkinetic modeling confirmed that inclusion of B and D did not alter the dynamics of a system with the characteristics shown in Figure 6.2 to any measurable extent. This conclusion is consistent with analogous studies of alkanes and hydroxyl radical which concluded that loosely-bound adducts were not important in the overall chemistry (Smith and Ravishankara, 2002). We note, however, that if the free energies of states B and D are significantly lower than the free energies of states A and E, respectively, the dynamics are affected by inclusion of species B and D because they have appreciable concentrations. This

[b]Each species individually has $3N - 6$ vibrational modes; thus there are $3(N_1 + N_2) - 12$ vibrational modes for species 1 and 2 and $3(N_1 + N_2) - 6$ vibrational modes for the complex.

has implications for other systems in which the enthalpy decrease of states B or D is larger than that observed here or when the entropy decrease of B/D compared to A/E , respectively, is smaller than that observed here. For all subsequent calculations, we calculated all rate coefficients as bimolecular transitions going from state A or E to state C. However, interesting characteristics of the structure-reactivity relationships derived using B and D versus A and E to calculate the activation energy will be highlighted in Section 6.3.3.

6.3.2 Tunneling is well approximated via the Wigner correction

Our usage of a straight-line fit of *ln* k vs 1/T implies that quantum tunneling is not substantial at low temperatures and that the temperature dependence of the activation energy is very slight. For some hydrogen transfer reactions, quantum tunneling is known to lead to substantial enhancement of the reaction rate at low to moderate temperatures (Gonzalez-Lafont et al., 1991). However, we recently reported that intramolecular hydrogen transfer of alkylperoxy radicals and also bimolecular hydrogen transfer of alkylperoxy radicals and phenolic antioxidants are not strongly affected by tunneling due to the very late transition states obtained (Pfaendtner and Broadbelt, 2007a; Pfaendtner et al., 2006c). To explore the effect of tunneling in this reaction family, several classical and semi-classical approximations to the transmission coefficient were calculated for reaction 1 in Figure 6.1, and the results are given in Table 6.1. The SCT coefficient is the most rigorous and computationally demanding calculation, requiring evaluation of the Hessian along the MEP (Gonzalez-Lafont et al., 1991). The data in Table 6.1 show that the Wigner correction agrees very well with the SCT model, even at very low temperatures, and that the SCT, ZCT, and

Table 6.1: Various transmission coefficients calculated for reaction 1 in Figure 6.1. The coefficients given are the semi-classical SCT and ZCT coefficients (κ_{SCT} and κ_{ZCT}), the Eckart approximation, κ_E, and Wigner correction, κ_W.

Temperature (K)	κ_{SCT}	κ_{ZCT}	κ_E	κ_W
200	3.6	2.5	1.36	4.0
250	2.6	2.0	1.29	2.9
300	2.1	1.8	1.22	2.3
400	1.7	1.5	1.15	1.7
500	1.5	1.3	1.12	1.5
600	1.3	1.3	1.10	1.3
700	1.3	1.2	1.08	1.2
800	1.2	1.2	1.07	1.2
900	1.2	1.2	1.06	1.1
1000	1.2	1.1	1.06	1.1

Wigner coefficients are relatively small. Typically, the Wigner correction does not agree well with the more rigorous SCT and ZCT methods for bimolecular hydrogen transfer, and the Eckart approximation is usually in better agreement with more rigorous methods (Gonzalez-Lafont et al., 1991; Truong et al., 1999). To understand why this was not the case in the reaction studied here, the adiabatic ground state potential, $V_a^G(s)$[c], was examined as shown in Figure 6.4. Reaction 1 has a very late transition state and the transmission probability is greatly reduced due to the extremely wide and short peak in the region where tunneling is permissible. The MEPs for the other reactions under consideration also have late transition states. Therefore, we generalized the result from reaction 1 to the other seven reactions. Given the good agreement between the Wigner and SCT approximations, we used the Wigner correction in calculating the rate coefficients from equation 6.1.

[c]The potential is simply the sum of electronic and zero point energies along the intrinsic reaction coordinate.

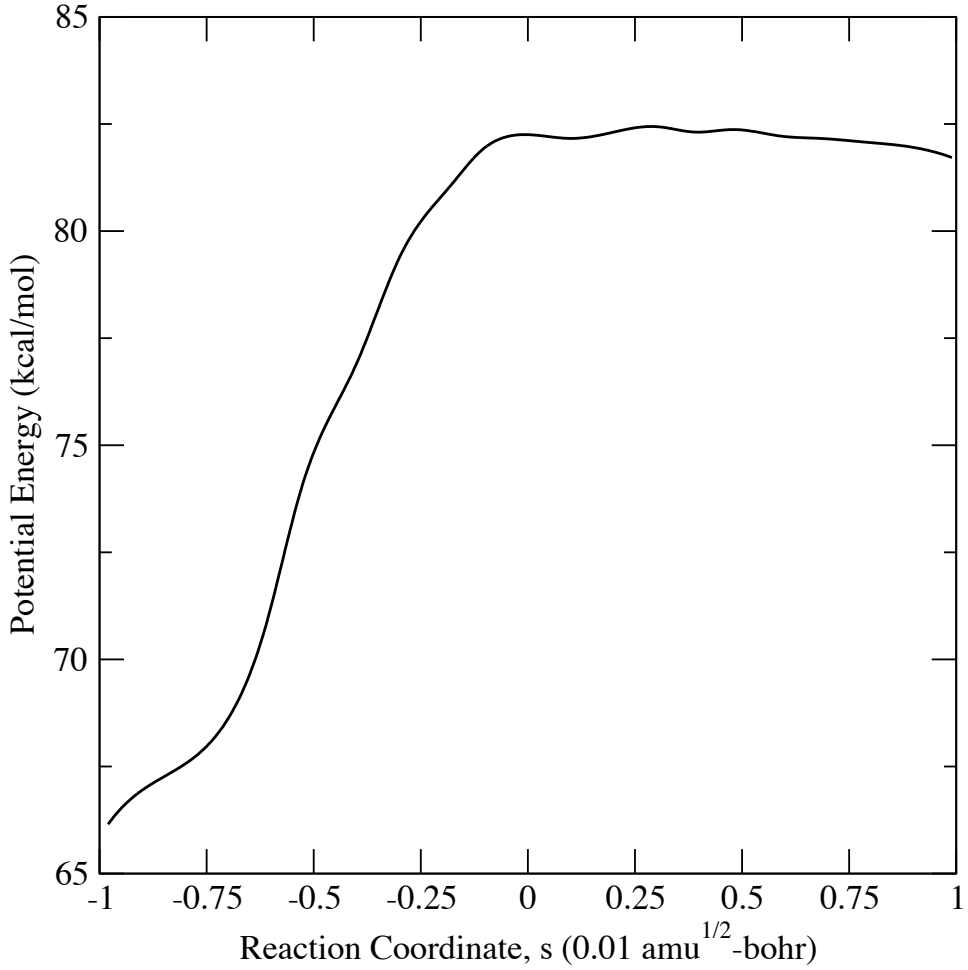

Figure 6.4: Adiabatic ground state potential for reaction 1 in Figure 6.1. The reaction coordinate (s) is given in Cartesian mass-weighted coordinates. The transition state is located at s=0 and the reactants are defined at $s = -\infty$.

6.3.3 A new structure-reactivitiy relationship for bimolecular hydrogen transfer of peroxy radicals

After accounting for tunneling and establishing the correct state from which to calculate the reaction rate coefficients, we next verified that CBS-QB3 predicts the requisite kinetic and thermodynamic data with reasonable accuracy. CBS-QB3 is known to calculate thermochemical properties with extremely high accuracy (Montgomery et al., 1999), and in many cases, CBS-QB3 has been shown to give very good agreement with experimentally observed kinetic data (Ess and Houk, 2005; Henry and Radom, 2001; Wijaya et al., 2003). Based on the experimental data provided in the introduction, we can compare rate coefficients for reactions 1-4, 7 and 8 in Figure 6.1. Table 6.2 gives a comparison of the reaction rate coefficients (reactions 1-4, 7, and 8) and the enthalpies of reaction (reactions 1-4) from experiment and those calculated using CBS-QB3. Note that the experimental data listed for reactions 7 and 8 are for *t*-butyl peroxy radical rather than isopropyl peroxy radical as studied here. Calculations showed that the heat of reaction was relatively constant for larger alkylperoxy radicals, and thus, the rate coefficients for *t*-butyl peroxy radical provide a meaningful comparison. The data in Table 6.2 show that CBS-QB3 does a very good job of estimating the experimental rate coefficients for reactions 3, 7, and 8. For reaction 3, the predicted value is within the uncertainty of the experimental value, and the predictions for reactions 7 and 8 are within a factor of 23 and 4.5, respectively. The method also does an excellent job of predicting the enthalpy of reaction (reactions 1-4). For all the reactions in Table 6.2, the CBS-QB3 value is lower than the corresponding experimental (or experimentally inferred) data. In particular, the rate coefficients from experiment for reactions 1,2 and 4 which are inferred from the reaction of HOO·

with the same substrate (Tsang, 1988, 1990; Tsang and Hampson, 1986) are noticeably higher than the corresponding data calculated using theory. We hypothesize that this is due to the impact of tunneling. Tunneling plays a larger role in hydrogen transfer of very small radicals (Gonzalez-Lafont et al., 1991; Truong et al., 1999) but was shown to be relatively unimportant for the reaction class studied here. Typical transmission coefficients for small radicals (hydroxy and hydroperoxy) can be greater than 10^2, which would bring our calculated data in line with the data inferred from experiment. The experimental value for reaction 3 was also inferred from the reaction of HOO·, so it is surprising that our predicted value is in such good agreement with the experimental rate coefficient. However, it is important to note the experimental result for reaction 3 does not follow the expected trend based on stability of the radical product. The isopropyl radical produced in reaction 3 is more stable than the ethyl radical produced in reaction 2. Thus, we would expect the rate coefficient for reaction 3 to be higher than that of reaction 2, even when reaction path degeneracy and entropic differences are taken into account. The data does not follow this trend; the experimental rate coefficient for reaction 2 is larger by a factor of five than that of reaction 3. In contrast, our results from CBS-QB3 do follow the expected trend; the rate coefficient for reaction 2 is approximately half that of the value for reaction 3. Overall, we recommend using the data inferred from other experimental systems (reactions 1-4) with caution. We note that the rate coefficients obtained from the Landolt-Bornstein compendium (reactions 7 and 8) were measured from the very similar systems, and our theoretical values for these reactions are in good to excellent agreement with experiment. We also compared the experimental rate coefficients to calculations performed using B3LYP/6-31G(d) as well as B3LYP/CBSB7. The calculations using only B3LYP

compare extremely poorly with both the experimental and CBS-QB3 data. Our results underscore the fact that CBS-QB3 can be used to provide reliable kinetic and thermodynamic properties from which structure-reactivity relationships may be derived. Finally, we tested the sensitivity of our results to a solvation model using a nonpolar medium as the solvent. Although hydrogen transfer reactions are well known to be very sensitive to the presence of a polar solvent (Avila et al., 1995), we have recently reported that calculated thermodynamic and kinetic properties of unimolecular and bimolecular hydrogen transfer of alkylperoxy radicals were not observed to be sensitive to the presence of a nonpolar solvent such as heptane (Pfaendtner and Broadbelt, 2007a; Pfaendtner et al., 2006c). We re-optimized the reactants and transition states for reactions 1 and 4 in Figure 6.1 using CBS-QB3 and PCM and calculated the rate coefficients at 300 K to compare to the data in Table 6.2. We found that for reaction 1 the ratio $k_{heptane}(300\ K)/k_{gas}(300\ K)$ was 1.3 and for reaction 4 the ratio was 1.1, in agreement with our previous results. Additionally, a comparison between the enthalpies of reaction and activation energies in solvent and in the gas phase is provided in Figure 6.5, which shows that they agree extremely well.

The calculated kinetic data and thermodynamic properties of reactions 1-8 (forward and reverse reactions) in Figure 6.1 are given in Table 6.3. Also given in Table 6.3 are the activation energies for each reaction when considering the reaction of the IRC-derived complexes going through the transition states (*i.e.*, unimolecular crossings) and also the enthalpy change upon formation of the loosely-bound complexes, *i.e.*, the enthalpy of each individual species subtracted from the enthalpy of the complex.

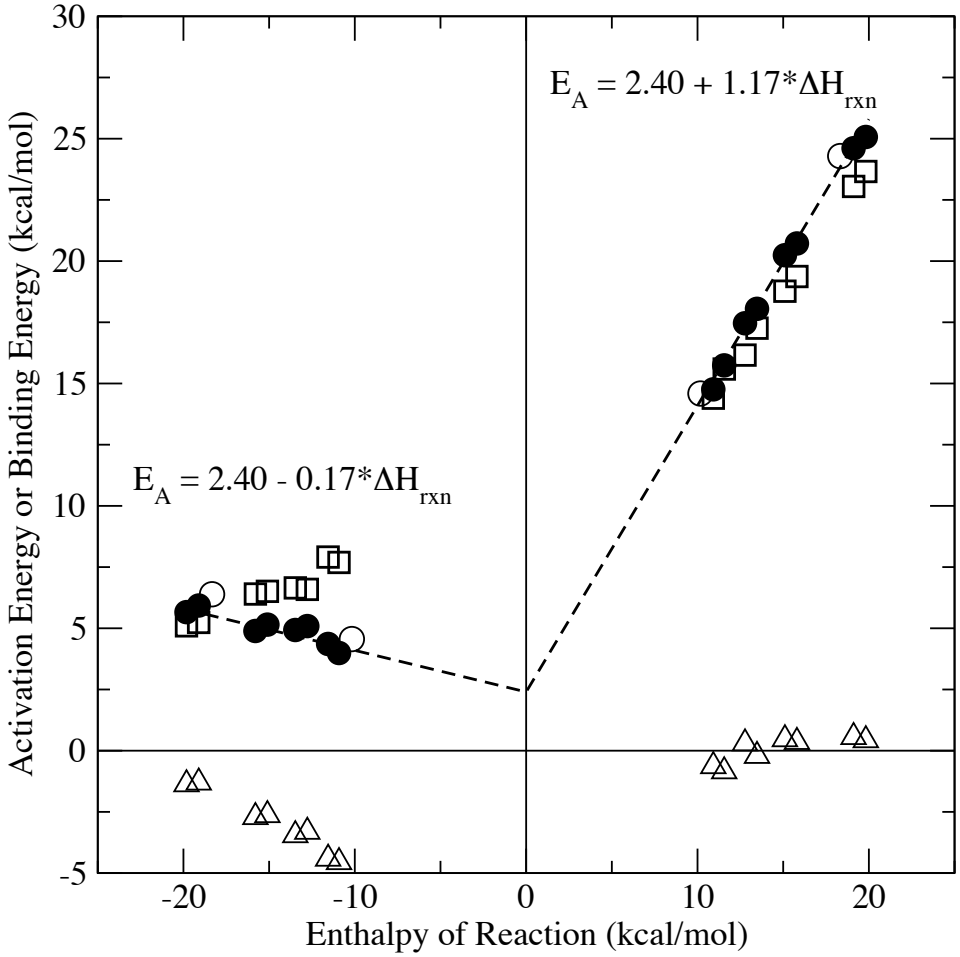

Figure 6.5: Plot of activation energy versus overall enthalpy of reaction (A→E or E→A in Figure 6.2) for the reactions shown in Figure 6.1 (forward and reverse pairs.) The data shown are the overall activation energy [filled circles] (A→C or E→C reaction in Figure 6.2), the activation energy for the complex→ TS reaction [open squares] (B→C or D→C transition in Figure 6.2), and the enthalpy change upon formation of the complex [open triangles] (A→B or E→D transition in Figure 6.2). All of the data in the plot are in kcal/mol. The dashed line is the best straight line fit to the overall activation energy with the equations shown. Activation energies and enthalpies of reaction calculated using the PCM solvation model using heptane as the model solvent are shown with open circles.

Table 6.2: Experimental and theoretical reaction rate coefficients (m^3/mol-s) (reactions 1-4, 7 and 8) and enthalpy of reaction (kcal/mol) (reactions 1-4) for a subset of the reactions in Figure 6.1.

reaction	T (K)	k expt[a]	k CBS-QB3	ΔH_{rxn} expt[b]	ΔH_{rxn} CBS-QB3
1	300	$6.22\text{x}10^{-9}$	$7.77\text{x}10^{-11}$	18.9	19.1
2	300	$3.83\text{x}10^{-6}$	$7.14\text{x}10^{-8}$	14.6	15.1
3	300	$7.52\text{x}10^{-7}$	$1.48\text{x}10^{-7}$	12.7	12.8
4	300	$1.59\text{x}10^{-4}$	$8.44\text{x}10^{-7}$	9.7	10.9
7	303	$3.50\text{x}10^{-7}$	$1.51\text{x}10^{-8}$		
8	373	$6.10\text{x}10^{-4}$	$1.37\text{x}10^{-4}$		

[a] Kinetic data obtained from NIST kinetics database or Landolt-Bornstein Compendium (Howard and Scaiano, 1997; NIST, 2006). See Section 6.1 for detailed discussion of the reported experimental values used here for comparison. The reported uncertainty for reactions 1, 2, and 4 is a factor of 10, and the reported uncertainty is a factor of 5 for reaction 3.

[b] All experimental thermodynamic properties were obtained from the NIST structures and properties database (Stein et al., 1991) except for the enthalpy of formation of $CH_3O_2\cdot$ which was obtained from Lightfoot et al. (1992).

Table 6.3: Kinetic and thermodynamic properties calculated for reactions 1-8 in Figure 6.1. The data given are the enthalpy of reaction (in kcal/mol), pre-exponential factor (forward and reverse reactions) (in m^3/mol-s), Arrhenius activation energy (for forward and reverse reactions) (in kcal/mol), Arrhenius activation energy considering the complex $\rightarrow$ TS transition (in kcal/mol) and the enthalpy change upon formation of the IRC-derived complexes ($H_{complex} - H_{reactants/products}$) (in kcal/mol).

reaction	ΔH_{rxn}^{fwd}	log A^{fwd}	$E_A{}^{fwd}$	log A^{rev}	$E_A{}^{rev}$	$E_{A_{complex \rightarrow TS}}^{fwd}$	$E_{A_{complex \rightarrow TS}}^{rev}$	$\Delta H_{complex}^{fwd}$	$\Delta H_{complex}^{rev}$
1	19.1	7.8	24.6	6.9	5.9	23.1	5.2	0.6	-1.3
2	15.1	7.6	20.2	5.8	5.2	18.8	6.5	0.5	-2.6
3	12.8	5.9	17.5	5.0	5.1	16.2	6.6	0.3	-3.3
4	10.9	4.7	14.8	4.0	4.0	14.4	7.7	-0.6	-4.6
5	19.8	6.9	25.1	6.1	5.7	23.7	5.1	0.4	-1.4
6	15.8	7.7	20.7	5.9	4.9	19.4	6.4	0.4	-2.7
7	13.5	5.2	18.1	4.4	4.9	17.3	6.7	-0.2	-3.5
8	11.6	5.4	15.7	4.8	4.4	15.6	7.9	-0.8	-4.4

It is first interesting to compare how the activation energy for the entire reaction, *i.e.*, the A→C or E→C reaction, correlates with the enthalpy of reaction. These data are plotted in Figure 6.5. The straight line fit in Figure 6.5 for the overall Arrhenius activation energy as a function of ΔH_{rxn} is nearly perfect and follows the relationship:

$$E_A = \begin{cases} 2.40 - 0.17 * \Delta H_{rxn} & \text{for } \Delta H_{rxn} \leq 0 \\ 2.40 + 1.17 * \Delta H_{rxn} & \text{for} \Delta H_{rxn} > 0 \end{cases} \tag{6.2}$$

To obtain this fit, the sum of the two transfer coefficients was fixed to be equal to one, *i.e.*, $\alpha_{fwd} + \alpha_{rev} = 1$, and the intrinsic barriers for the forward and reverse reactions were constrained to be equal. This enthalpic consistency is clarified by examining the relationship $E_A = \Delta H^{\ddagger} + nRT$ from transition state theory, where n is the molecularity of the reaction. When manipulated algebraically, this equation reveals that for forward and reverse reaction pairs of reactions in the intermolecular hydrogen transfer reaction family, the sum of the transfer coefficients is equal to 1, and the intrinsic barriers are equal, as imposed here. The sum of squared residuals for this fit (two parameters, equation 6.2) and the case when four parameters were used (two intrinsic barriers and two independent transfer coefficients) were almost identical, indicating that the thermodynamic consistency based on the approximation from TST for E_A is obeyed.

The Evans-Polanyí type relationship given in equation 6.2 and plotted in Figure 6.5 is highly counterintuitive. The negative value of the transfer coefficient for the exothermic hydrogen transfer reactions dictates that the activation energy increases with decreasing enthalpy of reaction. This result is contrary to what is predicted by the classic Evans-Polanyí relationship which is characterized by a typical transfer coefficient of $\alpha = 0.3$ for exothermic reactions. The Blowers-Masel

correlation is an improved fit for estimating the activation energy as a function of the enthalpy of reaction (Blowers and Masel, 1999), but it also fails to capture the observed trend in the activation energy. To our knowledge, this is the first such reporting of this type of contrathermodynamic behavior in hydrogen transfer reactions. This behavior was also observed when other high-level and MO calculations were used, but not for pure B3LYP results. We repeated calculations of reactions one and three in Figure 6.1 using G3//B3LYP (Baboul et al., 1999), MP2/6-31G(d), B3LYP/6-311+G(d,p), and B3LYP/6-31G(d) levels of theory. The results using CBS-QB3, G3//B3LYP and MP2/6-31G(d) all showed the contrathermodynamic behavior depicted in Figure 6.5, while none of the B3LYP results gave a trend that matched those of CBS-QB3, *i.e.*, the transfer coefficient for the reverse reactions was > 0 for all the B3LYP results.

The source of this behavior can best be understood in the context of the reaction coordinate diagram shown in Figure 6.2. The overall activation energy in the reverse, or exothermic, direction (E $\rightarrow$ C transition) can be approximated by adding the binding enthalpy for the formation of the complex (E $\rightarrow$ D enthalpy) to the activation energy for the complex crossing over the TS (D $\rightarrow$ C transition), all of which are plotted in Figure 6.5 as a function of the overall enthalpy of reaction. It is first interesting to note that the activation energies for the complex crossing the TS display classic Evans-Polanyí or Blowers-Masel behavior. When the reaction is modeled as the complex crossing over the TS and the activation energy and pre-exponential factor are calculated using equation 6.1, the data follow the expected trend. That is, the activation energy continues to decrease with decreasing enthalpy of the overall reaction. However, the binding strength of the complex decreases with decreasing enthalpy of reaction. As the overall reaction is more exothermic, the

complex is less strongly bound. When the binding strength and activation energy for the complex crossing the TS are summed, the more marked dependence of the binding energy dominates, and the overall activation energy follows the behavior of the binding energy as a function of the overall enthalpy of reaction. Thus, reactions 4 and 8 which have the lowest overall activation energy also have the most strongly bound complexes, whereas reactions 1 and 5 have the highest overall activation energies and have the weakest binding strength.

This dissection of the overall activation energy provides insight to help understand the origin of the contrathermodynamic behavior. However, it is not immediately apparent why the binding strength of the ROOH + R'· complex should be correlated to the overall enthalpy of reaction. One explanation is that the more exothermic reactions involve hydrocarbon species which have fewer groups substituted in the neighborhood of the radical (*i.e.*, a less stable radical); this in turn translates to a more weakly bound complex since there are fewer groups to form attractive interactions with the other species. While the detailed reaction coordinate has been mapped and its behavior is understood, the overall reaction is the most relevant for kinetic modeling given that the complexes do not play an important role in the dynamic behavior. Therefore, a reliable estimate of the activation energy as a function of the enthalpy of reaction for bimolecular hydrogen transfer of alkylperoxy radicals is that shown as equation 6.2.

It is important to understand the nature of equation 6.2 in the context of a more general understanding of radical reactivity. Donahue and coworkers (Donahue et al., 1998) have shown that for a wide range of radicals and substrates, the enthalpy of reaction is not a general predictor for chemical reactivity. We used a zero-order ionic curve crossing model to study the reactions shown

in Figure 6.1 and found that the curve crossing height was positively correlated to the overall activation energy, consistent with the findings of Donahue and coworkers. While models such as the ionic curve crossing model (Donahue et al., 1998) are very insightful for understanding reactivity trends, they are not easy to implement practically in complex kinetic models. Therefore, structure-reactivity relationships relating the activation energy to a quantity that is easy to obtain, *e.g.*, the heat of reaction, such as the one we have determined here as given in equation 6.2 still have tremendous practical value. An alternate scheme for estimating chemical reactivity could be found in recent reports by Sumathi et al. (2001a,b, 2002), Sabbe et al. (2005) and Saeys et al. (2004) who have developed approximate group additivity schemes that, in principle, allow for reliable estimation of E_A without parameters that are specific to radicals or substrates. However, widespread use of these models awaits development of large libraries/databases that are populated with specific groups for different reaction classes and transition states.

6.4 Conclusions

We have completed a detailed investigation of the reaction family $ROO\cdot + R'H \rightarrow ROOH + R'\cdot$ where $R'H$ are various substituted alkanes. The thermodynamic and kinetic properties of these reactions were determined using the hybrid model chemistry CBS-QB3 in conjunction with a rigorous treatment for internal rotation and including the effects of quantum tunneling. Based on the results presented here, the following conclusions can be drawn:

1. In surprising contrast to other reported studies of tunneling in bimolecular hydrogen transfer (Gonzalez-Lafont et al., 1991; Truong et al., 1999), tunneling does not play an important role

at low to moderate temperatures, and the transmission coefficient is very well approximated using the Wigner correction.

2. For the reactions considered here, loosely-bound complexes were detected. However, they are higher in free energy than the isolated reactants, and thus, their presence does not significantly alter the dynamics of the reaction.

3. The loosely-bound complexes $ROOH \cdots R'\cdot$ are less strongly bound as the overall enthalpy of reaction $ROOH + R'\cdot \rightarrow ROO\cdot + R'H$ becomes more exothermic.

4. The relationship between the binding energy of the loosely-bound complexes and the overall heat of reaction has a profound effect on the structure-reactivity relationship for the overall reaction and leads to the presence of contrathermodynamic behavior.

The results from this chapter are summarized by the structure-reactivity relationship given in equation 6.2. These results not only provide further evidence that quantum chemistry and transition state theory are useful tools for quantitative estimates of the reaction rate coefficient, but also give further insight into the nature of hydrogen transfer reactions in general.

Chapter 7

Mechanistic Modeling of Lubricant Degradation Part 1: Structure-Reactivity Relationships for Free-Radical Oxidation

7.1 Introduction

Lubricant degradation is a complicated free-radical process in which hundreds, or even possibly thousands, of species undergo simultaneous reactions. Degradation reduces lubricant functionality, decreases part lifetime and contributes to mechanical failure of moving parts (Blaine and Savage, 1991b). Understanding of the degradation of even the most simple model lubricants is still incomplete. This is in spite of the fact that improved attention to friction and wear could, by some estimates, save the US economy over $100 billion annually (Krim, 2002). Our current limited

understanding of lubricant degradation and the enormous cost-saving potential suggest that further studies of degradation would be valuable.

There have been a number of literature studies of lubricant degradation (Blaine and Savage, 1991a,b, 1992; Bowman and Stachowiak, 1996; Chen and Hsu, 2003; Feng and Karasek, 2000; Gunsel et al., 1988; Hunter et al., 1993; Jensen et al., 1981; Koh and Butt, 1995; Naidu et al., 1986; Nakanishi and Onodera, 1996; Natarajan et al., 2000; Stellman et al., 1999) that have aimed to develop a fundamental understanding of the underlying chemistry. The majority of these have focused on experimental investigation of the major product classes from a model lubricant. Some of these studies have even included development of a kinetic model at the pathways level, which used lumped species and kinetic parameters (Blaine and Savage, 1992; Chen and Hsu, 2003; Naidu et al., 1986; Natarajan et al., 2000). Models of chemical degradation of lubricants generally fall into two broad categories. The quantitative description of lubricant degradation is dominated by models of "model compounds". Because lubricants are a complex blend of many compounds (Pirro and Wessol, 2001; Rudnick and Shubkin, 1999), it is generally assumed that models focusing on a single, simpler compound will facilitate extraction of useful information. The focus of these models is to increase the knowledge of the fundamental chemistry of lubricant degradation (Koh and Butt, 1995; Naidu et al., 1986; Natarajan et al., 2000; Pickard and Jones, 1996; Stellman et al., 1999; Wang and Feng, 1997). Conversely, some researchers integrate, to varying degrees, the complexity of real systems in their studies of degradation. These works vary in complexity from simulating the catalytic effect of metal surfaces to building highly elaborate reactor models which capture the flow and temperature profile seen by a real lubricant (Bowman and Stachowiak, 1996;

Chen and Hsu, 2003; Feng and Karasek, 2000; Makowska et al., 2002). In either category, however, pathways-level models which govern the transformation of functional groups in a lubricant are formulated, and then lumped kinetic parameters are fit through regression.

Blaine and Savage (1991a,b, 1992) reported the most sophisticated degradation model available in the literature. The authors proposed a pathways-level model which describes the transformation of *n*-hexadecane to its stable degradation products. Lumped kinetic rate coefficients were used, and the parameters were regressed against experimental data collected by the authors. While the model correctly captured the order of appearance and order of magnitude of the yields of most of the degradation products, it did not agree qualitatively with many of the observed trends in the experimental data such as the induction time. Furthermore, since it was formulated at the pathways level, it inherently lacks predictive capability. The work of Chen and Hsu (2003) offers another demonstration of good qualitative agreement between lubricant tests typically carried out in industry, *e.g.*, bench engine testing, and a reactor model that captures engine operating conditions well.

These models have provided insight into the controlling reaction pathways but still can be improved upon. An ideal description of lubricant degradation is a chemical kinetics model which quantitatively describes the distribution and amount of degradation products but also is predictive, *i.e.*, applicable beyond the range of conditions for which it was specifically developed. Pathways-level models have limited extrapolation potential. The alternative is to formulate mechanistic models. A mechanistic model is defined as one comprised of elementary reaction steps which obey the law of microscopic reversibility and whose rate may be expressed by elementary rate laws. Key

results obtained from mechanistic models include identification of dominant reaction pathways and important intermediates. However, mechanistic models of lubricant degradation have not been developed to date. One chief reason for this is that the enormous complexity of lubricant degradation makes it prohibitive to assemble a mechanistic model by hand. Substantial progress using automated network generation techniques has been made for other chemistries including Fischer-Tropsch synthesis, atmospheric chemistry, pyrolysis and silicon nanoparticle formation (De Witt et al., 2000; Khan, 2005; Klinke and Broadbelt, 1999a; Wong et al., 2004a). The principles of automated network generation have yet to be applied to condensed-phase hydrocarbon oxidation.

A second challenge in developing mechanistic models is to specify rate constants for every elementary step in the mechanism (Broadbelt and Pfaendtner, 2005). The preferred source of kinetic parameters is from reliable experimental measurements. For the specific case of free-radical oxidation there are a number of comprehensive compilations available (Denisov, 1974; Howard and Scaiano, 1997; NIST, 2006) as well as the long-running series of papers by Howard and coworkers[a]. However, using these data for kinetic modeling of lubricant degradation is difficult since 1) model compounds, *i.e.*, small substrates or radicals, are often used, 2) much of the data collected has been for aromatic-containing compounds, or 3) the data reported are only for one or two different temperatures. An elementary-step reaction network of the degradation of a model lubricant will require $O(10^4)$ rate coefficients, and much less than 1% of these values is currently available from experimental measurements.

[a] The series of papers entitled "Absolute rate constants for hydrocarbon autoxidation" has been published since 1965. The reader is referred to Chemical Abstracts for further information.

Given that we cannot determine the requisite kinetic data from experiment alone, rate coefficients of individual reactions must be estimated using other approaches such as structure-reactivity relationships, where a kinetic parameter is related to a property that is easier to estimate. One of the most prominent structure-reactivity relationships is the Evans-Polanyí (Evans and Polanyí, 1938) relationship:

$$E_A = E_A^o + \alpha \Delta H_{rxn} \tag{7.1}$$

where the parameters E_A^o and α are constant for all reactions in the same reaction family or reaction class. Additionally, Blowers and Masel (1999, 2000) extended the Marcus equation (Cohen and Marcus, 1968) to give a general correlation for atom transfer reactions of any exo/endothermicity:

$$E_A = \begin{cases} 0 & \text{for } \Delta H_{rxn}/4E_A^o < -1 \\ E_A^o \left(1 + \Delta H_{rxn}/4E_A^o\right)^2 & \text{for } -1 \leq \Delta H_{rxn}/4E_A^o \leq 1 \\ \Delta H_{rxn} & \text{for } \Delta H_{rxn}/4E_A^o > 1 \end{cases} \tag{7.2}$$

For atom transfer reactions, recommended values for the transfer coefficient, α, and the intrinsic reaction barrier, E_A^o, have been published for different ranges of the enthalpy of reaction (Blowers and Masel, 2000). While the general forms of the structure-reactivity relationships given in equations 7.1 and 7.2 have been used for free-radical chemistry, their application to oxidative lubricant degradation has not been tested, and the specific parameters governing the majority of the reaction families comprising hydrocarbon oxidation chemistry are not available. The development of structure-reactivity relationships requires that rate parameters are available for at least a small set of members of a particular reaction family. When experimental data is lacking, theoretical esti-

mates of structure-reactivitity relationships can be obtained from quantum chemistry and transition state theory (Pfaendtner and Broadbelt, 2007a,b; Pfaendtner et al., 2006c).

However, it is important to be aware that some structure-reactivity relationships are only valid for limited subsets of a reaction family, *e.g.*, a homologous series of alkanes undergoing hydrogen abstraction, and that reaction "sub-reaction families" may be required to accurately capture reactivity trends. Donahue et al. (1998) have discussed this and point out that there is an ongoing question as to whether thermodynamic observables of chemical reactions, *i.e.*, the enthalpy of reaction, are indeed predictors of reactivity or if they merely correlate with reactivity. Accordingly, it is imperative to appropriately select the reactions from which to define a particular structure-reactivity relationship. Details of the approach we adopted to select the reactions for reaction families comprising oxidation chemistry are given in Section 7.2.

This chapter is devoted to the development of a library of kinetic correlations for the relevant free-radical chemistry in lubricant degradation. This is the first step in developing complex reaction networks that govern lubricant degradation and hydrocarbon oxidation. We have summarized available experimental data and augmented this with new theoretical estimates where sufficient data is not available. For key reaction families, we have also sought to compare our new relationships with structure-reactivity relationships that have been used previously for the same or related reaction families such as the Blowers-Masel correlation (Blowers and Masel, 1999). Specifically, we address the following issues:

1. For each of the three major classes of steps in free-radical oxidation (initiation, propagation, and termination), what are the key elementary-step reaction families that are relevant at low to moderate temperatures?

2. What are the governing structure-reactivity relationships for all reaction families in free-radical oxidation?

3. How do previously reported structure-reactivity relationships for other systems, *e.g.* pyrolysis, compare to analogous relationships for oxidation?

This chapter is organized into three sections. First, we describe our theoretical approach for estimating enthalpies of reaction and activation energies and elucidating structure-reactivity relationships. Next, we identify all of the relevant reaction families for free-radical oxidation and summarize relevant experimental data, previous theoretical calculations and new calculations performed in this work. Several of these relationships are then compared to structure-reactivity relationships that have been previously reported in the research literature. Finally, we discuss this data set in the context of its use in kinetic modeling.

7.2 Computational and Theoretical Details

All molecular orbital (MO) and density functional theory (DFT) calculations were completed using the Gaussian 03 (Frisch et al., 2003) software package. Transition states were identified as first-order saddle points on the potential energy surface. The quadratic synchronous transit method (Peng and Schlegel, 1993) was used to help locate many of the transition states. All transition

states were verified by obtaining the true reactant(s)/product(s) using intrinsic reaction coordinate following (Gonzalez and Schlegel, 1989). The chief computational method employed in this work was the hybrid model chemistry CBS-QB3 (Montgomery et al., 1999). CBS-QB3 relies on geometry optimization and frequency calculation using DFT and Becke's (Becke, 1993) three-parame-ter hybrid functional, B3LYP, in conjunction with the 6-311G(2d,d,p) basis set. This basis set is represented as an extension of the Pople formalism by adding an additional 2d polarization function to third row atoms (Montgomery et al., 1999). CBS-QB3 seeks to extrapolate the QCSID(T) energy using an infinite basis set and is well known to provide highly accurate estimates of thermochemical properties (Montgomery et al., 1999) and kinetic data (Ess and Houk, 2005; Henry and Radom, 2001; Pfaendtner and Broadbelt, 2007b; Pfaendtner et al., 2006c; Wijaya et al., 2003). According to the recommendation of Montgomery and coworkers, all vibrational frequencies within the CBS-QB3 calculation were scaled by 0.99. The calculations reported here are for the gas phase in the high pressure limit. However, we have recently reported that for inter- and intramolecular hydrogen transfer involving alkylperoxy radicals and hydrocarbon substrates, the presence of a nonpolar, low-dielectric solvent field does not significantly alter kinetic or thermodynamic properties calculated using quantum chemistry (Pfaendtner and Broadbelt, 2007a,b; Pfaendtner et al., 2006c). Additional calculations utilized B3LYP/6-31G(d).

Using the optimized geometry and frequencies obtained from a Hessian calculation, the total microcanonical partition function can be calculated for each molecule within the rigid-rotor harmonic oscillator (HO) assumption. It is known that the HO approximation incorrectly treats low-frequency torsional modes as harmonic oscillators (Pitzer and Gwinn, 1942). However, it has

recently been shown that the internal rotation correction has a very minor effect on the activation energy, even for molecules with many dihedrals (Pfaendtner and Broadbelt, 2007a; Van Cauter et al., 2006). Additionally, low-frequency vibrational modes contribute little to the vibrational contribution to the internal energy. Thus, the contribution of anharmonicity from hindered rotors can be neglected for studies in which the activation energy and enthalpy of reaction are the only properties desired. Once the partition function is known as a function of temperature, the rate constant as a function of temperature was calculated using the standard expression,

$$k_{TST} = c_o^{1-n} * \kappa\left(T\right) \frac{k_b T}{h} \frac{Q^{\ddagger}(T)}{Q^r(T)} \exp\left(-E_o/RT\right) \tag{7.3}$$

where c_o is the concentration in the standard state to which the thermodynamic parameters are referred, *i.e.*, P/RT, n is the molecularity of the reaction, $Q^{\ddagger}$ and Q^r are the total partition functions for the TS and reactants, respectively, and E_o is the reaction barrier, *i.e.*, the zero-point corrected difference between the ground-state electronic energies of the TS and the reactants. Once the temperature dependent partition functions were known, rate constants as a function of temperature were calculated, and the Arrhenius parameters A and E_A were obtained from a straight-line fit of $\ln k$ vs $1/T$. Unless otherwise stated, we used a temperature range of 300-1500 K for regression of A and E_A. To calculate the enthalpy of reaction, all thermodynamic parameters were obtained from ensemble energy averages <E> using standard formulae (McQuarrie and Simon, 1999). The enthalpy of reaction is obtained from quantum chemistry results by simply taking the difference in enthalpy between the reactants and products where the enthalpy of each species is obtained

by summing the respective electronic, zero-point, rotational, translational, vibrational and thermal contributions:

$$H = \epsilon_e + E_{ZPE} + E_{rot} + E_{trans} + E_{vib} + RT \tag{7.4}$$

Additionally, for some systems under consideration in this work, experimentally determined rate coefficients were available but experimental measurements of the enthalpy of reaction were unavailable. In these cases we either used the CBS-QB3 method in conjunction with equation 7.4 to calculate the enthalpy of reaction or we estimated the enthalpy of reaction using group additivity (Benson, 1976) and the NIST Structures and Properties (Stein et al., 1991) database.

For the reaction families we studied using quantum chemistry, we sought to survey the broadest landscape of heats of reaction and thereby widen the applicability of the structure-reactivity relationships. The substitution of carbon atoms adjacent to the reactive moiety/moieties was systematically varied by 1) specifying a prototypical reaction of a given reaction family and 2) increasing the complexity of the prototypical reaction by altering the substitution of the reactant(s). Truong and coworkers recommend defining the prototype for a reaction class to be the simplest reaction possible that preserves the changes in structure and electron configuration (Truong et al., 1999). This definition is merely a guideline and not absolute, but it is true to the localized nature of free-radical reactions. It is important to remember that the thermodynamic properties of charged species are affected by long-range effects (Masel, 2002). Therefore, the types of reactions selected for study may be different for reactions involving ions.

7.3 Key Reaction Families in Hydrocarbon Oxidation

This section summarizes experimental and theoretical results that have been previously reported and also details new calculations we have performed. We follow typical designations within free-radical chemistry and divide our discussion based on reaction families that fall into the broad category of initiation, propagation or termination. A prototypical reaction for each of the reactions families discussed is given in Figure 7.1. Since condensed-phase hydrocarbon autoxidation and the fundamental chemistry underlying lubricant degradation have been discussed in great detail elsewhere (Blaine and Savage, 1992; Denisov, 1974; Denisov and Denisova, 2000; Emanuel et al., 1967; Pirro and Wessol, 2001), we restrict subsequent discussion to the description and development of structure-reactivity relationships which will be used for kinetic modeling in part 2 of this work. The structure-reactivity relationships developed here follow the form given in equation 7.1 and will be discussed in terms of the intrinsic reaction barrier, E_A^o, and the transfer coefficient, α. To maintain thermodynamic consistency, we constrain the sum of two transfer coefficients for forward/reverse, or exothermic/endothermic, pairs to be equal to one, *i.e.*, $\alpha_{fwd} + \alpha_{rev} = 1$, and the intrinsic barriers for the forward/reverse or exothermic/endothermic pairs to satisfy the relationship $E_{o,fwd} = E_{o,rev} - \Delta nRT$, where Δn is the difference between the number of products and the number of reactants. This enthalpic consistency is clarified by examining the relationship $E_A = \Delta H^{\ddagger} + nRT$ from transition state theory, where n is the molecularity of the reaction. When manipulated algebraically, this equation reveals that for forward and reverse reaction pairs of reactions, the sum of the transfer coefficients is equal to 1, and the intrinsic barriers are related by the equation above. It is important to note that in the kinetic modeling performed in Chapter 8,

Reaction Family	Prototypical Reaction
Initiation Reactions	
Primary initiation	$RH + O_2 \rightarrow R\cdot + HOO\cdot$
Bond fission	$ROOH \rightarrow RO\cdot + HO\cdot$
Hydroperoxide decomposition	$RH + R'OOH \rightarrow R\cdot + R'O\cdot + H_2O$
Propagation Reactions	
Oxygen addition	$R\cdot + O_2 \rightarrow ROO\cdot$
Hydrogen shift	$HROO\cdot \rightarrow \cdot ROOH$
Alkoxy β-Scission	$RO\cdot \rightarrow R'C(O)H + R''\cdot$
β-Scission	$\cdot ROOH \rightarrow RO + \cdot OH$
Hydrogen transfer	$ROO\cdot + R'H \rightarrow ROOH + R'\cdot$
Termination Reactions	
Disproportionation	$2\,ROO\cdot \rightarrow RO + ROH + O_2$
Recombination	$2\,R\cdot \rightarrow RR$

Figure 7.1: Reaction families and prototypical reactions for lubricant degradation.

thermodynamic consistency was rigorously enforced by specifying a forward rate coefficient from experiment or a kinetic correlation and calculating the reverse rate coefficient from the Gibbs free energy of reaction, and thus the equilibrium constant. The forward direction was selected as the one that was deemed to have the more reliable information.

7.3.1 Initiation

Free-radical oxidation begins when primary initiation reactions occur between the substrate and oxygen. This is known as a "primary" initiation step since this is the first reaction in which radicals are created. Other initiation steps in which a molecule or molecules are consumed to form radicals

are bond fission of hydroperoxides and peroxide decomposition, shown in Figure 7.1. Primary initiation proceeds more slowly than the secondary initiation steps but is clearly critical due to its role in generating the first radical species.

7.3.1.1 Primary initiation

To develop a structure-reactivity relationship for primary initiation, we drew on limited experimental and theoretical reports given in the literature (Denisov and Denisova, 2000; O'Connor et al., 2002). O'Connor et al. (2002) used DFT to study the primary initiation reaction of O_2 and cyclohexane and reported a pre-exponential factor of 2.9 x 10^{19} L/mol-s and an activation energy of 54.1 kcal mol^{-1}, equal to the heat of reaction. Denisov and Denisova (2000) summarized many experimental reaction rate coefficients for primary initiation. Their data follow the general trend that the activation energy is equal to the heat of reaction and the range of pre-exponential factors they provide is 10^6-10^{18} L/mol-s, depending on the solvent system. The pre-exponential factor given by O'Connor and coworkers is abnormally high and to our knowledge is one of the largest bimolecular pre-exponential factors reported from a DFT calculation. Using all of this information, we recommend the following kinetic correlation for primary initiation in lubricant degradation: A = 10^{13} L/mol-s, E_A^o = 0, and α = 1. Thus, the activation energy for the initiation step is equal to the heat of reaction whereas the reverse reaction is unactivated, which is consistent with literature values (O'Connor et al., 2002). This correlation is the first entry in Table 7.1, which constitutes the database of kinetic correlations for lubricant degradation.

Table 7.1: Library of structure-reactivity relationships for use in low-temperature oxidation and lubricant degradation. The data provided are the intrinsic reaction barrier, E_A^o (kcal mol^{-1}), transfer coefficient for the forward direction, α_{fwd}, and pre-exponential factor, A, (in L/mol-s or 1/s).

reaction family	E_A^o	α_{fwd}	A
primary initiation	0	1	10^{13}
bond fission of hydroperoxides	0	1	10^{15}
hydroperoxide decomposition	24.6	−0.09	10^{6}
oxygen addition	0	0	10^{8}
1,3 hydrogen shift of peroxy radicals	35.0	1	10^{11}
β-scission of alkoxy radicals	9.5	0.85	10^{14}
β-scission of carbon-centered radicals	14.24	0.76	10^{14}
hydrogen transfer			10^{7}
alkyl radicals + alkanes [a,b]	17.8	0.83	
alkoxy radicals + alkanes [a]	11.9	0.91	
alkylperoxy radicals + alkanes [c]	2.4	1.17	
alkylperoxy radicals + aldehydes [d]	6.2	1	
alkylperoxy radicals + alkylhydroperoxides [b,d,e]	30.2	0.59	
alkylperoxy radicals + alkylhydroperoxides [d,f]	2.4	1.17	
hydrogen abstraction from ketones [g,h]	9.1	0.7	10^{5}
other hydrogen transfer reactions [h]	9.1	0.7	10^{7}
disproportionation of peroxy radicals	0	0	10^{6}
radical recombination	0	0	10^{8}

[a] The "forward" reactions are defined in Table 7.4 and are the exothermic reactions shown in Figure 7.6.

[b] Structure-reactivity relationship provided for informational use only and not used in Chapter 8 in development of models of lubricant degradation. The "alkyl radicals + alkanes" correlation is appropriate for methyl radicals only.

[c] This data is taken from Pfaendtner and Broadbelt (2007b). The α value is for endothermic reactions: ROO· + R'H → ROOH + R'·.

[d] The "forward" reactions are defined in Table 7.4 and are the endothermic reactions shown in Figure 7.6.

[e] This structure-reactivity relationship was calculated using only CBS-QB3 results and is based on reactions which automatically yield the β-scission products.

[f] This structure-reactivity relationship was calculated using the CBS-QB3 activation energies but estimating the heats of reaction for the individual hydrogen transfer component of the overall reaction using group additivity.

[g] This relationship is applicable for abstraction of hydrogens adjacent to the carbonyl group in ketones.

[h] E_A^o and α value taken from Blowers and Masel (2000). The α value given is for endothermic reactions.

7.3.1.2 Secondary initiation

Secondary initiation steps involve at minimum a first rank, *i.e.*, the first generation of stable molecular products produced from the substrate, or higher rank species and cause the formation of radicals from unimolecular or bimolecular reactions of molecules. The bond fission reaction shown in Figure 7.1 is a common secondary initiation step in which a hydroperoxide species decomposes to form hydroxyl and alkoxy radicals. Analogous to primary initiation, the activation energy for the bond fission reaction is equal to the heat of reaction owing to the fact that the reverse reaction, radical-radical recombination, proceeds without activation. Based on similar reactions from other oxidation systems, various Arrhenius pre-exponential factors have been reported, ranging from 10^{14}-10^{17} 1/s (Khan, 2005). We have constructed a general structure-reactivity relationship for bond fission: A = 10^{15} 1/s, $E_A^o = 0$, and $\alpha = 1$.

It has been observed that in the condensed phase, bond fission tends to proceed much more slowly than the other secondary initiation reaction, hydroperoxide decomposition (Emanuel et al., 1967; Emanuel and Gál, 1986). This can be understood by considering that collisions between a hydroperoxide species and the substrate (RH) in the condensed phase promote cleavage of the O-OH moiety compared to the unimolecular bond fission step. This reaction class is difficult to study both experimentally and theoretically, and there are very few reported rate coefficients from which to abstract a new structure-reactivity relationship. We found no reported theoretical investigations and our own efforts in locating a transition state for a representative hydroperoxide decomposition reaction were not successful. Table 7.2 summarizes the six experimental rate coefficients we found in the literature for this reaction family. The data are for reactions involving decane, ethylbenzene

Table 7.2: Rate coefficients (L/mol-s), enthalpies of reaction (kcal mol^{-1}) and activation energies (kcal mol^{-1}) for the hydroperoxide decomposition reaction family used in the regression of a new structure-reactivity relationship. Unless noted the data were obtained from Denisov (1974) and are measured with chlorobenzene as the solvent. The enthalpies of reaction were calculated using group additivity and the activation energies were obtained using the experimental rate coefficients and assuming a pre-exponential factor of 10^6 L/mol-s.

hydroperoxide	substrate	T ^{o}C	-log k	ΔH_{rxn}	E_A
sec-$C_{10}H_{21}OOH$	n-$C_{10}H_{22}$	130	6.22	23.74	22.53
sec-$C_{10}H_{21}OOH$	iso-$C_{10}H_{22}$	130	6.38	21.68	22.83
sec-$C_{10}H_{21}OOH$	$C_6H_5C_2H_5$	130	6.61	10.59	23.25
$C_6H_5CH(OOH)CH_3$[a,b]	$C_6H_5C_2H_5$	120	7.26	6.98	23.85
$C_6H_5C(CH_3)_2OOH$	$C_6H_5CH(CH_3)_2$	130	7.58	−5.61	25.04
$C_6H_5C(CH_3)_2OOH$[b]	$C_6H_5CH(CH_3)_2$	130	7.78	−5.61	25.41

[a]Data obtained by regression of this rate coefficient for mechanistic model of ethylbenzene oxidation (unpublished results).

[b]No additional solvent used for this reaction system. The substrate is the solvent.

and cumene that were either carried out neat or in a solvent. Since the data are for a limited temperature range (120-130 ^{o}C), we assumed a representative pre-exponential factor for bimolecular reactions in the liquid phase of 10^6 L/mol-s for this reaction class. Using the rate coefficients in Table 7.2, the representative A value, and enthalpies of reaction estimated using group additivity, the activation energies were calculated and correlated against ΔH_{rxn}. The E_A and ΔH_{rxn} values are summarized in Table 7.2, and the data are plotted in Figure 7.2. The data follow a clear trend, and the Evans-Polanyí relationship fit the data well with an R^2 value of 0.96, E_A^o = 24.6 kcal mol^{-1} and α = -0.09. The correlation for this reaction family is summarized in Table 7.1 and represents the first structure-reactivity relationship provided in the literature for hydroperoxide decomposition. There are several salient features of this new correlation that merit further discussion.

First, although it is typical that the forward and reverse transfer coefficients and intrinsic barriers discussed in section 7.3 correspond distinctly to endothermic and exothermic regimes, respec-

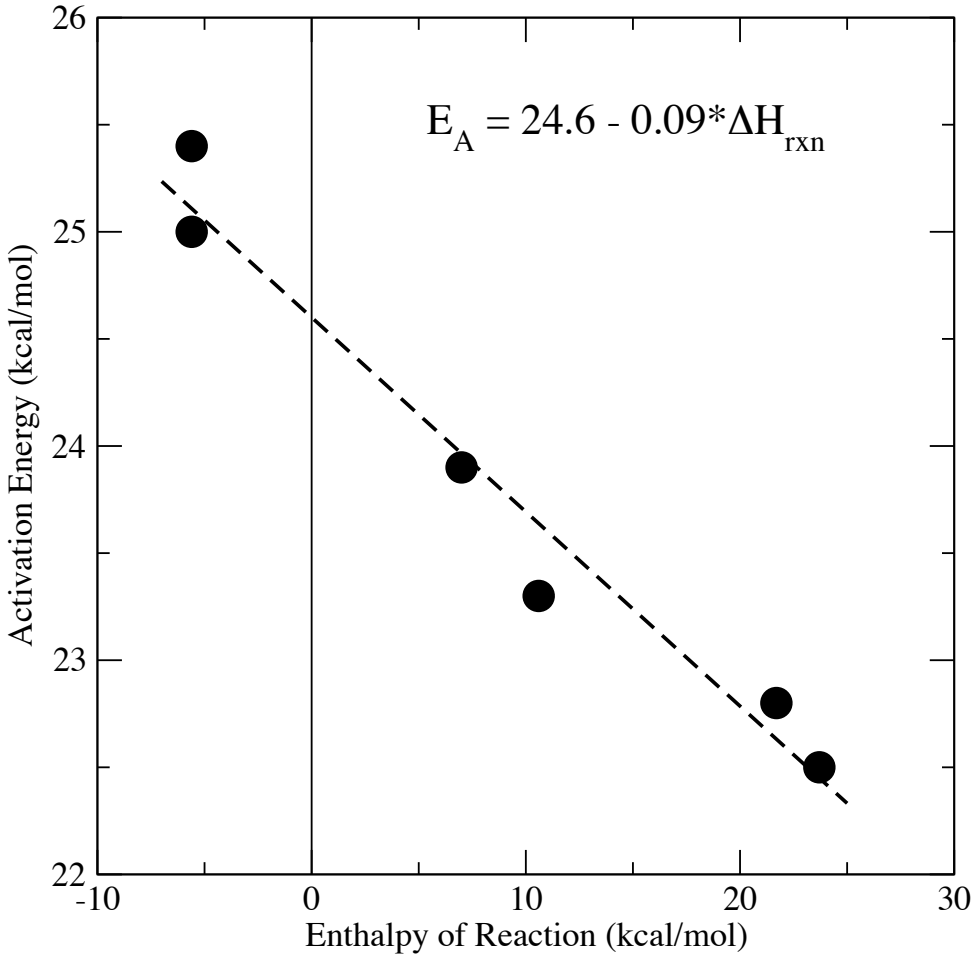

Figure 7.2: Structure-reactivity relationship for the hydroperoxide decomposition reaction family shown in Figure 7.1. The activation energies were calculated based on the data in Table 7.2 and assuming an overall pre-exponential factor of 10^6 L/mol-s. The correlation developed for this reaction family is given in the figure in units of kcal mol^{-1}.

tively, (or vice versa), this reaction family atypically has members in the forward direction with both exothermic and endothermic values. Thus, it is appropriate to regress all the data using a single slope and intercept. While another important reaction family, hydrogen transfer, has members with both exothermic and exothermic heats of reaction, hydrogen transfer is its own reverse reaction, so it is appropriate to regress the exothermic and endothermic regimes separately with thermodynamic constraints imposed. While in theory the structure-reactivity relationship could be used to specify E_A for the reverse of hydroperoxide decomposition, we do not recommend any representative A value because in practice we excluded the possibility of the reverse reaction of hydroperoxide decomposition given the extremely low probability of a trimolecular collision of water, alkoxy radical, and alkyl radical and the fact that alkyl radicals have an extremely short lifetime and low concentration due to the ease with which oxygen adds to carbon-centered radicals in free-radical oxidation. Furthermore, given the limited knowledge that exists about peroxide decomposition, it is possible that it is not an elementary step and proceeds through one or more intermediate species. However, this reaction class is clearly important in free-radical oxidation in the condensed phase (Emanuel et al., 1967; Emanuel and Gál, 1986), and the structure-reactivity relationship summarized in Table 7.1 is serviceable.

Finally, it is interesting to note that there is a slight, but clearly distinct, overall contrathermodynamic behavior exhibited by the data in Figure 7.2. That is, the activation energy is seen to *decrease* with *increasing* endothermicity. This behavior was also observed in radical addition to alkynes (Gomez-Balderas et al., 2003), theoretical and experimental studies of hindered-phenol antioxidants (Pfaendtner and Broadbelt, 2007a), and also hydrogen transfer between alkylperoxy

radicals and alkane substrates (Pfaendtner and Broadbelt, 2007b). In the case of bimolecular hydrogen transfer, it was shown that the contrathermodynamic behavior arose from the influence of loosely-bound intermediate states which exist on the potential energy surface as a precursor between isolated reactants and the transition state (Pfaendtner and Broadbelt, 2007b). Given that the reaction coordinate for the peroxide decomposition reaction family also involves interaction between the polar hydroperoxide moiety and the nonpolar alkane substrate, we hypothesize that intermolecular bonding may also be influencing this apparent overall structure-reactivity relationship.

7.3.2 Propagation

The next class of reactions shown in Figure 7.1 is propagation. Propagation reactions are typified by the consumption and production of at least one radical and may also consume and/or produce a stable molecular species. There are four main reaction families (two different β-scission reactions are shown for clarity) classified as propagation reactions in Figure 7.1 for which structure-reactivity relationships were developed as described here.

7.3.2.1 Oxygen addition

The first propagation reaction shown in Figure 7.1 is the oxygen addition reaction family. If the reacting system is under kinetic control, *i.e.*, no oxygen depletion from the condensed phase, then oxygen addition is assumed to proceed fast enough so that oxygen adds to any carbon-centered radical before it has time to continue to react via other channels. Most lubricant degradation

and oxidation experiments are performed under kinetic control to simplify interpretation of the kinetics and mechanism for a given system. The addition of molecular oxygen to carbon-centered radicals is very exothermic with heats of reaction ranging from -35 to -37 kcal mol^{-1} for typical reactions in lubricant degradation (Denisov and Denisova, 2000). The oxygen addition reaction appears to be unactivated for low-temperature condensed-phase oxidation and rate coefficients have been reported ranging from 10^7-10^9 L/mol-s (Denisov and Denisova, 2000). Because this reaction proceeds much faster than other reactions in the free-radical oxidation mechanism, the overall kinetics are not sensitive to this rate parameter as long as it is sufficiently high. Accordingly, we recommend a kinetic correlation for oxygen addition as follows: A=10^8 L/mol-s, $E_A^o = 0$ and $\alpha = 0$. The rate of oxygen addition is also clearly sensitive to the dissolved oxygen concentration in the condensed phase. Since this can be difficult to measure directly experimentally, rate laws for oxygen addition are often reported with a given oxygen partial pressure. The kinetic correlation given in Table 7.1 was formulated to require the concentration of oxygen in the condensed phase, which can be calculated easily given the assumption of kinetic control and based on O_2 solubility in hydrocarbons.

7.3.2.2 Hydrogen shift

The next reaction family involved in propagation is hydrogen shift. In free-radical oxidation, hydrogen shift reactions are typically written as a unimolecular transition from an alkylperoxy radical to an alkylhydroperoxide species. Hydrogen shift reactions are often classified with the designation "1,X hydrogen shift" where the term X refers to the number of bonds between the radical and the

atom being abstracted. The net result is a "shifting" of a hydrogen atom X spaces along the radical. The 1,3 hydrogen shift family could be an important reaction family in forming ketones given the instability of the $\cdot COOH$ radical (see discussion in section 7.3.2.4). Other hydrogen shift reactions are considered to be more important in the formation of secondary oxidation products (Jensen et al., 1981, 1992). We recently studied the 1,X hydrogen shift (for X = 3–7) reaction family involving alkylperoxy radicals using DFT in order to elucidate structure-reactivity relationships for kinetic modeling (Pfaendtner et al., 2006c). In building a model for lubricant degradation, the only hydrogen shift family we implemented was 1,3 hydrogen shift with the specific goal of determining its role in the formation of ketones. Based on our previous work (Pfaendtner et al., 2006c), the recommended structure-reactivity relationship for alkylperoxy radicals is: A=10^{11} L/mol-s, E_A^o = 35.0 kcal mol^{-1} and α = 1.0.

7.3.2.3 β-scission

The family of β-scission reactions represents an important route for the decomposition of alkoxy radicals in lubricant degradation and condensed-phase hydrocarbon oxidation. In β-scission of secondary or primary alkoxy radicals, one radical decomposes to form an aldehyde and one alkyl radical, as shown by the prototypical reaction in Figure 7.1. β-scission of tertiary alkoxy radicals leads to a ketone instead of an aldehyde. For these reactions, equilibrium strongly favors the forward direction. For example, we used CBS-QB3 to calculate the equilibrium constant for the β-scission of 3-pentoxyl radical and obtained a value for $K_c(400\ K)$ of 4.6 x 10^4 mol L^{-1}. Furthermore, the aldehydes produced in this reaction family have an acidic hydrogen that is read-

ily oxidized to form organic acids and esters. Experimentally, there are typically no aldehydes measured in condensed-phase oxidation of hydrocarbons or lubricants (Blaine and Savage, 1991a; Cullis et al., 1981; Garcia-Ochoa et al., 1989; Syroezhko et al., 1973). Based on this, the reverse reaction of β-scission, *i.e.* radical addition, is not considered to be an important reaction class in condensed-phase oxidation.

Méreau and coworkers used DFT (B3LYP/6-31G(d,p)) calculations to study structure-reactivity relationships for a series of alkoxy radicals undergoing β-scission (Méreau et al., 2000). A key finding of their work was that the structure-reactivity relationship depended strongly on the number of hydrogen atoms bonded to the carbon atom of the C-O· group. However, their work is based on a correlation between the enthalpy of reaction calculated from DFT and the activation energy approximated from DFT.[b] The enthalpies of reaction calculated from DFT and used in regression of their reported structure-reactivity relationship correlate very poorly with experimental enthalpies of reaction. We made a parity plot using the reported experimental and calculated enthalpies of reaction (Méreau et al., 2000). Perfect agreement is indicated by a slope of 1 and an intercept of 0. In contrast, the data had a slope of 0.55 and an intercept of 3.3 (kcal mol^{-1}). Given the error in the calculated enthalpies of reaction and the fact that our own kinetic models will rely on experimental or group additivity-based enthalpies of reaction, we created a new regression of their DFT activation energies using experimentally determined enthalpies of reaction. The data no

[b] Méreau and coworkers approximated the activation energy using the formula E_A=$\Delta H^{\ddagger} + RT$ where $\Delta H^{\ddagger}$ is the enthalpy of activation. This formula can be obtained by substituting k_{TST} in its thermodynamic form into the Arrhenius equation ($\frac{dlnk}{dT} = \frac{E_A}{RT^2}$), assuming the activation energy is not a function of temperature, and solving for the activation energy (Moore and Pearson, 1981).

longer followed the same trend, *i.e.*, they did not cluster according to the number of hydrogens on the carbon atom of the C-O· group.

Given the poor correlation between their theoretical activation energies and experimental enthalpies of reactions, we performed our own DFT (B3LYP/6-31G(d)) investigation of alkoxy β-scission of several radicals and sought a new correlation using both theoretical and experimental results. The reactions used to generate the new structure-reactivity relationship are given in Figure 7.3, and the specific values are summarized in Table 7.3. Combining the theoretical and experimental results produces a structure-reactivity relationship that follows the expected trend as shown in Figure 7.4. Given that the new correlation reproduces both experimentally and theoretically determined enthalpies of reaction and activation energies, we added it as an entry in the library of kinetic correlations in Table 7.1. Additionally, our theoretical calculations of the pre-exponential factor are in agreement with those reported from experiment, and we recommend a pre-exponential factor of 10^{14} 1/s.

There is an additional postulated β-scission step that plays an important role in lubricant degradation and free-radical oxidation (Emanuel and Gál, 1986). In alkylhydroperoxide species, abstraction of a hydrogen atom connected to the carbon atom of a COOH group yields a C·OOH moiety. This radical is highly unstable and yields the β-scission products, a ketone and hydroxyl radical, in a very exothermic reaction. In fact, the radical is so unstable that it was not possible for us to obtain a minimum energy structure using DFT calculations with the B3LYP functional. Geometry optimization of a species with a C·OOH moiety always yielded the β-scission products. However, to have a complete mechanistic understanding of lubricant degradation chemistry, we sought to

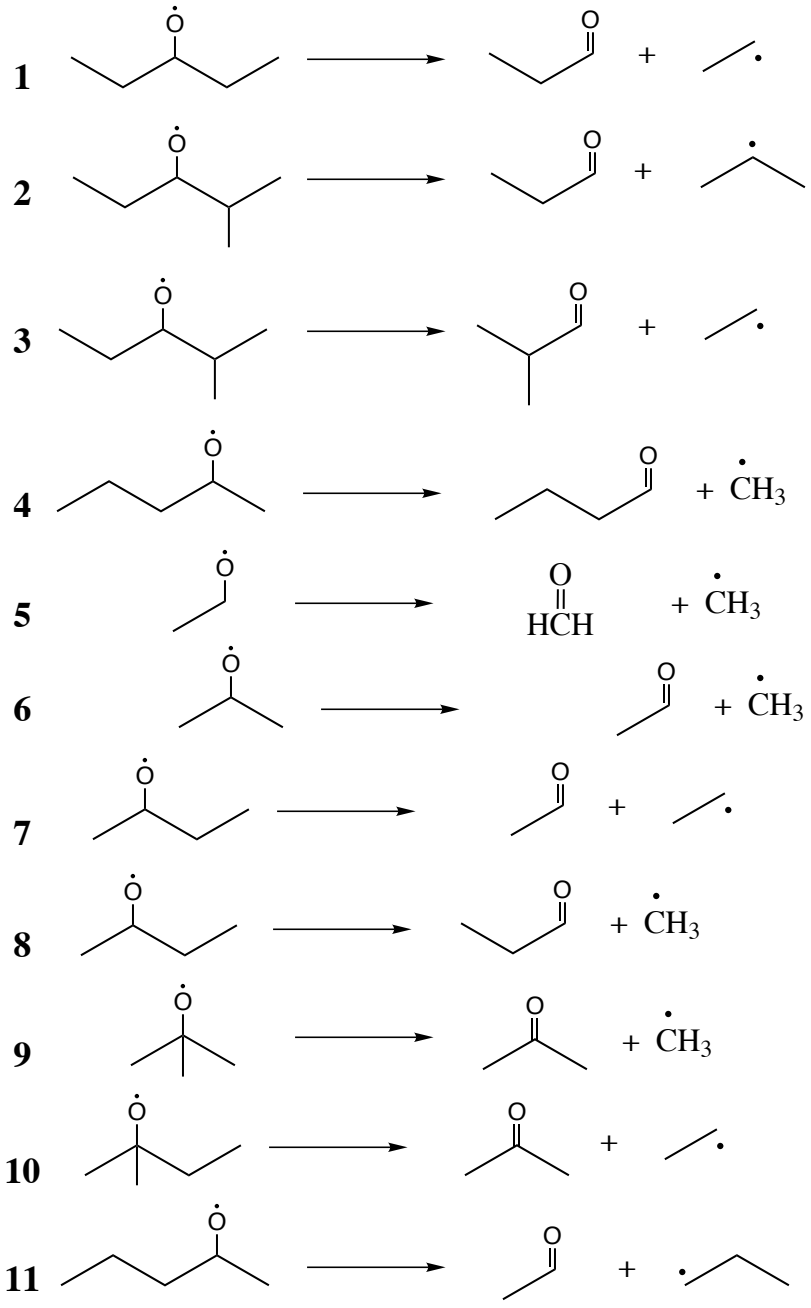

Figure 7.3: Reactions used to generate new structure-reactivity relationship for alkoxy β-scission reactions. The data for reactions 1-4 were calculated using DFT and the data for reactions 5-11 were obtained from experimental results reported by Méreau et al. (2000).

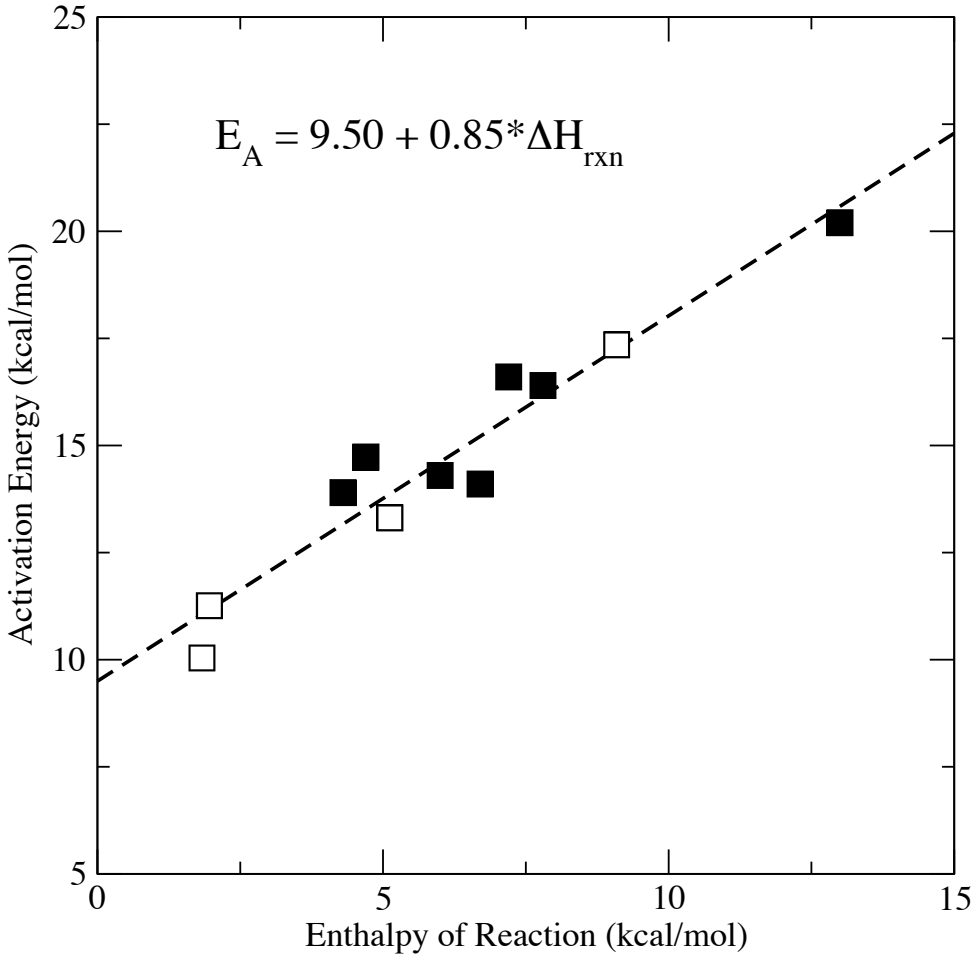

Figure 7.4: Structure-reactivity relationship for alkoxy β-scission reaction family shown in representative form in Figure 7.1 with specific reactions shown in Figure 7.3 and summarized in Table 7.3. All the data in the plot are for β-scission of alkoxy radicals, and the data were obtained from theory (open symbols) or experiment (filled symbols). The correlation coefficient (R^2) was 0.93. The correlation is given in the figure in units of kcal mol^{-1}.

Table 7.3: Kinetic and thermodynamic properties used to generate new structure-reactivity relationship for alkoxy β-scission. The data provided are ΔH_{rxn} (kcal mol^{-1}) and E_A (kcal mol^{-1}). Reactions 1–4 were calculated using DFT and reactions 5-11 were obtained from published experimental results (Méreau et al., 2000). A frequency factor of 10^{14} 1/s is recommended for use with this reaction family.

reaction	ΔH_{rxn}	E_A
1	1.96	11.26
2	1.83	10.04
3	5.12	13.31
4	9.09	17.35
5	13.00	20.20
6	7.80	16.40
7	6.00	14.30
8	7.20	16.60
9	4.70	14.73
10	4.30	13.90
11	6.70	14.10

include all possible elementary steps. For this additional β-scission reaction family we have employed a structure-reactivity relationship previously reported in the literature (Khan, 2005; Kruse et al., 2002) for carbon-centered radicals: A=10^{14} L/mol-s, E_A^o = 14.24 kcal mol^{-1} and α = 0.76. However, this class of β-scission reactions proceeds with heats of reaction ranging from -30 to -37 kcal mol^{-1} for reactions in lubricant degradation. The structure-reactivity relationship given above would predict a negative activation energy for these reactions. When an Evans-Polanyí correlation predicts a negative activation energy, the standard procedure is to assume the reaction is unactivated, *i.e.*, E_A = 0, which is done here and is consistent with the facility of these reactions.

7.3.2.4 Hydrogen transfer

The final propagation step in Figure 7.1 is hydrogen transfer. Hydrogen transfer reactions are extremely important in free-radical oxidation chemistry as they are the major consumption route

for the substrate. Additionally, this reaction family constitutes a majority of theoretically possible reactions in free-radical oxidation given the diversity of the radicals formed and the environments for abstractable hydrogens. As such, it is imperative to have high quality estimates for reactivity. A common strategy is to use the Evans-Polanyí or Blowers-Masel correlation to estimate activation energies for hydrogen transfer reactions and combine the estimated activation energy with a representative pre-exponential factor. We recently reported that reactions involving alkyl radicals and alkylhydroperoxides exhibited contrathermodynamic behavior when alkyl radicals abstracted the hydrogen from the -OOH moiety ($R\cdot + R'OOH \rightarrow RH + R'OO\cdot$) (Pfaendtner and Broadbelt, 2007b). Such behavior cannot be captured with the functional form of the structure-reactivity relationship given in equation 7.2. While usage of the Evans-Polanyí relationship required a transfer coefficient greater than one for alkylperoxy radicals abstracting hydrogen from alkanes, which is highly counterintuitive, the correlation nonetheless provides a practical summary of the kinetics of this reaction family. Of particular note was how different the parameters for this correlation were from the classic Evans-Polanyí relationship for alkyl radicals interacting with hydrocarbon substrates. While it is appealing to envision one general hydrogen abstraction correlation, our work clearly demonstrates that division into sub-families is warranted to achieve more accurate estimates of kinetic parameters. Although the Blowers-Masel correlation was put forth as a general relationship for all hydrogen transfer reactions, regression was carried out against a very large database of experimental activation energies spanning a range of 100 kcal mol^{-1} and enthalpies of reaction that ranged from -100 to +100 kcal mol^{-1}. The range of heats of reaction which is relevant for lubricant degradation is approximately -30 to +30 kcal mol $^{-1}$, which is precisely the

region in the Blowers and Masel data set that is heavily populated and has the highest deviation between the predicted and experimental values. Given our experience with alkylperoxy radicals and alkanes, we sought to examine hydrogen transfer reactions with a finer lens and generate new structure-reactivity relationships using quantum chemistry.

Specifically, we examined members of the following sub-families of hydrogen transfer:

1. alkyl radicals + alkanes
2. alkoxy radicals + alkanes
3. alkylperoxy radicals + aldehydes
4. alkylperoxy radicals + alkylhydroperoxides (abstraction of H-COOH)

26 different reactions (including forward/reverse pairs) were studied using CBS-QB3 and the methodology outlined in Section 7.2. The reactions investigated are listed in Table 7.4. Before developing new structure-reactivity relationships based on the CBS-QB3 calculations, we first verified that the enthalpies of reaction calculated using CBS-QB3 matched available experimental data. Figure 7.5 shows a parity plot of experimental and CBS-QB3 enthalpies of reaction for reactions 1-8 in Table 7.4 and reactions 1-4 from Table 3 in our previously reported (Pfaendtner and Broadbelt, 2007b) study of alkylperoxy radicals and alkanes. The agreement between CBS-QB3 and the experimental measurements is excellent as shown by the fact that the data all fall close to the line of parity. A best fit line of the data points gives a slope of 1.00, an intercept of 0.20 kcal mol^{-1} and an R^2 value of 0.99. The slight bias in the data indicates that CBS-QB3, in general, slightly over-predicts experimental enthalpies of reaction but the slope of 1.00 indicates that

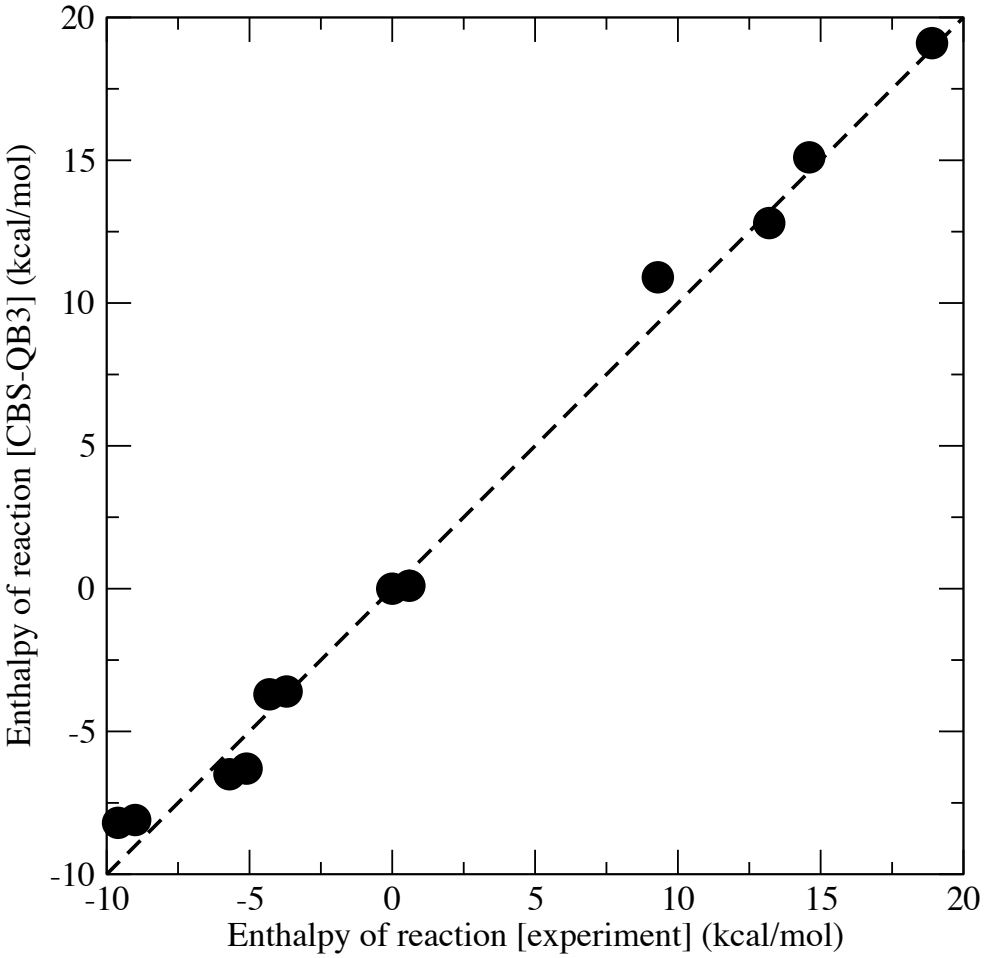

Figure 7.5: Parity plot showing the agreement between experimentally measured and CBS-QB3 calculated enthalpies of reaction for reactions 1-8 in Table 7.4 and reactions 1-4 in Table 3 of Pfaendtner and Broadbelt (2007b). The line of parity (dashed) is given for reference.

the error is distributed over both the endo- and exothermic regimes. This shows conclusively that structure-reactivity relationships generated based on CBS-QB3 calculations can be used equally well with experimental heats of reaction if they are available.

Using the properties calculated for the reactions in Table 7.4, we sought new structure-reactivity relationships for each of the individual sub-families. The activation energies are plotted against the enthalpies of reaction in Figure 7.6. A few experimental data points (reactions 2–8 in Table 7.4)

were obtained for comparison from the GRI (Smith et al., 2007) mechanism as shown by the filled squares and filled diamonds in Figure 7.6. Since we were interested in the low-temperature data only, we used the GRI rate coefficients for 300 K to 1500 K and re-optimized the activation energy and pre-exponential factor using the Arrhenius equation. For comparison, we have also included the data and new structure-reactivity relationship for alkylperoxy radicals and alkanes previously published by Pfaendtner and Broadbelt (2007b). The shaded region in the plot marks the space explored by Blowers and Masel (1999, 2000) in the development of their improved correlation (equation 7.2). As shown in the plot, there are clearly distinct structure-reactivity relationships for each of the sub-families we hypothesized.

Several interesting features of the data are particularly noteworthy. First, the data for "alkylperoxy radicals + alkylhydroperoxides" (open circles) are drastically different from the other hydrogen transfer reaction families. The main reason is that quantum chemistry calculations directly yield the β-scission products (as illustrated in Table 7.4), and the enthalpies of reaction given from CBS-QB3 are thus the enthalpy of reaction for the combined hydrogen abstraction/β-scission step. To explore this further, we calculated the enthalpy of reaction for the hydrogen transfer portion of these reactions using group additivity and re-optimized the structure-reactivity relationship using the CBS-QB3 activation energies and the estimated enthalpies of reaction. When the activation energies are plotted against the enthalpies of reaction for hydrogen transfer only (filled circles in Figure 7.6), a structure-reactivity relationship is obtained that is consistent with "alkylperoxy radicals + alkanes" (filled triangles). However, we elected to leave this as a separate structure-reactivity relationship in our model but initially use the same parameters as "alkylperoxy radicals + alkanes".

As will be shown in Chapter 8, this is an important component of obtaining the correct selectivity and yield of the ketone species. We also note that the data obtained for "alkyl radicals + alkanes" is in very good agreement with the experimental values available for this sub-family, but the data have an unusually high intrinsic barrier (17.8 kcal mol^{-1}). Therefore, it may not accurately reflect reactions of higher molecular weight alkyl radicals relevant to lubricant degradation. These data do add to our understanding of the diversity that is possible in hydrogen transfer reactions, and the correlation reported in Table 7.1 can be used for reactions of methyl radicals or methane explicitly. However, we did not use this correlation in the mechanistic modeling studies in Chapter 8. Rather, reactions of alkyl radicals with alkanes were lumped into "other hydrogen transfer reactions".

It is finally interesting to note that with the exception of "alkylperoxy radicals + alkylhydroperoxides" (open circles in Figure 7.6 which are for a combined hydrogen transfer/β-scission step) and two of the reactions in the "alkyl radicals + alkanes" sub-family, the data fall in the shaded region in Figure 7.6. This clearly illustrates that a structure-reactivity relationship can capture the general features of the relationship between activation energy and heat of reaction, but important details may be lost in the regression of a single parameter or set of parameters. The correlation given by Blowers and Masel for atom transfer reactions is an important tool for understanding reactivity trends in general. However, in the case of low-temperature oxidation the data clearly show that more refined structure-reactivity relationships are merited. Accordingly, we have delineated six separate sub-families for hydrogen transfer in the library of kinetic correlations in Table 7.1. Two of these are not used in the kinetic modeling in Chapter 8: (1) "alkyl radicals + alkanes" since this is valid for abstractions involving methyl radicals and alkanes or alkyl radicals and methane and (2)

"alkylperoxy radicals + alkylhydroperoxides" with E_A^o = 30.2 kcal mol^{-1} and α = 0.59, since this is for combined hydrogen transfer and β-scission. The remaining four that are used in Chapter 8 are the first four shown in bold in Table 7.1. We also recommend an average pre-exponential factor of 10^7 L/mol-s drawn from various experimental and theoretical studies (Denisov and Denisova, 2000; Howard and Scaiano, 1997; Pfaendtner and Broadbelt, 2007b). However, this value is known to vary several orders of magnitude, and values will be more precisely defined in the context of kinetic modeling in Chapter 8.

Two additional hydrogen transfer correlations are given in Table 7.1. The first one is for hydrogen transfer adjacent to a CO group in ketones. This sub-family was proposed based on our preliminary modeling results in which we observed that ketones are rapidly consumed if standard structure-reactivity relationships were used to estimate the reactivity of abstracting hydrogen atoms adjacent to CO moieties. This additional sub-family is also suggested by our previous studies of intramolecular hydrogen transfer reactions (Pfaendtner et al., 2006c) in which self-abstraction adjacent to a CO group followed a dramatically different structure-reactivity relationship compared to reactions that did not have a CO group. Finally, for all other hydrogen transfer reactions, including alkyl radicals abstracting from alkanes, we recommend the E_A^o and α parameters that were regressed by Blowers and Masel (2000) for use in the range $-30 < \Delta H_{rxn} < 30$ kcal mol^{-1} in conjunction with a representative pre-exponential factor $A = 10^7$ L/mol-s. The six specific sub-families used in Chapter 8 for mechanistic modeling are highlighted in bold in Table 7.1.

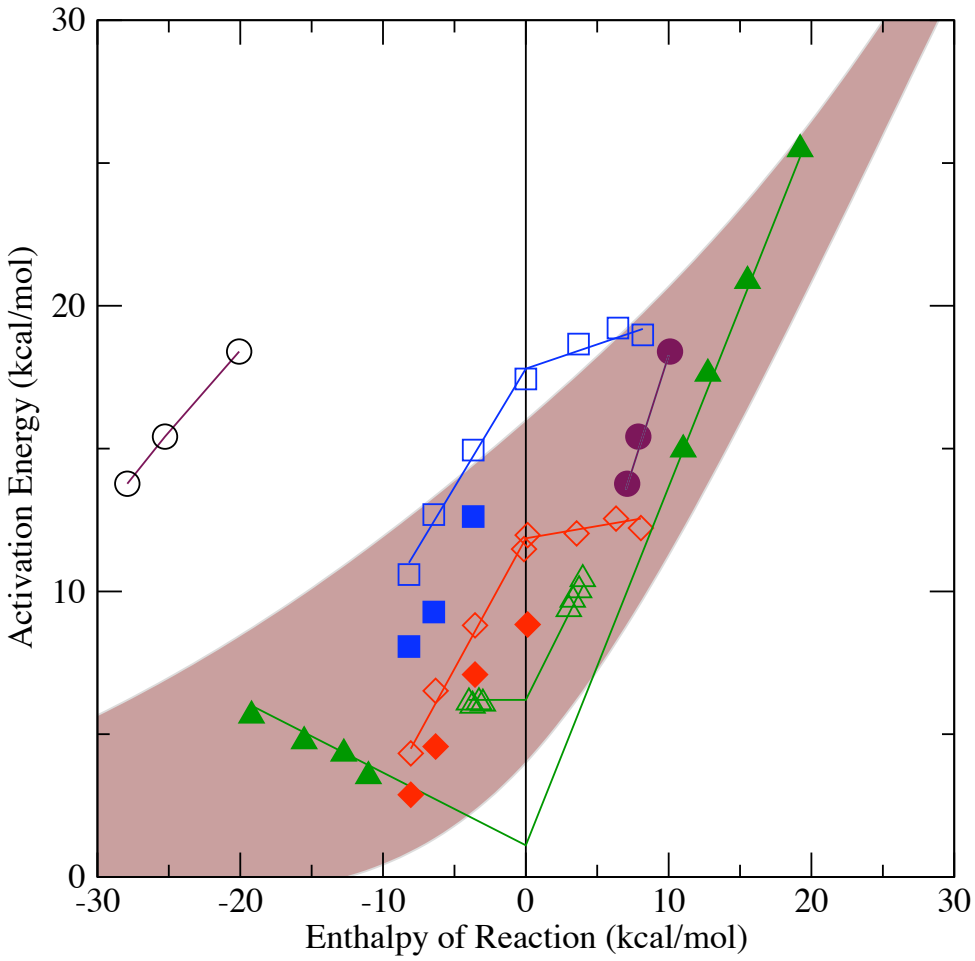

Figure 7.6: Structure-reactivity relationships for hydrogen transfer reactions relevant in free-radical oxidation chemistry. The data shown are CBS-QB3 calculations and available experimental data of the activation energy and enthalpy of reaction for reactions 1-15 in Table 7.4 (forward/reverse pairs when applicable) and reactions 1-8 in Table 3 of Pfaendtner and Broadbelt (2007b). The best-fit structure-reactivity relationships are given as solid lines and summarized in Table 7.1. The data shown for the various sub-families are: alkyl radicals + alkanes (open (CBS-QB3) and filled (experiment) squares), alkoxy radicals + alkanes (open (CBS-QB3) and filled (experiment) diamonds), alkylperoxy radicals + aldehydes (open triangles), alkylperoxy radicals + alkylhydroperoxides (open and filled circles – see text for description), and alkylperoxy radicals + alkanes (filled triangles). The shaded region in the plot marks the space explored by Blowers and Masel (1999, 2000).

Table 7.4: Hydrogen transfer reactions studied using CBS-QB3 and transition state theory. Unless noted the properties of the reverse reaction were also used in the development of structure-reactivity relationships.

reaction sub-family	reaction number	reaction	ΔH_{rxn} (CBS-QB3)	ΔH_{rxn} (experiment)
alkyl radicals + alkanes	1[a]	$CH_3\cdot + CH_4 \rightarrow CH_4 + CH_3\cdot$		
	2	$CH_3\cdot + C_2H_6 \rightarrow CH_4 + C_2H_5\cdot$	-4.27	-3.69
	3	$CH_3\cdot + C_3H_8 \rightarrow CH_4 + i\text{-}C_3H_7\cdot$	-5.69	-6.45
	4	$CH_3\cdot + C_4H_{10} \rightarrow CH_4 + tert\text{-}C_4H_9\cdot$	-9.64	-8.19
alkoxy radicals + alkanes	5	$CH_3O\cdot + CH_4 \rightarrow CH_3OH + CH_3\cdot$	0.61	0.13
	6	$CH_3O\cdot + C_2H_6 \rightarrow CH_3OH + C_2H_5\cdot$	-3.66	-3.56
	7	$CH_3O\cdot + C_3H_8 \rightarrow CH_3OH + i\text{-}C_3H_7\cdot$	-5.08	-6.32
	8	$CH_3O\cdot + C_4H_{10} \rightarrow CH_3OH + tert\text{-}C_4H_9\cdot$	-9.03	-8.06
alkylperoxy radicals + aldehydes	9	$CH_3O_2\cdot + C_2H_5COH \rightarrow$ $CH_3O_2H + C_2H_5C(O)\cdot$		
	10	$CH_3O_2\cdot + CH(CH_3)_2COH \rightarrow$ $CH_3O_2H + CH(CH_3)_2C(O)\cdot$		
	11	$CH(CH_3)_2O_2\cdot + C_2H_5COH \rightarrow$ $CH(CH_3)_2O_2H + C_2H_5C(O)\cdot$		
	12	$CH(CH_3)_2O_2\cdot + CH(CH_3)_2COH \rightarrow$ $CH(CH_3)_2O_2H + CH(CH_3)_2C(O)\cdot$		
alkylperoxy radicals + alkylhydroperoxides[b,c]	13	$CH_3O_2\cdot + CH_3O_2H \rightarrow$ $CH_3O_2H + CH_2O + HO\cdot$		
	14	$CH_3O_2\cdot + CH_2(CH_3)O_2H \rightarrow$		

Table 7.4: (continued)

reaction sub-family	reaction number	reaction	ΔH_{rxn} (CBS-QB3)	ΔH_{rxn} (experiment)
	15	$CH_3O_2H + CH_3CHO + HO\cdot$ $CH_3O_2\cdot + CH(CH_3)_2O_2H \rightarrow$ $CH_3O_2H + CH_3COCH_3 + HO\cdot$		

[a]Reverse reaction not used since the reaction is the reverse of itself.

[b]Reverse reaction not used.

[c]The DFT geometry optimized products of these reactions yield the β-scission products shown.

7.3.3 Termination

The final class of reactions in Figure 7.1 is termination. Termination reactions consume two radical species to produce one or more stable molecular products. Termination reactions are well characterized, and overall structure-reactivity relationships were straightforward to obtain from published reports. In the case of free-radical oxidation reactions, there are a number of different types of disproportionation reactions that may be relevant. However, since our focus here is on alkane and lubricant degradation, the dominant disproportionation reaction that occurs is the one shown in Figure 7.1 in which two alkylperoxy radicals react to form a ketone, an alcohol and oxygen (Denisov and Denisova, 2000). For this reaction family we have approximated the following structure-reactivity relationship based on available data (Denisov and Denisova, 2000; Khan, 2005): A=10^6 L/mol-s, $E_A^o = 0$ and $\alpha = 0$. Likewise, we assume that the radical-radical recombination step shown in Figure 7.1 is also unactivated and proceeds with the following structure-reactivity relationship: A=10^8 L/mol-s, $E_A^o = 0$ and $\alpha = 0$. The value for recombination was obtained by taking a corresponding gas phase value and lowering it according to the recommendation of Emanuel et al. (1967).

7.4 Oxidation chemistry requires specificity in reaction families

One of the primary goals of this work was to develop a new library of structure-reactivity relationships for use in kinetic modeling. We have taken an approach where experimental results are

supplemented with accurate theoretical calculations. As evidenced by the results given in Table 7.1, free-radical oxidation is a very diverse chemistry. As a consequence, greater specificity in our definitions of reaction families compared to, for example, pyrolysis chemistry, was warranted. Depending on the specific radicals involved, general structure-reactivity relationships for reaction families such as β-scission and hydrogen transfer do not adequately capture observed reactivity trends. Therefore, we developed new structure-reactivity relationships based on the concept of sub-families. While the data sets for the sub-families fall within a single region that was previously used (Blowers and Masel, 2000) for regression of a single correlation, their distinctiveness is clear from Figure 7.6. Chapter 8 applies these new structure-reactivity relationships to building models of alkane oxidation for use as a tool for understanding lubricant degradation.

Chapter 8

Mechanistic Modeling of Lubricant Degradation Part 2: The Autoxidation of Octane and Decane

8.1 Introduction

The quality of lubricating oils is critical to the overall performance and efficiency of an engine. One major indicator of lubricant performance is its serviceable lifetime, or the number of miles a car can drive before the oil must be changed. The chief reason lubricants need replacement is that once sacrificial antioxidants such as free-radical scavengers are consumed, the lubricant quickly begins to degrade and fail. The degradation of lubricating oils is deleterious to engine performance and operating lifetime (Blaine and Savage, 1991b; Kudish, 2005). Accordingly, much work has been

done to develop tests which can measure the relative performance of lubricants or even forecast the operating life of a lubricant. Common examples include the oxidation induction time (OIT), total acid number (TAN), or sludge formation tests (Rudnick, 2003; Rudnick and Shubkin, 1999). Although such tests provide a quantitative measure of lubricant performance, they typically do not give detailed insight into the mechanism by which a lubricant fails.

Since changes in lubricant performance are driven by molecular-level changes in the structure and makeup of the lubricant, it is desirable to have a complete description of the chemistry governing lubricant failure. Kinetic modeling is a necessary part of this process since it is not feasible to determine experimentally the complete set of reactions and reactive intermediates. A common strategy is to model the degradation of a single lubricant mimic in order to elucidate the kinetics and mechanism of lubricant degradation. For example, Blaine and Savage performed a detailed investigation of hexadecane oxidation under conditions similar to those under which a mineral oil or natural lubricants undergo degradation (Blaine and Savage, 1991a,b, 1992). Since lubricants degrade primarily through autoxidation, mechanistic studies of large hydrocarbons are ideal candidates for model systems from which information about lubricant failure can be inferred.

Experimentally, condensed-phase autoxidation of alkanes has been studied extensively, and there are numerous studies reported in the literature. Garcia-Ochoa et al. (1989) studied the oxidation of *n*-octane over 135 - 145 ^{o}C and measured the conversion of octane as well as appearance and concentrations of all C_8-based products, *i.e.*, peroxides, alcohols and ketones, as well as the appearance of five organic acids (C_2 to C_6 acids). The product concentrations were reported as lumped fractions, and no individual product concentrations were given. Over the timescale of

the experiments (6 hr) there was a maximum observed octane conversion of 5 percent, indicating that the experiments remained in the "early-oxidation" phase. Additionally, there are three studies of condensed-phase decane autoxidation from which experimental data can be derived for comparison to models (Cullis et al., 1981; Syroezhko et al., 1970, 1973). Data are reported for the appearance of individual decane-derived products and organic acids as well as some information about "late-oxidation" products (smaller alcohols, esters and lactones). All the data are reported at 150 ^{o}C. Surveying the available literature on condensed-phase autoxidation of hydrocarbons shows that although the early phases of oxidation are better understood, there are still many open questions about the dominant reaction pathways contributing to the formation of stable products, in particular the organic acids.

One attractive method for answering these questions and elucidating the key reaction pathways is mechanistic modeling. A mechanistic model is comprised of all the elementary steps in a reaction network. This is in contrast to a lumped model which simplifies the model through lumping species, reaction sequences, or both. However, it is not possible to manually construct mechanistic models of lubricant degradation due to the fact that there are literally hundreds of possible reactive intermediates and tens of thousands of reactions. Substantial progress using automated mechanism generation (AMG) techniques has been made for other chemistries including atmospheric chemistry, pyrolysis and silicon nanoparticle formation (Broadbelt and Pfaendtner, 2005; Broadbelt et al., 1994a, 1995, 1996, 1994b; Klinke and Broadbelt, 1997; Susnow et al., 1997; Van Geem et al., 2006; Wong et al., 2004a). However, the principles of automated mechanism generation have yet to be applied to condensed-phase hydrocarbon oxidation.

Chapter 7 established a library of kinetic correlations that are suitable for modeling condensed-phase autoxidation of hydrocarbons. This chapter is a computational study of the mechanism and kinetics of the autoxidation of decane and octane. We sought to answer the following questions related to oxidation and lubricant degradation:

1. Can AMG be used to generate reaction mechanisms for low-temperature oxidation of large hydrocarbons?

2. What is the optimum set of kinetic parameters so that experimental data is reliably reproduced?

3. How can this approach be used to *predict* the behavior of a reacting system?

The remainder of this chapter is divided into four sections. First, we give an overview of the AMG approach. Second, we discuss the mechanics and results of generating large reaction mechanisms for free-radical oxidation. Special attention is given to establishing criteria by which various mechanisms are discarded or selected for further use. Next, models of octane and decane are solved and analyzed. Finally, we discuss the results from both parts of this series together and draw overall conclusions.

8.2 Computational Details

8.2.1 Basis for AMG

A number of different formulations of AMG[a] have been put forth in the literature over the last 15 years (Broadbelt et al., 1994a, 1995, 1996, 1994b; De Witt et al., 2000; Green et al., 2001; Hatzimanikatis et al., 2005; Iyer et al., 1998; Klinke and Broadbelt, 1997; Li et al., 2004; Matheu et al., 2003; Prickett and Mavrovouniotis, 1997a,b,c; Ratkiewicz and Truong, 2003; Susnow et al., 1997; Wong et al., 2003). A central feature in the development of AMG is exploitation of the fact that although complex reaction networks can be incredibly large, the set of unique types of reactions which occur is relatively small. This is the "reaction family" or "reaction class" concept in which reactions are lumped based on the fundamental rearrangements in atomic connectivity and electronic structure. For example, hydrocarbons reacting via free-radical chemistry undergo a large variety of hydrogen transfer reactions. However, the amount of information needed to specify any hydrogen transfer reaction, namely the identity of the radical, hydrogen atom and the atom to which that hydrogen is connected, is general.

Thus, the minimum information required to apply AMG to a given system is the input compounds and the reaction families that are known to be active in that system. A given AMG algorithm will apply all reaction families to input compounds, generate new species, and continue generating new species/reactions until mechanism growth is stopped. A major consideration in the application of AMG to free-radical systems is the process by which mechanism growth is ter-

[a]Broadbelt and Pfaendtner (2005) gave an overview of AMG in the context of modeling complex reacting systems.

minated. Free-radical chemistry is not inherently convergent, and so mechanism growth must be halted using additional criteria. One option is simply to allow the mechanism to grow through successive generations of stable products. This rank-based criterion is attractive since all theoretically possible reactions between molecular species are included in the mechanism. However, a major detraction from the rank-based approach is computational cost and the enormous size of the ensuing reaction mechanisms. The rank-based methodology does not discriminate between species which are more or less kinetically significant in a mechanism, and thus the reaction mechanism becomes cumbersome to solve and analyze.

A more efficient method for applying AMG is known as rate-based mechanism generation (De Witt et al., 2000; Susnow et al., 1997). The central feature of rate-based generation is that the reaction network is simultaneously solved while it is undergoing generation so that the rates of formation of all species can be tracked. This additional information allows the user to classify species as either "core"/"reactive" or "unreactive". Only core species are allowed to continue to react further and generate new species/reactions. The decision to include a new species in the group of core species is based on comparing the rate of formation of a given new species against some characteristic rate of formation, R_{char}. This characteristic rate of formation is determined by taking the maximum rate of formation of all species in the mechanism and multiplying it by a user-defined threshold, ϵ. Additionally, mechanism generation begins by first specifying a pool of species whose size is designated by s. Thus, mechanism generation can be well controlled through two additional parameters: ϵ and s. Specific details of our implementation of rate-based AMG are given elsewhere (De Witt et al., 2000).

To implement the rate-based criterion, the mechanism is coupled with reactor design equations, and the model is solved on-the-fly. The experiments we sought to model were continually replenished with oxygen and were found to be under kinetic control. We modeled this semi-batch operational mode by setting the initial oxygen concentration at its saturation value and forcing the ODE governing oxygen, dC_{O_2}/dt, to be zero under all conditions. At 298.15 K and 1 atm of oxygen, O_2 is sparsely soluble in octane and decane and its liquid-phase mole fraction was reported to be 2.05 x 10^{-3} and 2.18 x 10^{-3}, respectively (Ashcroft and BenIsa, 1997). Using this data and the partial pressure of O_2 used under the given experimental conditions, the liquid-phase concentration of O_2 was calculated by assuming Henry's Law behavior.

8.2.2 Specification of reaction rules

Chapter 7 established a library of kinetic correlations suitable for use in estimating rate coefficients in hydrocarbon autoxidation. Each of the kinetic correlations given in Table 7.1 corresponds to a specific elementary reaction family. The reaction families represent all of the individual types of reactions that are applied when using AMG to generate mechanisms. In addition to specifying the change in atomic connectivity and electronic configuration, AMG also uses a set of "reaction rules" to intelligently apply reaction families and curb mechanism growth. For example, abstraction of hydrogen atoms from terminal methyl groups is well known to proceed much more slowly compared to abstraction of hydrogen atoms from methylene groups. Accordingly, we eliminated this reaction channel in the code through implementation of the appropriate reaction rule, *i.e.*, do not allow hydrogen atoms attached to methyl groups to be abstracted. The key reaction rules we

employed in this work along with the corresponding rationale are given in Table 8.1. In particular, reaction rules 2 and 3 in Table 8.1 exert a strong influence on the size of the mechanisms obtained from AMG. In section 8.3.2 we relax some of the reaction rules and demonstrate that the mechanisms are larger but their ability to capture experimental data is not substantially different. We note that many of the reaction rules implemented here were crafted with the intention of using AMG to build reaction networks of hexadecane or other systems that better represent real lubricants in future studies.

Table 8.1: Specific reaction rules for implementation of lubricant degradation via autoxidation in AMG.

rule #	reaction family	reaction rule	rationale
1	hydrogen abstraction	No abstraction of hydrogen from methyl groups	The activation energy is much higher for abstraction of these hydrogens, making this reaction route relatively unimportant over the temperature range of interest (400-420 K). This is also confirmed by the absence of any terminal-group functionalized products. No 1-peroxides, alcohols, or aldehydes were reported for octane (Garcia-Ochoa et al., 1989) or decane (Cullis et al., 1981; Syroezhko et al., 1970, 1973).
2		No abstraction by carbon-centered radicals	When lubricant degradation/hydrocarbon autoxidation are under kinetic control, molecular oxygen adds to carbon-centered radicals essentially instantaneously.
3		No hydrogen abstraction from a molecule containing more than two oxygen atoms	We are developing models for early oxidation/degradation of lubricants and tracking evolution of products up to organic acids.
4	primary initiation	Oxygen does not abstract hydrogen from methyl groups	(see rule 1 rationale)
5	hydroperoxide decomposition	Hydroperoxide decomposition may occur between any alkylhydroperoxide and a hydrogen atom on a CH_2 group of the substrate	In early oxidation, nearly all of the CH_2 groups in the system are on the substrate.
6	bond fission	Only peroxide linkages undergo bond fission	At the temperature range of interest, there is not enough thermal energy to result in appreciable breakage of C-C bonds.

Table 8.1: (continued)

rule #	reaction family	reaction rule	rationale
7	radical recombination	Recombination may not result in the formation of trioxy or tert-oxy linkages	It has been noted that disproportionation of peroxy radicals dominates their termination (Denisov and Denisova, 2000). In addition, XOOX and XOOOOX (X=C or H) species have not been detected experimentally.

8.2.3 Formulation of rate equations and model solution

Since our implementation of AMG relies on repeated solution of the growing mechanism during generation, the specification of all thermodynamic and kinetic parameters is crucial to accurate generation of reaction mechanisms. We have employed a systematic hierarchy for specification of thermodynamic and kinetic properties identical to that described in Chapter 2 and given in Figure 2.3. All thermodynamic properties were obtained from experimental data reported in the NIST Structures and Properties database (Stein et al., 1991) or estimated using group additivity (Benson, 1976). Missing group additivity values were augmented by calculations in our research group (Khan, 2005). All rate coefficients were specified using the library of kinetic correlations (Table 7.1) given in Chapter 7. Since the structure-reactivity relationships we developed in Chapter 7 faithfully reproduce the very small number of experimental rate coefficients available relevant to octane or decane autoxidation, we elected to simply use these structure-reactivity relationships in development of our kinetic models. Our approach strictly enforces thermodynamic consistency. When forward and reverse reaction pairs are written by the AMG algorithm, only one rate coefficient was specified from the correlations in Table 7.1, and the rate coefficient for the opposite direction is rigorously calculated using the equilibrium constant and the forward rate coefficient. For the specific case of hydrogen transfer reactions, the ordering in Table 7.1 reflects the priority in assigning which rate coefficient is calculated using a structure-reactivity relationship and which rate coefficient is calculated using thermodynamic consistency.

8.3 Free-Radical Octane Oxidation: Mechanism Generation and Results

8.3.1 Mechanism generation and selection

To begin building a kinetic model of octane autoxidation, we used the AMG approach to generate mechanisms with varying values of the threshold ϵ. Preliminary results confirmed that the mechanism size and quality were only influenced slightly by the size of the initial species pool, s. Accordingly, we selected a value of s=15 and used that for all remaining studies. As expected, however, the value of ϵ had an enormous impact on the size and quality of the mechanism obtained. We established three criteria in order to select a reaction mechanism for further consideration:

1. All experimentally observed molecular products must be present in the reactive core of species and the mechanism obtained from AMG.

2. The mechanism size as measured by the number of species and reactions should be increasing marginally (or have reached a plateau) with further increases in ϵ.

3. The error between the model results and the experimental data should be decreasing marginally (or plateaued) with further increases in ϵ.

Since the data provided by Garcia-Ochoa et al. (1989) are lumped, we also employed a lumping strategy for the model output. In calculating the error between the model results and the experimental data, we compared the octane concentration and concentrations of four lumped products: peroxides (2-, 3-, and 4-octanehydroperoxide), alcohols (2-, 3-, and 4-octanol), ketones (2-, 3-, and

4-octanone) as well as five organic acids (ethanoic, propanoic, butanoic, pentanoic, and hexanoic acids) at 140 ^{o}C and the octane concentration at 135 and 145 ^{o}C. The magnitude of the octane concentrations is much larger than the magnitude of the product concentrations, so we examined the behavior of the error between the model results and the experimental data using standard and weighted measures of error:

$$SSR_{standard} = \sum_{i} \left(y_{obs}[i] - y_{model}[i]\right)^2 \tag{8.1}$$

$$SSR_{weighted} = \sum_{i} \left(\frac{\left(y_{obs}[i] - y_{model}[i]\right)}{y_{obs}[i]} \right)^2 \tag{8.2}$$

where SSR is the sum of squared residuals, y are the species concentrations in mol L^{-1}, and the index i refers to the set of all species, temperatures, and times for which experimental data is available.

The growth of the model (species and reactions) versus the parameter ϵ and the convergence of error versus ϵ are given in Figure 8.1. The data in Figure 8.1 are plotted with an inverted x-axis because the model grows in size as the threshold is decreased, and also because the standard procedure in AMG is to begin with the smallest possible mechanism and increase its size until the convergence criteria are met. For models with a threshold value of -log ϵ of 3 and lower, *i.e.*, -log $\epsilon = [3 - 8]$, all of the observed products are included in the reactive core. Thus, the first criterion is met very early on in mechanism generation. For values of -log $\epsilon = [4 - 6]$, a definite plateau is seen in the numbers of species and reactions, as shown in panel (a) of Figure 8.1, satisfying the second criterion. Not surprisingly, though, the model begins to quickly increase in size for

the last two values of ϵ we investigated since very small threshold values will allow many more species and reactions to be included. The third criterion, the SSR, is therefore used as the more definitive criterion since this quantifies whether these additional species and reactions affect the ability of the model to capture the data. The SSR values (for both the standard and weighted errors) are clearly converged at a value of -log $\epsilon = 4$ as shown in Figure 8.1b. It is also interesting to note that the standard error initially has an increase for very large threshold values and then quickly decreases to the converged value, whereas the weighted error decreases monotonically to its converged value with increasing model size. The standard error is biased toward changes in the octane concentration, and at early stages of model growth additional reactions can strongly influence the conversion of the substrate and affect the error in unexpected ways. We note, however, that this anomalous behavior occurs before the first convergence criterion is met, *i.e.* -log $\epsilon = 3$, which is the primary convergence criterion that must be satisfied. Based on all of the data presented in Figure 8.1, we selected the mechanism corresponding to -log $\epsilon = 4$ (266 species and 6,044 reactions) for further analysis. However, before performing a detailed analysis of the kinetics and mechanism of octane oxidation, we used the -log $\epsilon = 4$ mechanism to investigate the impact of some of the reaction rules specified in Table 8.1.

8.3.2 Reaction rules curb mechanism growth effectively

In Chapter 7 we postulated that it was necessary to use six unique hydrogen abstraction sub-families in order to accurately specify the kinetics for these reactions. To test the impact of this hypothesis on the mechanisms generated using AMG, we built the mechanism using the Evans-

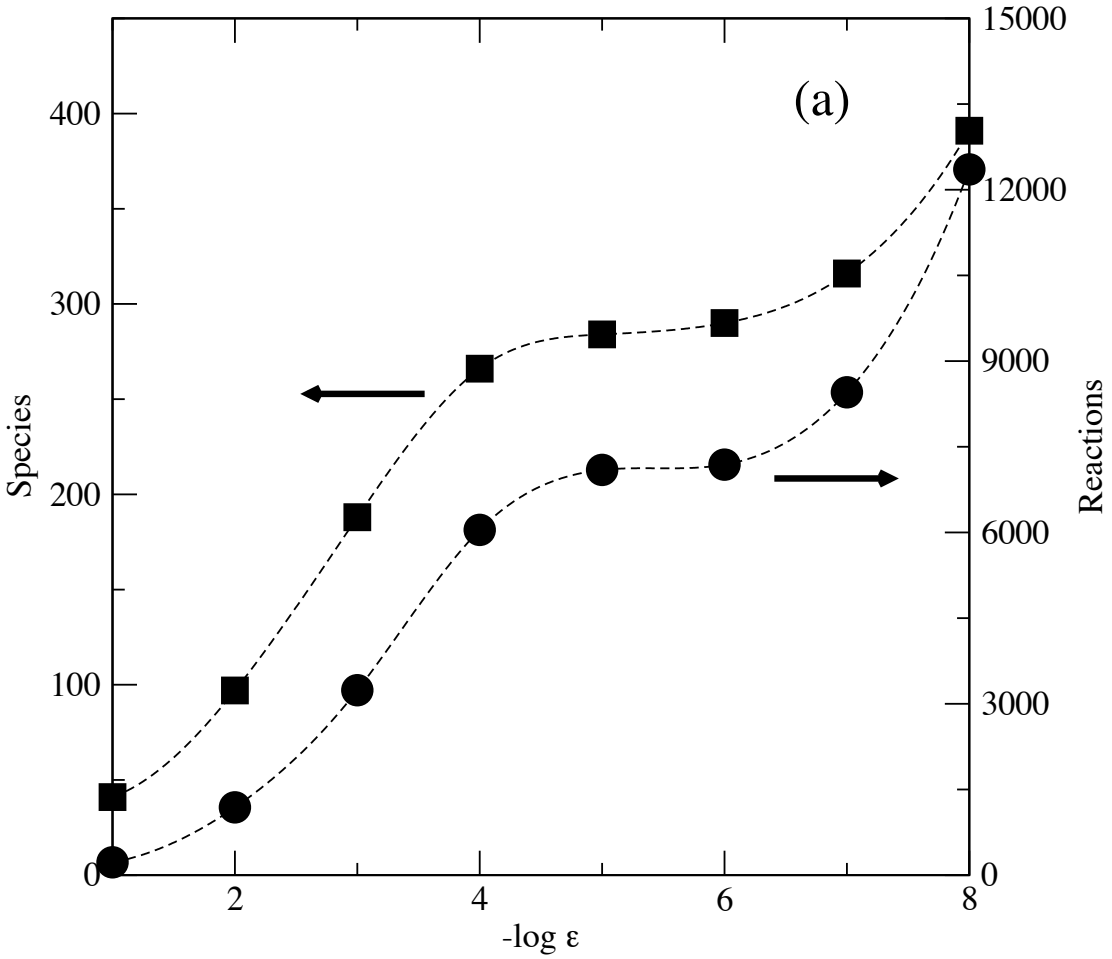

Figure 8.1: Changes in size and sum of squared residuals between the model results and the experimental data for the models generated using AMG as a function of ϵ. The data are plotted against the quantity "-log ϵ" on the x-axis with the largest threshold value (-log ϵ = 1) on the left. Panel (a) shows the changes in the number of species and reactions as the threshold decreases. Panel (b) shows the convergence of the SSR as a function of ϵ. Continued on next page.

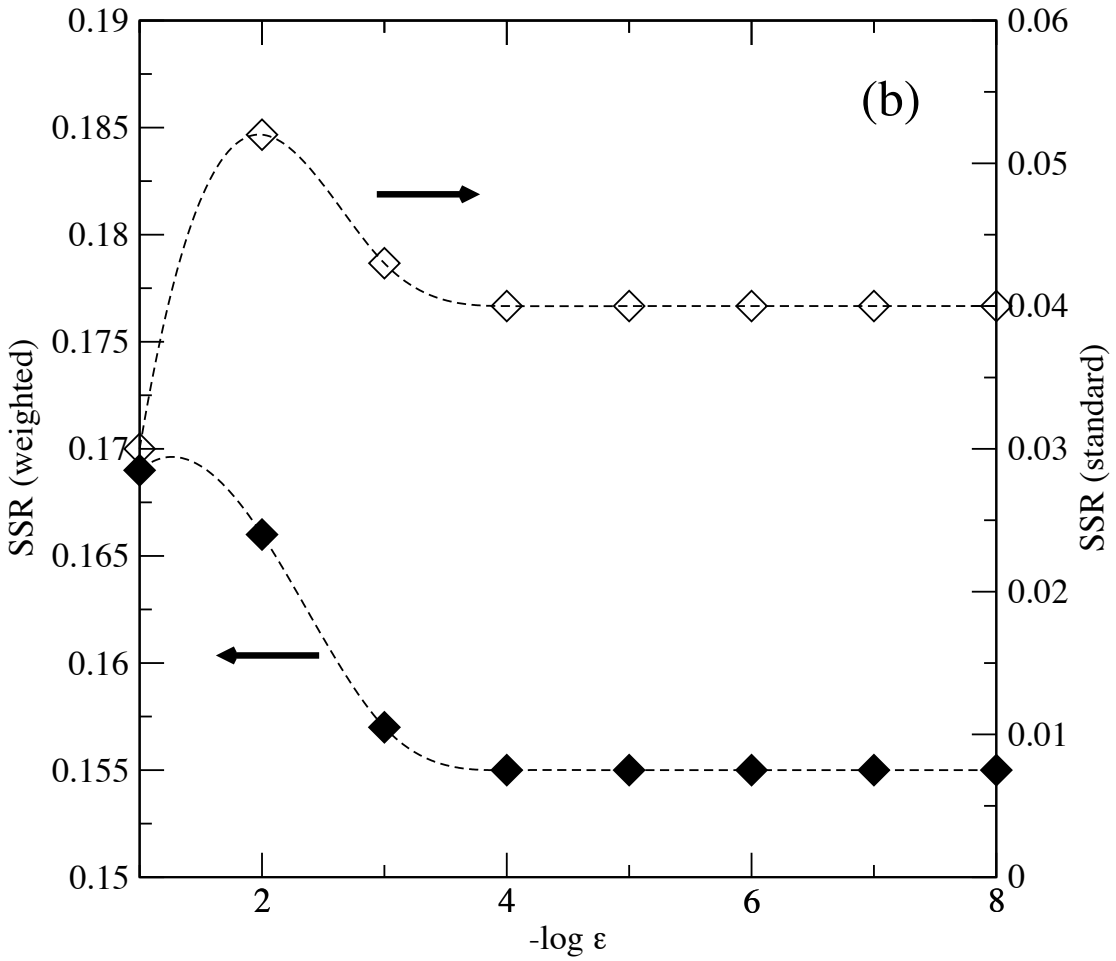

Figure 8.1: (continued)

Table 8.2: Characteristics of mechanisms generated for seven different mechanisms used to test some of the reaction rules in Table 8.1 and demonstrate the importance of using reaction sub-families for hydrogen transfer.

mechanism #	-log ϵ	species	reactions	$SSR_{weighted}$	$SSR_{standard}$
1	4	177	4,130	6.16	34.0
2 [a]	4	242	13,933	0.246	0.475
3	4	266	6,044	0.155	0.0399
4	4	288	7,663	0.154	0.0384
5	4	267	10,039	0.154	0.0384
6	4	272	10,803	0.154	0.0384
7	4	276	11,223	0.154	0.0384

[a] All of the experimentally observed products are in the mechanism except propanoic acid.

Polanyí relationship and the E_A^o and α values regressed by Blowers and Masel (2000) for all hydrogen transfer reactions.[b] The results from this are given as mechanism 1 in Table 8.2. Although the mechanism contained all of the experimentally observed species in the reactive core, the SSR values for the mechanism are very large. When reaction sub-families for hydrogen transfer are not used, the standard and weighted SSR values are over an order of magnitude larger than those for all of the mechanisms shown in Figure 8.1, even those with very high thresholds. While the experimental and theoretical results tabulated in Chapter 7 provided strong support for using reaction sub-families, the data given in Table 8.2 unequivocally show that the sub-families bring the reaction mechanism in much better agreement with experimental results.

The next test performed was to relax rule #2 in Table 8.1 while preserving the sub-families for hydrogen transfer. Carbon-centered radicals were allowed to react via hydrogen abstraction with

[b] For the range of heats of reaction relevant to lubricant degradation, the Evans-Polanyí relationship using the parameters in Table 7.1 (general correlation) has nearly identical RMS, average, and maximum errors compared to the Blowers and Masel correlation (see Table 4 in Blowers and Masel (2000)). Given this good agreement between the two correlations, we simply used the general Evans-Polanyí relationship for this analysis.

kinetics dictated by the kinetic correlation for "other", and oxygen addition to carbon-centered radicals was still permitted. The results from this mechanism are given as mechanism 2 in Table 8.2. As expected, the mechanism has many more reactions, with over twice as many as the comparable -log $\epsilon = 4$ mechanism generated with reaction rule #2 in force. However, the error in the mechanism is larger than all of the mechanisms shown in Figure 8.1, and not all of the experimentally observed products are in the reactive core.

Finally, we explored the impact of rule #3 in Table 8.2 on the characteristics of the mechanisms generated. Mechanism 3 in Table 8.2 corresponds to the mechanism summarized in Section 8.3.1 that was generated with rule #3 in place. We incrementally relaxed rule #3 by increasing the number of oxygen atoms in a stable molecule that was allowed to participate in hydrogen abstraction from 3 to 4 to 5. These results correspond to mechanisms 4–6 in Table 8.2, respectively, and mechanism #7 is the result of turning off rule #3, thereby allowing an unlimited number of oxygen atoms. As expected, the number of reactions in the mechanism grows, almost doubling by the time rule #3 is shut off. It is interesting to note that the number of species in the mechanism does not follow any discernible trend, increasing and decreasing as rule #3 is relaxed and eventually shut off. It is most interesting to see that mechanisms 4–7 all have the same error that is not significantly different from base mechanism #3. The additional species and reactions do not improve the agreement between the model results and the experimental data to any significant extent. Given all of these analyses, we proceeded with mechanism #3 as summarized in Table 8.2.

8.4 Model Solution and Analysis

8.4.1 Base model solution and parameter estimation

Using the semi-batch reactor model described above and a stiff ODE solver (Stewart et al., 1997a), the model solution for the -log $\epsilon = 4$ mechanism was obtained. The predicted concentration profiles are compared to the experimental data in Figure 8.2. To solve the model we used the 15 structure-reactivity relationships identified in Table 7.1 (six sub-families for hydrogen transfer and nine other families) for a total of 45 parameters (A, E_A^o, and α values) that were fixed at the values in Table 7.1. Note that rate coefficients for different reactions in a given family were distinct based on differences in the heat of reaction, such that 6,044 individual rate coefficients were quantified by these 45 parameters. It is also important to note that the A values are based on representative values, and although the assumption of a single A value to characterize all reactions in a given family is reasonable, variations of individual A values can be as great as, for example, two orders of magnitude for hydrogen transfer reactions (see Table 6.3 for example). Given that the model results are a pure prediction, the agreement between the model results and the experimental data shown in Figure 8.2 is very encouraging. The model did a very good job predicting the octane concentration at 408 K, but at higher temperatures the model under-predicted the conversion of the substrate. The effects of this are seen in Figure 8.2b where the peroxide concentration is captured very well by the model, but all other species (alcohols, ketones and acids) are dramatically under-predicted by the model. The relative concentrations of the ketone and alcohol species predicted by

the model are correct, with the ketones having a higher concentration at all times. However, the acid concentration did not follow the experimental trends quantitatively or qualitatively.

Given that representative values were used for the frequency factors, we sought to improve the agreement of the model with the experimental results through parameter estimation. All optimizations were performed using GREG (Stewart et al., 1997b), a nonlinear parameter estimation code that uses gradient-based searches to find local minima. To perform parameter estimation for the octane models, the data presented by Garcia-Ochoa et al. (1989) were used in the minimization of an objective function based on the sum of squared residuals shown in equation 8.3:

$$SSR_{GREG} = \sum_i \left(\frac{(y_{obs}[i] - y_{model}[i])}{\sqrt{0.1 * y_{obs}[i]}} \right)^2 \tag{8.3}$$

There are two important issues to note before the results obtained via parameter estimation are presented. First, the parameters that were optimized were selected based on conventional sensitivity analysis and insights based on experience with the solution of the model. Sensitivity analysis directly quantifies the relationship between model output (concentrations) and the input parameters (A, E_A^o, and α values). Specifically, we used the sensitivity matrix (Turanyi, 1990) "$\partial F_i/\partial k_j$" where F_i is the rate of change (dC_i/dt) of species i and k_j is a kinetic parameter (A, E_A^o, and α values). Parameters with large values of $\partial F/\partial k_j$, where $\partial F/\partial k_j$ is the sum over all experimentally measured species at a given time t, were selected for adjustment. Second, it is important to note that the -log $\epsilon = 4$ mechanism we obtained was created using the parameters given in Table 7.1 via rate-based AMG. The values of the optimized parameters were thus used to re-generate the -log $\epsilon = 4$ mechanism, and optimization was performed again on the same parameters using the new

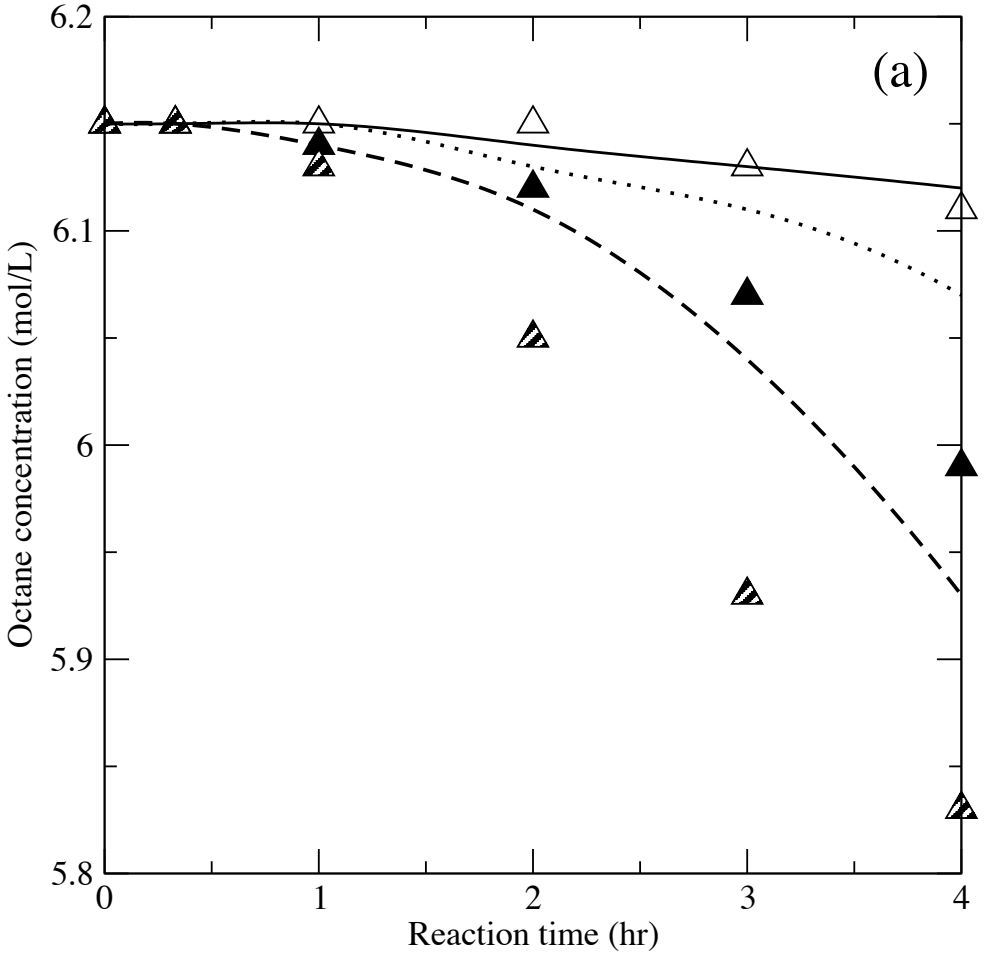

Figure 8.2: Predicted base model solution for octane oxidation. The model has 266 species and 6,044 reactions. The parameters used in solving the model are given in Table 7.1. Experimental data from Garcia-Ochoa et al. (1989) are given in symbols and the AMG modeling results are shown with lines. Octane conversion data are given in panel (a): 408 K (open symbols, solid line), 413 K (filled symbols, dotted line), 418 K (partially filled symbols, dashed line). Lumped product species are given in panel (b): peroxides (circles, heavy solid line), alcohols (squares, dotted line), ketones (diamonds, solid line), and acids (filled squares, dashed line). Continued on next page

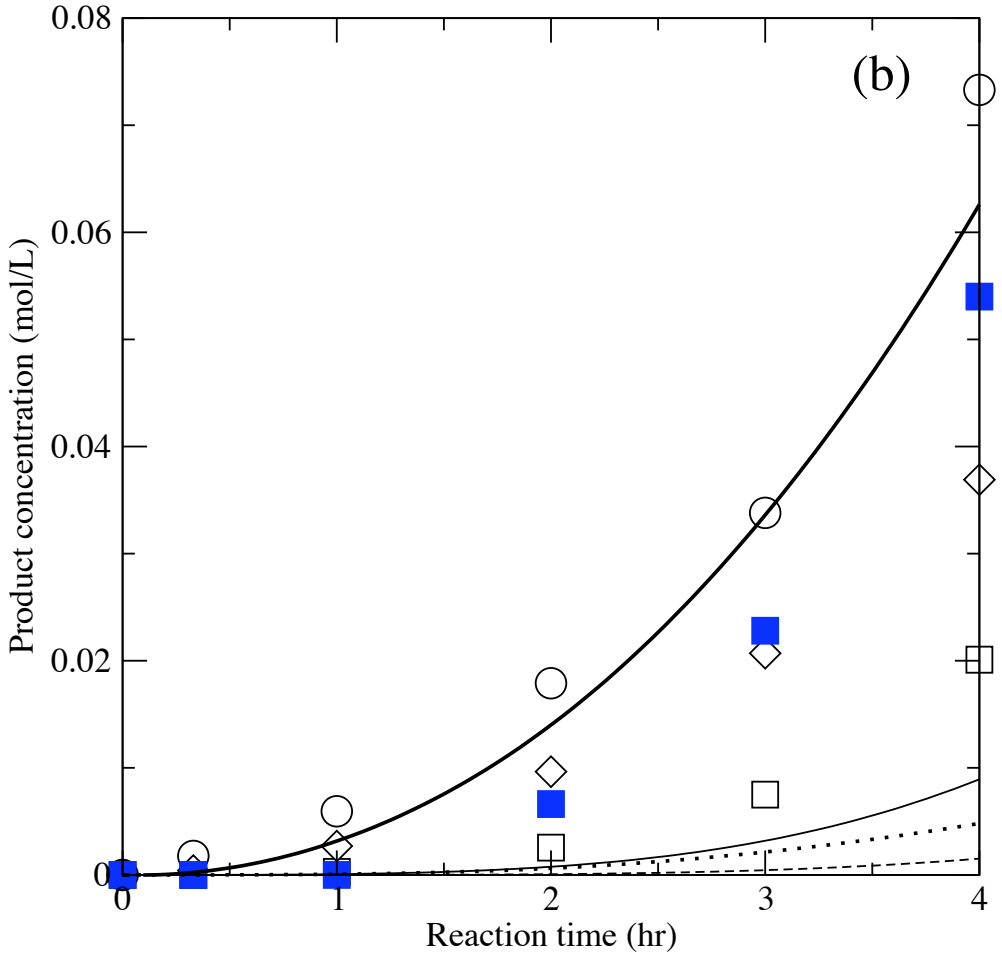

Figure 8.2: (continued)

mechanism. This iterative cycle was continued until the characteristics of the mechanism and the values of the optimized parameters converged.

In selecting which parameters were optimized, the sensitivity of the model to various parameters was explored manually to obtain a qualitative picture of how the concentrations of various species responded to changes in the parameters. It was immediately apparent that the model was never able to produce any appreciable quantities of acids, regardless of the parameter values. Further investigation revealed that although the model was not producing substantial quantities of carboxylic acids, sizable quantities of peracids, *i.e.*, RC(O)OOH species, were accumulating. However, we found no reported studies of alkane oxidation in which peracids were experimentally detected. The main route for consumption of peracids was hydroperoxide decomposition to form the radical precursor to acids (RC(O)O·), the kinetics of which were described by the same correlation used for the main secondary initiation pathway for the substrate. Based on this analysis, we established a distinct structure-reactivity relationship for the decomposition of peracids, "peracid decomposition". The initial values for the peracid decomposition structure-reactivity relationship were identical to hydroperoxide decomposition, A = 10^6 L/mol-s, E_A^o = 24.6 kcal mol^{-1} , and α = -0.09. It is interesting to note that although sensitivity analysis is a powerful and quantitative analytical tool, a key improvement in the model required manual interrogation of the reaction mechanism.

We next used sensitivity analysis in order to select a small set of parameters for optimization. Based on the results obtained from sensitivity analysis, we selected three parameters for optimization: A (hydrogen abstraction [*alkylperoxy radicals + alkanes*]), A (hydroperoxide de-

Table 8.3: Optimized parameters for octane oxidation. The initial and final pre-exponential factors (L/mol-s) are given. To obtain the final optimized parameter set, four cycles of optimization and AMG were required.

Reaction family	initial value	final value
A (hydrogen abstraction)[a]	10^7	4.57 x 10^6
A (hydroperoxide decomposition)	10^6	2.49 x 10^6
A (peracid decomposition)	10^6	2.54 x 10^{11}

[a]Pre-exponential factor for the "alkyperoxy radicals + alkanes" sub-family.

composition), and A (peracid decomposition). These three values had the highest positive value of the sensitivity coefficient $\partial F/\partial k$. Using the iterative approach described above, it took four cycles of parameter optimization and re-generating mechanisms to obtain convergence in the model size, optimum parameters, and SR_{GREG}. The final model had 331 species and 8,619 reactions, representing a marked increase from the original -log $\epsilon = 4$ model. The initial and final optimized parameters are given in Table 8.3.

The octane model was then solved again using the three optimized parameters and the additional reaction family. The total number of parameters for the improved octane model was 48, although two parameters (E_A^o and α for peracid decomposition) were constrained to be equal to E_A^o and α for hydroperoxide decomposition. The improved model results are given in Figure 8.3. As can be seen in Figure 8.3, the improved model results are in better agreement with the experimental results than the purely predictive model shown in Figure 8.2. The addition of "peracid decomposition" and the parameter estimation were both important in obtaining the improved fit. However, it is stressed that only a small number of parameters, two of which changed only subtly (approximately a factor of 2), were adjusted to obtain this agreement.

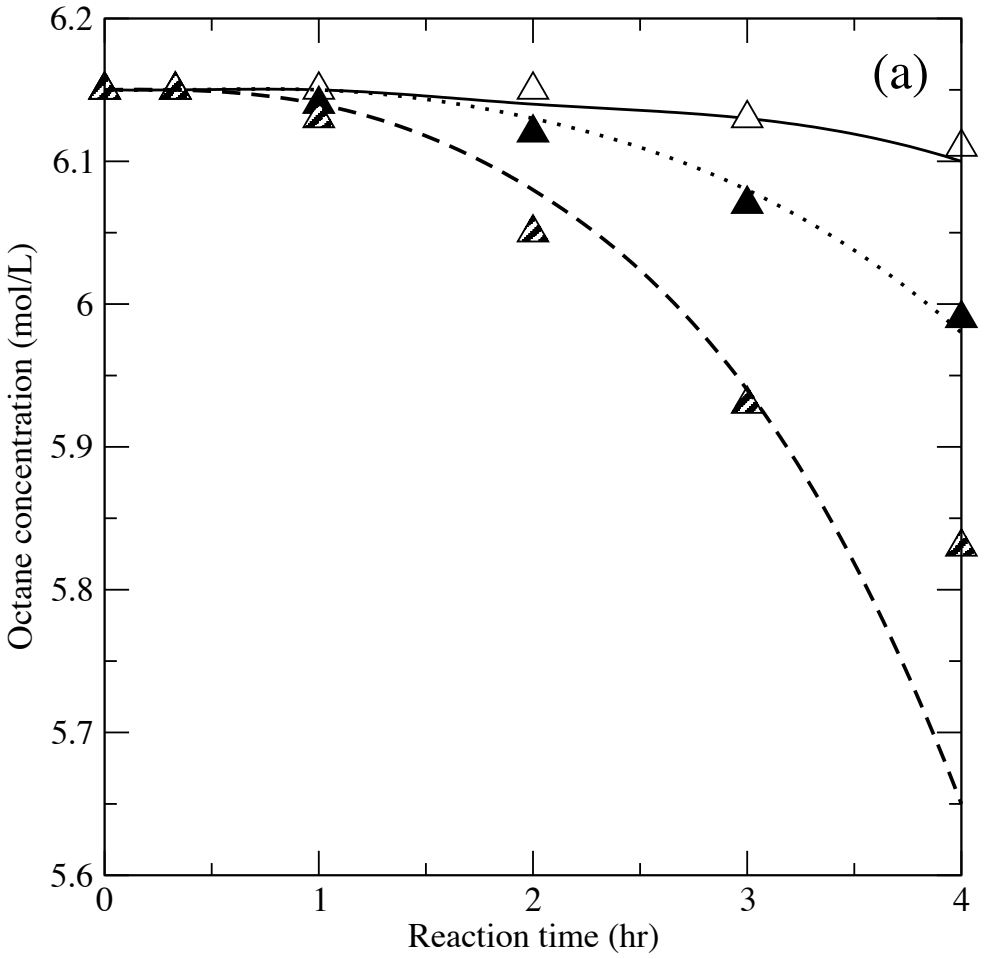

Figure 8.3: Improved model solution for octane oxidation. The model has 331 species and 8,619 reactions. The parameters used in solving the model are given in Table 7.1 and the optimized parameters are detailed in Table 8.3. Experimental data from Garcia-Ochoa et al. (1989) are given in symbols and the AMG modeling results are shown with lines. Octane conversion data are given in panel (a): 408 K (open symbols, solid line), 413 K (filled symbols, dotted line), 418 K (partially filled symbols, dashed line). Lumped product species are given in panel (b): peroxides (circles, heavy solid line), alcohols (squares, dotted line), ketones (diamonds, solid line), and acids (filled squares, dashed line). Continued on next page.

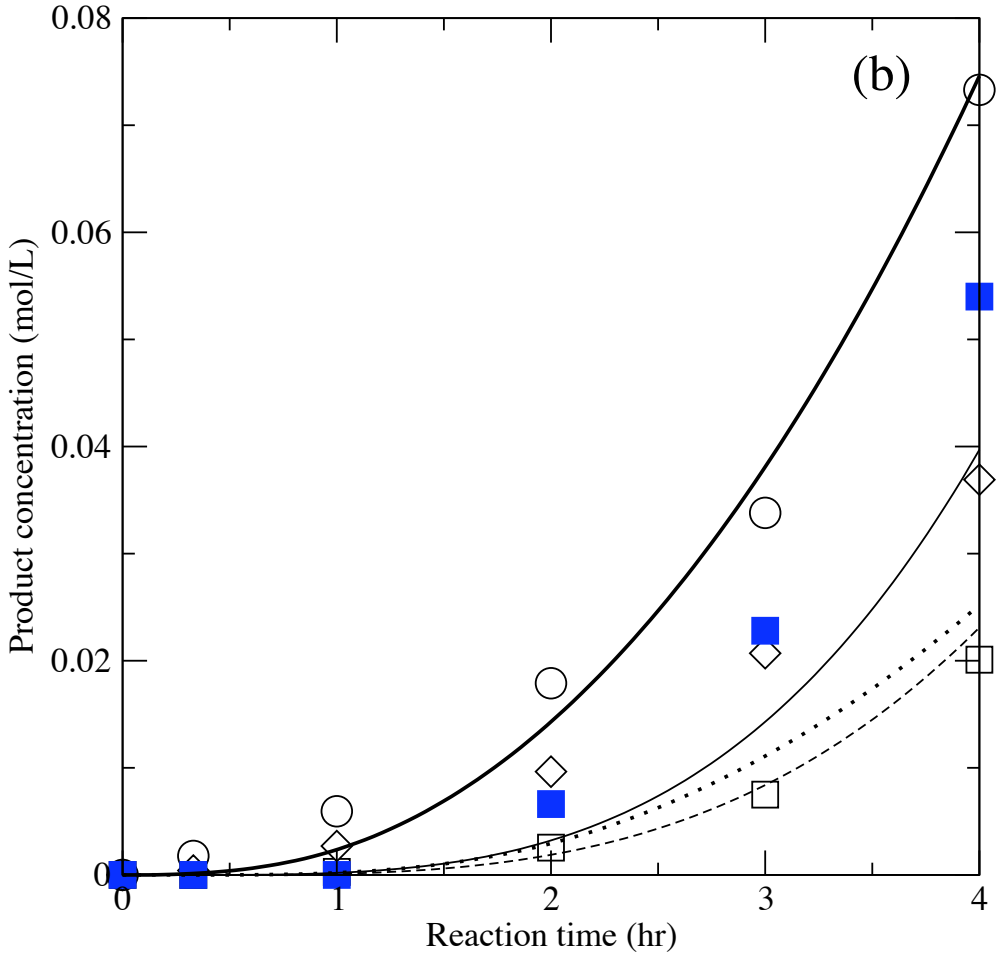

Figure 8.3: (continued)

8.4.2 Extension to decane oxidation

We next tested the applicability of these parameters to other systems by modeling the oxidation of decane at 150 ^{o}C. The data we sought to model were provided by Syroezhko et al. (1970) who reported the concentrations of the main primary (peroxides, alcohols and ketones) and secondary (acids) products over a longer time range than Garcia-Ochoa et al. (1989) did for octane, but they did not provide any information about the conversion of decane. Nonetheless, this data has great utility for testing the applicability of our modeling framework for longer times, higher temperatures, and a higher molecular weight substrate. Using the updated parameter library obtained by replacing the relevant values in Table 7.1 with the optimized frequency factors in Table 8.3, we used AMG to generate a mechanism for decane oxidation at 150 ^{o}C. All of the reaction rules in Table 8.1 were used, and we generated a mechanism corresponding to -log $\epsilon = 4$ and s=15. The mechanism had 332 species and 9,659 reactions. The model predictions are compared to the data from Syroezhko et al. (1970) in Figure 8.4. As can be seen in the figure, the model predictions do a reasonable job of capturing the experimental trends, but the ketones and acids are dramatically overpredicted. It is important to stress, however, that we have predicted this behavior with no parameter optimization. The agreement with experiment is still impressive given that the oxidation substrate is different and the comparison was performed at longer times and a higher temperature than studied in Section 8.4.1 for octane.

As an initial attempt at understanding why the model did not perform as well as the octane model, we adjusted two parameters without cycling through the parameter estimation/mechanism generation loop. We optimized two pre-exponential factors: A (alkyperoxy radicals + alkanes) and

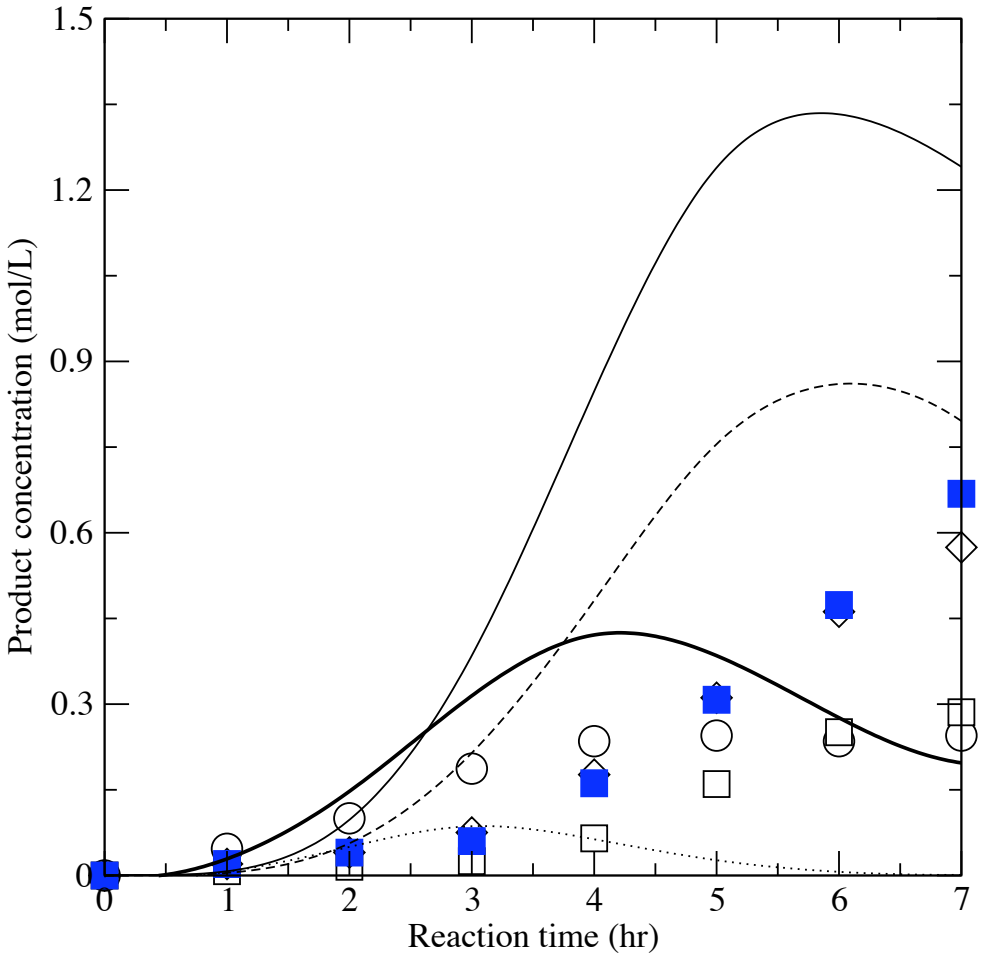

Figure 8.4: Base model solution for decane oxidation. The model has 332 species and 9,659 reactions. The parameters used in solving the model are given in Table 7.1 with the three frequency factors optimized against oxidation data for octane in Table 8.3 replacing their respective values. Experimental data from Syroezhko et al. (1970) (obtained at 150 ^{o}C) are given in symbols and the AMG modeling results are shown with lines. Lumped product species are given: peroxides (circles, heavy solid line), alcohols (squares, dotted line), ketones (diamonds, solid line), and acids (filled squares, dashed line).

Table 8.4: Optimized parameters for decane oxidation. The initial and final pre-exponential factors (L/mol-s) are given.

Reaction family	initial value	final value
A (alkyperoxy radicals + alkanes)	4.57 x 10^6	1.84 x 10^6
A (alkylperoxy radicals + alkylhydroperoxides)	10^7	6.04 x 10^6

A (alkylperoxy radicals + alkylhydroperoxides). The second pre-exponential factor was chosen since the yield of ketones is highly sensitive to its value and the model currently over-predicts the ketone yield. The optimized parameters are given in Table 8.4, and the updated model solution is given in Figure 8.5. As seen in Figure 8.5, the small adjustments in the parameters result in a much improved model, with all of the species in very good agreement with the experimental data. Using equation 8.1, the improved decane model has an SSR value 20 times smaller than the purely predictive decane model. The data in Table 8.4 further underscore the fact that using a representative pre-exponential factor greatly increases the sensitivity of the model solution to that value.

8.5 Conclusions

We have used AMG to create the most detailed reaction mechanism to date for low-temperature free-radical oxidation of hydrocarbons. Using the library of kinetic correlations developed in Chapter 7, we employed a rate-based AMG approach to build large mechanistic models that included key elementary reaction steps. Octane oxidation at 135-145 ^{o}C was used as a test system to probe the ability of AMG to generate models of free-radical autoxidation chemistry. It was shown that although the user-specified parameter ϵ is very important in controlling mechanism growth, the

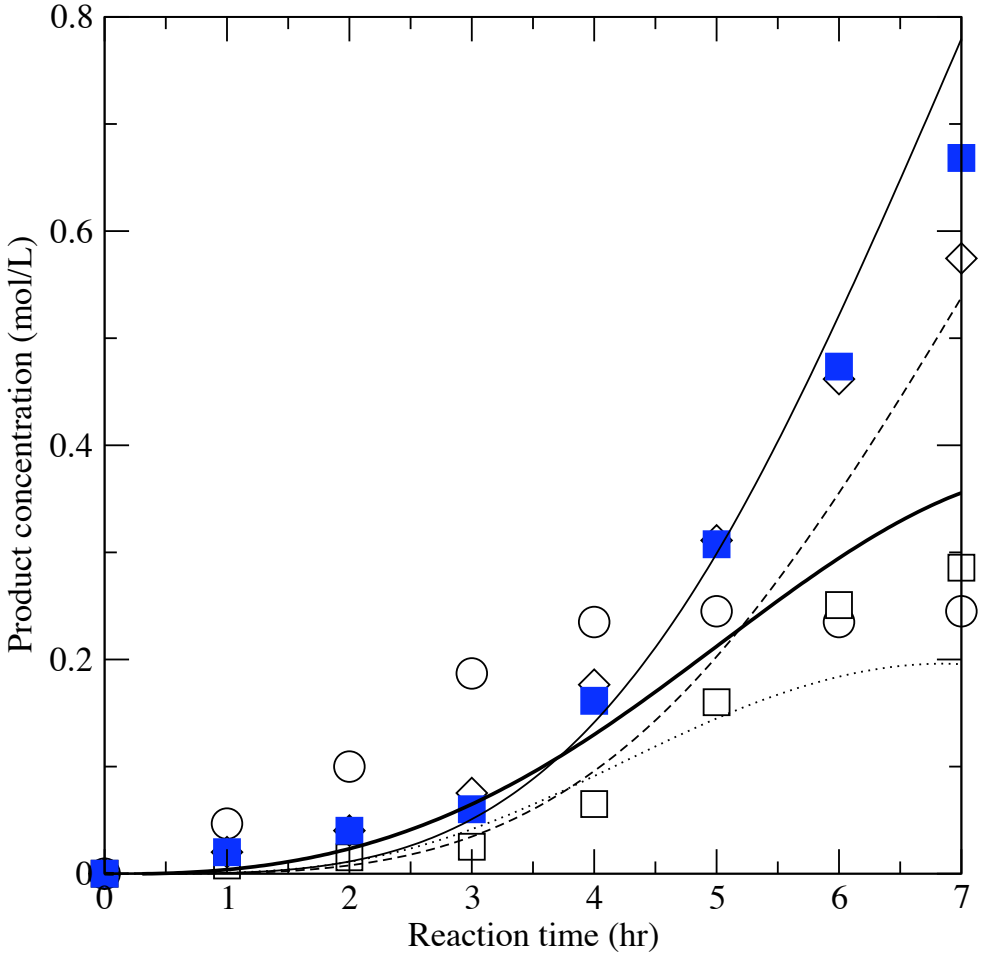

Figure 8.5: Improved model solution for decane oxidation. The model has 332 species and 9,659 reactions. The parameters used in solving the model were the same as those used for the model in Figure 8.4 but updated with the data in Table 8.4. Experimental data from Syroezhko et al. (1970) (obtained at 150 ^{o} C) are given in symbols and the AMG modeling results are shown with lines. Lumped product species are given: peroxides (circles, heavy solid line), alcohols (squares, dotted line), ketones (diamonds, solid line), and acids (filled squares, dashed line).

implementation of reaction rules is equally important in obtaining a tractable mechanism. It was demonstrated that very aggressive reaction rules can be employed within the AMG approach and that these reaction rules effectively control the mechanism size without appreciable impact on the model solution.

Without any parameter regression, the model results for octane oxidation were in reasonable agreement with experimental data, correctly capturing most of the experimentally observed trends. Using sensitivity analysis and qualitative model interrogation, three parameters were selected for adjustment. The improved model provided much better agreement with the experimental results. AMG was then applied to the modeling of decane based on the parameters obtained from octane, and with very minor adjustments of two frequency factors, very good agreement between the model results and the experimental data was achieved. Using the improved library of structure-reactivity relationships, the possibility now exists to build the first models of the thermal degradation of much more realistic lubricant-like molecules.

Chapter 9

Conclusions and Recommendations

This chapter gives overall conclusions about the research presented in this thesis and also makes recommendations for future work.

9.1 Overall Conclusions

9.1.1 It is possible to obtain accurate structure-reactivity relationships using computational quantum chemistry

As outlined in Chapter 2, it is imperative to have accurate structure-reactivity relationships when developing complex kinetic models via automated mechanism generation. For many chemistries, such relationships have not been developed due to a lack of reliable experimental data. This was true for lubricant degradation which was found to be especially complicated because of the variety of radicals and functional groups present in the system. Only a handful of experimentally deter-

mined activation energies were found in the literature, and therefore a computational approach was developed to facilitate theoretical determination of structure-reactivity relationships. In particular, we found that for all reaction families we investigated it was possible to obtain very good to excellent agreement between theoretical and experimental rate coefficients, activation energies, and enthalpies of reaction. This was accomplished by 1) making use of high-level quantum chemical methods such as CBS-QB3 and 2) performing a rigorous quantum-mechanical treatment of anharmonic motions. This finding is a marked departure from the conventional wisdom that quantum chemistry is useful for drawing qualitative conclusions but not for providing results which are quantitatively accurate (Jensen, 1999).

In Chapter 3, a computational algorithm for treating anharmonicity in molecular internal rotation was outlined. Performing this calculation is an important component in the overall framework for accurately obtaining theoretical estimates of kinetic and thermodynamic data. However, there were previously no known codes which performed this treatment *and* interfaced with common electronic structure codes such as Gaussian 03. Development of the algorithm and software described in Chapter 3 represents an important step forward in our ability to apply highly accurate methods to a large number of species/reactions.

Finally, the accuracy and wide applicability of our approach were demonstrated in Chapters 4–6 in which we developed structure-reactivity relationships for a number of different reaction families in free-radical chemistry. These relationships were based on calculations that were found to be in good agreement with available experimental data. In addition to providing quantitative estimates of reactivity for use in kinetic modeling, the structure-reactivity relationships revealed

fundamental information about the chemistry of the systems under consideration. For example, the surprising contrathermodynamic behavior discussed in Chapter 7 had not been previously reported in the literature for hydrogen transfer reactions.

9.1.2 Low-temperature oxidation requires specificity in kinetic correlations

The reacting systems under consideration in this work were studied at low to moderate temperatures. One consequence of this is that the rate coefficients for the individual reactions are more sensitive to small changes in the activation energy. We discovered that in order to provide accurate estimates for hydrogen transfer reactions, specific reaction sub-families had to be introduced. The structure-reactivity relationships for the hydrogen transfer sub-families we developed in Chapter 7 were grouped by radical type or by functional group and were found to be necessary to reproduce theoretical and experimental results. The necessity for hydrogen transfer sub-families can best be seen in Figure 7.5 in which five unique sub-families are visible in the regime where previously a single structure-reactivity relationship was used to model all of these reactions. Additionally, we demonstrated in Chapter 8 that kinetic models of alkane oxidation agreed very poorly with experiment if hydrogen transfer sub-families were not used. In addition to hydrogen transfer, we also used reaction sub-families for β-scission and hydroperoxide decomposition.

9.1.3 Automated mechanism generation can provide accurate models of alkane autoxidation

Using the new library of structure-reactivity relationships presented in Chapter 7, we used rate-based automated mechanism generation to study the autoxidation of octane and decane. With no parameter estimation, the models agreed reasonably well with experimental data. For the octane model, we performed a rigorous parameter estimation procedure to obtain improved values of three parameters in the library of structure-reactivity relationships. The new model agreed very well with available experimental data. Using these results, decane autoxidation was further investigated, and models were obtained that also agreed well with available data. These results indicate that it is possible to greatly expand the models we use to study lubricant degradation. Expanded models could provide new insights into controlling reaction pathways as well as provide a "virtual laboratory" for evaluating new additives and stabilizers.

9.2 Recommendations for Future Work

In addition to making future improvements to the types of models presented in Chapter 8, this work has given rise both to new questions about lubricant degradation and also to the ability to create enhanced models that more accurately represent lubricant degradation.

9.2.1 Kinetic modeling

In the area of kinetic modeling, the results presented here could be improved through future work in a number of ways. A major area for improvement is in the size of the models obtained. Even though rate-based automated mechanism generation was shown to control the mechanism size, there is still room for further mechanism reduction. Such approaches, for example the "important and necessary species" algorithm (Klinke and Broadbelt, 1997; Tomlin et al., 1995), have been shown to greatly reduce the size of kinetic models without significant sacrifice in the quality of the model. If the octane and decane models could be reduced in size, it would increase computational efficiency and also facilitate interrogation of the mechanism in order to elucidate the dominant reaction pathways. Additionally, it would be interesting to apply a global parameter optimization (Singer et al., 2006) technique to the models developed here in order to see if further improvements to the existing model are possible.

9.2.2 Realistic models of lubricant degradation

In relation to lubricant degradation there are several areas in which this work could be expanded. For the specific case of natural lubricants, it would be very interesting to use the approach developed here to build a model of hexadecane oxidation. Hexadecane is a standard lubricant mimic, and there is a wealth of experimental data in the literature about both the kinetics and mechanism of hexadecane oxidation. There are two further extensions from this work as well. First, real lubricant base oils have their properties tailored by creating specific blends of a number of different base components. It would be very helpful to quantify the effect on lubricant degradation of us-

ing blends of different base oils. Additionally, it would be interesting to extend this approach to synthetic lubricants such as polyol esters or poly(α) olefins. Synthetic lubricants are characterized by higher oxidation stability than natural lubricants. Automated mechanism generation is a good choice to investigate the kinetics and mechanism of the degradation of these high-performance lubricants.

9.2.3 Inclusion of antioxidant chemistry

Finally, mechanistic models of lubricant degradation can be slightly modified to make a connection to common lubricant performance tests. This is an important step in demonstrating the utility of kinetic modeling for the evaluation of existing lubricants and the development of new lubricants. For example, the quantity "total acid number", or TAN, is a macroscopic measure of additive performance and lubricant failure and is widely recognized for its simplicity and ability to give comparison between different lubricants. The quantity TAN is easy to calculate from data provided by a mechanistic model. If the models in Chapter 8 were expanded to include the type of antioxidant functionality described in Chapter 5, there would be a direct route to connect the molecular-scale properties/reactivity of antioxidants to macroscopic measures of oxidation inhibition. These same concepts could also be applied to other macroscopic lubricant performance tests like the "oxidation induction time" and the "oxidation inhibition test".

References

Alcala, R.; Greeley, J.; Mavrikakis, M.; Dumesic, J. A. Density-functional theory studies of acetone and propanal hydrogenation on Pt(111). *J. Chem. Phys.* **2002**, *116* (20), 8973–8980.

Alcala, R.; Mavrikakis, M.; Dumesic, J. A. DFT studies for cleavage of C-C and C-O bonds in surface species derived from ethanol on Pt(111). *J. Catal.* **2003**, *218* (1), 178.

Alcala, R.; Shabaker, J.; Huber, G.; Sanchez-Castillo, M.; Dumesic, J. A. Experimental and DFT studies of the conversion of ethanol and acetic acid on PtSn-based catalysts. *J. Phys. Chem. B* **2005**, *109* (6), 2074–2085.

Anglada, J. M.; Domingo, V. M. Mechanism for the gas-phase reaction between formaldehyde and hydroperoxyl radical. A theoretical study. *J. Phys. Chem. A* **2005**, *109* (47), 10786 – 10794.

Anglada, J. M.; Olivella, S.; Sole, A. Mechanistic study of the $CH_3O_2 + HO_2 \rightarrow CH_3O_2H + O_2$ reaction in the gas phase. Computational evidence for the formation of a hydrogen-bonded diradical complex. *J. Phys. Chem. A* **2006**, *110* (18), 6073 – 6082.

Ashcroft, S. J.; BenIsa, M. Effect of dissolved gases on the densities of hydrocarbons. *J. Chem. Eng. Data* **1997**, *42* (6), 1244–1248.

Aubanel, E. E.; Robertson, S. H.; Wardlaw, D. M. Hindered rotor model For radical association reactions. *J. Chem. Soc. Faraday. T* **1991**, *87* (15), 2291–2297.

Avila, D. V.; Ingold, K. U.; Lusztyk, J.; Green, Jr., W. H.; Procopio, D. R. Dramatic solvent effects on the absolute rate constants for abstraction of the hydroxylic hydrogen-atom from tert-butyl hydroperoxide and phenol by the cumyloxyl radical - the role of hydrogen-bonding. *J. Amer. Chem. Soc.* **1995**, *117* (10), 2929–2930.

Ayala, P. Y.; Schlegel, H. B. Identification and treatment of internal rotation in normal mode vibrational analysis. *J. Chem. Phys.* **1998**, *108* (6), 2314–2325.

Baboul, A. G.; Curtiss, L. A.; Redfern, P. C. Gaussian-3 theory using density functional geometries and zero-point energies. *J. Chem. Phys.* **1999**, *110* (16), 7650–7657.

Babushok, V. I.; Tsang, W. Kinetic modeling of heptane combustion and PAH formation. *J. Propul. Power* **2004**, *20* (3), 403–414.

Balasundram, N.; Sundram, K.; Samman, S. Phenolic compounds in plants and agri-industrial by-products: Antioxidant activity, occurrence, and potential uses. *Food Chem.* **2006**, *99* (1), 191–203.

Balint-Kurti, G. G.; Dixon, R.; Marston, C. C. Grid methods for solving the Schrödinger equation and time dependent quantum dynamics of molecular photofragmentation and reactive scattering Processes. *Int. Rev. Phys. Chem.* **1992**, *11*, 317–344.

Balint-Kurti, G. G.; Ward, C. L.; Marston, C. C. Two computer programs for solving the Schrödinger equation for bound state eigenvalues and eigenfunctions using the Fourier Grid Hamiltonian method. *Comput. Phys. Commun.* **1991**, *67*, 285–292.

Barone, V. Vibrational zero-point energies and thermodynamic functions beyond the harmonic approximation. *J. Chem. Phys.* **2004**, *120* (7), 3059–3065.

Becke, A. Density-functional thermochemistry. III. The role of exact exchange. *J. Chem. Phys.* **1993**, *98* (7), 5648–5652.

Benson, S. W. *Thermochemical Kinetics*; John Wiley, New York, 1976.

Bhattacharjee, B.; Schwer, D. A.; Barton, P. I.; Green, W. H. Optimally-reduced kinetic models: Reaction elimination in large-scale kinetic mechanisms. *Combust. Flame* **2003**, *135* (3), 191–208.

Blackmond, D. G. Requiem for the reaction-rate equation? (vol 83, pg 133, 2002). *Catal. Lett.* **2003**, *89* (3-4), 281–284.

Blaine, S.; Savage, P. E. Reaction pathways in lubricant degradation. 1. Analytical characterization of *n*-hexadecane autoxidation products. *Ind. Eng. Chem. Res.* **1991**a, *30* (4), 792–798.

Blaine, S.; Savage, P. E. Reaction pathways in lubricant degradation. 2. *n*-hexadecane autoxidation. *Ind. Eng. Chem. Res.* **1991**b, *30* (9), 2185–2191.

Blaine, S.; Savage, P. E. Reaction pathways in lubricant degradation. 3. Reaction model for *n*-hexadecane autoxidation. *Ind. Eng. Chem. Res.* **1992**, *31* (1), 69–75.

Blowers, P.; Masel, R. I. An extension of the Marcus equation for atom transfer reactions. *J. Phys. Chem. A* **1999**, *103* (35), 7047–7054.

Blowers, P.; Masel, R. I. Engineering approximations for activation energies in hydrogen transfer Reactions. *AIChE J*. **2000**, *46* (10), 2041–2052.

Boock, L. T.; Klein, M. T. Experimental Kinetics and Mechanistic Modeling of the Oxidation of Simple Mixtures in Near-Critical Water. *Ind. Eng. Chem. Res*. **1994**, *33* (11), 2554–2562.

Bowman, J. M. The self-consistent-field approach To polyatomic vibrations. *Acc. Chem. Res*. **1986**, *19* (7), 202–208.

Bowman, J. M.; Carter, S.; Huang, X. C. MULTIMODE: A code to calculate rovibrational energies of polyatomic molecules. *Int. Rev. Phys. Chem*. **2003**, *22* (3), 533–549.

Bowman, W.; Stachowiak, G. Determining the oxidation stability of lubricating oils using sealed capsule differential scanning calorimetry (SCDSC). *Tribol. Int*. **1996**, *29* (1), 27–34.

Brinck, T.; Lee, H.; Jonsson, M. Quantum chemical studies on the thermochemistry of alkyl and peroxyl Radicals. *J. Phys. Chem. A* **1999**, *103* (35), 7094–7104.

Broadbelt, L.; Snurr, R. Applications of molecular modeling in heterogeneous catalysis research. *Appl. Catal. A-Gen* **2000**, *200* (1-2), 23–46.

Broadbelt, L. J.; Pfaendtner, J. Lexicography of kinetic modeling of complex reaction networks. *AIChE J*. **2005**, *51* (8), 2112–2121.

Broadbelt, L. J.; Stark, S.; Klein, M. Computer generated pyrolysis modeling: On-the-fly Generation of species and Reactions and Rates. *Ind. Eng. Chem. Res*. **1994**a, *33*, 790–799.

Broadbelt, L. J.; Stark, S.; Klein, M. Termination of computer-generated reaction mechanisms: Species rank-based convergence criterion. *Ind. Eng. Chem. Res*. **1995**, *34*, 2566–2573.

Broadbelt, L. J.; Stark, S.; Klein, M. Computer generated reaction modeling: Decomposition and encoding algorithms for determining species uniqueness. *Comput. Chem. Eng*. **1996**, *20* (2), 113–129.

Broadbelt, L. J.; Stark, S. M.; Klein, M. T. Computer generated reaction networks: On-the-fly calculation of species properties using computational quantum chemistry. *Chem. Eng. Sci*. **1994**b, *49* (24B), 4991–5010.

Campbell, J. D.; Teymour, F.; Morbidelli, M. Production of hyperbranched polystyrene by high-temperature polymerization. *Macromolecules* **2005**, *38* (3), 752–760.

Cancés, E.; Mennucci, B.; Tomasi, J. A new integral equation formalism for the polarizable continuum model: Theoretical background and applications to isotropic and anisotropic dielectrics. *J. Chem. Phys.* **1997**, *107* (8), 3032–3041.

Carbonniere, P.; Barone, V. Coriolis couplings in variational computations of vibrational spectra beyond the harmonic approximation: implementation and validation. *Chem. Phys. Lett.* **2004**, *392* (4-6), 365–371.

Carstensen, H. H.; Naik, C. V.; Dean, A. M. Detailed modeling of the reaction of C_2H_5 + O_2. *J. Phys. Chem. A* **2005**, *109* (10), 2264–2281.

Carter, S.; Bowman, J. M. The adiabatic rotation approximation for rovibrational energies of many-mode systems: Description and tests of the method. *J. Chem. Phys.* **1998**, *108* (11), 4397–4404.

Carter, S.; Bowman, J. M.; Handy, N. C. Extensions and tests of 'multimodes': a code to obtain accurate vibration/rotation energies of many-mode molecules. *Theor. Chem. Acc.* **1998**, *100* (1-4), 191–198.

Carter, S.; Culik, S. J.; Bowman, J. M. Vibrational self-consistent field method for many-mode systems: A new approach and application to the vibrations of CO adsorbed on Cu(100). *J. Chem. Phys.* **1997**, *107* (24), 10458–10469.

Carter, S.; Handy, N. C.; Tarroni, R. A variational method for the calculation of spin-rovibronic energy levels of any triatomic molecule in an electronic triplet state. *Mol. Phys.* **2005**, *103* (6-8), 1131–1137.

Chan, W.; Hamilton, I.; Pritchard, H. Self-abstraction in aliphatic hydroperoxyl radicals. *J. Chem. Soc. Faraday Trans.* **1998**, *94* (16), 2303–2306.

Chempath, S.; Predescu, C.; Bell, A. T. Quantum mechanical single molecule partition function from path integral Monte Carlo simulations. *J. Chem. Phys.* **2006**, *124* (23), 234104.

Chen, C.; Hsu, S. A chemical kinetics model to predict lubricant performance in a diesel engine. Part I: Simulation methodology. *Tribol. Lett.* **2003**, *14* (2), 83–90.

Chen, C. J.; Bozzelli, J. W. Analysis of tertiary butyl radical plus O_2, isobutene plus HO_2, isobutene plus OH, and isobutene-OH adducts plus O_2: A detailed tertiary butyl oxidation mechanism. *J. Phys. Chem. A* **1999**, *103* (48), 9731 – 9769.

Chuang, Y. Y.; Truhlar, D. G. Statistical thermodynamics of bond torsional modes. *J. Chem. Phys.* **2000**, *112* (3), 1221–1228.

Ciobica, I. M.; Kramer, G. J.; Ge, Q.; Neurock, M.; van Santen, R. A. Mechanisms for chain growth in Fischer-Tropsch synthesis over Ru(0001). *J. Catal.* **2002**, *212* (2), 136–144.

Cohen, A.; Marcus, R. A. On the slope of free energy plots in chemical kinetics. *J. Phys. Chem.* **1968**, *72* (12), 4249–4256.

Coote, M. L.; Wood, G. P. F.; Radom, L. Methyl radical addition to C=S double bonds: Kinetic versus thermodynamic preferences. *J. Phys. Chem. A* **2002**, *106* (50), 12124–12138.

Cullis, C.; Hirschler, M.; Rogers, R. The oxidation of decane in the liquid and gaseous phases. *Proc. R. Soc. Lond. A. Mat.* **1981**, *1763* (375), 543–563.

Curran, H. J.; Gaffuri, P.; Pitz, W. J.; Westbrook, C. K. A comprehensive modeling study of iso-octane oxidation. *Combust. Flame* **2002**, *129* (3), 253–280.

Curtiss, L. A.; Raghavachari, K.; Redfern, P. C.; Rassolov, V.; Pople, J. A. Gaussian-3 (G3) theory for molecules containing first and second-row atoms. *J. Chem. Phys.* **1998**, *109* (18), 7764–7775.

Curtiss, L. A.; Redfern, P. C.; Frurip, D. J. Theoretical methods for computing enthalpies of formation in gaseous compounds. In *Reviews in Computational Chemistry*; John Wiley and Sons, 2000,; pp. 147–211.

Curtiss, L. A.; Redfern, P. C.; Raghavachari, K.; Rassolov, V.; Pople, J. A. Gaussian-3 theory using reduced Moller-Plesset order. *J. Chem. Phys.* **1999**, *110* (10), 4703–4709.

da Silva, G.; Kim, C.-H.; Bozzelli, J. W. Thermodynamic properties (enthalpy, bond energy, entropy, and heat capacity) and internal rotor potentials of vinyl alcohol, methyl vinyl ether, and their corresponding radicals. *J. Phys. Chem. A* **2006**, *110* (25), 7925–7934.

De Witt, M. J.; Dooling, D.; Broadbelt, L. J. Computer generation of reaction mechanisms using quantitative rate information: Application to long-chain hydrocarbon pyrolysis. *Ind. Eng. Chem. Res.* **2000**, *39* (7), 2228–2237.

Denisov, E.; Khudyakov, I. Mechanisms Of action and reactivities of the free-radicals of inhibitors. *Chem. Rev.* **1987**, *87* (6), 1313 – 1357.

Denisov, E. T. *Liquid-Phase Reaction Rate Constants*; Plenum Press, New York, 1974.

Denisov, E. T.; Denisova, T. G. *Handbook of Antioxidants, Bond Dissociation Energies, Rate Constants, Activation Energies and Enthalpies of Reactions*; CRC Press LLC, Boca Raton, 2000.

Denisova, T. G.; Denisov, E. T. Kinetic parameters of alkyl, alkoxy, and peroxy radical isomerization. *Kinet. Catal.* **2001**, *42* (5), 620–630.

Donahue, N. M.; Clarke, J. S.; Anderson, J. G. Predicting radical-molecule barrier heights: The role of the ionic surface. *J. Phys. Chem. A* **1998**, *102* (22), 3923–3933.

Dooling, D. J.; Nielsen, R. J.; Broadbelt, L. J. A density-functional study of the interaction of nitrogen with ruthenium clusters. *Chem. Eng. Sci.* **1999**a, *54* (15-16), 3399–3409.

Dooling, D. J.; Rekoske, J. E.; Broadbelt, L. J. Microkinetic models of catalytic reactions on nonuniform surfaces: Application to model and real systems. *Langmuir* **1999**b, *15* (18), 5846–5856.

Dumesic, J. A.; Rudd, D.; Aparicio, L.; Rekoske, J. E.; Trevino, A. *The Microkinetics of Heterogeneous Catalysis*; American Chemical Society: Washington, DC, 1993.

East, A. L. L.; Radom, L. *Ab initio* statistical thermodynamical models for the computation of third-law entropies. *J. Chem. Phys.* **1997**, *106* (16), 6655–6674.

Ellingson, B. A.; Lynch, V. A.; Mielke, S. L.; Truhlar, D. G. Statistical thermodynamics of bond torsional modes: Tests of separable, almost-separable, and improved Pitzer-Gwinn approximations. *J. Chem. Phys.* **2006**, *125* (8), 084305.

Emanuel, N.; Denisov, E. T.; Maizus, Z. *Liquid-phase Oxidation of Hydrocarbons*; Plenum Press, New York, 1967.

Emanuel, N.; Gál, D. *Modelling of Oxidation Processes. Prototype: The Oxidation of Ethylbenzene*; Akadémiai Kiadoó, Budapest, 1986.

Espinosa, E.; Molins, E.; Lecomte, C. Hydrogen bond strengths revealed by topological analyses of experimentally observed electron densities. *Chem. Phys. Lett.* **1998**, *285* (3-4), 170–173.

Ess, D. H.; Houk, K. N. Activation energies of pericyclic reactions: Performance of DFT, MP2, and CBS-QB3 methods for the prediction of activation barriers and reaction energetics of 1,3-dipolar cycloadditions, and revised activation enthalpies for a standard set of hydrocarbon pericyclic reactions. *J. Phys. Chem. A* **2005**, *109* (42), 9542–9553.

Evans, M.; Polanyí, M. Inertia and driving force of chemical reactions. *T. Faraday Soc.* **1938**, *34* (11), 11–29.

Feng, A.; Karasek, K. Coke formation from aircraft engine oils: Part II - effects of oil formulation and surface composition. *Tribol. T.* **2000**, *43* (4), 677–680.

Fournet, R.; Battin-Leclerc, F.; Glaude, P. A.; Judenherc, B.; Warth, V.; Come, G. M.; Scacchi, G.; Ristori, A.; Pengloan, G.; Dagaut, P.; Cathonnet, M. The gas-phase oxidation of n-hexadecane. *Int. J. Chem. Kinet.* **2001**, *33* (10), 574–586.

Frenkel, M.; Marsh, K. N.; Wilhoi, R. C.; Kabo, G. J.; Roganov, G. N. *Thermodynamics of Organic Compounds in the Gas State*; vol. 1; Thermodynamics Research Center: College Station, 1994.

Frisch, M. J.; Trucks, G. W.; Schlegel, H. B.; Scuseria, G. E.; Robb, M. A.; Cheeseman, J. R.; Montgomery, Jr., J. A.; Vreven, T.; Kudin, K. N.; Burant, J. C.; Millam, J. M.; Iyengar, S. S.; Tomasi, J.; Barone, V.; Mennucci, B.; Cossi, M.; Scalmani, G.; Rega, N.; Petersson, G. A.; Nakatsuji, H.; Hada, M.; Ehara, M.; Toyota, K.; Fukuda, R.; Hasegawa, J.; Ishida, M.; Nakajima, T.; Honda, Y.; Kitao, O.; Nakai, H.; Klene, M.; Li, X.; Knox, J. E.; Hratchian, H. P.; Cross, J. B.; Bakken, V.; Adamo, C.; Jaramillo, J.; Gomperts, R.; Stratmann, R. E.; Yazyev, O.; Austin, A. J.; Cammi, R.; Pomelli, C.; Ochterski, J. W.; Ayala, P. Y.; Morokuma, K.; Voth, G. A.; Salvador, P.; Dannenberg, J. J.; Zakrzewski, V. G.; Dapprich, S.; Daniels, A. D.; Strain, M. C.; Farkas, O.; Malick, D. K.; Rabuck, A. D.; Raghavachari, K.; Foresman, J. B.; Ortiz, J. V.; Cui, Q.; Baboul, A. G.; Clifford, S.; Cioslowski, J.; Stefanov, B. B.; Liu, G.; Liashenko, A.; Piskorz, P.; Komaromi, I.; Martin, R. L.; Fox, D. J.; Keith, T.; Al-Laham, M. A.; Peng, C. Y.; Nanayakkara, A.; Challacombe, M.; Gill, P. M. W.; Johnson, B.; Chen, W.; Wong, M. W.; Gonzalez, C.; Pople, J. A. Gaussian 03, Revision C.02, 2003; Gaussian, Inc., Wallingford, CT, 2004.

Froment, G. Single event kinetic modeling of complex catalytic processes. *Catal. Rev.* **2005**, *47* (1), 83.

Gang, J.; Pilling, M. J.; Robertson, S. H. Partition functions and densities of states for butane and pentane. *J. Chem. Soc. Faraday Trans.* **1996**, *92* (19), 3509–3518.

Gang, J.; Pilling, M. J.; Robertson, S. H. Asymmetric internal rotation: Application to the 2-C_4H_9 $\rightleftharpoons$ CH_3 + C_3H_6 reaction. *J. Chem. Soc. Faraday Trans.* **1997**, *93* (8), 1481–1491.

Gang, J.; Pilling, M. J.; Robertson, S. H. Monte Carlo calculation of partition functions for straight chain alkanes. *Chem. Phys.* **1998**, *231* (2-3), 183–192.

Gao, J. L.; Truhlar, D. G. Quantum mechanical methods for enzyme kinetics. *Annu. Rev. Phys. Chem.* **2002**, *53*, 467–505.

Garcia-Ochoa, F.; Romero, A.; Querol, J. Modeling Of the thermal normal-octane oxidation in the liquid-phase. *Ind. Eng. Chem. Res.* **1989**, *28* (1), 43–48.

Gasteiger, J.; Sadowski, J.; Schuur, J.; Selzer, P.; Steinhauer, L.; Steinhauer, V. Chemical information in 3D space. *J. Chem. Inf. Comp. Sci.* **1996**, *36* (5), 1030–1037.

Gomez-Balderas, R.; Coote, M.; Henry, D.; Fischer, H.; Radom, L. What is the origin of the contrathermodynamic behavior in methyl radical addition to alkynes versus alkenes? *J. Phys. Chem. A* **2003**, *107* (31), 6082–6090.

Gomez-Balderas, R.; Coote, M. L.; Hendry, D.; Radom, L. Reliable theoretical procedures for calculating the rate of methyl radical addition to carbon-carbon double and triple Bonds. *J. Phys. Chem. A* **2004**, *108* (15), 2874–2883.

Gonzalez, C.; Schlegel, H. B. An improved algorithm for reaction path following. *J. Chem. Phys.* **1989**, *90* (4), 2154–2161.

Gonzalez-Lafont, A.; Truong, T. N.; Truhlar, D. G. Interpolated variational transition-state theory: Practical methods for estimating variational transition-state properties and tunneling contributions to chemical reaction rates from electronic structure calculations. *J. Chem. Phys.* **1991**, *95* (12), 8875–8894.

Gorelsky, S. Software for Computational Chemistry. In *Comprehensive Coordination Chemistry - II*; Meyer, T.; McCleverty, J., Eds.; Elsevier; vol. 2, 2004; pp. 687–689.

Greeley, J.; Mavrikakis, M. Alloy catalysts designed from first principles. *Nat. Mater.* **2004**, *3* (11), 810–815.

Green, W. H.; Barton, P. I.; Bhattacharjee, B.; Matheu, D. M.; Schwer, D. A.; Song, J.; Sumathi, R.; Carstensen, H. H.; Dean, A. M.; Grenda, J. M. Computer construction of detailed chemical kinetic models for gas-phase reactors. *Ind. Eng. Chem. Res.* **2001**, *40* (23), 5362–5370.

Gunsel, S.; Klaus, E.; Duda, J. High temperature deposition characteristics of mineral oil and synthetic lubricant basestocks. *J. STLE* **1988**, *44* (8), 703–708.

Hamilton, E. J.; Korcek, S.; Mahoney, L. R.; Zinbio, M. Kinetics and mechanism of the autoxidation of pentaerythrityl tetraheptanoate at 180-220 ^{o}C. *Int. J. Chem. Kinet.* **1980**, *7*, 577–603.

Handy, N. C. The derivation of vibration-rotation kinetic-energy operators, in internal coordinates. *Mol. Phys.* **1987**, *61* (1), 207–223.

Handy, N. C.; Carter, S. Large vibrational variational calculations using ‘multimode’ and an iterative diagonalization technique. *Mol. Phys.* **2004**, *102* (21-22), 2201–2205.

Hatzimanikatis, V.; Li, C. H.; Ionita, J. A.; Broadbelt, L. J. Metabolic networks: enzyme function and metabolite structure. *Curr. Opin. Struct. Biol.* **2004**, *14* (3), 300–306.

Hatzimanikatis, V.; Li, C. H.; Ionita, J. A.; Henry, C. S.; Jankowski, M. D.; Broadbelt, L. J. Exploring the diversity of complex metabolic networks. *Bioinformatics* **2005**, *21* (8), 1603–1609.

Haubein, N. C.; McMillan, S. A.; Broadbelt, L. J. Many-body optimization using an ab initio Monte Carlo method. *J. Chem. Inf. Comp. Sci.* **2003**, *43* (1), 68–74.

Hemelsoet, K.; Van Speybroeck, V.; Marin, G. B.; De Proft, F.; Geerlings, P.; Waroquier, M. Reactivity indices for radical reactions involving polyaromatics. *J. Phys. Chem. A* **2004**, *108* (35), 7281–7290.

Henry, D. J.; Radom, L. Theoretical thermochemistry of radicals. In *Quantum-Mechanical Prediction of Thermochemical Data*; Cioslowski, J., Ed.; Kluwer Academic Publishers, Dordrecht; vol. 22 of *Understanding Chemical Reactivity*, 2001; pp. 161–197.

Herschbach, D. R.; Johnston, H. S.; Pitzer, K. S.; Powell, R. E. Theoretical pre-exponential factors for 12 bimolecular reactions. *J. Chem. Phys.* **1956**, *25* (4), 736–741.

Heuts, J. P. A.; Gilbert, R. G.; Radom, L. Determination of Arrhenius parameters for propagation in free-radical polymerizations: An assessment of ab initio procedures. *J. Phys. Chem.* **1996**, *100* (49), 18997–19006.

Heyden, A.; Peters, B.; Bell, A. T.; Keil, F. J. Comprehensive DFT study of nitrous oxide decomposition over Fe-ZSM-5. *J. Phys. Chem. B* **2005**, *109* (5), 1857–1873.

Hinnemann, B.; Norskov, J. K.; Topsoe, H. A density functional study of the chemical differences between type I and type II MoS_2-based structures in hydrotreating catalysts. *J. Phys. Chem. B* **2005**, *109* (6), 2245–2253.

Hinrichsen, O. Kinetic simulation of ammonia synthesis catalyzed by ruthenium. *Catal. Today* **1999**, *53* (2), 177–188.

Hirschfelder, J. O.; Wigner, E. J. Some quantum-mechanical considerations in the theory of reactions involving an activation energy. *J. Chem. Phys.* **1939**, *7* (8), 616–628.

Holzhutter, S.; Holzhutter, H. G. Computational design of reduced metabolic networks. *ChemBioChem* **2004**, *5* (10), 1401–1422.

Honkala, K.; Hellman, A.; Remediakis, I. N.; Logadottir, A.; Carlsson, A.; Dahl, S.; Christensen, C. H.; Norskov, J. K. Ammonia synthesis from first-principles calculations. *Science* **2005**, *307* (5709), 555–558.

Howard, J. A.; Scaiano, J. C. Chapter 8: Oxyl-, Peroxyl- and Related Radicals. In *Radical Reaction Rates in Liquids*; Fischer, H., Ed.; Springer-Verlag, Berlin; vol. 13d of *Landolt-Bornstein: Group II Molecules and Radicals*, 1997; pp. 325–336.

Hunter, M.; Klaus, E.; Duda, J. A kinetic study of antioxidation mechanisms. *Lubr. Eng*. **1993**, *49* (6), 492–498.

Hutchinson, R. A. Modeling of chain length and long-chain branching distributions in free-radical polymerization. *Macromol. Theory Simul*. **2001**, *10* (3), 144–157.

Isaacson, A. D.; Truhlar, D. G. The accuracy of the Pitzer-Gwinn method for partition-functions of anharmonic vibrational-modes. *J. Chem. Phys*. **1981**, *75* (8), 4090–4094.

Iyer, S. D.; Joshi, P. V.; Klein, M. T. Automated model building and modeling of alcohol oxidation in high temperature water. *Environ. Prog*. **1998**, *17* (4), 221–233.

Izgorodina, E. I.; Coote, M. L. Accurate ab initio prediction of propagation rate coefficients in free-radical polymerization: Acrylonitrile and vinyl chloride. *J. Chem. Phys*. **2006**, *324* (1), 96–110.

Jensen, F. *Introduction to Computational Chemistry*; John Wiley, 1999.

Jensen, R.; Korcek, S.; Mahoney, L.; Zinbo, M. Liquid-phase autoxidation of organic compounds at elevated temperatures. 2. Kinetics and mechanism of the formation of cleavage products in *n*-hexadecane autoxidation. *J. Amer. Chem. Soc*. **1981**, *103* (7), 1742–1749.

Jensen, R.; Korcek, S.; Zinbo, M. Formation and isomerization and cyclization reactions of hydroperoxyalkyl radicals in hexadecane autoxidation. *J. Amer. Chem. Soc*. **1992**, *114* (20), 7742–7748.

Katzer, G.; Sax, A. F. Beyond the harmonic approximation: Impact of anharmonic molecular vibrations on the thermochemistry of silicon hydrides. *J. Phys. Chem. A* **2002**a, *106* (31), 7204–7215.

Katzer, G.; Sax, A. F. Numerical determination of pseudorotation constants. *J. Chem. Phys*. **2002**b, *117* (8), 8219–8228.

Katzer, G.; Sax, A. F. A novel partition function for partially asymmetrical internal rotation. *Chem. Phys. Lett*. **2003**, *368* (3-4), 473–479.

Katzer, G.; Sax, A. F. Identification and thermodynamic treatment of several types of large-amplitude motions. *J. Comput. Chem*. **2005**, *26* (14), 1438–1451.

Khan, S. Computational Chemistry and Mechanistic Modeling of Atmospheric Chemistry: Models of Alkane and Oxygenate Chemistry; PhD Thesis; Northwestern University, 2005.

Kilpatrick, J. E.; Pitzer, K. S. Energy levels and thermodynamic functions for molecules with internal rotation. III. Compound rotation. *J. Chem. Phys.* **1949**, *17* (11), 1064–1075.

Klinke, D. J.; Broadbelt, L. J. Mechanism reduction during computer generation of compact reaction models. *AIChE J.* **1997**, *43* (7), 1828–1837.

Klinke, D. J.; Broadbelt, L. J. Construction of a mechanistic model of Fischer-Tropsch synthesis on Ni(111) and Co(0001) surfaces. *Chem. Eng. Sci.* **1999**a, *54* (15-16), 3379–3389.

Klinke, D. J.; Broadbelt, L. J. A theoretical study of hydrogen chemisorption on Ni(111) and Co(0001) surfaces. *Surf. Sci.* **1999**b, *429* (1-3), 169–177.

Klinke, D. J.; Dooling, D. J.; Broadbelt, L. J. A theoretical study of methylidyne chemisorption on Ni(111) and Co(0001) surfaces. *Surf. Sci.* **1999**, *425* (2-3), 334–342.

Klinke, D. J.; Wilke, S.; Broadbelt, L. J. A theoretical study of carbon chemisorption on Ni(111) and Co(0001) surfaces. *J. Catal.* **1998**, *178* (2), 540–554.

Knyazev, V. D. Density of states of one-dimensional hindered internal rotors and separability of rotational degrees of freedom. *J. Phys. Chem. A* **1998**, *102* (22), 3916–3922.

Knyazev, V. D.; Tsang, W. Nonharmonic degrees of freedom: Densities of states and thermodynamic functions. *J. Phys. Chem. A* **1998**, *102* (46), 9167–9176.

Koh, C.-S.; Butt, J. B. Experimental and modeling study of kinetics and selectivity in the oxidation of a poly*(alpha)*-olefin) lubricant. *Ind. Eng. Chem. Res.* **1995**, *34* (2), 524–535.

Krim, J. Surface science and the atomic-scale origins of friction: what once was old is new again. *Surf. Sci.* **2002**, *500* (1-3), 741–758.

Kruse, T. M.; Wong, H.-W.; Broadbelt, L. J. Mechanistic modeling of polymer pyrolysis: polypropylene. *Macromolecules* **2003**, *36* (25), 9594–9607.

Kruse, T. M.; Woo, O. S.; Wong, H.-W.; Khan, S. S.; Broadbelt, L. J. mechanistic modeling of polymer degradation: A comprehensive study of polystyrene. *Macromolecules* **2002**, *35* (20), 7830–7844.

Kudish, I. I. Effect of lubricant degradation on contact fatigue. *Tribol. Trans.* **2005**, *48* (1), 100–107.

Leach, A. *Molecular Modelling: Principles and Applications*; Prentice Hall, Harlow, 2001.

Li, C. H.; Henry, C. S.; Jankowski, M. D.; Ionita, J. A.; Hatzimanikatis, V.; Broadbelt, L. J. Computational discovery of biochemical routes to specialty chemicals. *Chem. Eng. Sci.* **2004**, *59* (22-23), 5051–5060.

Lightfoot, P. D.; Cox, R. A.; Crowley, J. N.; Destriau, M.; Hayman, G. D.; Jenkin, M. E.; Moortgat, G. T.; Zabel, F. Organic peroxy radicals: Kinetics, spectroscopy and tropospheric chemistry. *Atmos. Environ. A-Gen.* **1992**, *26* (10), 1805–1961.

Loader, R. J.; Singh, N.; O'Malley, P. J.; Popelier, P. The cytotoxicity of ortho alkyl substituted 4-X-phenols: A QSAR based on theoretical bond lengths and electron densities. *Bioorg. Med. Chem. Lett.* **2006**, *16* (5), 1249–1254.

Lundback, M.; Hedenqvist, M. S.; Mattozzi, A.; Gedde, U. W. Migration of phenolic antioxidants from linear and branched polyethylene. *Polym. Deg. Stab.* **2006**, *91* (7), 1571–1580.

Lynch, V. A.; Mielke, S. L.; Truhlar, D. G. Accurate vibrational-rotational partition functions and standard-state free energy values for H_2O_2 from Monte Carlo path-integral calculations. *J. Chem. Phys.* **2004**, *121* (11), 5148–5162.

Lynch, V. A.; Mielke, S. L.; Truhlar, D. G. High-precision quantum thermochemistry on nonquasiharmonic potentials: Converged path-integral free energies and a systematically convergent family of generalized Pitzer-Gwinn approximations. *J. Phys. Chem. A* **2006**, *110* (17), 5965–5965.

Mahoney, L.; Korcek, S.; Hoffman, S.; Willermet, P. Determination of antioxidant capacity of new and used lubricants - method and applications. *Ind. Eng. Prod. Res. Dev.* **1978**, *17* (3), 250–255.

Makowska, M.; Kajdas, C.; Gradkowski, M. Interactions of *n*-hexadecane with 52100 steel surface under friction conditions. *Tribol. Lett.* **2002**, *13* (2), 65–70.

Marcus, R. A. Theoretical relations among rate constants and barriers and Bronsted slopes of chemical reactions. *J. Phys. Chem.* **1968**, *72* (3), 891–899.

Marston, C. C.; Balint-Kurti, G. G. The Fourier grid Hamiltonian method for bound state eigenvalues and eigenfunctions. *J. Chem. Phys.* **1989**, *91* (6), 3571–3576.

Masel, R. I. *Chemical Kinetics and Catalysis*; John Wiley, New York, 2002.

Matheu, D. M.; Dean, A. M.; Grenda, J. M.; Green, W. H. Mechanism generation with integrated pressure dependence: A new model for methane pyrolysis. *J. Phys. Chem. A* **2003**, *107* (41), 8552–8565.

Mavrovouniotis, M. Group contributions for estimating standard Gibbs energies of formation of biochemical compounds in aqueous solution. *Biotechnol. Bioeng.* **1990**, *36*, 1070–1082.

McClurg, R. B.; Flagan, R. C.; Goddard, W. A. The hindered rotor density-of-states interpolation function. *J. Chem. Phys.* **1997**, *16* (2), 6675–6680.

McMillan, S. A.; Broadbelt, L. J.; Snurr, R. Q. Effect of local framework heterogeneity on NO adsorption in cobalt-ferrierite. *J. Catal.* **2003**a, *219* (1), 117–125.

McMillan, S. A.; Snurr, R. Q.; Broadbelt, L. J. Origin and characteristics of preferential adsorption on different sites in cobalt-exchanged ferrierite. *J. Phys. Chem. B* **2003**b, *107* (48), 13329–13335.

McQuarrie, D. A.; Simon, J. D. *Molecular Thermodynamics*; University Science Books: Sausalito, 1999.

Méreau, R.; Rayez, M. T.; Caralp, F.; Rayez, J. C. Theoretical study of alkoxyl radical decomposition reactions: structure-activity relationships. *Phys. Chem. Chem. Phys.* **2000**, *2* (17), 3765–3772.

Merle, J. K.; Hayes, C.; Zalyubovsky, S.; Glover, B.; Miller, T.; Hadad, C. Theoretical determinations of the amibent conformational distributino and unimolecular decompositino of *n*-propylperoxy radical. *J. Phys. Chem. A* **2005**, *109* (16), 3637–3646.

Mhadeshwar, A.; Kitchin, J.; Barteau, M.; Vlachos, D. The role of adsorbate-adsorbate interactions in the rate controlling step and the most abundant reaction intermediate of NH_3 decomposition on Ru. *Catal. Lett.* **2004**, *96* (1-2), 13–22.

Mhadeshwar, A.; Vlachos, D. Microkinetic modeling for water-promoted CO oxidation, water-gas shift, and preferential oxidation of CO on Pt. *J. Phys. Chem. B* **2004**, *108*, 15246–15258.

Migdal, C. Antioxidants. In *Lubricant Additives: Chemistry and Applications*; Rudnick, L., Ed.; Marcel Dekker, Inc., 2003; pp. 1–28.

Mill, T.; Hendry, D. Kinetics and mechanisms of free radical oxidation of alkanes and olefins in the liquid phase. In *Comprehensive Chemical Kinetics*; Elsevier, Amsterdam; vol. 16, 1980; pp. 2–87.

Mill, T.; Montosori, G. The liquid-phase oxidation of 2,4-dimethylpentane. *Int. J. Chem. Kinet.* **1973**, *5*, 119–136.

Miller, T. F.; Clary, D. C. Torsional path integral Monte Carlo method for the quantum simulation of large molecules. *J. Chem. Phys.* **2002**, *116* (19), 8262–8269.

Miller, T. F.; Clary, D. C. Torsional path integral Monte Carlo method for calculating the absolute quantum free energy of large molecules. *J. Chem. Phys.* **2003**, *119* (1), 68–76.

Mills, G.; Jonsson, H.; Schenter, G. K. Reversible work transition-state theory - application to dissociative adsorption of hydrogen. *Surf. Sci.* **1995**, *324* (2-3), 305–337.

Montgomery, J. A.; Frisch, M. J.; Ochterski, J. W.; Petersson, G. A. A complete basis set model chemistry. VI. Use of density functional geometries and frequencies. *J. Chem. Phys.* **1999**, *110* (6), 2822–2827.

Montgomery, J. A.; Frisch, M. J.; Ochterski, J. W.; Petersson, G. A. A complete basis set model chemistry. VII. Use of the minimum population localization method. *J. Chem. Phys.* **2000**, *112* (15), 6532–6542.

Montgomery, J. A.; Ochterski, J. W.; Petersson, G. A. A complete basis set model chemistry. IV. An improved atomic pair natural orbital method. *J. Chem. Phys.* **1994**, *101* (7), 5900–5909.

Moore, J.; Pearson, R. *Kinetics and Mechanism*; John Wiley, New York, 1981.

Murzin, D. Y. On surface heterogeneity and catalytic kinetics. *Ind. Eng. Chem. Res.* **2005**, *44* (6), 1688–1697.

Naidu, S.; Klaus, E.; Duda, J. Kinetic model for high-temperature oxidation of lubricants. *Ind. Eng. Chem. Res.* **1986**, *25* (4), 596–603.

Nakanishi, H.; Onodera, K. Oxidation Stability of Synthetic Lubricants. *J. STLE* **1996**, *53* (5), 29–37.

Narasimhan, C. S. L.; Thybaut, J. W.; Marin, G. B.; Denayer, J. F.; Baron, G. V.; Martens, J. A.; Jacobs, P. A. Relumped single-event microkinetic model for alkane hydrocracking on shape-selective catalysts: catalysis on ZSM-22 pore mouths, bridge acid sites and micropores. *Chem. Eng. Sci.* **2004**, *59* (22-23), 4765–4772.

Natarajan, S.; Olson, W.; Abraham, M. Reaction pathways and kinetics in the degradation of forging lubricants. *Ind. Eng. Chem. Res.* **2000**, *39* (8), 2837–2842.

Neeb, P. Structure-reactivity based estimation of the rate constants for hydroxyl radical reactions with hydrocarbons. *J. Atmos. Chem.* **2000**, *35* (3), 295–315.

NIST Standard Reference Database 17: NIST Chemical Kinetics Database on the Web, 2006; Version 7.0 (Web Version), Release 1.4.

Nordholm, S.; Bacskay, G. Generalized finite-element method applied to bound-state calculation. *Chem. Phys. Lett.* **1976**, *42* (2), 253–258.

Nyden, M.; Petersson, G. A. Complete basis set correlation energies. I. The asymptotic convergence of pair natural orbital expansions. *J. Chem. Phys.* **1981**, *75* (4), 1843–1862.

Ochterski, J. W.; Petersson, G. A.; Mongtomery, J. A. A complete basis set model chemistry. V. Extensions to six or more heavy atoms. *J. Chem. Phys.* **1996**, *104* (7), 2598–2619.

O'Connor, R.; Schmidt, L.; Deutschmann, O. Simulating cyclohexane millisecond oxidation: Coupled chemistry and fluid dynamics. *AIChE J.* **2002**, *48* (6), 1241–1256.

Peeters, J.; Fantechi, G.; Vereecken, L. A generalized structure-activity relationship for the decomposition of (substituted) alkoxy radicals. *J. Atmos. Chem.* **2004**, *48* (1), 59–80.

Peng, C.; Ayala, P. Y.; Schlegel, H. B. Using redundant internal coordinates to optimize equilibrim geometries and transition states. *J. Comp. Chem.* **1996**, *17* (1), 49–56.

Peng, C.; Schlegel, H. B. Combining synchronous transit and quasi-Newton methods to find transition states. *Israel. J. Chem.* **1993**, *33* (4), 449–454.

Peters, B.; Heyden, A.; Bell, A. T.; Chakraborty, A. A growing string method for determining transition states: Comparison to the nudged elastic band and string methods. *J. Chem. Phys.* **2004**, *120* (17), 7877–7886.

Petersson, G. A.; Al-Laham, M. A complete basis set model chemistry. II. Open-shell systems and the total energies of the first-row atoms. *J. Chem. Phys.* **1991**, *94* (9), 6081–6090.

Petersson, G. A.; Malick, D. K.; Wilson, W.; Ochterski, J. W.; Montgomery, J. A.; Frisch, M. J. Calibration and comparison of the Gaussian-2, complete basis set, and density functional methods for computational thermochemistry. *J. Chem. Phys.* **1998**, *109* (24), 10570–10579.

Pfaendtner, J.; Broadbelt, L. J. Elucidation of structure-reactivity relationships in hindered phenols via quantum chemistry and transition state theory. *Chem. Eng. Sci.* **2007**a, *in press*.

Pfaendtner, J.; Broadbelt, L. J. Uncovering the cause of contrathermodynamic behavior in intramolecular hydrogen transfer of alkylperoxy radicals, $ROO \cdot + R'H$. *Submitted to ChemPhysChem* **2007**b, .

Pfaendtner, J.; Yu, X.; Broadbelt, L. J. Calc*k* version 0.9. http: broadbelt.chem-eng.northwestern.edu **2006**a, Northwestern University, 2006.

Pfaendtner, J.; Yu, X.; Broadbelt, L. J. Calctherm version 0.9. http: broadbelt.chem-eng.northwestern.edu **2006**b, Northwestern University, 2006.

Pfaendtner, J.; Yu, X.; Broadbelt, L. J. Quantum chemical investigation of low-temperature intramolecular hydrogen transfer reactions of hydrocarbons. *J. Phys. Chem. A* **2006**c, *110* (37), 10863–10871.

Pfaendtner, J.; Yu, X.; Broadbelt, L. J. The 1D hindered rotor approximation. *Submitted to Theor. Chem. Acc.* **2007**, .

Pickard, J. M.; Jones, E. G. Kinetics of the autoxidation of a jet-A-fuel. *Energ. Fuel.* **1996**, *10* (5), 1074–1077.

Pirro, D.; Wessol, A. *Lubrication Fundamentals*; Exxon Mobil Corporation, New York, 2001.

Pitzer, K. S. Energy levels and thermodynamic functions for molecules with internal rotation. II. Unsymmetrical tops attached to a rigid frame. *J. Chem. Phys.* **1946**, *14* (4), 239–243.

Pitzer, K. S.; Gwinn, W. D. Energy levels and thermodynamic functions for molecules with internal rotation. I. Rigid frame with attached tops. *J. Chem. Phys.* **1942**, *10* (7), 428–440.

Prickett, S. E.; Mavrovouniotis, M. L. Construction of complex reaction systems - III. An example: alkylation of olefins. *Comput. Chem. Eng.* **1997**a, *21* (12), 1325–1337.

Prickett, S. E.; Mavrovouniotis, M. L. Construction of complex reaction systems. 2. Molecule manipulation and reaction application algorithms. *Comput. Chem. Eng.* **1997**b, *21* (11), 1237–1254.

Prickett, S. E.; Mavrovouniotis, M. L. Construction of complex reaction systems.1. Reaction description language. *Comput. Chem. Eng.* **1997**c, *21* (11), 1219–1235.

Ranzi, E.; Dente, M.; Goldaniga, A.; Bozzano, G.; Faravelli, T. Lumping procedures in detailed kinetic modeling of gasification, pyrolysis, partial oxidation and combustion of hydrocarbon mixtures. *Prog. Energ. Combust.* **2001**, *27* (1), 99–139.

Rappé, A.; Casewit, C.; Colwell, K.; Goddard, W.; Skiff, W. UFF, a full periodic table force field for molecular mechanics and molecular dynamics simulations. *J. Amer. Chem. Soc.* **1992**, *114* (25), 10024–10035.

Ratkiewicz, A.; Truong, T. N. Application of chemical graph theory for automated mechanism generation. *J. Chem. Inf. Comp. Sci.* **2003**, *43* (1), 36–44.

Redfern, P. C.; Zapol, P.; Curtiss, L. A.; Raghavachari, K. Assessment of Gaussian-3 and density functional theories for enthalpies of formation of C_1-C_{16} Alkanes. *J. Phys. Chem. A* **2000**, *104* (24), 5850–5854.

Roberts, B.; Steel, A. An extended form of the Evans-Polanyí equation - a simple empirical relationship for the prediction of activation-energies for hydrogen-atom transfer-reactions. *J. Chem. Soc. Perk. T. 2* **1994**, *2* (10), 2155–2162.

Rod, T. H.; Ryde, U. Quantum mechanical free energy barrier for an enzymatic reaction. *Phys. Rev. Lett.* **2005**, *94* (13).

Rudnick, L., Ed.; *Lubricant Additives: Chemistry and Applications*; Marcel Dekker, New York, 2003.

Rudnick, L.; Shubkin, R., Eds.; *Synthetic Lubricants and High-Performance Functional Fluids*; Marcel Dekker, Inc., 1999.

Rust, F. Intramolecular oxidation. The autoxidation of some dimethylalkanes. *J. Amer. Chem. Soc.* **1957**, *79* (15), 4000–4003.

Sabbe, M. K.; Saeys, M.; Reyniers, M. F.; Marin, G. B.; Van Speybroeck, V.; Waroquier, M. Group additive values for the gas phase standard enthalpy of formation of hydrocarbons and hydrocarbon radicals. *J. Phys. Chem. A* **2005**, *109* (33), 7466–7480.

Sadowski, J.; Gasteiger, J.; Klebe, G. Comparison of automatic 3-dimensional model builders using 639 X-ray structures. *J. Chem. Inf. Comp. Sci.* **1994**, *34* (4), 1000–1008.

Saeys, M.; Reyniers, M. F.; Marin, G. B.; Van Speybroeck, V.; Waroquier, M. Ab initio calculations for hydrocarbons: Enthalpy of formation, transition state geometry, and activation energy for radical reactions. *J. Phys. Chem. A* **2003**, *107* (43), 9147–9159.

Saeys, M.; Reyniers, M. F.; Marin, G. B.; Van Speybroeck, V.; Waroquier, M. *Ab Initio* group contribution method for activation energies for radical additions. *AIChE J.* **2004**, *50* (2), 426–444.

Santiso, E.; Gubbins, K. Multi-scale molecular modeling of chemical reactivity. *Mol. Simulat.* **2004**, *30* (11-12), 699–748.

Schmidt, M.; Baldridge, K.; Boatz, J. A.; Elbert, S.; Gordon, M. S.; Jensen, J.; Koseki, S.; Matsunaga, N.; Nguyen, K.; Su, S.; Windus, T.; Dupuis, M.; Montgomery, J. A. General Atomic and Molecular Electronic Structure System. *J. Comp. Chem.* **1993**, *14*, 1347–1363.

Schwer, D. A.; Lu, P. S.; Green, W. H. An adaptive chemistry approach to modeling complex kinetics in reacting flows. *Combust. Flame* **2003**, *133* (4), 451–465.

Scott, A.; Radom, L. Harmonic vibrational frequencies: an evaluation of Hartree-Fock, Møller-Plesset, quadratic configuration interaction, density functional theory, and semiempirical scale factors. *J. Phys. Chem.* **1996**, *100* (41), 16502–16513.

Sebbarand, N.; Bockhorn, H.; Bozzelli, J. W. Thermochemical properties, rotation barriers, and group additivity for unsaturated oxygenated hydrocarbons and radicals resulting from reaction of vinyl and phenyl radical systems with O_2. *J. Phys. Chem. A* **2005**, *109* (10), 2233–2253.

Sickle, D. V.; Mill, T.; Mayo, F.; Richardson, H.; Gould, C. Intramolecular propagation in the oxidation of *n*-alkanes. autoxidation of *n*-pentane and *n*-octane. *J. Org. Chem.* **1973**, *38* (26), 4435–4440.

Simon, S.; Duran, M.; Dannenberg, J. J. How does basis set superposition error change the potential surfaces for hydrogen-bonded dimers? *J. Chem. Phys.* **1996**, *105* (24), 11024–11031.

Singer, A.; Taylor, J.; Barton, P.; Green, W. Global dynamic optimization for parameter estimation in chemical kinetics. *J. Phys. Chem. A* **2006**, *110* (3), 971–976.

Singh, N.; Loader, R. J.; O'Malley, P. J.; Popelier, P. Computation of relative bond dissociation enthalpies of phenolic antioxidants from quantum topological molecular similarity. *J. Phys. Chem. A* **2006**, *110* (20), 6498–6503.

Singh, N.; O'Malley, P. J.; Popelier, P. Mechanistic aspects of hydrogen abstraction for phenolic antioxidants. Electronic structure and topological electron density analysis. *Phys. Chem. Chem. Phys.* **2005**, *7* (4), 614–619.

Smith, G. P.; Golden, D. M.; Frenklach, M.; Moriarty, N. W.; Boris Eiteneer, M. G.; Bowman, C. T.; Hanson, R. K.; Song, S.; William C. Gardiner, J.; Lissianski, V. V.; Qin, Z. GRI Mechanism 3.0; WWW, 2007; http://www.me.berkeley.edu/gri_mech/.

Smith, I. W. M.; Ravishankara, A. R. Role of hydrogen-bonded intermediates in the bimolecular reactions of the hydroxyl radical. *J. Phys. Chem. A* **2002**, *106* (19), 4798–4807.

Stein, S.; Rukkers, J.; Brown, R. NIST Standard Reference Database 25: NIST Structures and Properties Database and Estimation Program, 1991.

Stellman, C.; Ewing, K.; Bucholtz, F.; Aggarwal, I. Monitoring the degradation of a synthetic lubricant oil using infrared absorption and fluorescence emission and multivariate analysis: A feasibilty study. *Lubr. Eng*. **1999**, *54* (10), 42–52.

Stewart, W. E.; Caractosios, M.; Sørensen, J. P. Double precision differential-algebraic sensitive analysis code (DDASAC), 1997a; Version 1997.0. Madison, WI.

Stewart, W. E.; Caractosios, M.; Sørensen, J. P. Generalized regression software (GREG), 1997b; Version 1997.0. Madison, WI.

Sumathi, R.; Carstensen, H. H.; Green, Jr., W. H. Reaction rate prediction via group additivity Part 1: H abstraction from alkanes by H and CH_3. *J. Phys. Chem. A* **2001**a, *105* (28), 6910–6925.

Sumathi, R.; Carstensen, H. H.; Green, Jr., W. H. Reaction rate prediction via group additivity part 2: H-abstraction from alkenes, alkynes, alcohols, aldehydes, and acids by H atoms. *J. Phys. Chem. A* **2001**b, *105* (39), 8969–8984.

Sumathi, R.; Carstensen, H. H.; Green, Jr., W. H. Reaction rate prediction via group additivity part 3: Effect of substituents with CH_2 as the mediator. *J. Phys. Chem. A* **2002**, *106*, 5474–5489.

Sumathi, R.; Green, Jr., W. H. Missing thermochemical groups for large unsaturated hydrocarbons: Contrasting predictions of G2 and CBS-Q. *J. Phys. Chem. A* **2002**a, *106*, 11141–11149.

Sumathi, R.; Green, Jr., W. H. A priori rate constants for kinetic modeling. *Theor. Chem. Acc*. **2002**b, *108* (4), 187–213.

Suresh, A. K.; Sharma, M. M.; Sridhar, T. Engineering aspects of industrial liquid-phase air oxidation of hydrocarbons. *Ind. Eng. Chem. Res*. **2000**, *39* (11), 3958–3997.

Susnow, R.; Dean, A.; Green, Jr., W. H.; Peczak, P.; Broadbelt, L. J. Rate-based construction of kinetic models for complex systems. *J. Phys. Chem. A* **1997**, *101*, 3731–3740.

Swihart, M. T.; Girshick, S. L. Thermochemistry and kinetics of silicon hydride cluster formation during thermal decomposition of silane. *J. Phys. Chem. B* **1999**, *103* (1), 64–76.

Syroezhko, A.; Potekhin, V.; Proskury, V. Composition of normal decane liquid-phase oxidation products. *J. Appl. Chem. USSR*. **1970**, *43* (8), 1791–1809.

Syroezhko, A.; Potekhin, V.; Proskury, V. Sequence in formation of basic products of decane liquid-phase oxidation. *J. Appl. Chem. USSR*. **1973**, *46* (2), 388–393.

Tafipolsky, M.; Schmid, R. Calculation of rotational partition functions by an efficient Monte Carlo importance sampling technique. *J. Comput. Chem.* **2005**, *26* (15), 1579–1591.

Tomlin, A.; Pilling, M. J.; Merkin, J.; Brindley, J. Reduced mechanisms for propane pyrolysis. *Ind. Eng. Chem. Res.* **1995**, *34*, 3749–3760.

Tranter, R. S.; Sivaramakrishnan, R.; Brezinsky, K.; Allendorf, M. D. High pressure, high temperature shock tube studies of ethane pyrolysis and oxidation. *Phys. Chem. Chem. Phys.* **2002**, *4* (11), 2001–2010.

Truhlar, D. G. A simple approximation for the vibrational partition function of a hindered internal rotation. *J. Comp. Chem.* **1991**, *12* (2), 266–270.

Truhlar, D. G.; Garrett, B. Variational transition-state theory. *Ann. Rev. Phys. Chem.* **1984**, *35*, 159–189.

Truhlar, D. G.; Garrett, B.; Klippenstein, S. Current status of transition-state theory. *J. Phys. Chem.* **1996**, *100* (31), 12771–12800.

Truong, T. N.; Duncan, W.; Tirtowidjojo, M. A reaction class approach for modeling gas phase reaction rates. *Phys. Chem. Chem. Phys.* **1999**, *1* (6), 1061–1065.

Tsang, W. Chemical kinetic database for combustion chemistry. 3. Propane. *J. Phys. Chem. Ref. Data* **1988**, *17* (2), 887–952.

Tsang, W. Chemical kinetic database for combustion chemistry. 4. Isobutane. *J. Phys. Chem. Ref. Data* **1990**, *19* (1), 1–68.

Tsang, W.; Hampson, R. F. Chemical kinetic database for combustion chemistry. 1. Methane and related compounds. *J. Phys. Chem. Ref. Data* **1986**, *15* (3), 1087–1279.

Turanyi, T. Sensitivity analysis of complex kinetic systems. Tools and applications. *J. Math. Chem.* **1990**, *5*, 203–248.

Ugi, I.; Bauer, J.; Bley, K.; Dengler, A.; Dietz, A.; Fontain, E.; Gruber, B.; Herges, R.; Knauer, M.; Reitsam, K.; Stein, N. Computer-assisted solution of chemical problems - the historical development and present state of the art of a new discipline of chemistry. *Angew. Chem. Int. Edit. Engl.* **1993**, *32*, 201–227.

Van Cauter, K.; Van Speybroeck, V.; Vansteenkiste, P.; Reyniers, M. F.; Waroquier, M. Ab initio study of free-radical polymerization: polyethylene propagation kinetics. *ChemPhysChem* **2006**, *7* (1), 131–140.

Van Geem, K. M.; Reyniers, M. F.; Marin, G. B.; Song, J.; Green, Jr., W. H.; Matheu, D. M. Automatic reaction network generation using RMG for steam cracking of n-hexane. *AIChE J.* **2006**, *52* (2), 718–730.

Van Speybroeck, V.; Van Neck, D.; Waroquier, M. Ab initio study of radical reactions: Role of coupled internal rotations on the reaction kinetics (III). *J. Phys. Chem. A* **2002**, *106* (38), 8945–8950.

Van Speybroeck, V.; Van Neck, D.; Waroquier, M.; Wauters, S.; Saeys, M.; Marin, G. B. Ab initio study of radical addition reactions: Addition of a primary ethylbenzene radical to ethene. *J. Phys. Chem. A* **2000**, *104* (46), 10939–10950.

Van Speybroeck, V.; Vansteenkiste, P.; Van Neck, D.; Waroquier, M. Why does the uncoupled hindered rotor model work well for the thermodynamics of *n*-alkanes. *Chem. Phys. Lett.* **2005**, *402*, 479–484.

Vang, R. T.; Honkala, K.; Dahl, S.; Vestergaard, E. K.; Schnadt, J.; Laegsgaard, E.; Clausen, B. S.; Norskov, J. K.; Besenbacher, F. Controlling the catalytic bond-breaking selectivity of Ni surfaces by step blocking. *Nat. Mater.* **2005**, *4* (2), 160–162.

Vansteenkiste, P.; Van Neck, D.; Van Speybroeck, V.; Waroquier, M. An extended hindered-rotor model with incorporation of Coriolis and vibrational-rotational coupling for calculating partition functions and derived quantities. *J. Chem. Phys.* **2006**a, *124* (4), Art. No. 044314.

Vansteenkiste, P.; Van Speybroeck, V.; Marin, G. B.; Waroquier, M. Ab initio calculation of entropy and heat capacity of gas-phase *n*-alkanes using internal rotations. *J. Phys. Chem. A* **2003**, *107* (17), 3139–3145.

Vansteenkiste, P.; VanSpeybroeck, V.; Verniest, G.; DeKimpe, N.; Waroquier, M. Applicability of the hindered rotor scheme to the puckering mode in four-membered rings. *J. Phys. Chem. A* **2006**b, *110* (10), 3838–3844.

Wang, L. F.; Song, Y. G.; Zhang, X.; Liu, Y. An exploratory theoretical elucidation on the peroxyl-radical-scavenging mechanism and structure-activity relationship of nonsteroidal anti-inflammatory drugs. *Bioorg. Med. Chem. Lett.* **2006**, *16* (12), 3241–3244.

Wang, M.; Feng, W. The effect of unsaturated acids on the performance of trimethyloxyl propane ester of fatty acids. *Tribol. T.* **1997**, *40* (3), 521–527.

Weininger, D.; Weininger, A.; Weininger, J. L. Smiles. 2. Algorithm for generation of unique smiles notation. *J. Chem. Inf. Comp. Sci.* **1989**, *29* (2), 97–101.

Wells, D.; Delgass, W.; Thomson, K. Formation of hydrogen peroxide from H_2 and O_2 over a neutral gold trimer: a DFT study. *J. Catal.* **2004**a, *225* (1), 69–77.

Wells, D. H.; Delgass, W. N.; Thomson, K. T. Evidence of defect-promoted reactivity for epoxidation of propylene in titanosilicate (TS-1) catalysts: A DFT study. *J. Am. Chem. Soc.* **2004**b, *126* (9), 2956–2962.

Westbrook, C. K.; Pitz, W. J.; Curran, H. J.; Boercker, J.; Kunrath, E. Chemical kinetic modeling study of shock tube ignition of heptane isomers. *Int. J. Chem. Kinet.* **2001**, *33* (12), 868–877.

Wijaya, C.; Sumathi, R.; Green, Jr., W. H. Thermodynamic properties and kinetic parameters for cyclic ether formation from hydroperoxyalkyl radicals. *J. Phys. Chem. A* **2003**, *107* (24), 4908–4920.

Wong, B. M.; Green, Jr., W. H. Effects of large-amplitude torsions on partition functions: Beyond the conventional separability assumption. *Mol. Phys.* **2005**, *103* (6-8), 1027–1034.

Wong, B. M.; Thom, R. L.; Field, R. W. Accurate inertias for large-amplitude motions: Improvements on prevailing approximations. *J. Phys. Chem. A* **2006**, *110* (23), 7406–7413.

Wong, H. W.; Li, X. E.; Swihart, M. T.; Broadbelt, L. J. Encoding of polycyclic Si-containing molecules for determining species uniqueness in automated mechanism generation. *J. Chem. Inf. Comp. Sci.* **2003**, *43* (3), 735–742.

Wong, H. W.; Li, X. G.; Swihart, M. T.; Broadbelt, L. J. Detailed kinetic modeling of silicon nanoparticle formation chemistry via automated mechanism generation. *J. Phys. Chem. A* **2004**a, *108* (46), 10122–10132.

Wong, H. W.; Nieto, J. C. A.; Swihart, M. T.; Broadbelt, L. J. Thermochemistry of silicon-hydrogen compounds generalized from quantum chemical calculations. *J. Phys. Chem. A* **2004**b, *108* (5), 874–897.

Xie, L.; Liu, H. Y.; Yang, W. T. Adapting the nudged elastic band method for determining minimum-energy paths of chemical reactions in enzymes. *J. Chem. Phys.* **2004**, *120* (17), 8039–8052.

Yaluris, G.; Rekoske, J. E.; Aparicio, L.; Madon, R. J.; Dumesic, J. A. Isobutane cracking over Y-zeolites: I. Development of a kinetic model. *J. Catal.* **1995**, *153*, 54–64.

Zamboni, G., Ed.; *Additive Engine Oils*; Petroleum Educational Institute, 1945.

Zavitsas, A. Factors controlling reactivity in hydrogen abstractions by free radicals. *J. Chem. Soc. Perk. T. 2* **1996**, *3* (3), 391–393.

Zavitsas, A.; Chatgilialoglu, C. Energies Of activation - The paradigm of hydrogen abstractions by radicals. *J. Amer. Chem. Soc.* **1995**, *117* (43), 10645–10654.

Zhang, S.; Truong, T. N. VKLab version 1.0, 2001; University of Utah, 2001.

Zupanc, C.; Hornung, A.; Hinrichsen, O.; Muhler, M. The interaction of hydrogen with Ru/MgO catalysts. *J. Catal.* **2002**, *209* (2), 501–514.